Investigation of Airborne Particles by On-Line Single-Particle Mass Spectrometry with Novel Ionization Approaches

Kumulative Dissertation

zur Erlangung des akademischen Grades
doctor rerum naturalium (Dr. rer. nat.)
an der
Mathematisch-Naturwissenschaftlichen Fakultät
der Universität Rostock

vorgelegt von

Julian Alexander Schade

geboren am 29.09.1990 in Dortmund

Rostock, November 2020

Die vorliegende Arbeit wurde in der Zeit von Oktober 2016 bis November 2020 im Arbeitskreis Analytische Chemie von Prof. Dr. Ralf Zimmermann am Institut für Chemie an der Universität Rostock angefertigt.

Einreichung der Dissertation: 11.11.2020

Wissenschaftliches Kolloquium: 19.01.2021

1. Gutachter:

   Prof. Dr. Ralf Zimmermann, Lehrstuhl für Analytische Chemie, Abteilung Technische und Analytische Chemie, Institut für Chemie, Mathematisch-Naturwissenschaftliche Fakultät, Universität Rostock und Gruppenleiter Comprehensive Molecular Analytics, Helmholtz Zentrum München

2. Gutachter:

   Prof. Dr. Thomas Leisner, Lehrstuhl für Physik der Atmosphäre, Institut für Umweltphysik, Fakultät für Physik und Astronomie, Universität Heidelberg und Leiter des Instituts für Meteorologie und Klimaforschung, Fakultät für Physik, Karlsruher Institut für Technologie

Contributions to Scientific Publications

The following manuscripts were created with Julian Schade as first author or co-author with significant contribution and published in peer-reviewed journals. The contribution of Julian Schade to each publication is described in detail below.

Publication 1

Title:	Aerosol Mass Spectrometer for Simultaneous Detection of Polyaromatic Hydrocarbons and Inorganic Components from Individual Particles
Authors:	Johannes Passig, Julian Schade, Markus Oster, Matthias Fuchs, Sven Ehlert, Cornelia Jäger, Martin Sklorz, and Ralf Zimmermann
Journal:	Analytical Chemistry, 89, 6341-6345
Year:	2017

Johannes Passig and Julian Schade contributed equally to this work (shared first authorship). Julian Schade took part in the development of the instrumental setup, did the optimization and measurements, analyzed the data and worked on the manuscript.

Publication 2

Title:	Dynamic changes in optical and chemical properties of tar ball aerosols by atmospheric photochemical aging
Authors:	Chunlin Li, Quanfu He, Julian Schade, Johannes Passig, Ralf Zimmermann, Daphne Meidan, Alexander Laskin, and Yinon Rudich
Journal:	Atmospheric Chemistry and Physics, 19, 139-163
Year:	2019

Julian Schade contributed the single-particle REMPI-MS measurements and revised paragraphs in the manuscript.

Publication 3

Title:	Spatially Shaped Laser Pulses for the Simultaneous Detection of Polycyclic Aromatic Hydrocarbons as well as Positive and Negative Inorganic Ions in Single Particle Mass Spectrometry
Authors:	Julian Schade, Johannes Passig, Robert Irsig, Sven Ehlert, Martin Sklorz, Thomas Adam, Chunlin Li, Yinon Rudich, and Ralf Zimmermann
Journal:	Analytical Chemistry, 91, 10282-10288
Year:	2019

Julian Schade took part in the development of the instrumental setup, did the measurements, analyzed the data, prepared the figures and worked on the manuscript.

Publication 4

Title: Resonance-enhanced detection of metals in aerosols using single-particle mass spectrometry

Authors: Johannes Passig, <u>Julian Schade</u>, Ellen Iva Rosewig, Robert Irsig, Thomas Kröger-Badge, Hendryk Czech, Martin Sklorz, Thorsten Streibel, Lei Li, Xue Li, Zhen Zhou, Henrik Fallgren, Jana Moldanova, and Ralf Zimmermann

Journal: Atmospheric Chemistry and Physics, 20, 7139-7152

Year: 2020

Johannes Passig and Julian Schade contributed equally to this work (shared first authorship). Julian Schade performed the measurements, analyzed the data, prepared the figures and worked on the manuscript.

Rostock, den⎯⎯⎯⎯⎯⎯⎯⎯ Unterschrift⎯⎯⎯⎯⎯⎯⎯⎯⎯⎯⎯

Acknowledgements

The study of aerosol particles in analytical chemistry and atmospheric science utilizing advanced measurement techniques requires complex research and data interpretation from advanced experiments. Therefore, many people were involved in this work, providing their scientific and non-scientific knowledge and help for which I want to express my gratitude.

First of all, I would like to thank my supervisor **Professor Dr. Ralf Zimmermann**, who gave me the opportunity to work in this exciting research field and always encouraged and motivated me, especially when it came to new ideas and research topics. Furthermore, I want to express my deepest gratitude to my co-supervisor, **Dr. Johannes Passig**. He always stood behind me during this intense time while developing new measurement techniques and during long and extraordinary field measurements. Each day we work together, I learn something new, and he indeed is one of the main reasons for finishing this work.

I also want to thank **Dr. Martin Sklorz** and **Dr. Robert Irsig**, providing their time and help concerning instrumentational or theoretical issues. We always had excellent and helpful discussions and laboratory time together in Rostock or at several measurement campaigns.

A warm thanks belong to **Thomas Kröger-Badge**, who helped me with technical developments and supported the work at our complex mass spectrometers. We always had a good time during work in the laboratory or on measurement campaigns.

I have to thank all the colleagues at the Joint Mass Spectrometry Center in Rostock and Munich for integrating me into this group and for such a friendly and warm atmosphere. I hardly believe that there is a better environment in a working group for elaborating a dissertation.

I also want to thank **Anika Neumann** for introducing me to this working group and being a good friend for all these years. I also thank my office mates **Dr. Christopher Rüger**, **Marco Schmidt**, **Paul Kösling**, and **Lukas Friederici**, for long and interesting discussions, especially on non-scientific topics.

A special thanks belong to all my friends and family who helped me through this time and, of course, to my parents who always supported me. Finally, I want to thank **Anna-Lena** for being you, supporting me all the time, and giving me the strength, I needed during my PhD studies.

<div align="center">Thank you!</div>

Zusammenfassung

Die vorliegende Dissertation befasst sich mit der Entwicklung und Optimierung neuartiger Ionisationsmechanismen in der Einzelpartikel-Massenspektrometrie (SPMS). Diese Technologie ermöglicht in Echtzeit die massenspektrometrische Analyse der chemischen Zusammensetzung einzelner Partikel, in Abhängigkeit der jeweiligen Größe, in einem gesundheits- und klimarelevanten Bereich unterhalb von $2,5\,\mu m$ sowie Quellenzuordnung atmosphärischer Aerosole. Trotz der üblichen universellen Ionisationsmethode dieser Messtechnik, ist die Analyse karzinogener polyzyklischer aromatischer Kohlenwasserstoffe (PAKs) und deren Verteilung innerhalb einzelner Partikelklassen aufgrund von Limitierungen der Ionisation nur eingeschränkt möglich. Ziel dieser Arbeit ist die Entwicklung neuartiger Ionisationsansätze für die SPMS zur effizienteren Analyse organischer und anorganischer Schadstoffe (PAKs, Metalle), um zu einem besseren allgemeinen Verständnis atmosphärischer Aerosole und deren Auswirkungen auf das Klima und die Gesundheit beitragen zu können. Im Rahmen dieser Arbeit wurde erstmals in SPMS die Laser Desorption (LD) und anschließende Analyse von PAKs mittels Resonanz-Verstärkter Multiphotonen Ionisation (REMPI) mit der universellen Laser Desorption/Ionisation (LDI) gekoppelt. Der neuartige Ionisationsansatz erlaubt dabei die Analyse der Verteilung von PAKs auf Einzelpartikeln in Kombination mit klassischen Methoden zur Quellenzuordnung in Abhängigkeit der Partikelgröße. Zunächst wurden beide Flugzeit-Massenspektrometer eines SPMS Systems zur Detektion positiver Ionen aus unterschiedlichen Ionisationsprozessen verwendet, was einen Verlust der negativen Ionen aus dem LDI-Prozess zur Folge hat. Dem gegenüber steht jedoch der Informationsgewinn zur Verteilung der gesundheitsgefährdenden PAKs. Diese neuartige Ionisationstechnik ermöglicht neue und vertiefende Einblicke in Partikelsysteme, wie zum Beispiel tar balls. Diese Spezies bildet eine Unterkategorie der organischen Aerosole und tritt hauptsächlich bei Verbrennungsprozessen auf, die auch die Hauptursache der PAK-Emission darstellen. Detaillierte PAK-Massenspektren geben dabei Hinweise auf das Absorptions- und Alterungsverhalten dieser Partikel in der Atmosphäre. In einer weiteren Evolutionsstufe dieser Messtechnik konnten erstmals PAKs mittels LD-REMPI sowie organische und anorganische Bestandteile über einen vollständigen LDI-Prozess mit positiven und negativen Ionen von einzelnen Partikeln nachgewiesen werden. Diese Methode bietet dabei einen, bisher in dieser Tiefe nicht möglichen, Einblick in die chemische Zusammensetzung des Partikels bei gleichzeitiger Bestimmung der Verteilung organischer und aromatischer Schadstoffe. Neben dem Vorkommen und der Verteilung partikelgebundener PAKs ist auch der Metallgehalt atmosphärischer Partikel für marine Ökosysteme sowie die menschliche Gesundheit von großer Bedeutung. Die Resonante Ionisation partikelgebundener Metalle, wie sie in dieser Arbeit entwickelt wurde, führt zu einer Steigerung der Ionisationseffizienz in SPMS und damit zu einer verbesserten Analyse der Verteilung und dem atmosphärischen Transport dieser Elemente. Zusammenfassend konnten im Rahmen dieser Dissertation neue Ionisationsansätze zur chemischen Analyse von Einzelpartikeln entwickelt und optimiert werden. Insbesondere

durch die Kombination resonanter Ionisationsmethoden mit konventionellen Techniken konnten wesentliche Fortschritte in der Weiterentwicklung der Einzelpartikelanalyse und dem Verständnis atmosphärischer Partikel erzielt werden.

Abstract

The dissertation focuses on the development and optimization of novel ionization mechanisms in single-particle mass spectrometry (SPMS). This technology enables real-time mass spectrometric analysis of the chemical composition of single-particles as a function of their size in a health and climate-relevant size range below 2.5 μm as well as source apportionment of atmospheric aerosols. Despite the universal character of the standard ionization method in SPMS, the analysis of carcinogenic polycyclic aromatic hydrocarbons (PAHs) and their distribution within individual particle classes is limited due to ionization restrictions. This work aims to develop novel ionization approaches in SPMS for a more efficient analysis of organic and inorganic pollutants (PAHs, metals) to contribute to a better overall understanding of atmospheric aerosols and their effects on climate and health. For the first time in SPMS, laser desorption (LD) with subsequent analysis of PAHs using resonance-enhanced multiphoton ionization (REMPI) was coupled with universal laser desorption/ionization (LDI). The novel ionization approach allows the analysis of the distribution of PAHs on single particles in combination with classical methods of source apportionment depending on the particle size. Here, both time-of-flight mass spectrometers of the SPMS system are used to detect positive ions, which results in a loss of negative ions from the LDI process, but this is counterbalanced by the gain of information on the distribution of the health-endangering PAHs. This novel ionization technique provides new and deeper insights into particle systems such as tar balls, a species of organic aerosols and occurs mainly in combustion processes, which are also the leading cause of PAH emissions. Detailed PAH mass spectra provide information on the absorption and aging behavior of these particles in the atmosphere. In a further evolutionary stage of this measurement technique, PAHs could be detected for the first time employing LD-REMPI along with organic and inorganic constituents via a complete LDI process with positive and negative ions of individual particles. This method offers a complete insight into the chemical composition of the particle while simultaneously determining the distribution of organic aromatic pollutants. In addition to the occurrence and distribution of particle-bound PAHs, the metal content of atmospheric particles is of great importance for marine ecosystems and human health. Resonant ionization of particle-bound metals leads to an increase in ionization efficiency in SPMS and, thus, to an improved analysis of the distribution and atmospheric transport of these elements.

In summary, new ionization approaches for the chemical analysis of single particles could be developed and optimized in the context of this dissertation. By combining resonant ionization methods with conventional techniques, significant progress in the further development of single-particle analysis and the understanding of atmospheric particles could be achieved.

Table of Contents

List of Abbreviations

AMS	Aerosol Mass Spectrometer
ATOF	Aerosol Time-Of-Flight
ATOF-MS	Aerosol Time-Of-Flight Mass Spectrometry
BBCES	Broadband Cavita Enhanced Sepctrometer
BBOA	Biomass Burning Organic Aerosol
BC	Black Carbon
BrC	Brown Carbon
CCN	Cloud Condensation Nuclei
DE	Delayed Extraction
DNA	Desoxyribonucleic Acid
EAD	Eqivalent Daytime Oxydation Days
EC	Elemental Carbon
EI	Electron Impact Ionisation
ELVOC	Extremely Low-Volatile Organic Carbon
FHG	Fourth Harmonic Generation
GCMS	Gas Chromatography Mass Spectrometry
HNLC	High Nitrate Low Chlorophyll
HOA	Hydrocarbon-like Organic Aerosol
HR	High Resolution
IE	Ionization Energy
INP	Ice Nucleation Particle
IPCC	Intergovernmental Panel on Climate Change
IR	Infrared
IVOC	Intermediate Volatile Organic Carbon
LD	Laser Desorption
LDI	Laser Desorption/Ionization
LVOC	Low-Volatile Organic Carbon
MCP	Micro Channel Plate
MS	Mass Spectrometry
NIST	National Institute for Standards and Technology
NOC	Nitrogen-Containing Organic Compounds
OA	Organic Aerosol
OC	Organic Carbon
OFR	Oxygen Flow Reactor
OM	Organic Matter
OOA	Oxidized Organic Aerosol

OPO	Optical Parametric Oscillator
PAH	Polycyclic Aromatic Hydrocarbons
PI	Photoionization
PM	Particulate Matter
PMT	Photomultiplier
POA	Primary Organic Aerosol
PTOF	Particle Time-Of-Flight
REMPI	Resonance-Enhanced Multiphoton Ionization
RF	Radiative Forcing
RI	Refractive Index
ROS	Reactive Oxygen Species
SHG	Second Harmonic Generator
SOA	Secondary Organic Aerosol
SP	Songle-Particle
SPMS	Single-Particle Mass Spectrometry
SVOC	Semi-Volatile Organic Carbon
TD	Thermo Desorption
TEA	Transversaly Excited Atmospheric Pressure Laser
TOF	Time-Of-Flight
TOF-MS	Time-Of-Flight Mass Spectrometry
UV	Ultraviolet
VOC	Volatile Organic Carbon
VUV	Vacuum-Ultraviolet
WHO	World Health Organisation

List of Figures

List of Tables

1. Introduction

Aerosols are defined as a suspension of small liquid droplets or solids in gas, whereas the expression of atmospheric aerosols in the current discussion mostly refers to solid particles in air exclusively. In atmospheric science, the term particulate matter (PM) is commonly used. Aerosol particles cover a size range of 10^{-9} - 10^{-4} m and can have diverse natural and anthropogenic sources (mineral dust, sea salt, soot, etc.). The lower limit of the size distribution is determined by molecules and clusters, whereas the upper limit is formed by the prompt sedimentation of large particles or droplets. [1] Scientifically relevant size categories are PM0.1 ($< 0.1\,\mu$m, ultrafine particles), PM1, PM2.5 (fine particles), and PM10 (coarse particles), where the number indicates the maximum of the respective size range in micrometers (e.g., PM2.5, particles smaller than 2.5 μm).

1.1.   Sources and physical parameters of atmospheric aerosol

Particulate matter can be emitted into the air from a variety of sources. In general, they are either emitted directly into the air as particles (primary aerosol) or are formed in the atmosphere by gas-to-particle conversion processes (secondary aerosol). For example, semi-volatile organic compounds (SVOC), as well as condensable gases, condense in the cooling exhaust gas stream through homogeneous or heterogeneous condensation with ultrafine primary particles (nucleation mode). By coagulation with already emitted particles, the accumulation mode ($0.1 – 1\,\mu$m) is formed. Through reaction with volatile organic compounds (VOC) and further coagulation, atmospheric particles can continue to grow until sedimentation predominates due to their size (see Fig. 1 (b)). The most common natural particle classes are sea spray and soil erosion. However, volcanic activity, wildfires, and biological emissions such as pollen, plant debris, and microorganisms also contribute to the total volume of natural aerosols. [2] Anthropogenic aerosols are caused by the combustion of fossil and non-fossil fuels, road, rail, and air traffic, industrial production, heating and cooling, road dust, and cooking. [3], [2] Due to the daytime, position, weather conditions, and the particle formation mechanisms mentioned above, the size and chemical composition of the particles changes. In particular, condensation of gases on their surface, coagulation with other particles, a multitude of atmospheric chemical reactions, and activation to cloud or ice condensation nuclei play a significant role (see Fig. 1). Ultrafine particles (PM1) occur in a number concentration from 10 to 10^5 cm^{-3} with high values for smaller particles. [4], [5] Once particles of this size class are emitted into the atmosphere, they grow rapidly by the aforementioned chemical and physical processes or by uptake of gaseous precursors. [6] Particle deposition can occur through two different mechanisms: Sedimentation of large particles on the earth's surface, called dry deposition, or by precipitation droplet washing, called wet deposition. Due to these processes, particles of the accumulation mode ($0.2 – 1\,\mu$m) have a residence time in the atmosphere of a few days up to a few weeks. As a consequence, this size class dominates in natural environments, with ultrafine primary particles predominant in densely populated urban environments and a number concentration in the order of 10^5 cm^{-3}. [4]

Due to the variety of origin of aerosols, particles of the same diameter can possess different shapes and morphology. [7]–[9] Particle concentrations (e.g., number, mass, chemical species) are often specified and determined in relation to the particle size. In case of deviations from the ideal spherical shape and the standard density of 1 g cm^{-3} there are significant differences depending on the measuring technology. [10] The aerodynamic diameter, for example, which
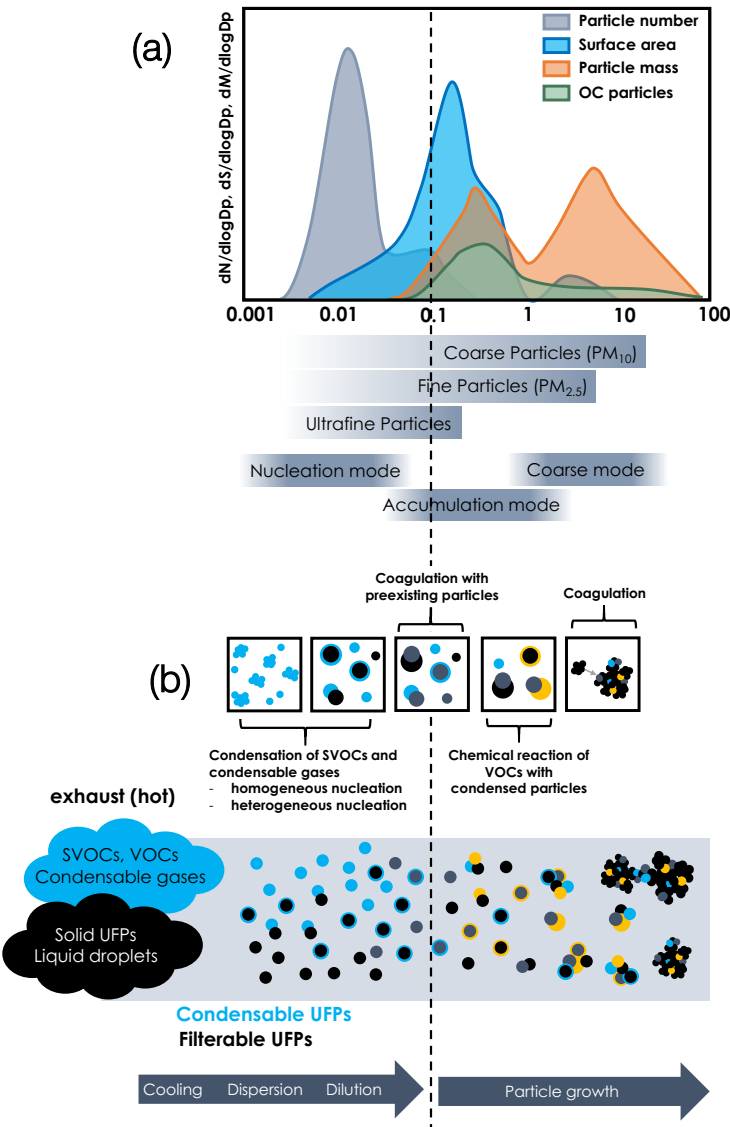
Fig. 1 Size modes and growth mechanism of aerosols. (a) Ultrafine particles typically show high particle numbers, whereas surface area, particle mass (PM), and OC (organic carbon) particles peak around the accumulation mode. However, the highest particle mass contribution is caused by large particles of the coarse mode. (b) Condensation, coagulation, and chemical reaction processes cause particle growth in the atmosphere.

plays a decisive role in the context of this work, is defined as the spherical diameter of a particle with standard density and the same terminal velocity as the considered particle. [9] Correlations between morphology, density, and the influences of the different measuring principles are extremely diverse and complex and are described and discussed in detail in the literature. [9], [10] However, the total mass of particles in the ambient air is usually relatively small and ranges from $1 - 100\,\mu g\,m^{-3}$. Whereas the average in Germany is in the lower range with about $15\,\mu g\,m^{-3}$, individual pollution events in metropolitan areas can cause concentrations of up to $400\,\mu g\,m^{-3}$. [11] In atmospheric particle analysis not only the particle size, density, morphology, and mass but also the particles mixing state is of major interest. Particle mixing state describes the distribution of chemical compounds in individual particles of a class in an aerosol. Internal mixing occurs when a particle class of an aerosol consists of the same mixture of chemical compounds, external mixing is present when all particles consist of pure chemical species. In atmospheric aerosols pure mixing states are extremely rare. [12]

1.2.   Chemical composition

Generally expressed, atmospheric particles are often composed of an organic and an inorganic fraction, the inorganic part mainly consisting of sulfate, nitrate, ammonium, and chloride, except mineral particles (see Tab. 1). [13] However, the total amount of both fractions depends on the respective emission source and atmospheric and environmental influences, such as solar radiation and photochemistry, and can vary considerably. Other inorganic elements such as alkali and transition metals and inorganic molecules also play an essential role in the evaluation and source apportionment. Some examples are listed in Tab. 1. The carbonaceous and organic aerosol (OA) fraction is much more complex and divided into different classes based on various analytical methods. One classification of OA was established by evaluating aerosol mass spectra (AMS) and is based on measurements of ambient particles: hydrocarbon-like OA (HOA), biomass burning organic aerosol (BBOA), and oxidized organic aerosol (OOA) resulting from fossil fuel and biomass combustion and associated with secondary organic aerosol (SOA). The atmospheric SOA formation process is extremely complex and is based on the interaction of anthropogenic aerosol species (SO_2, NO_x, sulfate, nitrate, ammonium) with natural biogenic aerosol. [6], [14] HOA and BBOA are released by primary emissions and belong to primary organic aerosols (POA). [15] Another approach to classify OA focuses on the condensation and mobility of the organic fraction. It was developed by Donahue et al.: volatile (VOC), intermediate volatile (IVOC), semi-volatile (SVOC), low-volatile (LVOC), and extremely low-volatile (ELVOC) organic compounds belong to the organic aerosol (OA) and are described by volatility and the oxidation states of carbon. [16], [17]

1.3.   Environmental impact

Despite their comparatively small mass, particles have a significant impact on global weather, climate, environment, and human health. [1], [3], [18], [19] Fine and ultrafine particles have a similar size as the incident light wavelength and, therefore, probably have a more significant effect on climate than large particles at comparable PM concentrations. Furthermore, they have a longer residence time in the atmosphere and can therefore have a more global and delocalized effect regarding emission location. [14] Atmospheric aerosols are capable of reflecting, refracting, diffracting, and absorbing solar radiation, which can have a considerable influence on the radiation balance of the earth's atmosphere, which describes the direct effect and is termed radiative forcing (RF). Radiative forcing is the difference between absorbed sunlight and reflected energy into space and is measured in W m^{-2}. Black carbon (BC), which is mainly produced by biomass burning and fossil fuels, can heat the earth's atmosphere by absorbing sunlight over a broad wavelength spectrum and representing, besides CO_2, one of the most important anthropogenic emissions. [20], [21] BC indicates, according to IPCC 2013, an RF of +0.64 W m^{-2} with uncertainty limits of (0.25 to 1.09), in contrast to the total aerosol output, which shows a negative value (-0.35 W m^{-2}). [18] Also, once emitted into the atmosphere, brown carbon (BrC), a fraction of OA which, unlike most OC compounds, absorbs light in the visible (380 – 750 nm) and near-UV (300 – 400 nm) range, has a negative value for radiative forcing, on snow and ice-

covered surfaces, in turn, the values shift to positive numbers. [18], [22], [23] Other aerosols (e.g., colorless particles) can also cause a cooling effect, for example, by scattering light back to space. Atmospheric aerosols can also act as cloud condensation nuclei (CCN) and ice nucleation particles (INP) and thus have an indirect climatic effect. [6] A modeling study of D'Andrea et al. 2013 indicates that in many continental locations, low-volatility SOA may be causing more than half of the total CCN. [24] Both the indirect effect of CCN/INP and the strength of scattering and absorption of solar radiation through atmospheric aerosols are strongly dependent on the chemical and physical particle properties. [25] However, anthropogenic particle emissions can also significantly impact the environment through sedimentation and the associated input of nutrients into the oceans. [26] Iron is considered a growth-limiting nutrient in high nitrate, low chlorophyll (HNLC) regions and plays a crucial role in marine primary production. Although the amount of iron introduced by mineral dust is significantly higher, anthropogenic bioavailability is considerably more significant due to its partially much higher solubility and stability in the oxidizing environment of seawater. [26]–[28] Solubility and bioavailability are strongly influenced by the oxidation state (Fe(II), Fe(III)), organic ligands and chelating agents, and particle pH. [28], [29] When deposited into ocean water, inorganic Fe(II) is oxidized within minutes to Fe(III), which has a significantly reduced solubility and immediately coagulates and forms nanoparticles. [28], [30] Organic ligands and chelating agents strongly increase the solubility, so it is assumed that $> 99\%$ of the bioavailable iron is present in this form. [28], [31] Also, particle pH, which can be significantly reduced by acidic secondary ions (e.g., NO_3^-, SO_4^{2-}, Cl^-), leads to a better Fe solubility in ocean water. [29] While cobalt, manganese, and zinc are also essential trace elements, copper is toxic to some species in high concentrations. [32], [33] Important elements, whose emission and input into the oceans has strongly increased due to industrialization, are Al, Ti, Mn, Fe, Co, Cu, Zn, Cd, and Pb, which can act as important catalysts or inhibitors in the context of biogeochemistry. [26], [34] This demonstrates the complex correlations between anthropogenic particle emissions and natural reaction processes in the atmosphere and reveals that PM emissions can have both positive and negative feedback on global warming. According to the IPCC Report 2013, there is nearly no doubt that the concentration, chemical composition, and spatial distribution of aerosols present in the earth's atmosphere have changed since the start of industrialization (1750). However, there still exist a variety of uncertainties in estimations of the aerosols climate effects. [18]
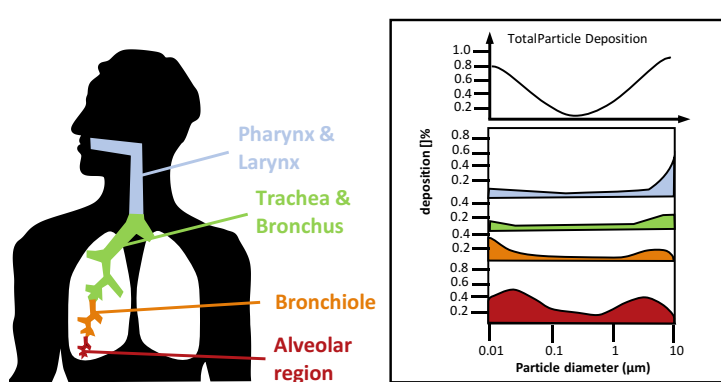

Fig. 2 Size-dependent regional deposition of PM in the human respiratory organs. Especially the ultrafine PM0.1, which reach the highest particle number concentrations in polluted regions, can deposit into the alveolar region, where the gas exchange between air and blood occurs. (adapted from Heyder 2004 [42])

1.4.   Health effects

In addition to the effects on the earth's climate, atmospheric aerosols also severely impact human health. Even low concentrations can lead to significant negative consequences and influence morbidity and mortality when exposed over a long period. A large variety of epidemiological and toxicological studies have shown and confirmed the health effect of PM. [19], [35]–[41] Both the cardiovascular system and the respiratory organs can be damaged by PM. The exact toxicity and direct effect of particles depend on many factors, such as chemical composition, size, and physical properties. Not all types of aerosols are harmful and dangerous to health. A good example is the high sea salt concentration in the air in coastal climatic health-resorts. When breathing in PM, not all of it reaches the alveoli, where the gas exchange between air and blood occurs. Only fine and ultra-fine particles (PM2.5, PM1, and PM0.1) can penetrate deep into the respiratory tract and cause damage there through deposition and reaction with the tissue. [42] While larger particles are already deposited in the upper airways (pharynx and larynx), PM0.1 particles can easily penetrate deep into the lungs and are effectively deposited in the alveoli (Fig. 2). Especially particles from combustion processes, which contain some very harmful substances (e.g., PAHs, soot, toxic combustion products, and metals), are increasingly found in this size class and well known for their long term toxicity. [37], [39], [43]–[46] Polycyclic aromatic hydrocarbons (PAH) form a subgroup in organic chemistry and consist of at least two aromatic rings. The PAH molecules are mainly formed during natural and anthropogenic combustion processes and partly have a strong carcinogenic and mutagenic effect. The most significant carcinogenic effect on human cells is caused by the reaction of PAH metabolites with DNA, resulting in complications in the subsequent replication and transcription of DNA. [39], [38] PAHs are metabolized through oxidative reaction pathways, resulting in electrophilic reactive products such as epoxides. [40], [47]

Fig. 3   One possible Metabolism reaction pathway of B[a]P with P_{450}Cytochrome and epoxide hydrolase and subsequent binding reaction to the DNA nucleobase Guanine.

Reactions with nucleophilic centers of DNA nucleobases and proteins result in covalent binding of PAH metabolites, which can lead to DNA mutations and genetic effects such as cancer, cardiovascular damage, and adverse reproductive outcomes. [41] Benz[a]pyrene is known for its strong carcinogenic effect and was used in Fig. 3 as an example substance for the metabolic pathway and the binding reaction with DNA. The carcinogenic effect of soot was already proven in the late 18th century. Through numerous studies, three main pathways of the disease could be proven and clarified: Cardiovascular diseases, which can be caused by reactions of lung cells and platelet cells, cancer via DNA

methylation and histone modification, respiratory diseases by infiltration of eosinophils and mast cells. [37] Besides PAHs and soot, also metals are often critical and harmful to human health, as they can cause and intensify inflammations via oxidative stress (e.g., zinc, lead, cadmium, iron, nickel, copper). [29], [48], [49] Due to their high redox activity, transition metals can contribute to an increased formation of ROS (reactive oxygen species) in the human body. [50] ROS are hydrogen peroxide (H_2O_2), superoxide (O_2^-), hydroxyl radicals ($\cdot OH$), and singlet oxygen ($^1O_2$), and an increase of these reactive species in the human body can lead to various reactions such as the substitution of unnatural metals in enzymes, disorders of metabolic and antioxidant pathways, and repression of DNA repair enzymes.

2. Analysis of atmospheric particles

In atmospheric science, many different ways of classifying particles are known: origin (volcanic ash, biomass combustion, desert dust, marine aerosols, etc.), regional occurrence (urban, forest, marine aerosol, etc.), function (cloud condensation nuclei), and chemical composition (soot, mineral dust, organic aerosol, salt, ammonium, sulfate, phosphate, etc.). Therefore, the enormous heterogeneity and variability of atmospheric particles complicate the analytical determination of detailed data regarding quantitative chemical speciation, so that characterization is frequently reliant on sum parameters or physical characteristics such as light absorption. Stationary off-line laboratory analysis methods offer various techniques for chemical characterization and can sometimes detect and determine thousands of substances in a single filter sample with enormous accuracy and high resolution. [27], [28] However, temporal information is not available, and artifacts (e.g., volatilization of organics from filter material during sampling) can partly influence the evaluation. [53] In contrast, on-line analysis techniques provide time-resolved data but only approximate information about the chemical composition due to significantly lower resolution and sample material. [54] Nevertheless, the large variety and number of different particle classes that are simultaneously present in the atmosphere show that the time-resolved on-line analysis of single particles offers an important element for a better understanding of the impact of atmospheric aerosols on the environment and human health. In the context of this work, on-line mass spectrometric analysis methods for the investigation of single particles were applied and further developed to contribute to a better chemical and physical understanding of atmospheric particles.

2.1.   Laser-based analysis of individual complex particles

Laser-based analysis of single particles using time-of-flight mass spectrometry (TOF-MS) has gained in importance over the last decades and is a powerful method for on-line analysis of the chemical composition of climate- and health-related atmospheric aerosols (PM2.5). Adapted to the different questions in atmospheric sciences, however, several different ionization techniques have been developed over time, which can roughly be divided into two categories: (1) laser desorption/ionization (LDI), (2) laser or thermal desorption prior to ionization. The first approaches

of LDI-SPMS (laser desorption/ionization single-particle mass spectrometry) date back to the 1970s. With LAMMA (laser microprobe mass analysis), it was possible to obtain either positive or negative mass spectra of single particles sampled on a substrate, selected by the operator through an optical microscope. [55] In the 1980s and 90s, techniques for analyzing single free-flying isolated airborne particles in positive or negative ion mode were developed. [56], [57] Further developments facilitated the simultaneous detection of positive and negative ions to obtain the full information capacity of LDI-SPMS. [28], [29] LDI is a non-selective and compelling ionization method, making it possible to analyze both organic and inorganic particles in SPMS. The process of LDI is explained in more detail in section 3.1.3.2. During the analysis of single particles through LDI, characteristic fragment ions are generated depending on the particle class, which plays an important role in evaluating mass spectra and particle source apportionment. In the positive mass spectra, carbon clusters (C_1^+, C_2^+, C_3^+, ...), electropositive metals, transition metals, alkali and alkaline earth metals (e.g. Na^+, K^+, Al^+, Fe^+, Pb^+), organic fragments ($[C_xH_y]^+$), and cluster ions (e.g., $[Na_2Cl]^+$, $[K_2Cl]^+$) are observed. In the negative spectra, however, electronegative elements (e.g. Cl^-), organic fragments ($[C_xH_y]^+$, also with heteroatoms N or O), carbon clusters (C_1^-, C_2^-, C_3^-, ...), oxygen-containing anions (e.g., NO_3^-, HSO_4^-, PO_3^-), and cluster ions (e.g., $[NaCl_2]^-$, $[KCl_2]^-$) can be found (see Tab. 1). Multi-step ionization techniques have been developed to further increase the ionization efficiency, and selecting information content, and, for example, to detect and investigate PAHs on single particles. [26] – [29]

2.2. Novel ionization approach in on-line SPMS

LDI-SPMS is a powerful tool for analyzing airborne particles and has already produced interesting and important research results in various studies. [54], [64], [65] Due to its universality concerning origin and chemical composition of the particles and sensitivity to the rather low numbers of produced ions from single particles, this technology is ideally suited for airborne particle analysis and source apportionment. [66]–[71] However, due to its high fragmentation, this method is not well suited for the analysis of polycyclic aromatic hydrocarbons (PAH), which are formed during combustion processes and adsorbed on the particles in the cooling exhaust gas stream. The formation process of particle-bound PAHs is e.g. described in detail by Frenklach 2002. [72] Besides, PAHs are classified as very hazardous to health and are therefore of particular research interest. In various studies PAHs could be detected in combustion particles with SPMS using multi-stage ionization processes (e.g., thermo desorption [73] or laser desorption [61], [62], [74]). One of the tasks of this work was to analyze PAHs from single particles in a multi-step photoionization process using sensitive and selective REMPI (resonance-enhanced multiphoton ionization) and to combine this with the universal LDI in one SPMS system, thus implementing an additional dimension of information to the single-particle analysis.

Tab. 1   Overview of major particle classes and their most frequent cations and anions in laser-based SPMS (laser desorption/ionization). The particle classes and their ion types listed here represent only a small selection of the most frequent atmospheric aerosols. Ambient aerosols are much more complex than possible to present here and contain various internally mixed compounds. The evaluation and source apportionment in SPMS experiments is not based on the mere presence of the ion signals but patterns and characteristic distributions of several ions, using computational methods.

Particle type	Source	Cations	Anions	References
sea salt	sea spray	$^{23}Na^+$, $^{46}Na_2^+$, $^{39}K^+$, $^{81}[Na_2Cl]^+$, $^{139}[Na_3Cl_2]^+$ humid: $^{62}[Na_2O]^+$, $^{63}[Na_2OH]^+$ aged: $^{63}[HNO_3]^+$	$^{35}Cl^-$, $^{37}Cl^-$, $^{23}Na^-$, $[NaCl]^-$, $[NaCl_2]^-$ humid: O^-, $[OH]^-$ aged: $^{46}[NO_2]^-$, $^{62}[NO_3]^-$, $^{97}[HSO_4]^-$	[75]–[77]
mineral dust	erosion	$^{23}Na^+$, $^{24}Mg^+$, $^{27}Al^+$, $^{39}K^+$, $^{40}Ca^+$, $^{48}Ti^+$, $^{56}Fe^+$	O^-, OH^-, $^{26}[CN]^-$, $^{42}[CNO]^-$, $^{59}[AlO_2]^-$, $^{60}[SiO_2]^-$, $^{63}[PO_2]^-$, $^{76}[SiO_3]^-$, $^{79}[PO_3]^-$, $^{103}[AlSiO_3]^-$	[78], [79]
bioaerosols	plant debris, pollen, bacteria	$^{39}K^+$, $^{40}Ca^+$, $CaOH^+$, $CaCN^+$	$^{26}[CN]^-$, $^{42}[CNO]^-$, $^{63}[PO_2]^-$, $^{79}[PO_3]^-$,	[80]–[82]
organic combustion aerosols	biomass combustion, wildfires	$^{39}K^+$, org. fragm., $^{12}C^+$, $^{27}[C_2H_3]^+$, $^{39}[C_3H_3]^+$, $^{43}[C_3H_7]^+$, $^{43}[C_2H_3O]^+$, PAHs	org. fragm., oligomers, $^{46}[NO_2]^-$, $^{62}[NO_3]^-$, $^{63}[PO_2]^-$, $^{79}[PO_3]^-$, C_n^-	[83], [84]
secondary nitrate and sulfate	secondary aerosol, often condensation on primary EC or OC	$^{39}K^+$, $^{43}[C_3H_7]^+$, C_n^+	$^{46}[NO_2]^-$, $^{62}[NO_3]^-$, C_n^-, $^{89}[C_2HO_4]^-$, $^{97}[HSO_4]^-$	[85], [86]
EC (soot)	traffic, fossil fuel combustion	C_n^+	C_n^-	[68], [69]
ship emissions	ship emissions from bunker fuels	C_n^+, $^{40}Ca^+$, $^{51}V^+$, $^{56}Fe^+$, $^{58}Ni^+$, $^{67}[VO]^+$	C_n^-, $^{46}[NO_2]^-$, $^{62}[NO_3]^-$, $^{97}[HSO_4]^-$	[87]–[89]
metal rich	industry, coal/waste combustion	C_n^+, $^{23}Na^+$, $^{39}K^+$, $^{56}Fe^+$, $^{206-208}Pb^+$	C_n^-, $^{35}Cl^-$, $^{37}Cl^-$, $^{46}[NO_2]^-$, $^{62}[NO_3]^-$, $^{97}[HSO_4]^-$	[90], [91]

3. Methodology

In the following sections, the fundamentals of the techniques applied in this work are described and briefly explained. The main focus of this PhD thesis lies on the mass spectrometric analysis of single-particles using different ionization and TOF-MS technology.

3.1.   Ionization

Ionization is of fundamental importance for analysis by mass spectrometric methods. Molecules and atoms are transformed into ions, separated according to their mass-to-charge ratio, and

detected employing secondary electron multipliers. Different methods and techniques for ionization depend on the respective analytes and the available mass analyzers. In general, these are divided into hard and soft ionization types, which mainly differ in the amount of fragmentation or the formation of molecular ions. In the following, the most frequently used hard ionization method (electron impact ionization) and two photoionization techniques are presented, as they were applied in the context of this thesis.

3.1.1. General aspects of ionization in mass spectrometry

The ionization of molecules, atoms, clusters, or particles can produce both positively and negatively charged ions. As explained in more detail in the following sections, a wide variety of ionization techniques are used in this work, which results in the formation of both positively and negatively charged ions. While positively charged ions are primarily formed by electron deprivation, negative ions can be formed by impact reactions and electron capture. To convert an analyte into ions by positive ionization (i.e., EI, REMPI), a certain amount of energy must be supplied to the analyte. This amount of energy is called ionization energy (IE). It is defined as the quantity of energy required to convert an analyte that is in its electronic and vibrational ground state into a positively charged analyte ion that is also in its ground state (adiabatic IE) by the ejection of an electron. Electrons can be ejected from σ-bonds as well as from π-bonds and free electron pairs, whereby the latter is generally preferred because it is the most preferential position for charge localization. [92]

According to the Born-Oppenheimer approximation and the Franck-Condon principle, electrons and nuclei movements can be viewed separately due to the high mass difference since the electronic transitions take place much faster than atomic nuclei need to adjust to a new equilibrium position. Therefore, it is assumed that the atoms' positions, i.e., the bond length, remain constant during ionization. The Franck-Condon factor indicates the probability of a certain transition from the ground state of the neutral particle to a certain oscillation state. The probability of a transition is highest for the maximum interference of the ground state's electronic wave functions and ionized state. The ionization leads to a weakening of the bonds within the ion, which usually causes longer bond lengths and increases the tendency to dissociate the bonds. The more significant the difference in the nuclear spacing of a transition, the higher is the probability that the dissociation barrier will be exceeded and that fragmentation of the molecule will occur. [92] However, since these are considerably simplified assumptions, the individual IEs, in reality, need to be determined individually.

3.1.2. Electron impact ionization (EI)

Electron impact ionization (EI) is the most commonly used ionization technique in the analysis of organic substances using mass spectrometry. Especially in combination with MS techniques and gas chromatography (GCMS), EI is often used, as the analytes already exist in the gaseous phase. In the context of this thesis, this technique was exclusively used in the Aerosol Mass

Spectrometer (AMS) for the analysis of tar balls. The single-particle analyses were all performed by laser-based photoionization.

The basic principle of ionization using EI is the interaction of high-energy electrons with the analytes' valence electrons. First, electrons are emitted from a heated tungsten filament and accelerated with a voltage of 70 V. The resulting kinetic energy of 70 eV is substantially above the ionization energies (IEs) of most existing organic components, which are in the range of 7 to 15 eV. In the mass analyzer's ion source, the accelerated electrons impact orthogonally on the beam of molecules from the inlet system, respectively, the cloud of vaporized analytes in the AMS. Due to the high excess energy of the electrons, ionization and fragmentation occur, which characterizes this method as a hard ionization technique. Molecular ions formed in the first step are in vibrationally and rotationally excited states, which may lead to the breaking of atomic bonds as due to relaxation. [92] An advantage of fragmentation is that it allows conclusions to be drawn about the underlying molecular structure, thus enabling the identification and quantification of the analytes. EI delivers reproducible mass spectra with the highest ionization efficiency at 70 eV, due to the plateau of ionization cross sections at 60 – 80 eV. Whereby, the plateau is caused by the fact that the de-Broglie wavelength directly corresponds to the typical inner atomic distance of the valence electrons. [93] This allows the direct comparison of different mass analyzers using the same ionization method and simplifies evaluation with the benefit of databases. A disadvantage of fragmentation is reflected in the large number of unspecific molecular fragments, making the analysis of complex samples considerably more difficult. For example, samples of different analytes of homologous series provide a large proportion of identical fragment ions and are challenging to identify and quantify in the absence of their molecular ions. Furthermore, the analysis by EI also ionizes the main components of the carrier gas (N_2, O_2, CO_2, noble gases), which makes the analysis of organic trace substances only possible in combination with mass analyzers with a large dynamic range. For these reasons, softer photoionization methods are widely used, which will be presented in the following sections.

3.1.3. Photoionization (PI)

In contrast to EI, photoionization (PI) involves predominantly soft ionization types. For the ionization of the analytes, different light sources can be utilized whose photon energies mostly correspond to the IEs of many organic substances, whereby many more molecular ions than fragment ions are formed. When selecting the light source, continuous light with usually significantly lower photon density or pulsed light can be chosen. For the analytes' ionization, light is required whose photon energy is sufficient to overcome the ionization energy or has a sufficiently high photon density to perform multi-photon processes. In the past, lasers and lamps have been successfully implemented for ionization in mass spectrometry in many scientific studies. [64], [94]–[98] In this thesis, the focus lies on the application of different lasers as light sources. In the following sections, different laser techniques are presented, which were used in this work for Laser Desorption (LD), Laser Desorption/Ionization (LDI), and Resonance Enhanced Multiphoton Ionization (REMPI).

3.1.3.1. Lasers as a light source for PI

Laser stands for Light Amplification by Stimulated Emission of Radiation and delivers intense and coherent light with a narrow bandwidth and low divergence. These properties enable a wide range of applications and have made lasers one of the most important sources of radiation in the natural sciences, technology, and medicine. [99]

Nd:YAG solid state laser

The laser medium of the Nd:YAG laser consists of an yttrium aluminum garnet grating in which Y^{3+} has been partially exchanged for Nd^{3+}. The laser medium is excited (pumped) by a strong external energy supply (flash lamp), resulting in the emission of photons, which produce further photons of the same wavelength and direction. Electrons of the laser medium are transferred from the ground state (E_1) by radiation of a xenon-filled flash lamp into a higher electronically and vibrationally excited state (E_4). Commonly, the E_4 state has a very short lifetime, so the electrons instantly switch to a metastable state (E_3) of lower energy, accompanied by fluorescence and non-radiative transitions.

Fig. 4 The figure illustrates the schematic representation of a Nd:YAG laser source. The laser medium is excited by the pump energy, causing it to emit radiation, which is reflected by the mirrors. By stimulated emission, further radiation of the same wavelength is generated, amplified in the resonator, and a parallel beam is generated. Utilizing a partially transparent mirror on one side of the resonator, a small portion of the light can be coupled out and utilized. To obtain short pulses with high peak power, a Pockels-cell is utilized as an active Q-switch.

If the E_3 state is also more persistent than a lower state E_2, a permanent population inversion occurs, which is essential for the stimulated emission. High intensities are achieved by continuously repeating this operation within the Perot-Fabry resonator, which consists of a fully reflecting mirror and a partially transmitting mirror with the laser medium in the center. Photons emitted by the process are reflected between the mirrors and pass through the laser medium, causing excitation of further electrons and releasing radiation of the same wavelength, direction, and phase. This is called stimulated emission. Through the partially transparent mirror, part of the radiation can be decoupled and used for technical applications. Due to the curvature and arrangement of the mirrors, only photons that travel parallel to the resonator axis can be coupled out and used for light amplification. Therefore the laser beam has a low divergence and small bandwidth of the wavelength corresponding to the energy difference from E_3 to E_2, which is 1064 nm for a Nd:YAG laser and is considered the fundamental radiation.[100] A Q-switch (quality switch) is utilized to provide the high pulse energies for photoionization in mass spectrometry. Therefore, the beam path between the mirrors is interrupted, or the internal losses in the resonator are increased. For this application, electro-optical modulators as Pockels-cells are utilized as active Q-switches. At the end of the pump pulse, the population inversion reaches its maximum, and the resonator is released, resulting in a short laser pulse with high peak

pumping level

E_4

upper laser level

E_3

E_2 lower laser level

E_1 ground level

Fig. 5 Displays the energy levels of a four-level laser. Excitation from E_1 to E_4 takes place by pumping, with an approximately direct transition to E_3. The laser light is emitted at the transition from E_3 to E_2. The population inversion can only be maintained if the decay rate from E_2 to E_1 is higher than from E_3 to E_2.

power. [101] Despite the high output power of typically several watts at a wavelength of 1064 nm, the photon energy amounts only to 1.17 eV, which is far below the level required to ionize the analytes for mass spectrometry. In the following, the high intensity of laser light is used in anisotropic crystals or isotropic gases to obtain photons of reduced wavelength and, therefore, higher energy. The linear relationship between the polarization P, the strength of the electric field E of the valence electrons, and the susceptibility α for the anisotropic medium

$$P = \alpha \cdot E \tag{3.1}$$

diminish at very high intensities and also induce inharmonic oscillations. If the field strengths increase to such an extent that the electrons oscillate inharmoniously, function 3.1 can be written as a series expansion where the terms of higher order exceed the first linear term.

$$P = \alpha \cdot E + \beta \cdot E^2 + \gamma \cdot E^3 + \ldots \tag{3.2}$$

Utilizing anisotropic crystals, the photon frequencies can be doubled (second harmonic generation, SHG) or even sequentially reach photons of $\lambda = 266$ nm (fourth harmonic generation, FHG) with a photon energy of 4.66 eV, suitable for REMPI experiments. [96]

CO_2-laser

CO_2-lasers represent one of the most important laser classes for industrial applications, and in the scientific field. In continuous and in pulsed operation, a broad energy spectrum from several kW to low watt range and pulse widths from ns to ms can be achieved. The light of CO_2-lasers, in general, is in the infrared range between 9 and 11 μm, the models used here have a maximum at 10.6 μm. Similar to the Nd:YAG laser, the CO_2-laser represents a 4-level laser system. However, the laser medium is composed of CO_2, N_2, and He, whereby all components assigned different tasks. The helium does not contribute to the laser process and is used to increase the pressure and, thus, stabilize the discharge and regulate the temperature. Furthermore, it plays a major role in the emptying of the lower laser levels, which can be done by impacts of helium with CO_2 molecules. The excitation of the CO_2 molecules into the upper energy level is done on the one hand by elastic collisions with the electrons of the gas discharge, on the other hand, by resonant energy transfer via metastable N_2 molecules, which is of great importance for inversion. Due to the geometry of the CO_2 molecule, three types of oscillations are possible, a) bending oscillation, b) symmetric stretching oscillation, and c) anti-symmetric stretching oscillation, whereby radiation of different wavelengths is generated during the laser process. The laser emission can occur in two wavelength ranges, which are 9.6 μm and 10.6 μm, depending on the vibration level into which the transition leads. The regular bands of the energy levels consist of hundreds of lines, as the vibration levels are split by rotation. In the context of this work, a so-called TEA-laser

(transversally excited atmospheric pressure laser) was used. Here, the laser medium is passed through the cell in a weak gas stream and pre-ionized by electron beams. The main pulse is generated by the direct excitation of the laser levels in the discharge. The slow decay of the pulse is caused by the subsequent energy transfer from N$_2$ to CO$_2$. The pulse width of the used laser was 150 μs and 50 – 100 mJ pulse energy. [101]

Excimer laser

Excimers are molecules that consist of two atoms and possess no stable ground state. The term excimer stands for a diatomic molecule (dimer), which is only stable in the excited state and only for very short periods. When the molecule returns from the excited state to the ground state by emitting radiation, it decays again into two atoms. The ground state, which is also the lower laser level, has a substantially shorter lifetime than the excited state, favoring a population inversion. In such excimer lasers, noble gas/halogen compounds are used. In the context of this work, ArF and KrF were used in particular. The technical design of such lasers corresponds approximately to N$_2$-lasers or TEA-CO$_2$-lasers.

The laser medium of the systems used in these applications consisted of 2 % noble gas, 0.15 % fluorine, and helium as a buffer gas. The general architecture is similar to the TEA-CO$_2$-laser, but the laser was operated in the overpressure range of up to 6 bar and not with a continuous gas flow. A homogeneous discharge is achieved by pre-ionization with electron densities of $\sim 10^9$ cm^{-3}, which can be caused by UV radiation (100 – 200 nm) from an additional spark or corona discharge or by X-rays. Within the gas discharges, the excimers are formed predominantly by collisions of excited noble gas atoms (Ar*, Kr*) with F$_2$:

$$Kr^* + F_2 \rightarrow KrF^* + F\cdot \qquad (3.3)$$

The excited states of e.g., KrF* have deep minima in which the atoms have a certain equilibrium distance so that the molecule is ionically bound in these states, similar to the alkali halides (e.g., NaCl). During the collision of Kr* with F$_2$, one of the outer electrons of Kr* passes to F$_2$, forming F$_2^-$ and
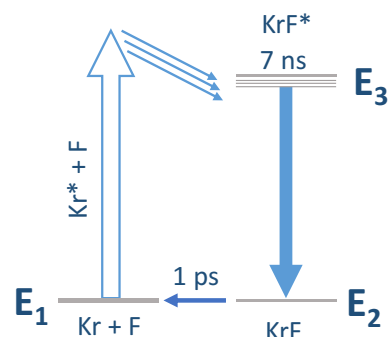
Kr^+. Now F^- and Kr^+ react to KrF*, which is called harpoon reaction. From the KrF* state, the laser radiation is emitted, then the molecule dissociates in the ground state within a very short time. While the excited state can be stabilized for a few nanoseconds, the dissociation proceeds in the picosecond range. Laser emission in the UV range is much more challenging to generate, has a broader emission spectrum, and a reduced efficiency compared to other techniques. One reason for this is the Einstein coefficient for stimulated emission, which states that the cross-section is inversely proportional to the third power of the frequency. Furthermore, the spontaneous emission is very high, so that the excited state decays faster. Besides, the laser state of the excimers is hardly bound, so that the transitions into these states show a broader frequency spectrum. For these reasons, the cross-section for stimulated emission is considerably smaller compared to other lasers and requires very strong pumping. The efficiency of such an excimer laser is about 1 - 2 %. [101]

3.1.3.2. Laser desorption ionization (LDI)

Laser desorption/ionization is the most commonly used ionization method in single-particle analysis and is usually performed using pulsed UV-lasers. Often the fourth harmonic of a Nd:YAG with $\lambda = 266$ nm is used, but also excimer lasers (ArF, $\lambda = 193$ nm; KrF, $\lambda = 248$ nm) or N_2-lasers ($\lambda = 337$ nm) are applied. [91], [102]–[104] Such a laser pulse is typically $5 - 10$ ns in duration and has a peak intensity of $10^7 - 10^{10}$ W cm^{-2} in the focus. [105] When a particle enters the ionization zone and is exposed to the focused laser beam, positively, and negatively charged ions are generated during the ionization process, whereby this proceeds in two phases. Laser desorption of neutrals from the particle produces a plume, wherein PI generates positive ions and electrons in the first phase of ionization. In the second ionization phase, electron capture and charge transfer result in the formation of negatively charged ions. Depending on the density of the plume, the formation of ions, stable enough to be detected by the mass analyzer, is influenced. If the density of the plume is higher, mainly stable and long-lived ions of both charge types are formed. However, if the plume is less dense, there are fewer collisions and charge transfer effects, so that less stable ions can also be detected in the mass spectrometer. [106] Since a single particle in a vacuum represents a closed system, the sum of the charges must always be balanced. If not all electrons are captured, the negative ion yield is lower than the positive ion yield. The formation of positively charged molecules and atoms is therefore clearly predominant. [21], [33], [34] Generally stated, energetically preferred ions of both charges show a positive correlation to each other (e.g., low ionization potential, high electron affinity), and less preferentially formed ions show a negative correlation. [105], [109]

3.1.3.3. Resonance-enhanced multiphoton ionization (REMPI)

Resonance enhanced multiphoton ionization (REMPI) is a selective ionization method in which molecules are ionized by absorption of several photons, although the energy of the individual photon is lower than the ionization potential of the molecule or atom. [95] The excitation of one or more photons (UV-spectroscopic step) is followed by the absorption of another photon for ionization (ionization step). The REMPI method uses photon energy in resonance with an excited molecular or atomic state. The different REMPI processes are distinguished according to the number of photons required and the excited states. Processes in which x photons lead to a transition state and y photons to ionization, thus exceeding the ionization potential, are called (x + y) REMPI processes. Aromatic, organic compounds can be ionized with a simple (1 + 1) - REMPI process at wavelengths of 248 nm (KrF) or 266 nm (FHG, Nd:YAG), whereby only 248 nm was used in this work. In principle, efficient and soft multiphoton ionization is only feasible if the wavelength of the laser is in resonance with the excitation energy of a UV-spectroscopic transition and the sum of the energies of two photons exceeds the ionization potential, so that two-photon ionization is energetically achievable. However, the lifetime of the excited states must not be significantly longer than the pulse duration of the laser (usually 5 ns). [35], [36] Due to different ionization potentials and UV-transitions of the different molecules, only certain compounds can be ionized at given laser wavelengths. For example, aromatic compounds absorb photons with energies from 3.9 eV (320 nm) to 5.0 eV (250 nm).

Fig. 8   In REMPI at least two photons are necessary for the ionization process. The absorption of one photon leads to excitation, while another photon triggers the ionization.

Thus, by two-photon ionization, the molecules are exposed to energies between 7.8 eV and 10.0 eV. This energy is already sufficient for aromatic compounds to generate a molecular ion. This means that the selectivity of REMPI can be controlled by various parameters such as photon wavelength, laser pulse duration, and light intensity. At the wavelength of 248 nm and laser intensity of 10^6 to 10^8 W cm^{-2} this method shows very high selectivity for aromatic compounds. Due to the much lower excess energy supplied to the analytes compared to electron impact ionization (70 eV), an almost fragment free ionization process is achieved.[37], [38]

3.2.   Time-of-flight mass analyzer

The first time-of-flight (TOF) mass analyzer was introduced in 1946 by W. E. Stephens and impressed with its simple operating principle and enormous speed of analysis. [113] After ionization, the analytes are accelerated in a static field, and ions with different mass-to-charge ratios (m/z) are dispersed in time during flight along a field-free drift path. [113] Only a few years later, in the 1950s, the new mass analyzer was able to establish its position in some areas against the conventional sector field systems and was mainly used in combination with gas

chromatography. [114] The work of Wiley and McLaren in 1955 [115] with two-stage ion extraction and Mamyrin in 1973 [116] with the development of the so-called reflectron system led to significant improvements in the field and paved the way for the development of high-resolution TOF systems.

The general working principle of a TOF analyzer is to separate analyte ions in time according to their mass-to-charge ratio. In a TOF, ions are accelerated at a defined time by a high voltage U. Afterwards, they travel a field-free drift distance s and hit the detector. If we compare single charged ions of different masses, their drift time t depends on the respective mass m. Considering the same kinetic energy, for example, the same acceleration voltage, heavier ions need more time for the same distance. The electric charge q of an ion of mass m is equal to the number z of elementary charges e, independent of the ionization method:

$$q = z \cdot e \tag{3.4}$$

The energy absorption E caused by the acceleration voltage U results:

$$E_{el} = q \cdot U = z \cdot e \cdot U \tag{3.5}$$

Thereby E_{el} is converted into kinetic energy E_{kin} of the ions:

$$E_{el} = E_{kin} = \frac{1}{2} \cdot m \cdot v^2 \tag{3.6}$$

Assuming that the ions were initially at rest, the ion velocity can be formulated as follows:

$$v = \sqrt{\frac{2 \cdot e \cdot z \cdot U}{m}} \tag{3.7}$$

With $v = s \cdot t^{-1}$ and a constant drift distance s the formula can be changed to t:

$$t = \frac{s}{\sqrt{2 \cdot e \cdot U}} \cdot \sqrt{\frac{m}{z}} \tag{3.8}$$

This means that v is inversely proportional to the square root of the m/z of the associated ion, which must be considered in the mass calibration of the system. An important parameter of a mass spectrometer is the mass resolution (R) of the instrument. The mass resolution of a mass spectrometer describes the ability to detect two signals of different ions with small mass differences in optically separated signals. Two such peaks are called separated from each other if the signal between the peaks decreases by at least 50 %. R is defined as:

$$R = \frac{m}{\Delta m} = \frac{t}{2\Delta t} \tag{3.9}$$

where Δm is the smallest mass difference between two peaks, and Δt is the pulse length. [117] The mass resolution in a TOF is mainly influenced by three factors: spatial, velocity, and time blur. Regardless of the ionization method used, the ionization location is not infinitesimal, so the starting point of the ions slightly differs relative to the acceleration electrodes. This causes an uneven acceleration of ions, which leads to a signal broadening at the detector due to the different drift distances and flight times of ions with the same m/z. The so-called spatial focus describes the point where this blurring is minimal so that this represents the optimal location for the detector. However, if the detector is positioned too close to the ion source due to excessive spatial blur, sufficient mass separation cannot occur. Furthermore, the acceleration of the generated ions does not start at the same time. The neutral molecules and atoms in the ion source are not at rest so that after the ionization, an ion can initially move oppositional to the electric extraction field and requires time to change direction. In 1955, Wiley and McLaren invented two-stage ion extraction, whereby the spatial focus of the ions can be adjusted for longer

drift distances using the first and second extraction voltage. Here the Wiley-McLaren criterion applies:

$$s = 2x_1 \cdot \sqrt{k^3} \left(\frac{1 - x_2}{(k + \sqrt{k}) \cdot x_1} \right)$$

(3.10)

with the flight path s, the distance between the first extractor and ionization zone x_1, the distance between the first and second extractor x_2, and the ratio of the first and second acceleration voltage k to calculate the spatial focus equal to the flight path s. [115]

The development of the two-stage reflectron TOF by Mamyrin et al. [116] brought a further significant improvement in mass resolution. To compensate for the energy errors of the ions, one or more units are used to reflect the ions. Electrostatic fields decelerate the ions and reflect them at a certain angle to the incident ion beam, which is then focused on the detector. Faster ions of the identical mass dip deeper into the reflector field and thus have to travel a longer distance. The structure of such a TOF-MS system is depicted schematically in Fig. 9.
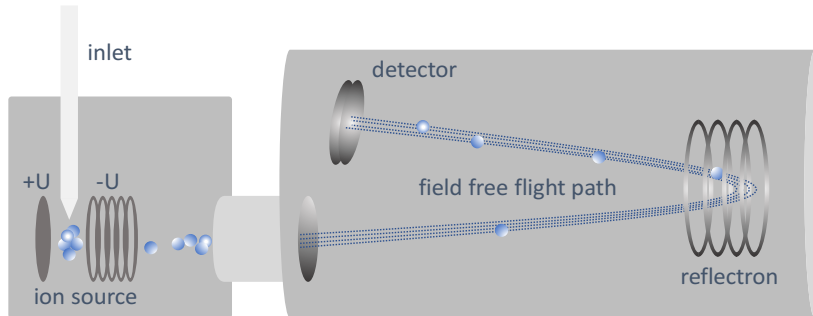
Fig. 9 Schematic view of a time-of-flight mass spectrometer with Wiley-McLaren optics and reflectron. The analyte enters the vacuum through the inlet and is ionized by EI or PI, for example. The ions are accelerated by Wiley-McLaren optics and separated by their m/z on the field-free drift path. The reflectron unit is capable of correcting the energy errors and increasing the detector resolution.

By applying this technique, the broadening of the ion packages after the Wiley-McLaren spatial focus can be partly corrected by extending the drift distance. All TOF-MS systems used in this work are reflectron mass spectrometers.

In a static electric field of the extraction electrodes in the ion source, subsequent to PI, electrons would be accelerated in the direction of the repeller plate, and the fragmentation e.g. of the PAHs would be significantly increased by electron impact. To effectively reduce this effect, time lag energy focusing, also known as delayed extraction, can be used. [118], [119] The delay enables free electrons generated during the ionization process to exit the ion source. Since that the speed of the electrons is orders of magnitude higher than the velocity of molecules, this process takes place in nanoseconds. After a specific time, typically a few hundred nanoseconds, when the plume has expanded to macroscopic size, the ions are extracted from the ion source. Here, the energy spread can be compensated, and the resolution enhanced utilizing the Wiley McLaren ion optics. [115], [120], [121]

Fast detectors with very short response times are essential for analysis using TOF-MS. In modern measuring systems, so-called microchannel plates are used, which have a similar function as a linear channeltron. The MCP usually measures between 20 and 50 mm in diameter and has several million channels with a size of several micrometers. To prevent the ions from passing through the channel without colliding with the channel wall, the channels are tilted relative to the ions' flight axis. Each channel is capable of generating secondary electrons by impacting ions. The secondary electron multiplication of a single MCP results in a gain of 10^3 - 10^4, which is less

than in a classical secondary electron multiplier, but the MCPs can be stacked in packets of usually two (Chevron-plate) to three plates (z - stack). In this case, the gain factor increases to 10^6 respectively 10^8, using voltages of about 1 kV per plate [92]

3.2.1.   Bipolar single-particle mass spectrometer

The main objective of a single particle mass spectrometer (SPMS) is the analysis of the chemical composition and size of individual particles, utilizing mass spectrometers such as ion traps, [122], [123] and time-of-flight analyzers. [58], [91], [124], [125] In the second half of the 20th century, significant progress has been made in this field through TOF-MS and laser technology, [57], [124], [126] whereupon the principle of the bipolar single-particle mass spectrometer or an aerosol time-of-flight mass spectrometer (ATOF-MS) was developed in 1996 by Hinz et al. [58] The ATOF-MS essentially consists of a vacuum inlet, the particle detector and sizing system, the ionization region with ion optics, and two orthogonally oriented TOF-MS systems. The particles are sampled directly at atmospheric pressure and, with the assistance of an
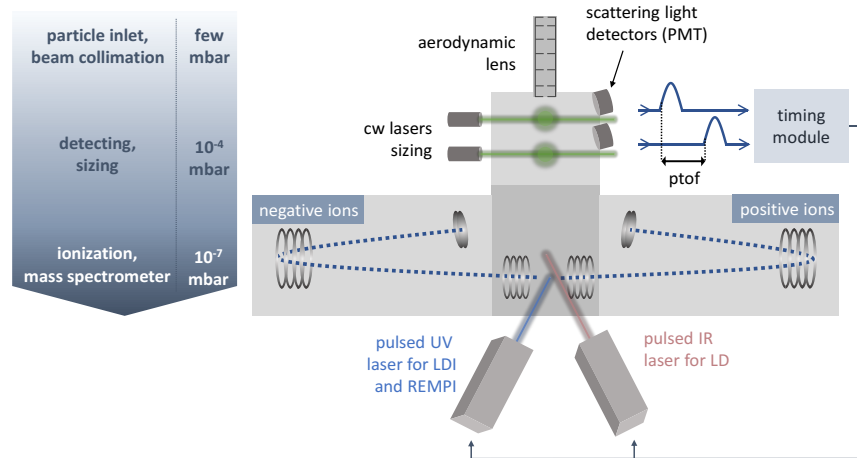
Fig. 10   Instrumental setup of an ATOF-MS, based on two reflectron TOF-MS, a velocimetric sizing unit, and an aerodynamic lens as the inlet for introducing single-particles into the vacuum system. Single-particles are detected in the sizing unit using the scattered light of two cw-lasers, and via the particle-time-of-flight (ptof), the ionization process is triggered, and the aerodynamic diameter of the particle is calculated. Positively and negatively charged ions are formed within a laser desorption ionization (LDI) process, performed by intense UV laser light pulses. As described in section 3.3.3, REMPI can also be performed in combination with laser desorption on single particles.

aerodynamic lens, transferred as a narrow particle beam to the first pressure stage of the vacuum system or via a nozzle-skimmer inlet and accelerated into the vacuum through gas expansion. In this pressure stage ($\sim 10^{-4}$ mbar), the sizing unit is localized, here the particles are sized by laser velocimetry, and the timing for ionization with intense UV-laser pulses is determined. Based on the signals of two photomultipliers (PMT) detectors, the so-called particle-time-of-flight (PTOF) is determined and provides the foundation for triggering the ionization laser and the calculation for the vacuum aerodynamic diameter of the individual particles. However, the aerodynamic diameter, which depends on the flow regime, differs from the shape and geometric diameter of the respective particle. In contrast, the electric mobility diameter, which determines the migration velocity of the particles in a constant electric field, is often determined by standard measurement technology for particle size distribution. [9] The most common ionization scheme used in SPMS

is laser desorption/ionization (LDI). This involves the use of intense UV-laser pulses to desorb and ionize the analytes bound on the particle, most commonly Nd:YAG (FHG, $\lambda = 266$ nm), excimer laser (ArF, $\lambda = 193$ nm; KrF, $\lambda = 248$ nm), and N_2-laser ($\lambda = 337$ nm). [91], [102]–[104] Both positively and negatively charged ions are generated and analyzed in the two TOF-MS instruments, mounted orthogonally to the ion source. The ionization process is described in detail in section 3.2.3.2. A schematic overview of this setup is given in Fig. 10. Due to the strong fragmentation of ions upon LDI with high UV-laser intensities, several multi-step ionization methods were developed in the context of this work. Herein, laser desorption (LD) and ionization are decoupled. Therefore, a laser desorption (LD) step using a CO_2-laser ($\lambda = 10.6\,\mu m$) was added, especially for predominantly organic combustion particles. The ionization is subsequently carried out in the second step using a UV-laser. [61] Another approach is using LD to volatilize surface-bound organic and aromatic compounds and ionize them in the first ionization step using REMPI. [74] In the subsequent second ionization step, the residual of the particle is analyzed with LDI. [30], [52] This design is also shown in Fig. 10 and is explained in more detail in section 3.3.3.

3.2.2. Aerosol mass spectrometer (AMS)

The Aerosol Mass Spectrometer (AMS) is designed for on-line analysis and characterization of aerosols and was first presented by Jayne et al. 2000. It utilizes a TOF analyzer for on-line investigation of the chemical composition of nanoparticles in the aerodynamic diameter range of 70 – 500 nm. [127] The measurement system contains three main components, the inlet, the particle sizing unit, and the detection unit. Similar to the SPMS, particles are sampled under atmospheric conditions, pass through an aerodynamic lens, and enter the vacuum within a focused particle beam. The sizing unit mainly consists of a mechanical chopper wheel, spinning with a high frequency of >100 Hz, only allow small packages of particles to pass. A small infrared photodiode detector pair delivers the exact starting time of the particles and facilitates the calculation of aerodynamic diameters. After the flight path, particles of the selected size hit the tungsten vaporizer at 600°C in a pressure range of 10^{-5} to 10^{-6} mbar. Here, non-refractory organic and inorganic particle components are volatilized, ionized by EI, separated, and detected by a mass spectrometer. [128] The early aerosol mass spectrometers were equipped with a quadrupole MS, but in this work, a high-resolution TOF-MS system was used (HR-TOF-AMS, Aerodyne Research Inc., USA). [22], [127]–[129]
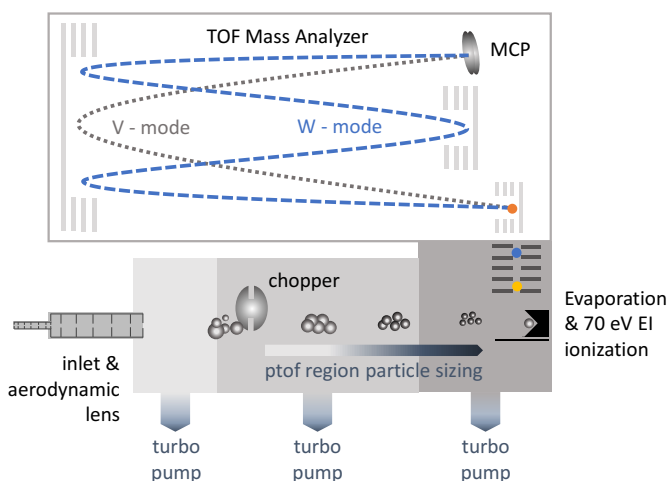

Fig. 11 Schematic of the Aerodyne HR-TOF-AMS comprising of an inlet system with an aerodynamic lens, particle sizing unit, thermal vaporizer, ionization unit for EI, and a time-of-flight mass spectrometer. To substantially enhance the mass resolution, the TOF-MS can be operated in W mode. Thereby, the ions are reflected three times with a considerably extended drift path.

With the instrumentation used, the analyzable particle size range is $35-1500\,nm$, and the resolution of this instrument is in the range of 2100 in V $-$ mode and 4300 at $m/z = 200$ in W $-$ mode of the TOF-MS which allows direct separation of ions from several organic and inorganic species, quantification of some organic fragments, and the direct identification of organic nitrogen and sulfur. [129] The complete fraction of particle-bound organic substances is called organic matter (OM) and is quantified together with nitrate, ammonium, sulfate, and chloride from the measured fragment ions. Furthermore, particle analysis using AMS provides elemental ratios such as O:C, H:C, and N:C and organic mass to organic carbon (OM/OC), which are important parameters in data analysis. [130] In the aerosol sciences, TOF-AMS has prevailed over other techniques and represents a commercially successful and established on-line method of mass spectrometric particle analysis due to its speed and accuracy.

3.3.   Instrumentational setup for single-particle analysis

3.3.1.   On-line analysis of single-particles and simultaneous detection of polycyclic aromatic hydrocarbons using ATOF-MS technique – Publication 1

Two opposite time-of-flight (TOF) mass analyzers (Reflectron RFT10, Firma Stefan Kaesdorf, Geräte für Forschung und Industrie, Germany) attached to the central inlet and ion source constitute the main components of the measurement system. In this setting, one flight tube provides the possibility to change polarity for combined measurements of either LDI^+/LDI^- or polycyclic aromatic hydrocarbons (PAH) with LD-REMPI ionization and the following LDI^+ experiment giving information about the chemical composition of the particles' residual structure. The velocimetric sizing unit is a key part of the experimental setup providing the essential timing of the whole experiment and information concerning the particles' aerodynamic diameter. It is equipped with two continuous-wave (cw) Nd:YAG lasers ($\lambda = 532\,nm$, GCI-050-L, CrystaLaser Inc., USA) and photomultipliers (PMT, model 931B, Hamamatsu, Japan) and detects single-particles (in the size-range of $200-3000\,nm$). To detect PAHs, condensed on a particles' surface, the measurement system is equipped with a pulsed CO_2-laser ($\lambda = 10.6\,\mu m$, Urenco ML104, Uranit GmbH, Germany) to heat each particle individually to evaporate the PAHs. Within this plume, PAHs are ionized with a single pulse of a KrF excimer laser ($\lambda = 248\,nm$, Excistar XS, Coherent Inc., USA) using REMPI. For subsequent analysis of the residual particle, utilizing an LDI scheme, an ArF excimer laser was installed ($\lambda = 193\,nm$, Atlex 300, ATL GmbH, Germany). The basic idea of this experiment is the separation of the positively charged ions from both ionization steps. Therefore, both mass analyzers are operated in positive mode, and the polarity of the ion extraction electrodes is inverted between the two ionization processes (fast high voltage switches, HTS31-03-GSM, Behlke GmbH, Germany). Due to the high time difference between the two ionization steps, a separate mass calibration is necessary.

Single-particle measurements were performed either with redispersed combustion particles or ambient aerosol.[63] The combustion particles, namely, diesel particles (VW Transporter Typ 3, 1.7 D) and ash from coniferous wood combustion, were introduced into the ATOF-MS using a

turntable powder disperser (Model 3433 SSPD, TSI Inc., USA) and a flow rate of 1 l min^{-1} of clean Nitrogen (N$_2$ 5.0), whereas only 0.1 l min^{-1} is guided into the MS. To achieve an adequate number of particles for analyzing ambient aerosols, an aerosol concentrator was applied (Model 4240, MSP Corp., USA).

3.3.2. Dynamic changes in optical and chemical properties of tar ball aerosols by atmospheric photochemical aging – Publication 2

Similar to the formation mechanism of tar balls during biomass combustion, polydisperse tar ball particles were generated. [131] Commercially available wood pellets were crushed, heated, and dry distilled at 530°C in the absence of oxygen. After filtration and separation into polar (water-soluble) and non-polar tar solution, the samples were dissolved and nebulized separately in methanol. The solvent was dried in a constant nitrogen flow, and the tar balls were artificially aged in the OFR (oxidation flow reactor) by adding O$_3$, vaporized water, and UV light. The construction and operation of the reactor are described elsewhere in detail. [132] Besides measurements of chemical and physical parameters, two mass spectrometers were used to characterize the tar balls. The HR-TOF-AMS (Aerodyne Research Inc., Billerica, USA) was operated alternately in the highly sensitive V-mode and high-resolution W-mode (scheme Fig. 11) to detect chemical mass fragments and elemental ratios for quantifying OM. The SP-LD-REMPI-TOF-MS has already been described in detail in the previous section. [63] In this experiment, only LD-REMPI of single-particles was performed, and LDI was omitted entirely, because the PAHs in the tar balls were the main focus. The experimental setup is shown and described in detail in Appendix 7.2.

3.3.3. Simultaneous detection of PAHs as well as positive and negative inorganic ions in on-line single-particle mass spectrometry – Publication 3

The SPMS instrument is based on two opposite TOF-MS systems, described in an earlier section of this work (section 3.2.1). Modifications to the instrument as mentioned earlier incorporate the complete optical setup, the inlet system, and high voltage supplies.
Through an aerodynamic lens, which minimizes the divergence of particles entering the vacuum [133], [134] (optimal work range at 0.1 l min^{-1} and $> 3\,\mu$m aerodynamic diameter), the narrow particle beam passes the velocimetric sizing unit. Accordingly, the particles are individually exposed to an intense pulse of a CO$_2$-laser ($\lambda = 10.6\,\mu$m, MTL-3 mini-TEA, Edinburgh, UK) for fast and efficient desorption of PAHs. As distinguished from previous instrumental setups, here, the spatial beam profile of only one laser is needed for ionization ($\lambda = 248$ nm, PhotonEx Excimer, Photonion GmbH, Germany). As depicted in Fig. 12, the parallel laser beam traverses the gaseous plume of desorbed PAHs for REMPI with relatively low intensity (~ 3 MW cm^{-2}). A concave mirror (f = 150 mm) back-reflects the light and focuses the laser beam to the center of the ionization region. The laser beam hits the particle residue with high intensity (~ 2 GW cm^{-2}) for LDI. The short delay time from optical path difference of ~ 1 ns and the longer laser pulse duration of 5 ns enables the simultaneous execution of both ionization

steps by one laser. Ions from both ionization processes are extracted from the ion source after a delay of 0.6 μs, enhancing the peak quality. [44], [45] Whereas anions from LDI are detected in one flight tube, cations from LDI plus REMPI are measured in the second TOF mass analyzer. No individual calibration is needed for ions from different ionization steps because all are formed and extracted simultaneously. To overcome adverse suppression effects of the weak PAH signals in the mass spectra from the large dynamic range of LDI-signals, the transmission of lighter LDI-ions in the positive flight tube is reduced. Fast high voltage switches (HTS31-03-GSM, Behlke GmbH, Germany) change the voltage of a lateral deflection element for a time frame of

Fig. 12   Shows the ionization scheme for simultaneous detection of PAHs as well as positive and negative inorganic ions in on-line single-particle mass spectrometry. (a) Through LD PAHs are volatilized from the particles' surface. (b) With 248 nm and low intensity, the aromatic compounds are ionized within a REMPI scheme. The back-reflected and focused laser light hits the particles' residue and ionizes via LDI.

2.5 μs, which corresponds to m/z $\approx$ 100 in the detected mass spectra. Thus, the sensitivity for LDI cations is reduced by 20, which helped increase the data quality. [91]

3.3.4.   Resonance-enhanced detection of metals in single-particles with on-line SPMS measurements using an Nd:YAG laser and optical parametric oscillator – Publication 4

The basic setup of the SPMS system used in this research was already described in other publications. [58], [59] Shortly, the particles enter the vacuum through an aerodynamic lens and an optical sizing unit, consisting of two Nd:YAG cw lasers (λ = 532 nm), ellipsoidal mirrors, and photomultipliers for velocimetric sizing. The central part of the SPMS instrument deployed in this research (Hexin Instruments Ltd., Guangzhou, China, and Photonion GmbH, Germany) is the bipolar TOF mass analyzer with z-shaped drift paths, which was firstly described by Pratt et al. 2009. [136] Fundamental modifications to the commercial system are made to the electronics, the optical setup, and the ionization laser. [137] To improve the peak quality of the mass spectra, delayed ion extraction enabled with high voltage switches (HTS31-03-GSM, Behlke GmbH, Germany) were deployed within this setup. Besides, the standard Nd:YAG ionization laser and its appropriate optical setup were removed and changed to a tunable laser system (parametric optical oscillator, OPO, Opolette HE 355 LD UV, Opotek LLC, USA), and two additional excimer lasers at λ = 248 nm (KrF, PhotonEx, Photonion GmbH, Germany) and λ = 193 nm (ArF, ATLEX-I 300, ATL GmbH, Germany). To detect resonance effects in laboratory experiments, different types of standard particles with both organic and inorganic matrixes were analyzed. Diesel exhaust particles as samples with preponderant organic matrix (well described in

publications 1 & 2 [30], [52]), Arizona test dust $0 - 3\,\mu m$ diameter (Powder Technology Inc., USA) for mineral dust particles, hemoglobin as a complex organic matrix with high metal content, and as a complex anthropogenic matrix with trace metals NIST urban dust 1649b [138] were chosen. To introduce the particles into a 1 l min^{-1} gas stream (N$_2$, 5.0 purity) from which 0.1 l min^{-1} were guided into the SPMS, a turntable powder disperser (Model 3433 SSPD, TSI Inc., USA) was used. The ambient air experiment took place at a meteorological station in rural surroundings at the western coast of Sweden, approximately 30 km south of Gothenburg (Map coordinates: 57° 23' 37.8''N, 11° 54' 51.4''E). The ambient air was sampled at the height of 15 m above sea level and was concentrated from 300 l min^{-1} airflow to 1 l min^{-1} carrier gas stream using a virtual impactor device (Model 4240, MSP Corp., USA). The carrier gas stream was dried (MD-700-12S-1, Perma Pure LLC, USA) and further concentrated to 0.1 l min^{-1} directly at the inlet system. The two ionization excimer lasers used in this experiment were alternately fired on particles to ionize, using a custom build trigger box. Here a complex programmable logic device (Intel Max V) with 8.5 ns pin-to-pin delay was used and programmed with Very High-Speed Integrated Circuit Hardware Description Language (VHDL).

4. Results

In this section, the results regarding the development of novel ionization approaches for the investigation of airborne particles with on-line single-particle analysis are shown. Although the technical development of the analytical methods was the main focus of this work, the results are presented in the context of the analyzed aerosols. The exact instrument setup is described in the publications, which can be found in the appendix of this thesis; a short description was also given in the previous sections.

4.1. Implementing Resonance-Enhanced Multiphoton Ionization to the ionization scheme of single-particle analysis

4.1.1. Research objective

On-line single-particle MS techniques are essential and powerful tools for detecting the chemical composition of airborne particles and are an important part of current atmospheric research. Various devices and technical advancements in ionization allow on-line monitoring and source apportionment of both natural and anthropogenic aerosols. It is an important element in research to determine the influence of aerosols on climate and human health. PAHs are of particular research interest due to their high persistence in the environment and their carcinogenic effects on the human body. PAHs are formed during combustion processes and adsorbed onto particles during the cooling process of exhaust gas, which has brought the analysis of particle-bound PAHs into focus. Here, the distribution of the pollutants on the particles plays a major role, as they can either be dispersed in low concentrations or occur in very high concentrations distributed

over a few particles. The latter leads to a higher local dose when deposited in the lungs and could overcome cell defense. In previous studies, [73], [74] PAHs could be detected in single particles, but the information on source apportionment was lost due to the ionization process. In the context of this PhD thesis, new ionization schemes have been developed to allow the analysis of hazardous PAHs and source apportionment from individual particles.

4.1.2. Simultaneous detection of PAHs and positively charged inorganic compounds – Publication 1
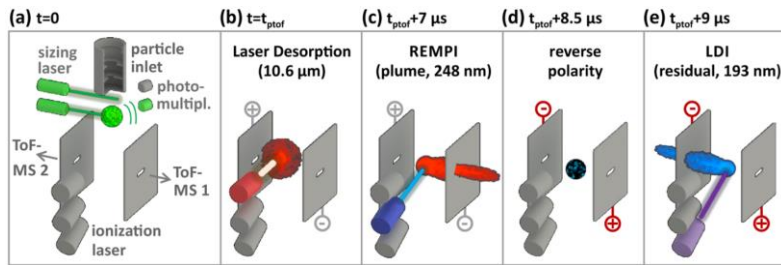
Fig. 13 (a) Illustrates the basic principle of ATOF-MS. Particles enter the vacuum through an aerodynamic lens, are accelerated and sized by laser velocimetry. On entering the ionization zone of the MS, the sequence for ionization is initiated. (b) Above the ion source, several microseconds before ionization, the particle is heated by an IR-pulse. (c) The desorbed PAHs are selectively ionized via REMPI and analyzed in one of two TOF-MS. (d) Fast field inversion of the ion source for the following ionization step. (e) The residual particle is hit by a strong UV-pulse for LDI$^+$ and analyzed in the opposite TOF-MS.

Current research shows the enormous importance of PAHs and their derivatives for the environment and human health, underlining the importance of developing sophisticated analytical techniques. [139]–[141] ATOF-MS provides an excellent technical basis for analyzing particle-bound PAHs on airborne particles and determining their origin and mixing state, which is crucial for a better understanding of atmospheric processes and health effects. The classical instrument design and ionization scheme are described in more detail in sections 3.2.1 and 3.1.3.2 and appendix 7.1. LDI provides a good basis for classifying particles and determining their chemical composition via organic and inorganic fragments and elements and identifying their origin. In numerous field campaigns and laboratory experiments, a large number of particle classes could be identified and analyzed (see Tab. 1). [67]–[70], [86], [142]–[144] However, to improve the detection of organic substances more efficiently and reduce the number of fragments, desorption and ionization can be decoupled, and PAHs can be ionized from the resulting plume via REMPI. [61], [74] The desorption is performed with an infrared pulse of a CO_2-laser via laser desorption (LD). In the context of this study, the LD-REMPI process was coupled with LDI$^+$ and implemented in an ATOF-MS with classical design. The basic idea here is to analyze positively charged ions from both ionization processes in separate TOF-MS-analyzers to get a deeper insight into the mixing state of the particles and the detection of PAHs and determine their origin. To achieve this, both TOF mass analyzers have to operate in positive mode, which in this opposite configuration requires a complex ionization scheme (see Fig. 13). The particles enter the vacuum through an aerodynamic lens and are accelerated. Velocimetric sizing is used to determine the vacuum aerodynamic diameter and velocity and start the electronic trigger cascade. Slightly

above the ionization zone, the particle is heated by an IR-pulse so that PAHs are desorbed, which have been adsorbed on the surface. After a few microseconds, the PAHs are selectively ionized from the expanding plume by REMPI and analyzed in one of the two orthogonally aligned TOF-MS. Subsequent to the fast field inversion, the remaining particle is hit by a strong UV-pulse ($\lambda = 193$ nm), and the positively charged ions from the LDI process are detected in the second TOF-MS. Since this method focuses on the analysis of single particles mainly from combustion aerosols, two different test particle systems were selected for testing and optimizing the method: (a) Diesel exhaust and (b) wood ash particles (Fig. 14). The diesel particles were sampled from the exhaust pipe of a car, milled and re-dispersed with a turntable powder disperser (for exact description see appendix 7.1). Fig. 14 (a) shows the mass spectra of a single diesel exhaust particle, LDI+ in blue, and REMPI in red. The LDI spectra show mainly signals for carbon clusters (C_n^+), smaller signals for Na^+, K^+, Fe^+, and smaller organic fragments (e.g., $^{27}[C_2H_3]^+$). This underlines the soot character of the particles as described in the literature. [68], [69] But in this experiment, the LDI process delivers spectra slightly modified from the literature since the UV-pulse does not hit an unaffected particle but a heated, complex system of a residual particle embedded in an expanding gas plume. For this reason, the mass spectra show, for example, a higher proportion of organic fragments. The REMPI spectra of PAHs are dominated by non-alkylated species, such as phenanthrene/anthracene and pyrene/fluoranthene, but other signals are also clearly evident (Tab. 2). The pattern of the signals does not directly indicate the frequency distribution of PAHs, which is strongly dependent on the cross-section of the ionization, which varies significantly for the individual substances. [145] The most dominant signals are listed in Tab. 2 and form a typical pattern, described and documented in the literature. [146]–[149] All diesel particles showed a high uniformity, due to the repeated exposure to combustion gases in the exhaust pipe, making these particles a unique test system for the new ionization scheme.
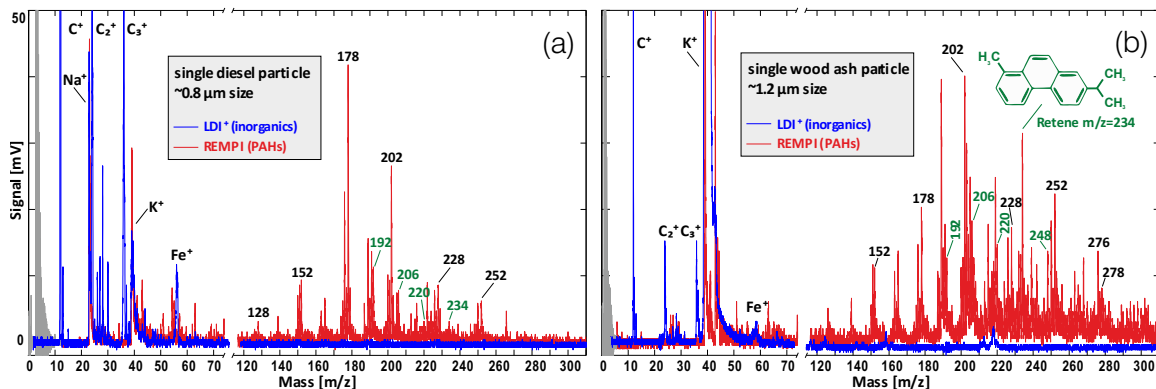
Fig. 14 (a) Mass spectra of a single diesel exhaust particle, with LDI+ (blue) and REMPI (red) superimposed. The mass spectra show a soot matrix with predominantly non-alkylated PAHs (black m/z numbers). (b) Mass spectrum of a single wood ash particle, with LDI+ (blue) and REMPI (red) superimposed. The mass spectra show a soot and potassium matrix with increasing numbers of alkylated (green m/z labels) and oxidized PAHs.

Tab. 2 Polyaromatic compounds detected in the mass spectrometric data of this study. Black m/z of Fig.14 and 15 are found in column 2 and green m/z in columns 3-6.

# of C in aliphatic side chains	0	1	2	3	4
PAHs			m/z		
naphthalene	128	142	156	170	184
acenaphthylene	152				
phenanthrene; anthracene	178	192	206	220	234
pyrene; fluoranthene	202	216	230		
benzanthracenes; benzphenanthrenes	228	242			
Benzpyrenes; benzfluoranthenes	252	266			
benz[ghi]perylene; indeno(1,2,3)[c,d]pyrene	276				
dibenzphenanthrenes; dibenzanthracenes	278				

An important parameter in ATOF-MS is the hit rate, measured in laboratory experiments with diesel exhaust particles at 60% for REMPI exclusive and 50% for REMPI and LDI$^+$ simultaneously. Hit rates of this magnitude are extremely high compared to literature values but may be explained by the high IR-pulse energy applied in this setup. In Fig. 14 (b), the typical mass spectra of a single wood ash particle from a lambda-probe controlled 20 kW log wood combustion furnace are depicted. The LDI$^+$ spectrum is dominated by the strong K$^+$ peak, with carbon clusters (C$_n^+$) also occurring, indicating a soot matrix. These results are consistent with previous single-particle studies in which K$^+$ was introduced in conjunction with C$_n^+$ as marker ions for biomass combustion. [61], [150]–[152] However, the most important application of this measurement technique is the on-line analysis of ambient particles. Fig. 15 shows an example of the respective mass spectra of two different particles measured during an ambient air measurement directly in front of the laboratory building (54° 04' 41.0''N, 12° 06' 31.9''E) in a suburban environment with low traffic and strong winds from northern directions, directly from the Baltic Sea. To be capable of analyzing a sufficiently high number of particles, an aerosol concentrator (model see section 3.3.1) was used. Within a period of 2 hours, 1000 particles could be detected, whereby a majority of these were sea salt particles (Fig. 15 (a)). Characteristic ions for sea salt particles in the LDI+ spectrum are Na$^+$, K$^+$, [Na$_2$]$^+$, [Na$_2$Cl]$^+$, [NaKCl]$^+$, and [Na$_3$Cl$_2$]$^+$, which have been described in detail in the literature, PAH signals are not observed in sea salt particles. [75]–[77] In addition to predominantly inorganic particles, single-particles containing PAH were observed. The mass spectra of such a particle are shown in Fig. 15 (b). In the LDI$^+$ spectrum, dominant signals are K$^+$, Al$^+$, C$_n^+$, and small molecular fragments, most likely organic fragment ions. The strong K$^+$ peak combined with the other elements and fragment ions suggests that this particle originates from wood combustion. While source apportionment based on LDI mass spectra is also feasible with other approaches, [70], [83] this new method can additionally include a REMPI spectrum of PAHs in the data evaluation and provide important information on the origin of the particle and its chemical composition. The strong retene peak at m/z = 234, a marker for (soft) wood

combustion, provides information about the origin and, together with the strong K^+ peak, confirms the indication of wood combustion. Also, the large number of alkylated and oxidized PAHs indicates incomplete combustion or smoldering, which occurs mainly when a fire is lit in domestic heating. With this study, it is now possible for the first time to perform an on-line analysis of single-particles to determine their chemical composition and PAH load. The analysis of PAHs on single-particles opens up a new dimension of information on health-relevant combustion aerosols.
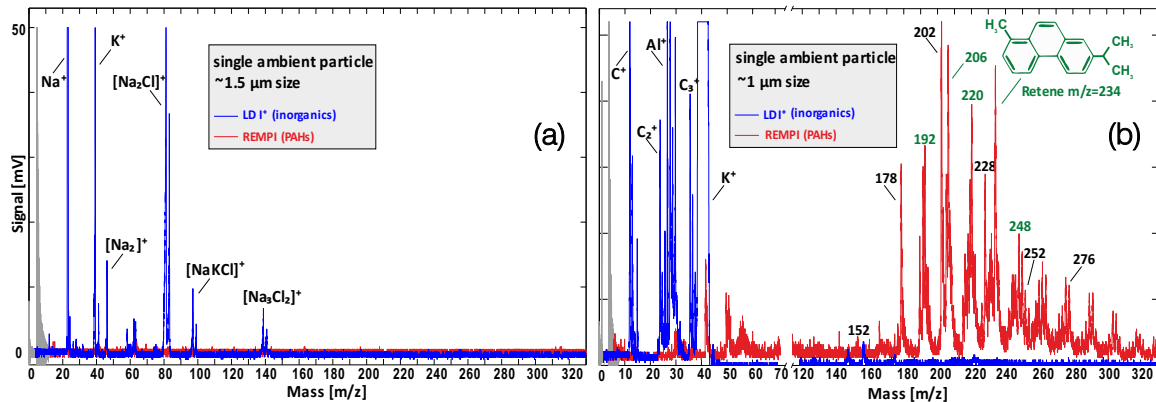
Fig. 15 Ambient air particles: (a) Mass spectra of a typical single sea salt particle. (b) Mass Spectra of a PAH-containing particle with intense PAH pattern. Black and green m/z show non-alkylated and alkylated PAHs, for this particle source apportionment to incomplete biomass or wood combustion is appropriate.

4.1.3. Chemical and physical properties of tar ball aerosols – Publication 2

Organic aerosol (OA) plays a crucial role in atmospheric science and the balance of regional and global radiation and is, therefore, one of the main sources of aerosol pollution in the troposphere. [6], [14], [15] An indirect effect of OA on the earth's climate is the reaction with water and the formation of cloud condensation nuclei (CCN), which influences cloud formation, the hydrological cycle, and the earth's albedo. [18], [153] The most important part of this effect is caused by the light-absorbing carbonaceous aerosol fraction with the established term brown carbon (BrC). [154] Due to the complex physical and chemical properties of BrC, its behavior and evolution in the atmosphere are poorly understood. [23] However, BrC contributes 10 % - 40 % to the total light absorption in the atmosphere, [155], [156] and reaches a global forcing of 0.10 - 0.25 W m^{-2} with partly regionally much higher values. [157] BrC is emitted as primary particles but can also be formed secondarily by reactions of aromatic or carbonyl compounds in clouds or particles. [23] In total, two-thirds of the primary BrC worldwide originates from biomass burning, which is mainly responsible for OA formation. [158], [159] Tar balls are a particular type of BrC, which is produced by wood combustion and, in particular, by smoldering combustion, which occurs abundantly in natural and anthropogenic environments. [160], [161] Tar balls are homogeneous, spherical, carbonaceous particles that occur in sizes from tens to hundreds of nanometers and have been identified collectively in many biomass combustions plumes. Tar balls represent a significant fraction of the BrC from biomass combustion. [160],

[162], [163] Tar balls can be formed under different combustion conditions, occur consistently together with other particle classes, and react rapidly after their release into the atmospheric environment. [160], [162], [163] In the context of this study, tar balls were generated by flameless wood pyrolysis, [131] and the refractive index (RI) as a function of wavelength (365 – 425 nm, 0.5 nm resolution) was determined with a broadband cavity-enhanced spectrometer (BBCES). The chemical characterization of the tar balls was performed with an HR-TOF-AMS and an LD-REMPI-ATOF-MS. Dynamic changes of the optical properties in correlation with the chemical composition were investigated, with a focus on the atmospheric aging process and the influence on the earth's climate. The experimental setup is briefly described in section 3.3.2 and is more precisely described in appendix 7.2.

4.1.3.1. Single-particle analysis - LD-REMPI-ATOF-MS

Single-particle analyses were performed on non-polar and polar tar balls, and an exemplary spectrum is shown in Fig. 16: (a) red, non-polar tar ball, (b) blue, polar tar ball. Both mass spectra show a distinct PAH signal pattern, with the non-polar and polar tar balls differing significantly.
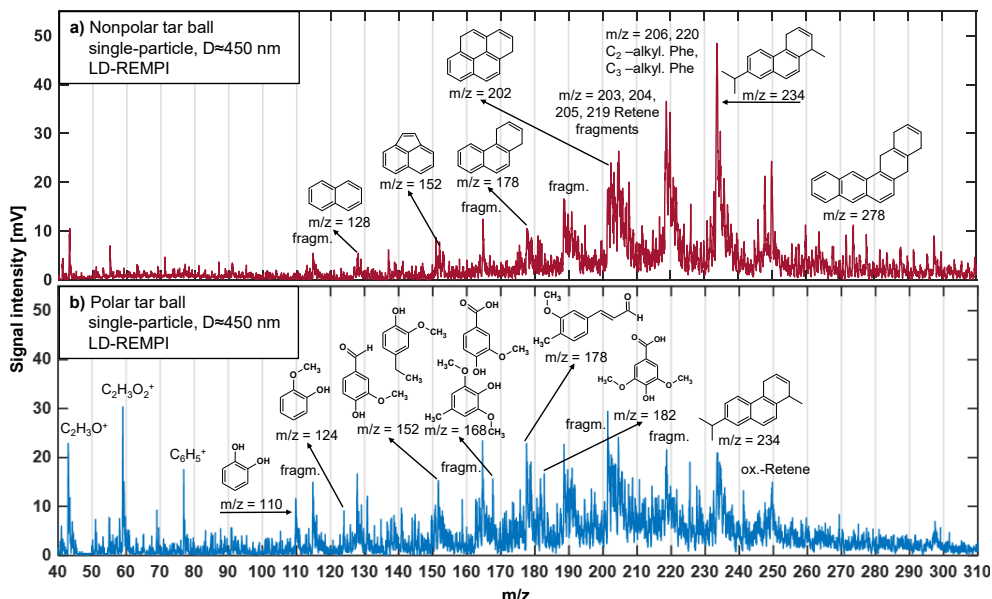
Fig. 16   SP-LD-REMPI mass spectra of exemplary tar ball particles of (a) non-polar Tar Balls with predominantly alkyl-substituted and unsubstituted PAHs and (b) polar Tar Balls with many oxidized aromatic species such as methoxy-phenol and benzenediol.

The features found in the mass spectra are consistent with the polarity of the examined samples and ambient BBOA. [164] A detailed list of the substances identified in the mass spectra is given in Tab. 3. The REMPI spectra show a rather complex pattern, with the spectrum of non-polar tar balls dominated by unsubstituted and partially alkylated PAHs. Especially naphthalene, acenaphthylene, phenanthrene, and pyrene show intense signals. The softwood combustion marker retene at $m/z = 234$ is the most intense signal and also possible derivatives as oxidized retene at $m/z = 250$ (one oxygen oxidation), methyl retene at $m/z = 248$ (one methyl addition),

and common fragments at m/z = 203, 204, 205, 219 can be identified. [165], [166] Although, several of the previously mentioned PAHs, including retene, are also found in the REMPI mass spectrum of polar tar balls. The spectrum is dominated by oxidized aromatics, such as benzenediol and methoxy-phenols (e.g., catechol, guaiacol, acetovanillone, syringaldehyde, conifery aldehyde). A variety of studies show consistent results on the dominance of aromatic compounds in laboratory experiments, [73], [74], [167], [168] and ambient BBOA. [164] The SP-LD-REMPI spectra show a high correspondence to the analyses with the HR-TOF-AMS. Non-polar tar balls show a large fraction of $C_xH_y^+$ fragments with strong signals at typical fragment ions for aromatic compounds, whereas polar tar balls show a large fraction of $C_xH_yO^+$ and $C_xH_yO_z^+$ fragments and a high O:C ratio. Biomass combustion is a major source of environmental PAHs (alkylated PAHs, oxygenated PAHs, nitrogen-substituted PAHs, etc.) and poses a severe risk to human health due to its carcinogenicity. [43], [162], [169] As precursors for ambient BrC and tar balls, PAHs can also participate in a strong climatic effect. The newly developed instrumentation (section 4.1.2 [63]) can contribute to a better understanding of tar balls and their climatic effects by chemical analysis.

Tab. 3 Exemplary aromatic compounds indicated by the SP-LD-REMPI-ATOF-MS spectra in Fig. 16. Only major and the most proper aromatic compounds were listed.

m/z	name	formula	polar	nonpolar	reference
110	catecol	$C_6H_6O_2$	+		[170], [171]
115	PAHs fragments		+	+	[172], [173]
124	guaiacol	$C_7H_8O_2$	+		[162], [171]
128	naphthalene	$C_{10}H_8$	+	+	[43], [63], [173]
138	4-methylguaiacol	$C_8H_{10}O_2$	+	+	[171], [172]
152	vanillin	$C_8H_8O_3$	+	+	[63], [171], [174]
	4-ethylguaiacol	$C_9H_{12}O_2$			
	methoxynaphthalene	$C_{11}H_{10}O$			
158	1,4-naphthalenedione	$C_{10}H_6O_2$	+		[171], [175], [176]
	methylnaphthol	$C_{11}H_{10}O$			
165	PAHs fragments		+	+	[172], [173]
168	4-methylsyringol	$C_9H_{12}O_3$	+		[173], [175], [176]
	vanillic acid	$C_8H_8O_4$			
178	phenanthrene	$C_{14}H_{10}$	+	+	[43], [63], [73], [74]
	conifery aldehyde	$C_{10}H_{10}O_3$			
182	syringaldehyde	$C_9H_{10}O_4$	+		[171], [175], [176]
	4-ethylsyringol	$C_{10}H_{14}O_3$			
189,190,191	retene fragments		+	+	[73], [74], [177]
192	methylphenanthrene	$C_{15}H_{12}$	+	+	[43], [63], [73], [74]
202	pyrene	$C_{16}H_{10}$	+	+	[63], [73], [74], [172]
	fluoranthene				

m/z	name	formula	polar	nonpolar	reference
202	pyrene fluoranthene	$C_{16}H_{10}$	+	+	[63], [73], [74], [172]
203,204,205	retene fragments		+	+	[63], [177]
206	ethylphenanthrene	$C_{16}H_{14}$		+	[43]
219,220	retene fragments		+	+	[63], [73], [74]
234	retene	$C_{18}H_{18}$	+	+	[43], [63], [73], [74]
248	methyl. retene	$C_{19}H_{20}$		+	[63], [177]
250	ox. retene	$C_{18}H_{18}O$	+	+	[43]

4.1.3.2. Chemical composition of tar balls

The chemical composition of the tar balls was determined by HR-TOF-AMS. It was confirmed that tar balls contain mainly carbonaceous compounds and less N, S, and Cl. [160], [163] In the following only the organic fraction in the specimens was considered for the evaluation. In Fig. 17, the mass spectra of bulk organics from non-polar and polar tar balls before photooxidation or NO_x-dependent oxidation are given. The mass spectrum of non-polar tar balls is dominated by alkyl fragments such as $C_nH^+_{2n-1}$ and $C_nH^+_{2n+1}$. However, characteristic fragment ions for organic aromatic compounds are also detected ($C_4H_3^+$, $C_4H_4^+$, $C_5H_5^+$, $C_6H_5^+$, $C_6H_6^+$, $C_6H_9^+$, $C_7H_7^+$), which indicate that tar balls from the non-polar phase contain a significant proportion of aromatic compounds. [178] Both, nonpolar and polar tar ball mass spectra show distinct signals at m/z = 28 (CO^+), m/z = 29 (CHO^+), and m/z = 43 ($C_2H_3O^+$), indicating carbonyl ions. Oxidized species, therefore, dominate the mass spectra of polar tar balls. Characteristic fragment ions from levoglucosan m/z = 60, 73 ($C_2H_4O_2^+$, $C_3H_5O_2^+$) show higher signal intensities in polar tar balls due to the higher solubility in water. [179] $f44$ represents a fraction of a mass spectrum signal at m/z = 44 and presents the degree of oxidation in OA. Therefore, higher values represent more oxidized OA, and $f44$ has been shown to conduct linear correspondence to the elemental O:C ratio. [180] The values for O:C ratio are 0.25 and 0.44 for non-polar and polar tar balls, which results in an OSc (OSc $\approx$ 2O:C – H:C) of -1.05 - 0.76 in this study and corresponds well to literature values (-1.0 - 0.7 for primary BBOA [181]). Aerosols can achieve atmospheric residence times of hours to several days and are subject to various atmospheric aging processes during this time, which can lead to changes in chemical composition and physical properties. [15] In this study, photochemical oxidation of non-polar tar balls was investigated, which occur during the atmospheric aging process. In the oxidation flow reactor (OFR), two aging experiments were performed, NO_x-free and NO_x-dependent photochemical aging. The oxidation of NO_x-free oxidation covers 0.7 – 6.7 equivalent daytime oxidation days (EAD). The average complex refractive index (RI) of non-polar tar balls was measured during aging and dropped in a range of 0 - 3.9 EAD from 1.661 + 0.020i to 1.632 + 0.007i and remained stable at one value. This implies that the tar balls bleached out during the aging process, which was also observed in previous studies. [182] This bleaching reveals a direct correlation between photochemical aging and the light scattering and absorption of the tar balls. Chemical analysis of the aged non-polar tar balls
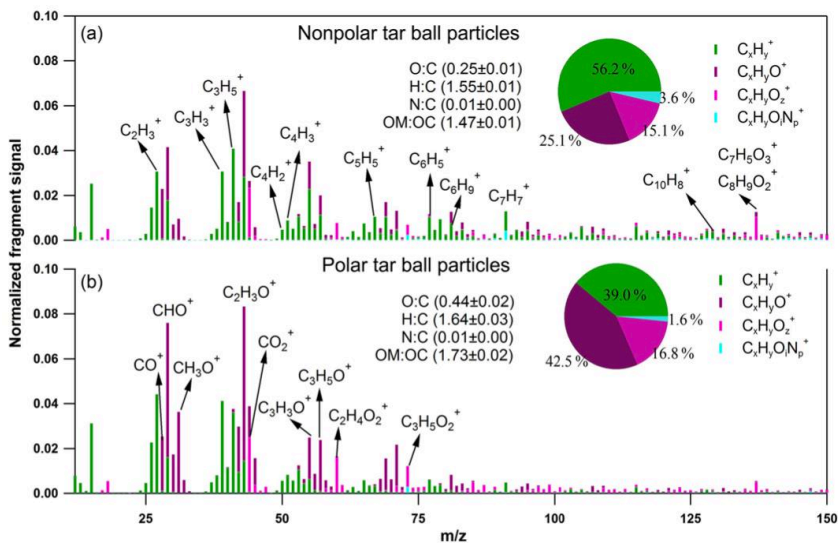
Fig. 17 High-resolution TOF-AMS spectra from (a) nonpolar tar balls with the highest signals for $C_xH_y^+$ fraction and (b) polar tar balls with the highest amount of $C_xH_yO_z^+$ fragments. The percentage distribution of the four ion groups are visualized by pie charts. (adapted from Li et al. 2019 [22])

shows an increase of O:C (0.25 to 0.38), H:C (1.55 to 1.62), and a decrease of alkyl/alkenyl chains (e.g., $C_nH^+_{2n-1}$ and $C_nH^+_{2n+1}$) as well as aromatic ring structure fragments (e.g., $C_6H_5^+$, $C_6H_9^+$). In contrast, AMS mass spectra of NO_x-dependent photochemical aging reveal several different effects. Compared to NO_x-free photochemical aging, the O:C ratio increased, and H:C decreased. Furthermore, NO_y^+ fragments appear in the mass spectra, and $C_xH_yO^+$, $C_xH_yO_z^+$, and $C_xH_yO_iN_p^+$ fragment ions also showed significantly increased signal intensities. The RI increased from 1.632 + 0.007i to 1.648 + 0.019i at 2 % vol N_2O due to NOC (nitrogen-containing organic compounds) formation. This implies that photochemical oxidation with NO_x addition increases the oxidation level and increases both absorption and light scattering of the tar balls. During photochemical aging with OH^- radicals, aromatic rings, and methoxy phenolic structures, which presumably represent the chromophores in tar balls, are broken down. This explains the change in light scattering and absorption of the tar balls. On the other hand, NO_x dependent aging promotes the formation of N-containing chromophores, which outweigh the bleaching of the aging process. This shows that the optical and chemical properties of tar balls are related to atmospheric aging via dynamic processes.

4.1.4. Simultaneous detection of PAHs as well as positive and negative inorganic ions – Publication 3

On-line single-particle analysis of complex aerosol samples with SPMS is a powerful technology for determining the chemical composition of anthropogenic and natural airborne particles. Positive and negative ions are generated in a vacuum through LDI and detected in a bipolar mass spectrometer. [58] Metals, salts, ammonia, organic fragments, and carbon clusters can be detected as cations. In the negative mass spectrum, nitrate, sulfate, phosphate, and carbon clusters of organic or elemental carbon dominate. In diverse studies of ambient particles, certain marker substances such as oxalic acid as photooxidation marker, [183], [184] methanesulfonates for marine environments, [85] and alkylamines [185] were detected, EC/OC content, [186], [187] and oligomer formation (negative peak series) [84] were investigated.

Fig. 18 Single particle mass spectra obtained using SP-LD-REMPI-LDI$^{+/-}$-ATOF-MS with negative LDI (black), positive LDI (blue), and REMPI (red). (a) Shows a single particle mass spectrum of an diesel particle consisting mainly of an EC matrix of soot, iron and some organic fragments, the REMPI spectrum reveals predominantly unsubstituted PAHs. (b) Single-particle mass spectrum of a wood ash particle with a soot matrix as well as stronger organic, also oxygen-containing fragment ions and a very strong signal for K$^+$ for LDI. The REMPI spectrum shows a different distribution compared to (a), which contains the (coniferous) wood combustion marker retene. (c) Purely organic tar ball particles with a weakly pronounced negative LDI spectrum, a large number of organic fragments in the positive LDI range and a pronounced REMPI spectrum (see Tab. 3).

Source apportionment with LDI-SPMS was further developed in numerous field studies, and many natural and anthropogenic aerosols could be identified and classified (see Tab. 1). In contrast, the analysis of particle-bound PAHs constitutes a particular challenge. Detailed PAH mass spectra can be obtained by multi-step ionization processes, whereby the ionization is preceded by a desorption step through either TD, [73], [188] or LD. [61], [62], [74] Decoupling the desorption and ionization steps can reduce fragmentation and improve quality significantly, but usually, the information about inorganic refractory components is lost, making source apportionment impossible. In a three-step ionization process, this limitation could recently be overcome (4.1.2 and appendix 7.1), but this process allows only positive ion detection, which strongly limits the information content of the LDI compared to the conventional method. [63] A new ionization method has been developed to address this limitation that allows the analysis of particle-bound PAHs via REMPI and the analysis of positive and negative ions of individual particles via LDI in a two-step ionization process. [91] A detailed description of the experimental design is given in section 3.3.3 and appendix 7.3. The modifications to the previous instrument configuration concern the optical setup and the high voltage supply. A brief description is provided here. Subsequently to the velocimetric sizing, the individual particles are hit by an IR-pulse of a CO$_2$ - laser ($\lambda = 10.6\,\mu m$) for efficient desorption of organic aromatic compounds (Fig. 12 (a)). The UV-laser beam of the KrF excimer laser ($\lambda = 248$ nm) traverses the plume for REMPI of desorbed PAHs with relatively low intensity. The laser beam is then reflected by a concave mirror ($f = 150$ mm) and focused on the remaining particle (Fig 12 (b)). In contrast to the three-step method, REMPI and LDI are performed by the identical laser at the same time (time

difference due to distance and speed of light ~ 1ns, laser pulse duration 5ns). While the negatively charged ions are analyzed in one TOF-MS, positive ions from LDI and REMPI are detected together in an orthogonally positioned positive TOF-MS. By using delayed extraction (DE), the quality of the detected TOF-MS spectra can be significantly improved. [120], [121], [189] High dynamic range of the LDI signals is already very demanding from an instrumental perspective in classical detection, but the analysis of LDI and REMPI ions in one mass spectrometer requires dynamic adjustments since the REMPI signals are much weaker. To achieve the maximum quality of the positive mass spectra in all ranges, the transmission of the lighter LDI ions is attenuated by detuning a lateral deflector of the ion optics without affecting the flight time. In several aspects, this method is different from a straightforward combination of LD-REMPI with LDI$^{+/-}$. A pure gas-phase REMPI experiment with the laser parameters used in this study could be operated fragment free. [110] The fragmentation in this setup of LD-REMPI depends on the internal energy of the particle transmitted by the IR-pulse. [190] In the optical setup of this study, the laser pulse for LDI traverses a part of the desorbed plume, leading to an additional formation of fragment ions. Due to an expansion time of the plume of 14 μs, the fraction of these ions in the total spectrum is relatively small. In contrast to laboratory plume expansion experiments, [60], [190], [191] laser desorption of ambient air particles is strongly affected by matrix effects and hit efficiency of the IR-pulse, which can lead to the increased fragmentation. However, the degree and proportion of aromatic compounds can be evaluated using PAH-specific fragment ions (e.g., m/z = 189 from alkylated phenanthrenes [73], [74]). In Fig. 18, three single-particle mass spectra of different particle classes are depicted as an example, showing the possibilities and the information gain of the new method. In laboratory experiments, hit rates
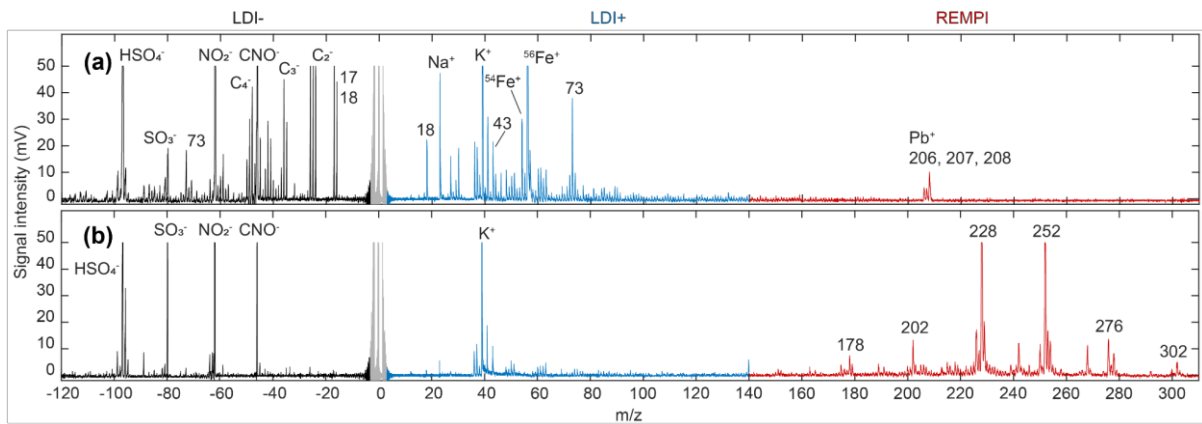
Fig. 19 Single-particle mass spectra of ambient air particles. (a) Exemplary particle for classes without PAHs, here the method yields conventional bipolar LDI spectra. (b) The negative LDI reveals strong signals for important secondary components such as sulfate and nitrate, positive LDI shows a strong signal for potassium and some organic fragments. Photooxidation processes in the atmosphere become apparent through peaks at m/z = 43 ($C_2H_3O^+$, $C_3H_7^+$) und oxalate at m/z = -89. The dominant PAH signals at m/z = 228/252 (e.g., chrysene/benzo(k)fluoranthene) in combination with the strong K^+ peak indicate coal or wood combustion.

of 60 % for LD-REMPI and 40 %, including bipolar LDI signature, were achieved. LDI of diesel soot particles (Fig. 18 (a)) produce strong signals for carbon clusters in both the negative (black) and positive (blue) range, and organic fragments are detectable in both mass spectra. [83], [192] The REMPI spectrum (red) shows mainly lighter and unsubstituted PAHs, which are typical for

diesel emissions [46] and are listed in Tab. 2. Comparable to previous studies (4.1.2 and 4.1.3), Fig. 18 (b), (c) shows single particle mass spectra of wood ash and tar ball. Negative LDI of wood ash shows an EC matrix similar to diesel, but both spectra differ in the organic fragments, which show a higher oxygen content in wood ash. A typical characteristic of wood/biomass combustion in positive LDI is a very strong potassium peak at m/z = 39/41 and 113 for $[K_2Cl]^+$. [150] The REMPI spectrum of PAHs is slightly shifted into the higher mass range than diesel and shows additional alkylated PAHs such as the (soft) wood combustion marker retene at m/z = 234. [73], [165] Tar balls represent an important particle subclass of BrC, which is of major interest in atmospheric and environmental research. Fig. 18 (c) shows single-particle mass spectra from a laboratory-generated homogeneous and spherical particle from wood pyrolysis, [22], [131] described in detail in section 4.1.3 and by Li et al. 2019. [22] In contrast to the aforementioned diesel and wood ash particles, the REMPI spectrum of PAHs show more alkylated and also lighter PAHs from incomplete combustion. Both, positive and negative LDI-spectra exclusively reveal organic fragments. Basically, this corresponds to previous studies but adding a third information channel leads to substantial enhancements, especially for analysis of ambient aerosols. In a short on-line experiment with ambient particles from 16th of December 2018, 20:00 to the 17th of December 2018 12:00 local time, a total of 69,900 particles could be detected and sized. With a hit rate of 36 % for positive LDI, 42 % for negative LDI, 30 % for bipolar LDI, and 29 % for PAHs, mass spectra for several thousand particles were detected. However, negative ion formation is strongly influenced by humidity. [193] Nevertheless, in this experiment, almost all particles with evaluable mass spectra showed signals in negative LDI for important secondary components from long-range transport (Fig. 19). [68] The size distribution of the detected particles is shown in Fig. 20 and represents a typical progression for long-range transported particles, [2] with the maximum in the range of the highest detection efficiency of velocimetric sizing of standard SPMS systems. [194] In Fig. 20, the composition of particles without (a) and with (b) PAH signature is plotted as a function of three ion signals. Particles from wood and biomass combustion can be identified in LDI-SPMS by a strong K^+ peak, which often suppresses other element and fragment ions (Fig. 19 (b)). [85], [195], [196] These particles are shown in the lower-left corner of the ternary plot. Strong Fe^+ signals in ambient particles are often associated with coal, waste incineration, industry or traffic. [197] These particles are shown in the lower-right corner of the plot. An example of this particle class is shown in Fig. 19 (a). Signals from organic fragments and carbon clusters are overlaid in the negative LDI by nitrate and sulfate, which are aerosol aging markers and indicate long-range transport. In the positive LDI spectrum, organic fragments and strong signals for iron and other metals such as Pb^+ are also detectable. In the upper corner of the ternary plot, the anion signal of $^{49}[C_4H]^-$ is evaluated, which is a common fragment of aromatic
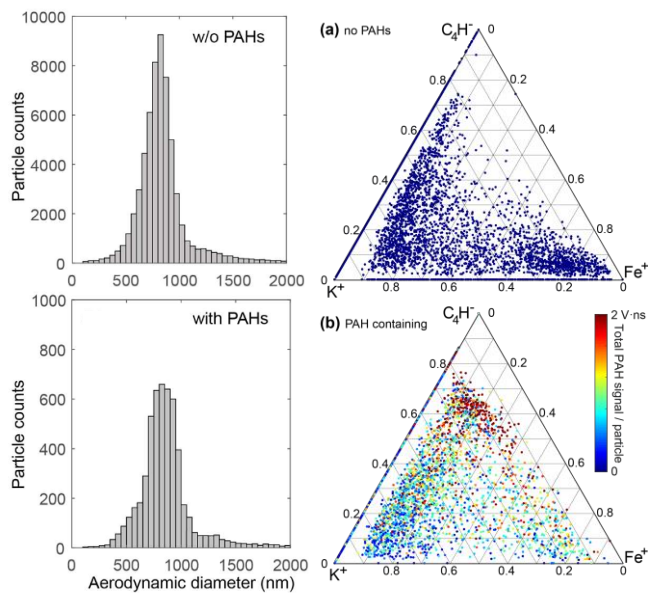
Fig. 20 Size distribution for ambient particles with and without PAHs (left side). The right side shows two ternary plots of the single-particle composition in dependence to three specific ions from LDI for ambient particle with (a) and without (b) PAHs. (a) Shows a distribution for particles without PAHs with dominant K^+ (wood/biomass combustion, left corner) and Fe^+ (coal combustion/industry/traffic, right corner). This cluster contains of 19,866 Particles. (b) Shows a more even distribution but with a maximum at the top with pure organic particles. This cluster contains 6762 particles.

and aliphatic organic compounds in the negative LDI spectrum. [83] Fig. 20 (a) and (b) show a relatively even distribution of aged particles on the three indicator ions, with PAHs more frequently occurring with higher intensity on organic and biomass combustion particles, while particles without PAHs hardly occur in the upper corner of the plot. For the first time, it is possible to detect bipolar LDI spectra with on-line SPMS simultaneously to REMPI analysis of individual particles. This new method allows the analysis of hazardous PAHs and metals and chemical composition for source apportionment and detection of atmospheric aging mechanisms with the same instrument. The three mass spectra contain complex correlations. Therefore, novel cluster methods will be necessary for the future to evaluate and determine the environmental and health impacts of the particles.

4.2. Wavelength dependent amplification effects of metals induced by resonance in laser desorption ionization single-particle mass spectrometry

4.2.1. Research objective

Natural and anthropogenic aerosols play a significant role in biogeochemical cycles, the earth's climate, and human health. Under this premise, countless studies have been conducted on aerosols containing carbon and also sulfate, [2], [14], [20], [198], [199] whereby particle-bound metals can also have far-reaching effects on the environment and human health. Through redox cycling activity, inhaled transition metals are able to induce oxidative stress [29], [48], [49], [200] and introduced into the oceans, they provide essential sources of nutrients and influence the biological ecosystem and climate. [26], [27], [34] In the context of this work, the resonant ionization of particle-bound metals was applied with on-line LDI-SPMS to contribute to a better understanding of the occurrence and distribution of metals in aerosols and a more efficient ionization scheme in SPMS.

4.2.2. Resonance-enhanced detection of metals in single-particle mass spectrometry – Publication 4

As described in the previous sections, SPMS is a powerful technique for single-particle analysis and is capable of detecting not only organic and inorganic molecules but also particle-bound metals, which are important for source apportionment. [64], [68], [85] Vanadium, for example, is a marker for ship emissions, [87], [201] and specific patterns of Al, Si, Ca indicate dust from soil erosion. [79] Resonant laser ablation and ionization of metals from solid samples have been studied for laser microprobe mass analysis (LAMMA) from surfaces, [202], [203] but not for single aerosol particles. In this study, wavelength-dependent amplification effects in single-particles with an SPMS and OPO system for resonant ionization of Fe, Mn, Zn were investigated in laboratory experiments. Furthermore, resonant absorption of iron coincides with the spectrum of a KrF excimer laser and, therefore, the REMPI absorption spectra of aromatic compounds, which provides the possibility to connect this feature with the detailed LD-REMPI-LDI-SPMS, [91]
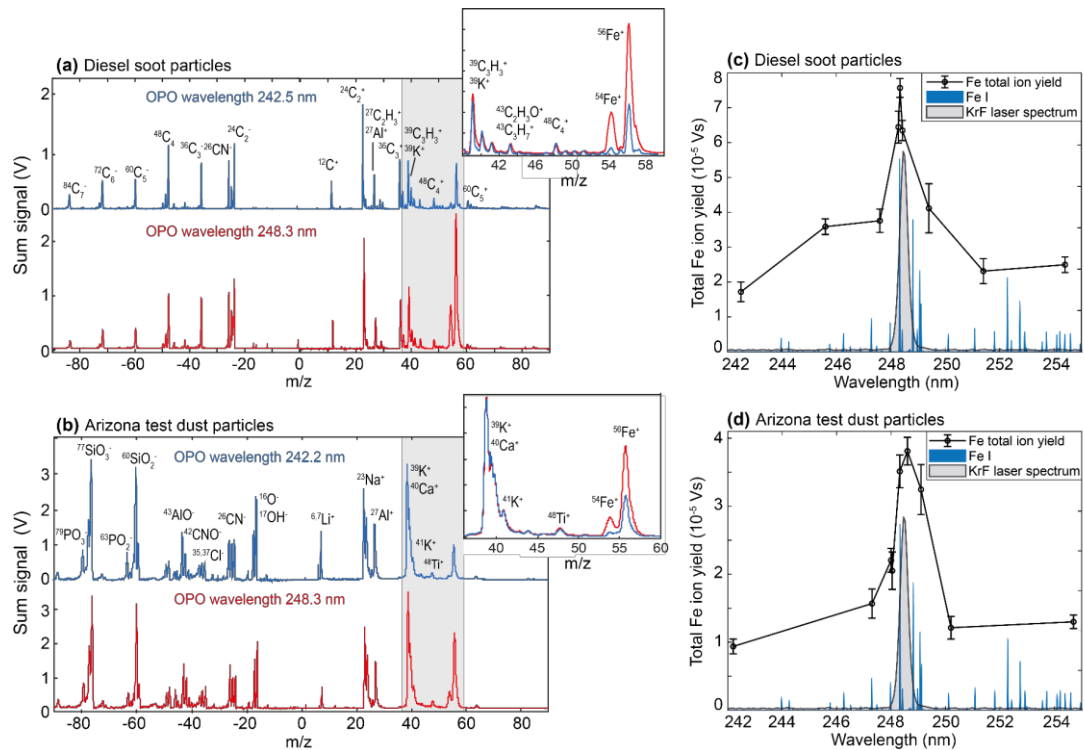
Fig. 21   Shows accumulated mass spectra (each n = 400) for re-dispersed car diesel exhaust particles (a) as an example of anthropogenic combustion particulates and Arizona desert dust (b) as a natural and mineral particulate system. The OPO was applied to both particle systems via LDI to ionize iron resonantly at a wavelength of 248.3 nm. The mass spectra with resonant ionization are shown in red and non-resonant ionization in blue, both particle systems show a significant increase of iron in resonant ionization. (c) and (d) show the total ion yield (black circles) of ^{54}Fe in SPMS (n=1200; three replicates of 400 each) for (c) diesel soot and (d) Arizona desert dust in a wavelength range of 242 – 255 nm. In blue important atomic transitions of Fe (Kramida et al. 2019 [205]) are plotted and in grey the spectrum of the KrF excimer laser.

described in section 4.1.4. The application potential of resonance effects is demonstrated in a field campaign comparing a KrF excimer laser with the more commonly used ArF excimer laser

concerning their iron detection capabilities of metal-containing ambient aerosols. The SPMS measurement system utilized in this study is described in other publications, [125] and a detailed experimental setup is given in section 3.3.4 and appendix 7.4. Briefly, the instrumental setup in principle is close to the ATOF-MS of Su et al. 2004 [204] equipped with an aerodynamic lens, introducing and focusing the particles into the vacuum, a sizing unit for velocimetric sizing and two TOF-MS systems designed in Z-shape, as introduced by Pratt et al. 2009. [136] The basic Nd:YAG solid-state laser ($\lambda = 266$ nm) was removed for both a tunable optical parametric oscillator (OPO) system and KrF and ArF excimer lasers ($\lambda = 248$ nm and $\lambda = 193$ nm). As representative model systems for both anthropogenic and natural particles, diesel exhaust and Arizona desert dust were measured with LDI-SPMS at different wavelengths. The cumulated raw mass spectra are shown in Fig. 21 without normalization or post-processing,

which caused here the side-effect of signal broadening. The mass spectra show the typical chemical composition of the two particle classes. Fig. 21 (a) predominantly carbon clusters (EC from soot), small fragments of organic molecules, predominantly hydrocarbons, and alkali metals (low ionization energy). Fig. 21 (b) shows mainly signals for metals and metal oxides, typical for natural mineral particles from soil erosion. The mass spectra of the two ionization wavelengths are almost identical, only the iron signature changes drastically (see insets Fig. 21 (a) and (b)). The wavelength of 248.3 nm matches the $3d^6 4s^2$ to $3d^6 4s4p$ transition of Fe atoms, which is commonly used for Fe determination in atomic absorption spectroscopy. For further analysis of this wavelength effect, the wavelength-dependent total ion yield of ^{54}Fe within a wavelength range of $242 - 255$ nm was measured from 1200 particles (three replicates of 400 each) all wavelengths with the OPO at constant laser energy (Fig. 21 (c) and (d)). Due to potential interferences of ^{56}Fe in the positive mass spectrum with CaO^+ and $[C_3H_4O]^+$, the signal of the ^{54}Fe isotope was applied
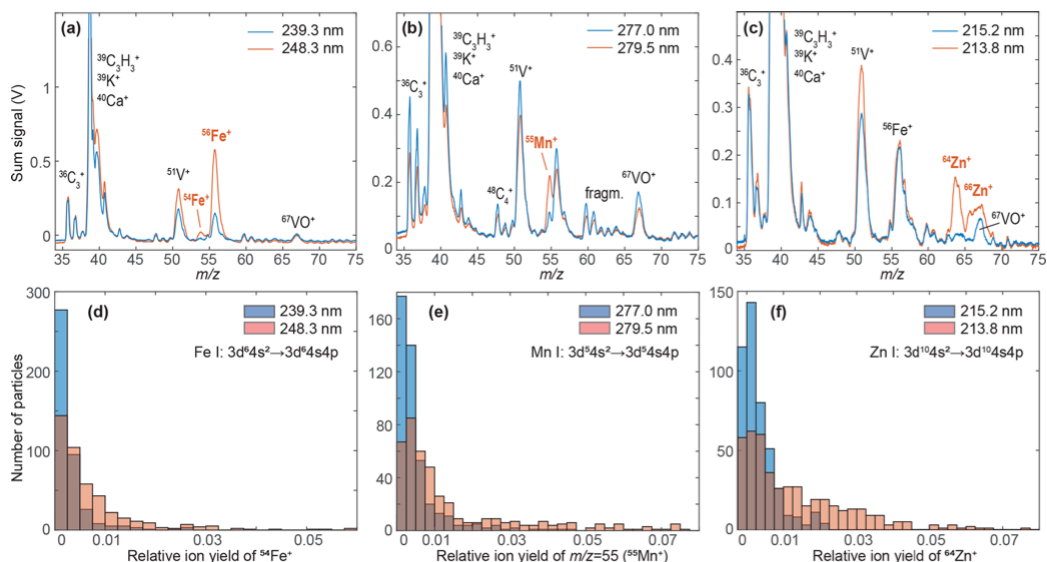
Fig. 22 Shows accumulated cation mass spectra (each n = 400) of re-dispersed standard reference material (NIST urban dust 1649b). The spectra were obtained at resonance wavelengths with constant laser pulse energies of Fe (a), Mn (b), and Zn (c) and plotted in red and at slightly different and non-resonant wavelengths in blue. Enhancement effects are clearly visible, while signals of molecular fragments and other elements stay constant. (d – f) Show the single-particle distribution of the relative ion signals and indicate higher numbers for detected metal-containing particles.

for evaluation. Superpositions of this signal with other organic and inorganic fragments and molecules are considered to be significantly smaller. The blue lines represent the absorption Spectrum of Fe atoms from the NIST atomic spectra library. [205] Near the main absorption line at 248.3 nm an enhancement effect of factor 3 - 4 is achieved in both particle systems. Such an effect has not been described in SPMS so far. Wade et al. 2008 found minimal wavelength effects on ion yields but strongly superimposed of laser intensity and particle size effects. [206] However, various studies show that effects in the plume after desorption during LDI dominate the ion yield in SPMS rather than the absorption of the particle itself. [106], [107], [206] The resonance effect occurs when Fe atoms are formed during the first phase of the laser pulse and vaporized from the particle. The shown resonance amplification effect during the ionization of iron in single-particles raises the question of whether other biologically important and health-relevant metals can be analyzed in this manner with SPMS. Fig. 22 illustrates the results of resonance enhancements experiments in SPMS, conducted with NIST urban dust 1649b as standard reference material and well-characterized anthropogenic and metal-containing particle model. Accumulated cation mass spectra show in pairwise comparison the resonance enhancements for Fe (a), Mn (b), and Zn (c). The histograms in Fig. 22 (d – f) illustrate the single-particle distribution of the relative ion signals and reveal a higher number of individual metal-containing particles, which indicates a more sensitive and efficient detection. In a field campaign in Sweden (~30 km south of Gothenburg), the resonance effect of the laboratory tests on ambient long-range transported aerosols could be investigated and applied. In this field study, the OPO system was replaced by more robust, powerful, and freely triggerable excimer lasers (see instrumental setup [137]), with the spectrum of the KrF excimer laser, coincidingly matching the strongest absorption line of Fe (Fig. 21 (c, d)). A custom electronic circuit triggers the 193 nm ArF excimer and 248 nm KrF excimer alternately for focusing on long-range particles with the minimum time difference. On the 14th of November 2019, between 15:00 and 24:00 local time, with each laser, 15,000 particles were analyzed, whereas spectra of the ArF laser achieved higher hit rates for positive, negative, and bipolar mass spectra due to its higher photon energy and lower intensity thresholds for ion formation. [207] Almost all negative mass spectra contained nitrate signals, which occur due to condensation of NO_3 and replacement of Cl^- by NO_3^- during long-range transport. [68], [85], [197], [208] The majority of the detected mass spectra showed either sea salt signatures (Tab. 1), [209] predominantly organic fragments [83] or showed internal mixtures of these dominant signals. A cluster analysis with ART-2a (described in more detail [210]–[212]) was performed to determine at the single-particle level the iron extension and the role and distribution of the major components of the particles. The dominating particle classes of this dataset are shown in Fig. 23. Despite the significantly lower hit rate, Fe can be detected in almost all particle classes with ionization at 248 nm, whereas with ionization at 193 nm, Fe can only be detected in EC particles despite a significantly higher hit rate and thus a more than twice as large total particle count. The dark grey fractions show peak area at m/z = 56 (only for signals larger than m/z = 40, Ca^+ and m/z = 55 fragment signal) possibly interfering with CaO^+ and $[C_3H_4O]^+$,
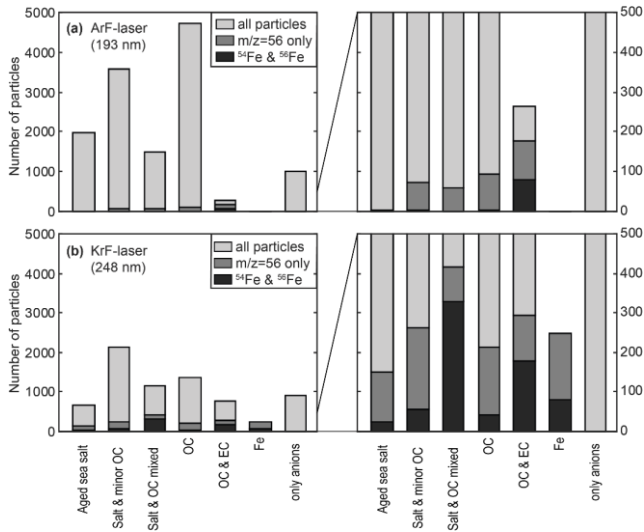
Fig. 23 Number of particles within the main classes revealed from ART-2a clustering of ambient long-range transport particles. Dark grey fractions show peak area at m/z = 56, possibly interfering with CaO^+, black fractions show peak area at m/z = 54 for $^{54}Fe^+$. (a) Particles ionized with 193 nm UV-laser show a noteworthy Fe signal almost exclusively with EC signatures, whereas the spectra from ionization with 248 nm reveal much larger iron signatures for all clusters. This shows impressively that iron signatures are not only contained in EC particles, but are distributed over considerably more particle classes and can be detected with resonance-enhanced ionization

to strengthen the criteria black fractions show peak area at m/z = 54 for $^{54}Fe^+$. The Fe signal in the dominating cluster in Fig. 23 (b) Salt & OC mixed even completely disappears in (a). For Fe dissolution and, therefore, the anthropogenic increase of bioavailable iron input to the oceans, the mixing of Fe containing aerosols with sulfate and nitrate are assumed to be crucial. [213] Previous studies suggest that anthropogenic Fe transport to the oceans is mainly caused by coal combustion aerosols containing large amounts of sulfate and traffic emissions mixed with nitrate. [197], [214], [215] These studies also showed strongly internally mixed particles, but SPMS found only small fractions of Fe mixed with OC and Fe containing sea salt particles were completely neglected. These results contrast the data from the cluster analysis shown in Fig. 23, where this particle class showed the highest iron content using resonance-enhanced ionization. Considering that previous SPMS studies were performed with non-resonant ionization, the Fe transport in organic and saline ore mixed particles could be underestimated.

5. Summary and Outlook

Different methods for the analysis and characterization of complex laboratory-generated and airborne single-particles were developed, optimized, and applied in the presented dissertation. For this objective, the fast and sensitive on-line TOF-MS measurement technique was utilized and equipped with multiple ionization techniques to perform analyses of both natural and anthropogenic organic and inorganic, ambient, and tar ball particles. The focus was on developing and improving new ionization approaches to strengthen the information yield and, thus, the understanding of atmospheric particles. Laser desorption/ionization mass spectrometry of individual particles allows the determination of the chemical composition depending on the particle's aerodynamic diameter. Especially anthropogenic aerosols from combustion processes are of great interest since they contain a large number of environmental and health-relevant substances. The combination of LD, REMPI, and LDI^+ has opened up the possibility to directly assess the health risks from PAHs in air pollution, providing information on the distribution of

PAHs among particle types and sizes, and assigning them to specific sources. Despite the limitation to positive ions, this approach provides new and meaningful information for the analysis of climate and health-related aerosols. Tar balls are a component of brown carbon, form a subcategory of organic aerosols, and are considered highly climate and health-relevant. Dynamic changes in the simulated atmospheric evolution of laboratory-generated tar ball particles show their relation between optical and chemical properties by photobleaching and secondary chromophore formation. LD-REMPI analysis of single tar balls reveals a considerable aromatic fraction of alkylated PAHs, oxygenated PAHs, phenols, and nitrogen-substituted PAHs that contribute to higher UV vis-absorption and therefore increases atmospheric and climatic implications. By spatial separation of laser-desorbed and refractory components and further development of the ionization scheme, a full bipolar LDI mass spectrum and detailed PAH signature of single-particles have been achieved for the first time. This technology enables the detection of carcinogenic PAHs via REMPI, health-relevant metals by LDI$^+$, atmospheric aging parameters through LDI$^-$, and allows source apportionment and mixing state determination to estimate the local dose on inhalation as a function of particle size within a single instrument. Concerning previous methods, this approach, by gaining an additional layer of information, allows new insights into the single-particle distribution of PAHs and expands the understanding of OA and atmospheric PM. In addition to PAHs, another focus of single-particle analysis is the detection of particle-associated metals that affect the environment and climate as well as human health through multiple and complex mechanisms of interaction. Material cycles and mechanisms of interaction are the basis of numerous studies but have not yet been fully elucidated. By enhancement effects based on resonant light absorption in the ionization process (LDI) of single-particle analysis, metal detection efficiency could be increased considerably. The KrF laser line at 248 nm coincidentally encounters a strong absorption line of iron atoms and enables the application of this resonance effect. The combination of resonant and efficient analysis of Fe with other key substances such as sulfate, nitrate, and phosphate allows the detection of atmospheric iron transport and important Fe distribution and bioavailability parameters at the single-particle level.

Single-particle bipolar LD-REMPI-LDI-TOF-MS provides a basis for analyzing climate and health-relevant aerosols and allows deep insights into the distribution of particle-bound pollutants, aging processes, and improved source apportionment and size-related evaluation. To push the limits of this technology even further, the development of an improved sizing unit to enable the efficient detection of atmospheric particles < 200 nm will be necessary. The development of adapted and complex evaluation mechanisms through data clustering for the analysis of atmospheric particles and extensive field studies enables a wide range of applications and future projects. PAH-source apportionment, investigation of health-relevant aerosols with both a specific metal and PAH content (e.g., ship emissions), aerosol transport of metal micronutrients into the oceans, and atmospheric particle aging are of considerable interest in this field of research. These studies will benefit considerably from the new developments presented in this dissertation.

6. References

[1] U. Pöschl, "Aerosol particle analysis: Challenges and progress," *Anal. Bioanal. Chem.*, vol. 375, no. 1, pp. 30–32, 2003, doi: 10.1007/s00216-002-1611-5.

[2] J. H. Seinfeld and S. N. Pandis, *Atmospheric Chemistry and Physics: From air pollution to climate change*, 3rd ed. Wiley: Hoboken, New Jersey, 2016.

[3] S. Fuzzi *et al.*, "Particulate matter, air quality and climate: Lessons learned and future needs," *Atmos. Chem. Phys.*, vol. 15, no. 14, pp. 8217–8299, 2015, doi: 10.5194/acp-15-8217-2015.

[4] S. N. Pandis, A. S. Wexler, and J. H. Seinfeld, "Dynamics of tropospheric aerosols," *J. Phys. Chem.*, vol. 99, no. 24, pp. 9646–9659, 1995, doi: 10.1021/j100024a003.

[5] P. R. Buseck and K. Adachi, "Nanoparticles in the atmosphere," *Elements*, vol. 4, no. 6, pp. 389–394, 2008, doi: 10.2113/gselements.4.6.389.

[6] M. Shrivastava *et al.*, "Recent advances in understanding secondary organic aerosol: Implications for global climate forcing," *Rev. Geophys.*, vol. 55, no. 2, pp. 509–559, 2017, doi: 10.1002/2016RG000540.

[7] R. Zhang *et al.*, "Morphology and property investigation of primary particulate matter particles from different sources," *Nano Res.*, vol. 11, no. 6, pp. 3182–3192, 2018, doi: 10.1007/s12274-017-1724-y.

[8] U. Pöschl, "Atmospheric aerosols: Composition, transformation, climate and health effects," *Angew. Chemie - Int. Ed.*, vol. 44, no. 46, pp. 7520–7540, 2005, doi: 10.1002/anie.200501122.

[9] P. F. DeCarlo, J. G. Slowik, D. R. Worsnop, P. Davidovits, and J. L. Jimenez, "Particle morphology and density characterization by combined mobility and aerodynamic diameter measurements. Part 1: Theory," *Aerosol Sci. Technol.*, vol. 38, no. 12, pp. 1185–1205, 2004, doi: 10.1080/027868290903907.

[10] J. G. Slowik *et al.*, "Particle morphology and density characterization by combined mobility and aerodynamic diameter measurements. Part 2: Application to combustion-generated soot aerosols as a function of fuel equivalence ratio," *Aerosol Sci. Technol.*, vol. 38, no. 12, pp. 1206–1222, 2004, doi: 10.1080/027868290903916.

[11] R. J. Huang *et al.*, "High secondary aerosol contribution to particulate pollution during haze events in China," *Nature*, vol. 514, no. 7521, pp. 218–222, 2015, doi: 10.1038/nature13774.

[12] N. Riemer, A. P. Ault, M. West, R. L. Craig, and J. H. Curtis, "Aerosol Mixing State: Measurements, Modeling, and Impacts," *Rev. Geophys.*, vol. 57, no. 2, pp. 187–249, 2019, doi: 10.1029/2018RG000615.

[13] Q. Zhang *et al.*, "Ubiquity and dominance of oxygenated species in organic aerosols in anthropogenically-influenced Northern Hemisphere midlatitudes," *Geophys. Res. Lett.*, vol. 34, no. 13, pp. 1–6, 2007, doi: 10.1029/2007GL029979.

[14] M. Kanakidou *et al.*, "Organic aerosol and global climate modelling: A review," *Atmos. Chem. Phys.*, vol. 5, no. 4, pp. 1053–1123, 2005, doi: 10.5194/acp-5-1053-2005.

[15]   J. L. Jimenez *et al.*, "Evolution of organic aerosols in the atmosphere," *Science*, vol. 326, no. 5959, pp. 1525–1529, 2009, doi: 10.1126/science.1180353.

[16]   N. M. Donahue, S. A. Epstein, S. N. Pandis, and A. L. Robinson, "A two-dimensional volatility basis set: 1. organic-aerosol mixing thermodynamics," *Atmos. Chem. Phys.*, vol. 11, no. 7, pp. 3303–3318, 2011, doi: 10.5194/acp-11-3303-2011.

[17]   N. M. Donahue, J. H. Kroll, S. N. Pandis, and A. L. Robinson, "A two-dimensional volatility basis set-Part 2: Diagnostics of organic-aerosol evolution," *Atmos. Chem. Phys.*, vol. 12, no. 2, pp. 615–634, 2012, doi: 10.5194/acp-12-615-2012.

[18]   T. F. Stocker *et al.*, "Technical Summary. In: Climate Change 2013: The Physical Science Basis. Contribution of Working Group I to the Fifth Assessment Report of the Intergovernmental Panel on Climate Change," *Clim. Chang. 2013 - Phys. Sci. Basis*, pp. 33–116, 2013, doi: 10.1017/cbo9781107415324.005.

[19]   WHO, "Ambient air pollution: A global assessment of exposure and burden of disease," 2016.

[20]   T. C. Bond *et al.*, "Bounding the role of black carbon in the climate system: A scientific assessment," *J. Geophys. Res. Atmos.*, vol. 118, no. 11, pp. 5380–5552, 2013, doi: 10.1002/jgrd.50171.

[21]   M. O. Andreae, "The dark side of aerosols," *Nature*, vol. 409, pp. 671–672, 2001, doi: 10.1038/35055640.

[22]   C. Li *et al.*, "Dynamic changes in optical and chemical properties of tar ball aerosols by atmospheric photochemical aging," *Atmos. Chem. Phys.*, vol. 19, no. 1, pp. 139–163, 2019, doi: 10.5194/acp-19-139-2019.

[23]   A. Laskin, J. Laskin, and S. A. Nizkorodov, "Chemistry of Atmospheric Brown Carbon," *Chem. Rev.*, vol. 115, no. 10, pp. 4335–4382, 2015, doi: 10.1021/cr5006167.

[24]   S. D. D'Andrea *et al.*, "Understanding global secondary organic aerosol amount and size-resolved condensational behavior," *Atmos. Chem. Phys.*, vol. 13, no. 22, pp. 11519–11534, 2013, doi: 10.5194/acp-13-11519-2013.

[25]   J. H. Seinfeld *et al.*, "Improving our fundamental understanding of the role of aerosol-cloud interactions in the climate system," *Proc. Natl. Acad. Sci. U. S. A.*, vol. 113, no. 21, pp. 5781–5790, 2016, doi: 10.1073/pnas.1514043113.

[26]   N. M. Mahowald *et al.*, "Aerosol trace metal leaching and impacts on marine microorganisms," *Nat. Commun.*, vol. 9, no. 1, 2018, doi: 10.1038/s41467-018-04970-7.

[27]   A. Ito and Z. Shi, "Delivery of anthropogenic bioavailable iron from mineral dust and combustion aerosols to the ocean," *Atmos. Chem. Phys.*, vol. 16, no. 1, pp. 85–99, 2016, doi: 10.5194/acp-16-85-2016.

[28]   N. Meskhidze *et al.*, "Perspective on identifying and characterizing the processes controlling iron speciation and residence time at the atmosphere-ocean interface," *Mar. Chem.*, vol. 217, p. 103704, 2019, doi: 10.1016/j.marchem.2019.103704.

[29]   M. Oakes *et al.*, "Iron solubility related to particle sulfur content in source emission and ambient fine particles," *Environ. Sci. Technol.*, vol. 46, no. 12, pp. 6637–6644, 2012, doi: 10.1021/es300701c.

[30] N. Meskhidze, D. Hurley, T. M. Royalty, and M. S. Johnson, "Potential effect of atmospheric dissolved organic carbon on the iron solubility in seawater," *Mar. Chem.*, vol. 194, pp. 124–132, 2017, doi: 10.1016/j.marchem.2017.05.011.

[31] M. Gledhill and K. N. Buck, "The organic complexation of iron in the marine environment: A review," *Front. Microbiol.*, vol. 3, pp. 1–17, 2012, doi: 10.3389/fmicb.2012.00069.

[32] T. J. Browning *et al.*, "Strong responses of Southern Ocean phytoplankton communities to volcanic ash," *Geophys. Res. Lett.*, vol. 41, pp. 2851–2857, 2014, doi: 10.1002/2014GL059364.

[33] A. Jordi, G. Basterretxea, A. Tovar-Sánchez, A. Alastuey, and X. Querol, "Copper aerosols inhibit phytoplankton growth in the Mediterranean Sea," *Proc. Natl. Acad. Sci. U. S. A.*, vol. 109, no. 52, pp. 21246–21249, 2012, doi: 10.1073/pnas.1207567110.

[34] T. D. Jickells *et al.*, "Global iron connections between desert dust, ocean biogeochemistry, and climate," *Science*, vol. 308, no. 5718, pp. 67–71, 2005, doi: 10.1126/science.1105959.

[35] A. J. Cohen *et al.*, "Estimates and 25-year trends of the global burden of disease attributable to ambient air pollution: an analysis of data from the Global Burden of Diseases Study 2015," *Lancet*, vol. 389, no. 10082, pp. 1907–1918, 2017, doi: 10.1016/S0140-6736(17)30505-6.

[36] R. Burnett *et al.*, "Global estimates of mortality associated with longterm exposure to outdoor fine particulate matter," *Proc. Natl. Acad. Sci. U. S. A.*, vol. 115, no. 38, pp. 9592–9597, 2018, doi: 10.1073/pnas.1803222115.

[37] R. Niranjan and A. K. Thakur, "The toxicological mechanisms of environmental soot (black carbon) and carbon black: Focus on Oxidative stress and inflammatory pathways," *Front. Immunol.*, vol. 8, pp. 1–20, 2017, doi: 10.3389/fimmu.2017.00763.

[38] W. Xue and D. Warshawsky, "Metabolic activation of polycyclic and heterocyclic aromatic hydrocarbons and DNA damage: A review," *Toxicol. Appl. Pharmacol.*, vol. 206, no. 1, pp. 73–93, 2005, doi: 10.1016/j.taap.2004.11.006.

[39] P. Vineis and K. Husgafvel-Pursiainen, "Air pollution and cancer: Biomarker studies in human populations," *Carcinogenesis*, vol. 26, no. 11, pp. 1846–1855, 2005, doi: 10.1093/carcin/bgi216.

[40] H. Jiang, S. L. Gelhaus, D. Mangal, R. G. Harvey, I. A. Blair, and T. M. Penning, "Metabolism of benzo[a]pyrene in human bronchoalveolar H358 cells using liquid chromatography-mass spectrometry," *Chem. Res. Toxicol.*, vol. 20, no. 9, pp. 1331–1341, 2007, doi: 10.1021/tx700107z.

[41] J. Lewtas, "Air pollution combustion emissions: Characterization of causative agents and mechanisms associated with cancer, reproductive, and cardiovascular effects," *Mutat. Res. - Rev. Mutat. Res.*, vol. 636, no. 1–3, pp. 95–133, 2007, doi: 10.1016/j.mrrev.2007.08.003.

[42] J. Heyder, "Deposition of inhaled particles in the human respiratory tract and consequences for regional targeting in respiratory drug delivery.," *Proc. Am. Thorac. Soc.*, vol. 1, no. 4, pp. 315–320, 2004, doi: 10.1513/pats.200409-046TA.

[43]   V. Samburova *et al.*, "Polycyclic aromatic hydrocarbons in biomass-burning emissions and their contribution to light absorption and aerosol toxicity," *Sci. Total Environ.*, vol. 568, pp. 391–401, 2016, doi: 10.1016/j.scitotenv.2016.06.026.

[44]   O. Uski *et al.*, "Effect of fuel zinc content on toxicological responses of particulate matter from pellet combustion in vitro," *Sci. Total Environ.*, vol. 511, pp. 331–340, 2015, doi: 10.1016/j.scitotenv.2014.12.061.

[45]   L. D. Claxton, "The history, genotoxicity, and carcinogenicity of carbon-based fuels and their emissions. Part 3: Diesel and gasoline," *Mutat. Res. - Rev. Mutat. Res.*, vol. 763, pp. 30–85, 2015, doi: 10.1016/j.mrrev.2014.09.002.

[46]   K. Ravindra, R. Sokhi, and R. Van Grieken, "Atmospheric polycyclic aromatic hydrocarbons: Source attribution, emission factors and regulation," *Atmos. Environ.*, vol. 42, no. 13, pp. 2895–2921, 2008, doi: 10.1016/j.atmosenv.2007.12.010.

[47]   P. Y. Bruice, *Organische Chemie*, 5th ed. Pearson Education Deutschland GmbH München, 2011.

[48]   D. Ye *et al.*, "Estimating acute cardiovascular effects of ambient PM2.5 metals," *Environ. Health Perspect.*, vol. 126, no. 2, pp. 1–10, 2018, doi: 10.1289/EHP2182.

[49]   T. Fang, H. Guo, L. Zeng, V. Verma, A. Nenes, and R. J. Weber, "Highly Acidic Ambient Particles, Soluble Metals, and Oxidative Potential: A Link between Sulfate and Aerosol Toxicity," *Environ. Sci. Technol.*, vol. 51, no. 5, pp. 2611–2620, 2017, doi: 10.1021/acs.est.6b06151.

[50]   C. Angelé-Martínez, C. Goodman, and J. Brumaghim, "Metal-mediated DNA damage and cell death: Mechanisms, detection methods, and cellular consequences," *Metallomics*, vol. 6, no. 8, pp. 1358–1381, 2014, doi: 10.1039/c4mt00057a.

[51]   T. Streibel *et al.*, "Aerosol emissions of a ship diesel engine operated with diesel fuel or heavy fuel oil," *Environ. Sci. Pollut. Res.*, vol. 24, no. 12, pp. 10976–10991, 2017, doi: 10.1007/s11356-016-6724-z.

[52]   C. P. Rüger, M. Sklorz, T. Schwemer, and R. Zimmermann, "Characterisation of ship diesel primary particulate matter at the molecular level by means of ultra-high-resolution mass spectrometry coupled to laser desorption ionisation - Comparison of feed fuel, filter extracts and direct particle measurements," *Anal. Bioanal. Chem.*, vol. 407, no. 20, pp. 5923–5937, 2015, doi: 10.1007/s00216-014-8408-1.

[53]   B. Nozière *et al.*, "The Molecular Identification of Organic Compounds in the Atmosphere: State of the Art and Challenges," *Chem. Rev.*, vol. 115, no. 10, pp. 3919–3983, 2015, doi: 10.1021/cr5003485.

[54]   J. Laskin, A. Laskin, and S. A. Nizkorodov, "Mass Spectrometry Analysis in Atmospheric Chemistry," *Anal. Chem.*, vol. 90, no. 1, pp. 166–189, 2018, doi: 10.1021/acs.analchem.7b04249.

[55]   D. Wechsung, F. Hillenkamp, R. Kaufmann, R. Nitsche, E. Unsöld, and H. Vogt, "LAMMA - A new laser- microprobe-mass-analyzer," *Microsc. Acta*, vol. 2, pp. 281–296, 1978.

[56]   M. P. Sinha, "Laser- induced volatilization and ionization of microparticles," *Rev. Sci. Instrum.*, vol. 55, no. 6, pp. 886–891, 1984, doi: 10.1063/1.1137851

[57]   K. A. Prather, T. Nordmeyer, and K. Salt, "Real-Time Characterization of Individual Aerosol Particles Using Time-of-Flight Mass Spectrometry," *Anal. Chem.*, vol. 66, no. 9, pp. 1403–1407, 1994, doi: 10.1021/ac00081a007.

[58]   K. P. Hinz, R. Kaufmann, and B. Spengler, "Simultaneous detection of positive and negative ions from single airborne particles by real-time laser mass spectrometry," *Aerosol Sci. Technol.*, vol. 24, no. 4, pp. 233–242, 1996, doi: 10.1080/02786829608965368.

[59]   E. Gard, J. E. Mayer, B. D. Morrical, T. Dienes, D. P. Fergenson, and K. A. Prather, "Real-Time Analysis of Individual Atmospheric Aerosol Particles: Design and Performance of a Portable ATOFMS," *Anal. Chem.*, vol. 69, no. 20, pp. 4083–4091, 1997, doi: 10.1021/ac970540n.

[60]   E. Woods, G. D. Smith, Y. Dessiaterik, T. Baer, and R. E. Miller, "Quantitative detection of aromatic compounds in single aerosol particle mass spectrometry," *Anal. Chem.*, vol. 73, no. 10, pp. 2317–2322, 2001, doi: 10.1021/ac001166l.

[61]   B. D. Morrical, D. P. Fergenson, and K. A. Prather, "Coupling two-step laser desorption/ ionization with aerosol time-of-flight mass spectrometry for the analysis of individual organic particles," *J. Am. Soc. Mass Spectrom.*, vol. 9, no. 10, pp. 1068–1073, 1998, doi: 10.1016/S1044-0305(98)00074-9.

[62]   A. Zelenyuk and D. Imre, "Single particle laser ablation time-of-flight mass spectrometer: An introduction to SPLAT," *Aerosol Sci. Technol.*, vol. 39, no. 6, pp. 554–568, 2005, doi: 10.1080/027868291009242.

[63]   J. Passig *et al.*, "Aerosol Mass Spectrometer for Simultaneous Detection of Polyaromatic Hydrocarbons and Inorganic Components from Individual Particles," *Anal. Chem.*, vol. 89, no. 12, pp. 6341–6345, 2017, doi: 10.1021/acs.analchem.7b01207.

[64]   K. A. Pratt and K. A. Prather, "Mass Spectrometry of Atmospheric Aerosols - Recent Developments and Applications. Part II: On-Line Mass Spectrometry Techniques," *Mass Spectrom. Rev.*, vol. 31, pp. 17–48, 2012.

[65]   Y. J. Li *et al.*, "Real-time chemical characterization of atmospheric particulate matter in China: A review," *Atmos. Environ.*, vol. 158, pp. 270–304, 2017, doi: 10.1016/j.atmosenv.2017.02.027.

[66]   A. M. Middlebrook *et al.*, "A comparison of particle mass spectrometers during the 1999 Atlanta supersite project," *J. Geophys. Res. Atmos.*, vol. 108, no. 7, pp. 1–13, 2003, doi: 10.1029/2001jd000660.

[67]   R. M. Harrison *et al.*, "Atmospheric chemistry and physics in the atmosphere of a developed megacity (London): An overview of the REPARTEE experiment and its conclusions," *Atmos. Chem. Phys.*, vol. 12, no. 6, pp. 3065–3114, 2012, doi: 10.5194/acp-12-3065-2012.

[68]   M. Dall'Osto, D. C. S. Beddows, E. J. McGillicuddy, J. K. Esser-Gietl, R. M. Harrison, and J. C. Wenger, "On the simultaneous deployment of two single-particle mass spectrometers at an urban background and a roadside site during SAPUSS," *Atmos. Chem. Phys.*, vol. 16, no. 15, pp. 9693–9710, 2016, doi: 10.5194/acp-16-9693-2016.

[69]   R. M. Healy *et al.*, "Sources and mixing state of size-resolved elemental carbon particles in a European megacity: Paris," *Atmos. Chem. Phys.*, vol. 12, no. 4, pp. 1681–1700, 2012, doi: 10.5194/acp-12-1681-2012.

[70]   R. M. Healy *et al.*, "Quantitative determination of carbonaceous particle mixing state in Paris using single-particle mass spectrometer and aerosol mass spectrometer measurements," *Atmos. Chem. Phys.*, vol. 13, no. 18, pp. 9479–9496, 2013, doi: 10.5194/acp-13-9479-2013.

[71]   L. Li *et al.*, "Ambient particle characterization by single particle aerosol mass spectrometry in an urban area of Beijing," *Atmos. Environ.*, vol. 94, pp. 323–331, 2014, doi: 10.1016/j.atmosenv.2014.03.048.

[72]   M. Frenklach, "Reaction mechanism of soot formation in flames," *Phys. Chem. Chem. Phys.*, vol. 4, no. 11, pp. 2028–2037, 2002, doi: 10.1039/b110045a.

[73]   M. Bente, M. Sklorz, T. Streibel, and R. Zimmermann, "Thermal desorption-multiphoton ionization time-of-flight mass spectrometry of individual aerosol particles: A simplified approach for online single-particle analysis of polycyclic aromatic hydrocarbons and their derivatives," *Anal. Chem.*, vol. 81, no. 7, pp. 2525–2536, 2009, doi: 10.1021/ac802296f.

[74]   M. Bente, M. Sklorz, T. Streibel, and R. Zimmermann, "Online laser desorption-multiphoton postionization mass spectrometry of individual aerosol particles: Molecular source indicators for particles emitted from different traffic-related and wood combustion sources," *Anal. Chem.*, vol. 80, no. 23, pp. 8991–9004, 2008, doi: 10.1021/ac801295f.

[75]   C. J. Gaston *et al.*, "The cloud nucleating properties and mixing state of marine aerosols sampled along the Southern California coast," *Atmosphere (Basel).*, vol. 9, no. 2, 2018, doi: 10.3390/atmos9020052.

[76]   M. Dall'Osto, D. C. S. Beddows, R. P. Kinnersley, R. M. Harrison, R. J. Donovan, and M. R. Heal, "Characterization of individual airborne particles by using aerosol time-of-flight mass spectrometry at Mace Head, Ireland," *J. Geophys. Res. D Atmos.*, vol. 109, no. 21, 2004, doi: 10.1029/2004JD004747.

[77]   M. Dall'Osto and R. M. Harrison, "Chemical characterisation of single airborne particles in Athens (Greece) by ATOFMS," *Atmos. Environ.*, vol. 40, no. 39, pp. 7614–7631, 2006, doi: 10.1016/j.atmosenv.2006.06.053.

[78]   M. Dall'Osto *et al.*, "Variation of the mixing state of Saharan dust particles with atmospheric transport," *Atmos. Environ.*, vol. 44, no. 26, pp. 3135–3146, 2010, doi: 10.1016/j.atmosenv.2010.05.030.

[79]   R. C. Sullivan, S. A. Guazzotti, D. A. Sodeman, and K. A. Prather, "Direct observations of the atmospheric processing of Asian mineral dust," *Atmos. Chem. Phys.*, vol. 7, no. 5, pp. 1213–1236, 2007, doi: 10.5194/acp-7-1213-2007.

[80]   C. M. Sultana, H. Al-Mashat, and K. A. Prather, "Expanding Single Particle Mass Spectrometer Analyses for the Identification of Microbe Signatures in Sea Spray Aerosol," *Anal. Chem.*, vol. 89, no. 19, pp. 10162–10170, 2017, doi: 10.1021/acs.analchem.7b00933.

[81] A. Srivastava *et al.*, "Comprehensive assignment of mass spectral signatures from individual Bacilluss atrophaeus spores in matrix-free laser desorption/ionization bioaerosol mass spectrometry," *Anal. Chem.*, vol. 77, no. 10, pp. 3315–3323, 2005, doi: 10.1021/ac048298p.

[82] S. C. Russell, "Microorganism characterization by single particle mass spectrometry," *Mass Spectrom. Rev.*, vol. 28, no. 2, pp. 376–387, 2009, doi: 10.1002/mas.20198.

[83] P. J. Silva and K. A. Prather, "Interpretation of mass spectra from organic compounds in aerosol time-of-flight mass spectrometry," *Anal. Chem.*, vol. 72, no. 15, pp. 3553–3562, 2000, doi: 10.1021/ac9910132.

[84] D. S. Gross *et al.*, "Real-time measurement of oligomeric species in secondary organic aerosol with the aerosol time-of-flight mass spectrometer," *Anal. Chem.*, vol. 78, no. 7, pp. 2130–2137, 2006, doi: 10.1021/ac060138l.

[85] J. Arndt *et al.*, "Sources and mixing state of summertime background aerosol in the north-western Mediterranean basin," *Atmos. Chem. Phys.*, vol. 17, no. 11, pp. 6975–7001, 2017, doi: 10.5194/acp-17-6975-2017.

[86] S. Decesari *et al.*, "Measurements of the aerosol chemical composition and mixing state in the Po Valley using multiple spectroscopic techniques," *Atmos. Chem. Phys.*, vol. 14, no. 22, pp. 12109–12132, 2014, doi: 10.5194/acp-14-12109-2014.

[87] R. M. Healy, I. P. O'Connor, S. Hellebust, A. Allanic, J. R. Sodeau, and J. C. Wenger, "Characterisation of single particles from in-port ship emissions," *Atmos. Environ.*, vol. 43, no. 40, pp. 6408–6414, 2009, doi: 10.1016/j.atmosenv.2009.07.039.

[88] A. P. Ault, M. J. Moore, H. Furutani, and K. A. Prather, "Impact of emissions from the Los Angeles Port region on San Diego air quality during regional transport events," *Environ. Sci. Technol.*, vol. 43, no. 10, pp. 3500–3506, 2009, doi: 10.1021/es8018918.

[89] Q. Xiao *et al.*, "Characteristics of marine shipping emissions at berth: Profiles for particulate matter and volatile organic compounds," *Atmos. Chem. Phys.*, vol. 18, no. 13, pp. 9527–9545, 2018, doi: 10.5194/acp-18-9527-2018.

[90] Y. Zhang, X. Wang, H. Chen, X. Yang, J. Chen, and J. O. Allen, "Source apportionment of lead-containing aerosol particles in Shanghai using single particle mass spectrometry," *Chemosphere*, vol. 74, no. 4, pp. 501–507, 2009, doi: 10.1016/j.chemosphere.2008.10.004.

[91] J. Schade *et al.*, "Spatially Shaped Laser Pulses for the Simultaneous Detection of Polycyclic Aromatic Hydrocarbons as well as Positive and Negative Inorganic Ions in Single Particle Mass Spectrometry," *Anal. Chem.*, vol. 91, no. 15, pp. 10282–10288, 2019, doi: 10.1021/acs.analchem.9b02477.

[92] J. H. Gross, *Mass Spectrometry - A Textbook*, 2nd ed. Springer-Verlag Berlin-Heidelberg, 2011.

[93] T. D. Märk, "Fundamental aspects of electron impact ionization," *Int. J. Mass Spectrom. Ion Phys.*, vol. 45, no. C, pp. 125–145, 1982, doi: 10.1016/0020-7381(82)80103-4.

[94] F. P. Lossing and I. Tanaka, "Photoionization as a Source of Ions for Mass Spectrometry," *J. Chem. Phys.*, vol. 25, no. 5, pp. 1031–1034, 1956, doi: 10.1063/1.1743092.

[95]   U. Boesl, H. J. Neusser, and E. W. Schlag, "Two-Photon Ionization of Polyatomic Molecules in a Mass Spectrometer," *Zeitschrift fur Naturforsch. - Sect. A J. Phys. Sci.*, vol. 33, no. 12, pp. 1546–1548, 1978, doi: 10.1515/zna-1978-1218.

[96]   N. P. Lockyer and J. C. Vickerman, "Single photon ionisation mass spectrometry using laser-generated vacuum ultraviolet photons," *Laser Chem.*, vol. 17, no. 3, pp. 139–159, 1997, doi: 10.1155/1997/53174.

[97]   T. Streibel and R. Zimmermann, "Resonance-Enhanced Multiphoton Ionization Mass Spectrometry (REMPI-MS): Applications for Process Analysis," *Annu. Rev. Anal. Chem.*, vol. 7, pp. 361–381, 2014, doi: 10.1146/annurev-anchem-062012-092648.

[98]   R. Zimmermann, "Photo ionisation in mass spectrometry: Light, selectivity and molecular ions," *Anal. Bioanal. Chem.*, vol. 405, no. 22, pp. 6901–6905, 2013, doi: 10.1007/s00216-013-7187-4.

[99]   R. C. Powell, *Physics of solid-state laser materials*. Springer-Verlag Berlin-Heidelberg, 1998.

[100]   D. A. Skoog and J. J. Leary, *Instrumentelle Analytik: Grundlagen, Geräte, Anwendungen*. Springer-Verlag Berlin-Heidelberg, 1996.

[101]   J. Eichler and H. J. Eichler, *Laser - Bauformen, Strahlführung, Anwendungen*. Springer-Verlag Berlin-Heidelberg, 2010.

[102]   M. J. Dale, A. C. Jones, S. J. T. Pollard, and R. R. Langridge-Smith, "Direct Determination of Polycyclic Aromatic Hydrocarbons in Environmental Matrices Using Laser Desorption Laser Photoionization Time-of-flight Mass Spectrometry," *Analyst*, vol. 119, pp. 571–578, 1994, doi: 10.1039/AN9941900571.

[103]   D. A. Lake, M. P. Tolocka, M. V. Johnston, and A. S. Wexler, "Mass spectrometry of individual particles between 50 and 750 nm in diameter at the Baltimore supersite," *Environ. Sci. Technol.*, vol. 37, no. 15, pp. 3268–3274, 2003, doi: 10.1021/es026270u.

[104]   A. Trimborn, K. P. Hinz, and B. Spengler, "Online analysis of atmospheric particles with a transportable laser mass spectrometer," *Aerosol Sci. Technol.*, vol. 33, no. 1–2, pp. 191–201, 2000, doi: 10.1080/027868200410921.

[105]   D. M. Murphy, "The Design of Single Particle Laser Mass Spectrometers," *Mass Spectrom. Rev.*, vol. 26, pp. 150–165, 2007, doi: 10.1002/mas.

[106]   M. S. Reinard and M. V. Johnston, "Ion Formation Mechanism in Laser Desorption Ionization of Individual Nanoparticles," *J. Am. Soc. Mass Spectrom.*, vol. 19, no. 3, pp. 389–399, 2008, doi: 10.1016/j.jasms.2007.11.017.

[107]   P. G. Carson, M. V. Johnston, and A. S. Wexler, "Real-time monitoring of the surface and total composition of aerosol particles," *Aerosol Sci. Technol.*, vol. 26, no. 4, pp. 291–300, 1997, doi: 10.1080/02786829708965431.

[108]   D. B. Kane, J. Wang, K. Frost, and M. V. Johnston, "Detection of negative ions from individual ultrafine particles," *Anal. Chem.*, vol. 74, no. 9, pp. 2092–2096, 2002, doi: 10.1021/ac011126x.

[109]   M. S. Reinard, K. Adou, J. M. Martini, and M. V. Johnston, "Source characterization and identification by real-time single particle mass spectrometry," *Atmos. Environ.*, vol. 41, no. 40, pp. 9397–9409, 2007, doi: 10.1016/j.atmosenv.2007.09.001.

[110] F. Gunzer, S. Krüger, and J. Grotemeyer, "Photoionization and photofragmentation in mass spectrometry with visible and UV lasers," *Mass Spectrom. Rev.*, vol. 38, no. 2, pp. 202–217, 2019, doi: 10.1002/mas.21579.

[111] U. Boesl, H. J. Neusser, and E. W. Schlag, "Multi-Photon Ionization in the Mass Spectrometry of Polyatomic Molecules: Cross Sections," *Chem. Phys.*, vol. 55, pp. 193–204, 1981, doi: 10.1016/0301-0104(81)85020-3.

[112] U. Boesl, "Laser mass spectrometry for environmental and industrial chemical trace analysis," *J. Mass Spectrom.*, vol. 35, no. 3, pp. 289–304, 2000, doi: 10.1002/(SICI)1096-9888(200003)35:3<289::AID-JMS960>3.0.CO;2-Y.

[113] W. E. Stephens, "A Pulsed Mass Spectrometer with Time Dispersion," *Phys. Rev.*, vol. 69, p. 691, 1946.

[114] R. S. Gohlke and F. W. McLafferty, "Early gas chromatography/mass spectrometry," *J. Am. Soc. Mass Spectrom.*, vol. 4, pp. 367–371, 1993, doi: 10.1016/1044-0305(93)85001-E.

[115] W. C. Wiley and I. H. McLaren, "Time-of-Flight Mass Spectrometer with Improved Resolution," *Rev. Sci. Instrum.*, vol. 26, no. 12, pp. 1150–1157, 1955.

[116] B. A. Mamyrin, V. I. Karataev, D. V. Shmikk, and V. A. Zagulin, "The mass-reflectron, a new nonmagnetic time-of-flight mass spectrometer with high resolution," *J. Exp. Theor. Phys.*, vol. 37, no. 1, pp. 45–48, 1973.

[117] K. Cammann, *Instrumentelle Analytische Chemie: Verfahren, Anwendungen, Qualitätssicherung*. Spektrum Akademischer Verlag GmbH Heidelberg Berlin, 2001.

[118] S. M. Colby, T. B. King, J. P. Reilly, and D. M. Lubman, "Improving the resolution of matrix-assisted laser desorption/ionization time- of- flight mass spectrometry by exploiting the correlation between ion position and velocity," *Rapid Commun. Mass Spectrom.*, vol. 8, no. 11, pp. 865–868, 1994, doi: 10.1002/rcm.1290081102.

[119] R. M. Whittal and L. Li, "High-Resolution Matrix-Assisted Laser Desorption/Ionization in a Linear Time-of-Flight Mass Spectrometer," *Anal. Chem.*, vol. 67, no. 13, pp. 1950–1954, 1995, doi: 10.1021/ac00109a007.

[120] C. Costa-Vera, A. Trimborn, K. P. Hinz, and B. Spengler, "Initial velocity distributions of ions generated by in-flight laser desorption/ionization of individual polystyrene latex microparticles as studied by the delayed ion extraction method," *Rapid Commun. Mass Spectrom.*, vol. 19, no. 2, pp. 133–146, 2005, doi: 10.1002/rcm.1753.

[121] L. Li *et al.*, "Improvement in the Mass Resolution of Single Particle Mass Spectrometry Using Delayed Ion Extraction," *J. Am. Soc. Mass Spectrom.*, vol. 29, no. 10, pp. 2105–2109, 2018, doi: 10.1007/s13361-018-2037-4.

[122] J. M. Dale, M. Yang, W. B. Whitten, and J. M. Ramsey, "Chemical Characterization of Single Particles by Laser Ablation/Desorption in a Quadrupole Ion Trap Mass Spectrometer," *Anal. Chem.*, vol. 66, no. 20, pp. 3431–3435, 1994, doi: 10.1021/ac00092a021.

[123] S. J. Hanna *et al.*, "A new broadly tunable (7.4-10.2 eV) laser based VUV light source and its first application to aerosol mass spectrometry," *Int. J. Mass Spectrom.*, vol. 279, no. 2–3, pp. 134–146, 2009, doi: 10.1016/j.ijms.2008.10.024.

[124] P. J. McKeown, M. V. Johnston, and D. M. Murphy, "On-Line Single-Particle Analysis by Laser Desorption Mass Spectrometry," *Anal. Chem.*, vol. 63, no. 18, pp. 2069–2073, 1991, doi: 10.1021/ac00018a033.

[125] L. Li *et al.*, "Real time bipolar time-of-flight mass spectrometer for analyzing single aerosol particles," *Int. J. Mass Spectrom.*, vol. 303, no. 2–3, pp. 118–124, 2011, doi: 10.1016/j.ijms.2011.01.017.

[126] P. Wieser, R. Wurster, and H. Seiler, "Identification of airborne particles by laser induced mass spectroscopy," *Atmos. Environ.*, vol. 14, no. 4, pp. 485–494, 1980, doi: 10.1016/0004-6981(80)90214-0.

[127] J. T. Jayne *et al.*, "Development of an aerosol mass spectrometer for size and composition analysis of submicron particles," *Aerosol Sci. Technol.*, vol. 33, no. 1–2, pp. 49–70, 2000, doi: 10.1080/027868200410840.

[128] M. R. Canagaratna *et al.*, "Chemical and microphysial characterization of ambient Aerosols with the Aerodyne Aerosol Mass Spectrometer," *Mass Spectrom. Rev.*, vol. 26, pp. 185–222, 2007, doi: 10.1002/mas.20115 The.

[129] P. F. DeCarlo *et al.*, "Field-deployable, high-resolution, time-of-flight aerosol mass spectrometer," *Anal. Chem.*, vol. 78, no. 24, pp. 8281–8289, 2006, doi: 10.1021/ac061249n.

[130] M. R. Canagaratna *et al.*, "Elemental ratio measurements of organic compounds using aerosol mass spectrometry: Characterization, improved calibration, and implications," *Atmos. Chem. Phys.*, vol. 15, no. 1, pp. 253–272, 2015, doi: 10.5194/acp-15-253-2015.

[131] A. Tóth, A. Hoffer, I. Nyiro-Kósa, M. Pósfai, and A. Gelencsér, "Atmospheric tar balls: Aged primary droplets from biomass burning?," *Atmos. Chem. Phys.*, vol. 14, no. 13, pp. 6669–6675, 2014, doi: 10.5194/acp-14-6669-2014.

[132] Q. He *et al.*, "Evolution of the Complex Refractive Index of Secondary Organic Aerosols during Atmospheric Aging," *Environ. Sci. Technol.*, vol. 52, no. 6, pp. 3456–3465, 2018, doi: 10.1021/acs.est.7b05742.

[133] P. Liu, P. J. Ziemann, D. B. Kittelson, and P. H. McMurry, "Generating particle beams of controlled dimensions and divergence: II. Experimental evaluation of particle motion in aerodynamic lenses and nozzle expansions," *Aerosol Sci. Technol.*, vol. 22, no. 3, pp. 314–324, 1995, doi: 10.1080/02786829408959749.

[134] P. Liu, P. J. Ziemann, D. B. Kittelson, and P. H. McMurry, "Generating particle beams of controlled dimensions and divergence: I. Theory of particle motion in aerodynamic lenses and nozzle expansions," *Aerosol Sci. Technol.*, vol. 22, no. 3, pp. 293–313, 1995, doi: 10.1080/02786829408959748.

[135] Y. Zhou *et al.*, "A field measurement based scaling approach for quantification of major ions, organic carbon, and elemental carbon using a single particle aerosol mass spectrometer," *Atmos. Environ.*, vol. 143, pp. 300–312, 2016, doi: 10.1016/j.atmosenv.2016.08.054.

[136] K. A. Pratt *et al.*, "Development and Characterization of an Aircraft Aerosol Time-of-Flight Mass Spectrometer," *Anal. Chem.*, vol. 81, no. 5, pp. 1792–1800, 2009, doi: 10.1021/ac801942r.

[137] J. Passig *et al.*, "Resonance-enhanced detection of metals in aerosols using single-particle mass spectrometry," *Atmos. Chem. Phys.*, vol. 20, no. 12, pp. 7139–7152, 2020, doi: 10.5194/acp-20-7139-2020.

[138] C. A. Gonzalez and S. J. Choquette, "Certificate of Analysis: Standard Reference Material 1649b," *Certificate of Analysis: Standard Reference Material 1649b*, 2016. https://www-s.nist.gov/srmors/certificates/1649b.pdf (accessed Sep. 24, 2020).

[139] E. Wincent, F. Le Bihanic, and K. Dreij, "Induction and inhibition of human cytochrome P4501 by oxygenated polycyclic aromatic hydrocarbons," *Toxicol. Res. (Camb).*, vol. 5, no. 3, pp. 788–799, 2016, doi: 10.1039/c6tx00004e.

[140] T. Ohura, R. Kurihara, and S. Hashimoto, "Aryl hydrocarbon receptor activities of hydroxylated polycyclic aromatic hydrocarbons in recombinant yeast cells," *Toxicol. Environ. Chem.*, vol. 92, no. 4, pp. 737–742, 2010, doi: 10.1080/02772240903109043.

[141] C. E. Boström *et al.*, "Cancer risk assessment, indicators, and guidelines for polycyclic aromatic hydrocarbons in the ambient air," *Environ. Health Perspect.*, vol. 110, pp. 451–488, 2002, doi: 10.1289/ehp.110-1241197.

[142] L. Ma *et al.*, "Real time analysis of lead-containing atmospheric particles in Beijing during springtime by single particle aerosol mass spectrometry," *Chemosphere*, vol. 154, pp. 454–462, 2016, doi: 10.1016/j.chemosphere.2016.04.001.

[143] H. Wang *et al.*, "Mechanism for the formation and microphysical characteristics of submicron aerosol during heavy haze pollution episode in the Yangtze River Delta, China," *Sci. Total Environ.*, vol. 490, pp. 501–508, 2014, doi: 10.1016/j.scitotenv.2014.05.009.

[144] G. Zhang *et al.*, "Mixing state of individual submicron carbon-containing particles during spring and fall seasons in urban guangzhou, china: A case study," *Atmos. Chem. Phys.*, vol. 13, no. 9, pp. 4723–4735, 2013, doi: 10.5194/acp-13-4723-2013.

[145] C. Gehm, T. Streibel, J. Passig, and R. Zimmermann, "Determination of relative ionization cross sections for resonance enhanced multiphoton ionization of polycyclic aromatic hydrocarbons," *Appl. Sci.*, vol. 8, no. 9, pp. 1–14, 2018, doi: 10.3390/app8091617.

[146] H. Czech, B. Stengel, T. Adam, M. Sklorz, T. Streibel, and R. Zimmermann, "A chemometric investigation of aromatic emission profiles from a marine engine in comparison with residential wood combustion and road traffic: Implications for source apportionment inside and outside sulphur emission control areas," *Atmos. Environ.*, vol. 167, pp. 212–222, 2017, doi: 10.1016/j.atmosenv.2017.08.022.

[147] A. Faccinetto, P. Desgroux, M. Ziskind, E. Therssen, and C. Focsa, "High-sensitivity detection of polycyclic aromatic hydrocarbons adsorbed onto soot particles using laser desorption/laser ionization/time-of-flight mass spectrometry: An approach to studying the soot inception process in low-pressure flames," *Combust. Flame*, vol. 158, no. 2, pp. 227–239, 2011, doi: 10.1016/j.combustflame.2010.08.012.

[148] M. Sklorz, J. Schnelle-Kreis, Y. Liu, J. Orasche, and R. Zimmermann, "Daytime resolved analysis of polycyclic aromatic hydrocarbons in urban aerosol samples - Impact of sources and meteorological conditions," *Chemosphere*, vol. 67, no. 5, pp. 934–943, 2007, doi: 10.1016/j.chemosphere.2006.11.006.

[149] T. E. Hauler, U. Boesl, S. Kaesdorf, and R. Zimmermann, "Mobile resonance enhanced multiphoton ionisation-time-of-flight mass spectrometer with a novel hybrid laser desorption/molecular beam ion source for rapid detection of aromatic trace compounds from gas phase and solid samples," *J. Chromatogr. A*, vol. 1058, no. 1–2, pp. 39–49, 2004, doi: 10.1016/j.chroma.2004.08.097.

[150] A. K. Y. Lee *et al.*, "Single-particle characterization of biomass burning organic aerosol (BBOA): Evidence for non-uniform mixing of high molecular weight organics and potassium," *Atmos. Chem. Phys.*, vol. 16, no. 9, pp. 5561–5572, 2016, doi: 10.5194/acp-16-5561-2016.

[151] J. Pagels, D. D. Dutcher, M. R. Stolzenburg, P. H. Mcmurry, M. E. Gälli, and D. S. Gross, "Fine-particle emissions from solid biofuel combustion studied with single-particle mass spectrometry: Identification of markers for organics, soot, and ash components," *J. Geophys. Res. Atmos.*, vol. 118, no. 2, pp. 859–870, 2013, doi: 10.1029/2012JD018389.

[152] J. Li, M. Pósfai, P. V. Hobbs, and P. R. Buseck, "Individual aerosol particles from biomass burning in southern Africa: 2. Compositions and aging of inorganic particles," *J. Geophys. Res. D Atmos.*, vol. 108, no. 13, pp. 1–12, 2003, doi: 10.1029/2002jd002310.

[153] P. M. d. F. Forster and K. E. Taylor, "Climate forcings and climate sensitivities diagnosed from coupled climate model integration," *J. Clim.*, vol. 19, no. 23, pp. 6181–6194, 2006, doi: 10.1175/JCLI3974.1.

[154] M. O. Andreae and A. Gelencsér, "Black carbon or brown carbon? the nature of light-absorbing carbonaceous aerosols," *Atmos. Chem. Phys.*, vol. 6, no. 10, pp. 3131–3148, 2006, doi: 10.5194/acp-6-3131-2006.

[155] R. Bahadur, P. S. Praveen, Y. Xu, and V. Ramanathan, "Solar absorption by elemental and brown carbon determined from spectral observations," *Proc. Natl. Acad. Sci. U. S. A.*, vol. 109, no. 43, pp. 17366–17371, 2012, doi: 10.1073/pnas.1205910109.

[156] R. J. Park, M. J. Kim, J. I. Jeong, D. Youn, and S. Kim, "A contribution of brown carbon aerosol to the aerosol light absorption and its radiative forcing in East Asia," *Atmos. Environ.*, vol. 44, no. 11, pp. 1414–1421, 2010, doi: 10.1016/j.atmosenv.2010.01.042.

[157] Y. Feng, V. Ramanathan, and V. R. Kotamarthi, "Brown carbon: a significant atmospheric absorber of solar radiation?," *Atmos. Chem. Phys.*, vol. 13, pp. 8607–8621, 2013, doi: 10.5194/acp-13-8607-2013.

[158] D. S. Jo, R. J. Park, S. Lee, S. W. Kim, and X. Zhang, "A global simulation of brown carbon: Implications for photochemistry and direct radiative effect," *Atmos. Chem. Phys.*, vol. 16, no. 5, pp. 3413–3432, 2016, doi: 10.5194/acp-16-3413-2016.

[159] M. Z. Jacobson, "Effects of biomass burning on climate, accounting for heat and moisture fluxes, black and brown carbon, and cloud absorption effects," *J. Geophys. Res. Atmos.*, vol. 119, pp. 8980–9002, 2014.

[160] M. Pósfai *et al.*, "Atmospheric tar balls: Particles from biomass and biofuel burning," *J. Geophys. Res. Atmos.*, vol. 109, no. 6, pp. 1–9, 2004, doi: 10.1029/2003jd004169.

[161] J. Chen *et al.*, "A review of biomass burning: Emissions and impacts on air quality, health and climate in China," *Sci. Total Environ.*, vol. 579, no. November 2016, pp. 1000–1034, 2017, doi: 10.1016/j.scitotenv.2016.11.025.

[162] C. Li *et al.*, "Multi-pollutant emissions from the burning of major agricultural residues in China and the related health-economic effects," *Atmos. Chem. Phys.*, vol. 17, no. 8, pp. 4957–4988, 2017, doi: 10.5194/acp-17-4957-2017.

[163] J. L. Hand *et al.*, "Optical, physical, and chemical properties of tar balls observed during the Yosemite Aerosol Characterization Study," *J. Geophys. Res. Atmos.*, vol. 110, no. 21, pp. 1–14, 2005, doi: 10.1029/2004JD005728.

[164] P. Lin, L. T. Fleming, S. A. Nizkorodov, J. Laskin, and A. Laskin, "Comprehensive Molecular Characterization of Atmospheric Brown Carbon by High Resolution Mass Spectrometry with Electrospray and Atmospheric Pressure Photoionization," *Anal. Chem.*, vol. 90, no. 21, pp. 12493–12502, 2018, doi: 10.1021/acs.analchem.8b02177.

[165] G. Shen *et al.*, "Retene emission from residential solid fuels in China and evaluation of retene as a unique marker for soft wood combustion," *Environ. Sci. Technol.*, vol. 46, no. 8, pp. 4666–4672, 2012, doi: 10.1021/es300144m.

[166] J. D. Mcdonald, B. Zielinska, E. M. Fujita, J. C. Sagebiel, J. C. Chow, and J. G. Watson, "Fine particle and gaseous emission rates from residential wood combustion," *Environ. Sci. Technol.*, vol. 34, no. 11, pp. 2080–2091, 2000, doi: 10.1021/es9909632.

[167] H. Czech *et al.*, "Time-resolved analysis of primary volatile emissions and secondary aerosol formation potential from a small-scale pellet boiler," *Atmos. Environ.*, vol. 158, pp. 236–245, 2017, doi: 10.1016/j.atmosenv.2017.03.040.

[168] J. J. Schauer, M. J. Kleeman, G. R. Cass, and B. R. T. Simoneit, "Measurement of emissions from air pollution sources. 3. C1-C29 organic compounds from fireplace combustion of wood," *Environ. Sci. Technol.*, vol. 35, no. 9, pp. 1716–1728, 2001, doi: 10.1021/es001331e.

[169] T. Sigsgaard *et al.*, "Health impacts of anthropogenic biomass burning in the developed world," *Eur. Respir. J.*, vol. 46, no. 6, pp. 1577–1588, 2015, doi: 10.1183/13993003.01865-2014.

[170] P. Veres, J. M. Roberts, I. R. Burling, C. Warneke, J. De Gouw, and R. J. Yokelson, "Measurements of gas-phase inorganic and organic acids from biomass fires by negative-ion proton-transfer chemical-ionization mass spectrometry," *J. Geophys. Res. Atmos.*, vol. 115, no. 23, pp. 1–15, 2010, doi: 10.1029/2010JD014033.

[171] L. D. Yee *et al.*, "Secondary organic aerosol formation from biomass burning intermediates: Phenol and methoxyphenols," *Atmos. Chem. Phys.*, vol. 13, no. 16, pp. 8019–8043, 2013, doi: 10.5194/acp-13-8019-2013.

[172] G. Adler, J. M. Flores, A. Abo Riziq, S. Borrmann, and Y. Rudich, "Chemical, physical, and optical evolution of biomass burning aerosols: a case study," *Atmos. Chem. Phys. Discuss.*, vol. 10, no. 10, pp. 24371–24407, 2010, doi: 10.5194/acpd-10-24371-2010.

[173] E. A. Bruns *et al.*, "Characterization of primary and secondary wood combustion products generated under different burner loads," *Atmos. Chem. Phys.*, vol. 15, no. 5, pp. 2825–2841, 2015, doi: 10.5194/acp-15-2825-2015.

[174] Y. J. Li, D. D. Huang, H. Y. Cheung, A. K. Y. Lee, and C. K. Chan, "Aqueous-phase photochemical oxidation and direct photolysis of vanillin - A model compound of methoxy phenols from biomass burning," *Atmos. Chem. Phys.*, vol. 14, no. 6, pp. 2871–2885, 2014, doi: 10.5194/acp-14-2871-2014.

[175] D. Hoffmann, Y. Iinuma, and H. Herrmann, "Development of a method for fast analysis of phenolic molecular markers in biomass burning particles using high performance liquid chromatography/atmospheric pressure chemical ionisation mass spectrometry," *J. Chromatogr. A*, vol. 1143, no. 1–2, pp. 168–175, 2007, doi: 10.1016/j.chroma.2007.01.035.

[176] G. T. A. D. Santos, P. S. M. Santos, and A. C. Duarte, "Vanillic and syringic acids from biomass burning: Behaviour during Fenton-like oxidation in atmospheric aqueous phase and in the absence of light," *J. Hazard. Mater.*, vol. 313, pp. 201–208, 2016, doi: 10.1016/j.jhazmat.2016.04.006.

[177] M. Mandalakis *et al.*, "Contribution of biomass burning to atmospheric polycyclic aromatic hydrocarbons at three european background sites," *Environ. Sci. Technol.*, vol. 39, no. 9, pp. 2976–2982, 2005, doi: 10.1021/es048184v.

[178] Y. J. Li, J. W. T. Yeung, T. P. I. Leung, A. P. S. Lau, and C. K. Chan, "Characterization of organic particles from incense burning using an aerodyne high-resolution time-of-flight aerosol mass spectrometer," *Aerosol Sci. Technol.*, vol. 46, no. 6, pp. 654–665, 2012, doi: 10.1080/02786826.2011.653017.

[179] S. Weimer, M. R. Alfarra, D. Schreiber, M. Mohr, A. S. H. Prévôt, and U. Baltensperger, "Organic aerosol mass spectral signatures from wood-burning emissions: Influence of burning conditions and type," *J. Geophys. Res. Atmos.*, vol. 113, no. 10, pp. 1–10, 2008, doi: 10.1029/2007JD009309.

[180] A. C. Aiken *et al.*, "O/C and OM/OC ratios of primary, secondary, and ambient organic aerosols with high-resolution time-of-flight aerosol mass spectrometry," *Environ. Sci. Technol.*, vol. 42, no. 12, pp. 4478–4485, 2008, doi: 10.1021/es703009q.

[181] J. H. Kroll *et al.*, "Carbon oxidation state as a metric for describing the chemistry of atmospheric organic aerosol," *Nat. Chem.*, vol. 3, pp. 133–139, 2011, doi: 10.1038/nchem.948.

[182] B. J. Sumlin, A. Pandey, M. J. Walker, R. S. Pattison, B. J. Williams, and R. K. Chakrabarty, "Atmospheric Photooxidation Diminishes Light Absorption by Primary Brown Carbon Aerosol from Biomass Burning," *Environ. Sci. Technol. Lett.*, vol. 4, no. 12, pp. 540–545, 2017, doi: 10.1021/acs.estlett.7b00393.

[183] R. C. Sullivan and K. A. Prather, "Investigations of the diurnal cycle and mixing state of oxalic acid in individual particles in Asian aerosol outflow," *Environ. Sci. Technol.*, vol. 41, no. 23, pp. 8062–8069, 2007, doi: 10.1021/es071134g.

[184] F. Yang, H. Chen, X. Wang, X. Yang, J. Du, and J. Chen, "Single particle mass spectrometry of oxalic acid in ambient aerosols in Shanghai: Mixing state and formation mechanism," *Atmos. Environ.*, vol. 43, no. 25, pp. 3876–3882, 2009, doi: 10.1016/j.atmosenv.2009.05.002.

[185] R. M. Healy *et al.*, "Single-particle speciation of alkylamines in ambient aerosol at five European sites," *Anal. Bioanal. Chem.*, vol. 407, no. 20, pp. 5899–5909, 2015, doi: 10.1007/s00216-014-8092-1.

[186] T. Ferge *et al.*, "Fast determination of the relative elemental and organic carbon content of aerosol samples by on-line single-particle aerosol time-of-flight mass spectrometry," *Environ. Sci. Technol.*, vol. 40, no. 10, pp. 3327–3335, 2006, doi: 10.1021/es050799k.

[187] M. Spencer and K. Prather, "Using ATOFMS to determine OC/EC mass fractions in particles," *Aerosol Sci. Technol.*, vol. 40, no. 8, pp. 585–594, 2006, doi: 10.1080/02786820600729138.

[188] D. Craig Sykes, E. Woods, G. D. Smith, T. Baer, and R. E. Miller, "Thermal vaporization-vacuum ultraviolet laser ionization time-of-flight mass spectrometry of single aerosol particles," *Anal. Chem.*, vol. 74, no. 9, pp. 2048–2052, 2002, doi: 10.1021/ac011225a.

[189] A. Chudinov *et al.*, "Improvement of peaks identification and dynamic range for bi-polar Single Particle Mass Spectrometer," *Int. J. Mass Spectrom.*, vol. 436, pp. 7–17, 2019, doi: 10.1016/j.ijms.2018.11.013.

[190] D. G. Nash, X. F. Liu, E. R. Mysak, and T. Baer, "Aerosol particle mass spectrometry with low photon energy laser ionization," *Int. J. Mass Spectrom.*, vol. 241, no. 2-3 SPEC.ISS., pp. 89–97, 2005, doi: 10.1016/j.ijms.2004.12.016.

[191] J. Cabalo, A. Zelenyuk, T. Baer, and R. E. Miller, "Two-color laser induced evaporation dynamics of liquid aerosols probed by time-of-flight mass spectrometry," *Aerosol Sci. Technol.*, vol. 33, no. 1–2, pp. 3–19, 2000, doi: 10.1080/027868200410813.

[192] S. M. Toner, D. A. Sodeman, and K. A. Prather, "Single particle characterization of ultrafine and accumulation mode particles from heavy duty diesel vehicles using aerosol time-of-flight mass spectrometry," *Environ. Sci. Technol.*, vol. 40, no. 12, pp. 3912–3921, 2006, doi: 10.1021/es051455x.

[193] K. R. Neubauer, M. V. Johnston, and A. S. Wexler, "Humidity effects on the mass spectra of single aerosol particles," *Atmos. Environ.*, vol. 32, no. 14–15, pp. 2521–2529, 1998, doi: 10.1016/S1352-2310(98)00005-3.

[194] N. Marsden, M. J. Flynn, J. W. Taylor, J. D. Allan, and H. Coe, "Evaluating the influence of laser wavelength and detection stage geometry on optical detection efficiency in a single-particle mass spectrometer," *Atmos. Meas. Tech.*, vol. 9, no. 12, pp. 6051–6068, 2016, doi: 10.5194/amt-9-6051-2016.

[195] R. M. Healy *et al.*, "Source apportionment of PM2.5 in Cork Harbour, Ireland using a combination of single particle mass spectrometry and quantitative semi-continuous measurements," *Atmos. Chem. Phys.*, vol. 10, no. 19, pp. 9593–9613, 2010, doi: 10.5194/acp-10-9593-2010.

[196] R. C. Moffet, B. De Foy, L. T. Molina, M. J. Molina, and K. A. Prather, "Measurement of ambient aerosols in northern Mexico City by single particle mass spectrometry," *Atmos. Chem. Phys.*, vol. 8, no. 16, pp. 4499–4516, 2008, doi: 10.5194/acp-8-4499-2008.

[197] M. Dall'osto, D. C. S. Beddows, R. M. Harrison, and B. Onat, "Fine Iron Aerosols Are Internally Mixed with Nitrate in the Urban European Atmosphere," *Environ. Sci. Technol.*, vol. 50, no. 8, pp. 4212–4220, 2016, doi: 10.1021/acs.est.6b01127.

[198] G. Wang *et al.*, "Persistent sulfate formation from London Fog to Chinese haze," *Proc. Natl. Acad. Sci. U. S. A.*, vol. 113, no. 48, pp. 13630–13635, 2016, doi: 10.1073/pnas.1616540113.

[199] M. Sofiev *et al.*, "Cleaner fuels for ships provide public health benefits with climate tradeoffs," *Nat. Commun.*, vol. 9, no. 1, pp. 1–12, 2018, doi: 10.1038/s41467-017-02774-9.

[200] S. Gaur and R. Agnihotri, "Health Effects of Trace Metals in Electronic Cigarette Aerosols—a Systematic Review," *Biol. Trace Elem. Res.*, vol. 188, no. 2, pp. 295–315, 2019, doi: 10.1007/s12011-018-1423-x.

[201] A. P. Ault, C. J. Gaston, Y. Wang, G. Dominguez, M. H. Thiemens, and K. A. Prather, "Characterization of the single particle mixing state of individual ship plume events measured at the port of Los Angeles," *Environ. Sci. Technol.*, vol. 44, no. 6, pp. 1954–1961, 2010, doi: 10.1021/es902985h.

[202] F. R. Verdun, G. Krier, and J. F. Muller, "Increased Sensitivity in Laser Microprobe Mass Analysis by Using Resonant Two-Photon Ionization Processes," *Anal. Chem.*, vol. 59, no. 10, pp. 1383–1387, 1987, doi: 10.1021/ac00137a003.

[203] C. J. McLean *et al.*, "Resonant laser ablation (RLA)," *Int. J. Mass Spectrom. Ion Process.*, vol. 96, no. 1, pp. 1–7, 1990, doi: 10.1016/0168-1176(90)80047-7.

[204] Y. Su, M. F. Sipin, H. Furutani, and K. A. Prather, "Development and Characterization of an Aerosol Time-of-Flight Mass Spectrometer with Increased Detection Efficiency," *Anal. Chem.*, vol. 76, no. 3, pp. 712–719, 2004, doi: 10.1021/ac034797z.

[205] A. Kramida, Y. Ralchenko, J. Reader, and NIST ASD Team, "NIST Atomic Spectra Database (version 5.7.1)," *National Institute of Standards and Technology, Gaithersburg, MD*. 2019, doi: 10.18434/T4W30F.

[206] E. E. Wade, G. R. Farquar, P. T. Steele, E. L. McJimpsey, C. B. Lebrilla, and D. P. Fergenson, "Wavelength and size dependence in single particle laser aerosol mass spectra," *J. Aerosol Sci.*, vol. 39, no. 8, pp. 657–666, 2008, doi: 10.1016/j.jaerosci.2008.03.007.

[207] D. S. Thomson, A. M. Middlebrook, and D. M. Murphy, "Thresholds for laser-induced ion formation from aerosols in a vacuum using ultraviolet and vacuum-ultraviolet laser wavelengths," *Aerosol Sci. Technol.*, vol. 26, no. 6, pp. 544–559, 1997, doi: 10.1080/02786829708965452.

[208] E. E. Gard *et al.*, "Direct observation of heterogeneous chemistry in the atmosphere," *Science*, vol. 279, no. 5354, pp. 1184–1187, 1998, doi: 10.1126/science.279.5354.1184.

[209] D. M. Murphy *et al.*, "The distribution of sea-salt aerosol in the global troposphere," *Atmos. Chem. Phys.*, vol. 19, no. 6, pp. 4093–4104, 2019, doi: 10.5194/acp-19-4093-2019.

[210] X. H. Song, P. K. Hopke, D. P. Fergenson, and K. A. Prather, "Classification of single particles analyzed by ATOFMS using an artificial neural network, ART-2A," *Anal. Chem.*, vol. 71, no. 4, pp. 860–865, 1999, doi: 10.1021/ac9809682.

[211] T. P. Rebotier and K. A. Prather, "Aerosol time-of-flight mass spectrometry data analysis: A benchmark of clustering algorithms," *Anal. Chim. Acta*, vol. 585, no. 1, pp. 38–54, 2007, doi: 10.1016/j.aca.2006.12.009.

[212] P. J. G. Rehbein, C. H. Jeong, M. L. Mcguire, and G. J. Evans, "Strategies to enhance the interpretation of single-particle ambient aerosol data," *Aerosol Sci. Technol.*, vol. 46, no. 5, pp. 584–595, 2012, doi: 10.1080/02786826.2011.650334.

[213] W. Li *et al.*, "Air pollution–aerosol interactions produce more bioavailable iron for ocean ecosystems," *Sci. Adv.*, vol. 3, no. 3, pp. 1–7, 2017, doi: 10.1126/sciadv.1601749.

[214] H. Furutani *et al.*, "Single-particle chemical characterization and source apportionment of iron-containing atmospheric aerosols in Asian outflow," *J. Geophys. Res. Atmos.*, vol. 116, no. 18, pp. 1–17, 2011, doi: 10.1029/2011JD015867.

[215] R. C. Moffet *et al.*, "Iron speciation and mixing in single aerosol particles from the Asian continental outflow," *J. Geophys. Res. Atmos.*, vol. 117, no. 7, pp. 1–12, 2012, doi: 10.1029/2011JD016746.

7. Appendix: Scientific Publications

7.1. Publication 1: Passig and Schade et al., *Anal. Chem.*, 89 (2017), 6341-6345

Title: Aerosol Mass Spectrometer for Simultaneous Detection of Polyaromatic Hydrocarbons and Inorganic Components from Individual Particles

Authors: Johannes Passig, Julian Schade, Markus Oster, Matthias Fuchs, Sven Ehlert, Cornelia Jäger, Martin Sklorz, and Ralf Zimmermann

Journal: Analytical Chemistry, 89, 6341-6345

Year: 2017

DOI: 10.1021/acs.analchem.7b01207

7.2.   Publication 2: Li et al., *Atmos. Chem. Phys.,* 19 (2019), 139-163

Title: Dynamic changes in optical and chemical properties of tar ball aerosols by atmospheric photochemical aging

Authors: Chunlin Li, Quanfu He, <u>Julian Schade</u>, Johannes Passig, Ralf Zimmermann, Daphne Meidan, Alexander Laskin, and Yinon Rudich

Journal: Atmosperic Chemistry and Physics, 19, 139-163

Year: 2019

DOI: 10.5194/acp-19-139-2019

Atmospheric
Chemistry
and Physics

Dynamic changes in optical and chemical properties of tar ball aerosols by atmospheric photochemical aging

Chunlin Li[1], **Quanfu He**[1], **Julian Schade**[2], **Johannes Passig**[2,3], **Ralf Zimmermann**[2,3], **Daphne Meidan**[1], **Alexander Laskin**[4], **and Yinon Rudich**[1]

[1]Department of Earth and Planetary Sciences, Weizmann Institute of Science, Rehovot 76100, Israel
[2]Joint Mass Spectrometry Centre, University of Rostock, Dr.-Lorenz-Weg 2, 18059 Rostock, Germany
[3]Joint Mass Spectrometry Centre, Cooperation Group "Comprehensive Molecular Analytics" (CMA),
Helmholtz Zentrum München, Ingolstädter Landstrasse 1, 85764 Neuherberg, Germany
[4]Department of Chemistry, Purdue University, West Lafayette, Indiana 47907, USA

Correspondence: Yinon Rudich (yinon.rudich@weizmann.ac.il)

Abstract. Following wood pyrolysis, tar ball aerosols were laboratory generated from wood tar separated into polar and nonpolar phases. Chemical information of fresh tar balls was obtained from a high-resolution time-of-flight aerosol mass spectrometer (HR-ToF-AMS) and single-particle laser desorption/resonance enhanced multiphoton ionization mass spectrometry (SP-LD-REMPI-MS). Their continuous refractive index (RI) between 365 and 425 nm was retrieved using a broadband cavity enhanced spectroscopy (BBCES). Dynamic changes in the optical and chemical properties for the nonpolar tar ball aerosols in NO_x-dependent photochemical process were investigated in an oxidation flow reactor (OFR). Distinct differences in the chemical composition of the fresh polar and nonpolar tar aerosols were identified. Nonpolar tar aerosols contain predominantly high-molecular weight unsubstituted and alkyl-substituted polycylic aromatic hydrocarbons (PAHs), while polar tar aerosols consist of a high number of oxidized aromatic substances (e.g., methoxy-phenols, benzenediol) with higher O : C ratios and carbon oxidation states. Fresh tar balls have light absorption characteristics similar to atmospheric brown carbon (BrC) aerosol with higher absorption efficiency towards the UV wavelengths. The average retrieved RI is $1.661 + 0.020i$ and $1.635 + 0.003i$ for the nonpolar and polar tar aerosols, respectively, with an absorption Ångström exponent (AAE) between 5.7 and 7.8 in the detected wavelength range. The RI fits a volume mixing rule for internally mixed nonpolar/polar tar balls. The RI of the tar ball aerosols decreased with increasing wavelength under photochemical oxidation. Photolysis by UV light (254 nm), without strong oxidants in the system, slightly decreased the RI and increased the oxidation state of the tar balls. Oxidation under varying OH exposure levels and in the absence of NO_x diminished the absorption (bleaching) and increased the O : C ratio of the tar balls. The photobleaching via OH radical initiated oxidation is mainly attributed to decomposition of chromophoric aromatics, nitrogen-containing organics, and high-molecular weight components in the aged particles. Photolysis of nitrous oxide (N_2O) was used to simulate NO_x-dependent photochemical aging of tar balls in the OFR. Under high-NO_x conditions with similar OH exposure, photochemical aging led to the formation of organic nitrates, and increased both oxidation degree and light absorption for the aged tar ball aerosols. These observations suggest that secondary organic nitrate formation counteracts the bleaching by OH radical photooxidation to eventually regain some absorption of the aged tar ball aerosols. The atmospheric implication and climate effects from tar balls upon various oxidation processes are briefly discussed.

1 Introduction

Organic aerosol (OA), which represent a ubiquitous and dominant burden of the tropospheric particulate pollutants, play important roles in atmospheric chemistry and balance of regional and global radiation (Jimenez et al., 2009; Kanakidou et al., 2005; Seinfeld and Pandis, 2016; Shrivastava et al., 2017). An indirect climate influence of OA relies on their interaction with water, thus acting as cloud condensation nuclei (CCN) that may alter the hydrological cycle (cloud formation and perception) and modify Earth's albedo (Forster and Taylor, 2006; IPCC, 2013; Seinfeld and Pandis, 2016). The direct climate effect of OA is through extinction of incoming solar radiation and outgoing longwave radiation. Of particular importance is the warming effect due to light-absorbing carbonaceous aerosol commonly termed brown carbon (BrC) (Andreae and Gelencsér, 2006). BrC is an important yet poorly understood OA component due to its complex physical properties, undefined chemical composition, and dynamic evolution under atmospheric processes (Adler et al., 2010; Moise et al., 2015; Laskin et al., 2015). It has been estimated that BrC accounts for 10 %–40 % of the total light absorption in the atmosphere and when deposited on snowpack (Bahadur et al., 2012; Park et al., 2010), and contributes a global forcing of 0.10–0.25 W m^{-2}, with even higher values on regional scales (Feng et al., 2013).

The origin of BrC can be either primary (i.e., directly emitted) or secondary (i.e., generated by reactions of aromatic or carbonyl compounds in clouds or particles) (Laskin et al., 2015). On a global scale, biomass burning releases over two-thirds of primary BrC and also contributes substantially to overall secondary OA formation (Jacobson, 2014; Jo et al., 2016). Better understanding of the optical properties of biomass burning BrC aerosols is crucial for constraining its atmospheric and climatic implications and Earth's energy balance. Unlike black carbon that absorbs light strongly throughout the entire UV–visible range, different chromophores that may also be coupled via charge transfer complexes enable BrC absorption in a much more pronounced and complicated wavelength-dependence manner (Phillips and Smith, 2004; Reid et al., 2005; Lin et al., 2016, 2017).

Tar balls are a specific type of particle produced from wood combustion (especially from biomass smoldering burning) which is abundant in the troposphere (Pósfai et al., 2004; Hand et al., 2005; Chen et al., 2017). Tar ball particles have been collected and identified in many biomass burning plumes (Pósfai et al., 2004; Fu et al., 2012; Li et al., 2017). Microanalysis has found that tar balls are homogeneous spherical carbonaceous particles with sizes ranging from tens to hundreds of nanometers. These particles contribute a considerable fraction of the biomass burning BrC (Pósfai et al., 2004; Hand et al., 2005; Li et al., 2017). The estimated burden of tar balls on regional and global climatic forcing has been emphasized (Chung et al., 2012; Jacobson,

2012, 2014). Tar balls from different burning conditions and bio-fuels coexist with many other types of particles (e.g., inorganic salts, soot, and other carbonaceous aerosols in the form of internal or external mixing), and these smoke particles undergo rapid atmospheric processing once they are released from the fire (Pósfai et al., 2004; Hand et al., 2005; Li et al., 2015, 2017). However, in situ determination of the optical properties of these particles during their lifetimes in the air has seldom been reported due to inherent difficulty in selective tar ball sampling out of complex particle ensembles typical of field burning emissions.

The complex refractive index (RI $= n + ki$; n and k are real and imaginary parts, corresponding to scattering and absorption, respectively) is an intrinsic optical property of aerosols. Quantifying the RI of OA is highly needed for evaluating the related radiative forcing influence (Moise et al., 2015). Recently, several studies have investigated the optical properties of tar ball particles (Chakrabarty et al., 2010; Hoffer et al., 2016; Sedlacek et al., 2018). The optical measurements reported for tar balls or other biomass burning BrC were discrete over several wavelengths that were constrained by instruments measuring particle light coefficients, or indirectly inferred from calculations based on their electron energy-loss spectra or from UV–visible absorption of solutions containing dissolved tar balls (Alexander et al., 2008). Hand et al. (2005) measured light scattering coefficients of tar ball-dominated fire plumes using a nephelometer, and reconstructed the scattering coefficients with simplified organic carbon (OC) and elemental carbon (EC) data to get an average RI of $1.56 + 0.02i$ for tar balls at $\lambda = 632$ nm. Chakrabarty et al. (2010) measured the RI of tar ball particles from smoldering biomass combustion at 405, 532, and 780 nm; they observed a clear wavelength-, biofuel-, and even burning condition-dependent RI. The light absorption by tar balls was similar to humic-like substance (HULIS) with an imaginary part (0.002–0.015) that increased exponentially towards the near-UV wavelengths. Recently, Hoffer et al. (2016) generated tar ball particles from flameless wood pyrolysis in the laboratory. They reported a higher RI value of $1.84 + 0.20i$ at 550 nm, which fell closer to RI of soot than to that of HULIS. Large discrepancies reside in these results and discrete RI values make it difficult to decipher the complicated wavelength-dependence character of tar ball optical properties, which finally constrains the assessment of its radiative forcing effect.

Freshly emitted smoke BrC contains chromophores with diverse chemical structures, polarity, and volatility (Lin et al., 2016, 2017). After emission into the atmosphere, smoke particles undergo dynamic changes as a result of dilution, precipitation, and chemical processing on scales of seconds to days, which eventually affect the physiochemical properties of BrC particles during their lifetimes in the atmosphere (Reid et al., 2005; Li et al., 2015; Laskin et al., 2015). Sumlin et al. (2017) simulated atmospheric photooxidation of biomass burning BrC and reported that photooxidation di-

minishes their light absorption. Zhong and Jang (2014) investigated the influence of humidity and NO_x presence in photochemical aging of biomass burning BrC. They found that sunlight faded the color of BrC and humidity facilitated the decay of light absorption by BrC, while the presence of NO_x delayed the fading. Overall, they concluded that light absorption by BrC is governed by chromophore formation and bleaching by sunlight in the atmosphere. Therefore, evaluating the climatic impacts of tar ball particles requires more extensive investigation of its optical properties and understanding of the dynamic transformations of the optical properties during atmospheric aging.

In this study, we generated proxies for tar ball particles by flameless wood pyrolysis (Tóth et al., 2014; Hoffer et al., 2016). This method allows consistent and continuous generation of tar ball proxy aerosols for studying their properties and processes. The RI of the tar aerosols as a function of wavelength in the ultraviolet–short visible region (365–425 nm, 0.5 nm resolution) was determined using a broadband cavity enhanced spectrometer (BBCES). A high-resolution time of flight aerosol mass spectrometer (HR-ToF-AMS) and a single-particle mass spectrometer applying laser desorption/resonantly enhanced multiphoton ionization (SP-LD-REMPI-MS) were used for probing the chemical profile of tar ball aerosols under NO_x-dependent multiple-day photochemical oxidation. Specifically, the dynamic changes in their optical properties in correlation with their chemical composition were investigated. The atmospheric implications and climate forcing due to atmospheric aging of tar aerosols and evolution of their optical properties were also explored.

2 Experiment

2.1 Tar ball particle generation

Following the formation mechanism in biomass burning process, polydisperse tar ball particles were generated from droplets of wood tar in the laboratory (Tóth et al., 2014; Hoffer et al., 2016). In this study, a similar procedure was applied for producing tar ball aerosols. In brief, commercial wood pellets (Hallingdal Trepellets, water content of 6.55 wt %, size of 2–3 cm in length, 0.2–0.3 cm in diameter) were smashed, heated and dry-distilled in the absence of air (25 °C min^{-1} increase to 530 °C from room temperature, and held for 20 min at 530 °C) to produce liquid tar-water emulsions ($\sim$ 25 mL per hundred grams of used wood pellets). The emulsions were filtrated using 0.45 μm pore size filters (PTFE membrane, diameter 47 mm, Pall Corp.) to remove particulate matter or solid precipitation. After overnight static stabilization, the wood tar solution was phase-separated into water soluble and non-soluble oily phases at an initial 3 : 1 volume ratio. Herein, we will term these two fractions as "polar" and "nonpolar" phases, respec-

tively. The phase-separated solution was further concentrated using a heating plate at 300 °C with N_2 purge flow to prevent oxidation. A final 1 : 1 volume ratio of polar to nonpolar phase was obtained; then the concentrated solutions were sealed and stored in the dark under 2 °C for following experiments. With respect to their potential reactivity and instability, the distillation products were used within a few days.

For particle optical measurement, tar balls were produced from aerosolization of above predefined wood tar diluted in methanol (Gradient grade for HPLC, purity $\geq$ 99.9 wt %, Merck) using a constant output atomizer (Model 3076, TSI) with high-purity N_2 as a carrier gas. As the actual fractions of the polar and nonpolar compounds contributing to the mass of ambient tar ball or biomass burning organic aerosol (BBOA) can vary with biofuel sources, burning condition, atmospheric process, and also method/efficiency to classify the polar and nonpolar materials from the sample (Sengupta et al., 2018; Lin et al., 2017, 2018; Chen and Bond, 2010; Rajput et al., 2014), tar ball aerosols in this study were generated from polar, nonpolar, and mixtures of these two phase tar solutions at volume mixing ratio of 2 : 1, 1 : 1, and 1 : 2, respectively. Activated charcoal denuders and quartz heating tube (150 °C, residence time $\sim$ 0.7 s for particles at a nitrogen flow of 1.0 L min^{-1}) were used after the atomizer to outgas the methanol from the gaseous and particulate phases. Mesh filters (TSI) downstream were used to filter out some ultrafine (less than 100 nm) particles.

2.2 NO_x-dependent OH oxidation of tar ball aerosols

Heterogeneous oxidation of tar ball aerosols was simulated using an oxidation flow reactor (OFR), shown schematically in Fig. 1. The OFR has been characterized (Kang et al., 2007; Peng et al., 2015, 2016) and the operational procedures have been described previously (He et al., 2018). Briefly, the OFR consists of a horizontal 13.3 L aluminum cylindrical chamber (46 cm long × 22 cm ID) operating in continuous flow mode. The chamber is equipped with two power-controllable ozone-free mercury lamps with peak emission at $\lambda = 254$ nm (82-934-08, BHK Inc., CA, USA). The two UV lamps are surrounded by Pyrex sheath tubes that are continuously purged with N_2 to cool the lamps and remove outgassing compounds. OH radicals in the OFR are produced through photolysis of externally introduced O_3 under 254 nm illumination and further reaction of singlet oxygen (O^1D) with water vapor:

$$O_3 + h\nu(254\,\text{nm}) \rightarrow O^1D + O_2, \qquad (R1)$$

$$O^1D + H_2O \rightarrow 2OH. \qquad (R2)$$
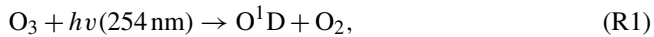
External O_3 was produced by irradiation of 0.2 L min^{-1} high-purity O_2 using a mercury lamp ($\lambda = 185$ nm, 78-2046-07, BHK Inc., CA). The O_3 concentration downstream of the OFR was measured by an O_3 monitor (2B Technology). A Nafion membrane humidifier (Perma Pure LIC, NJ) was used
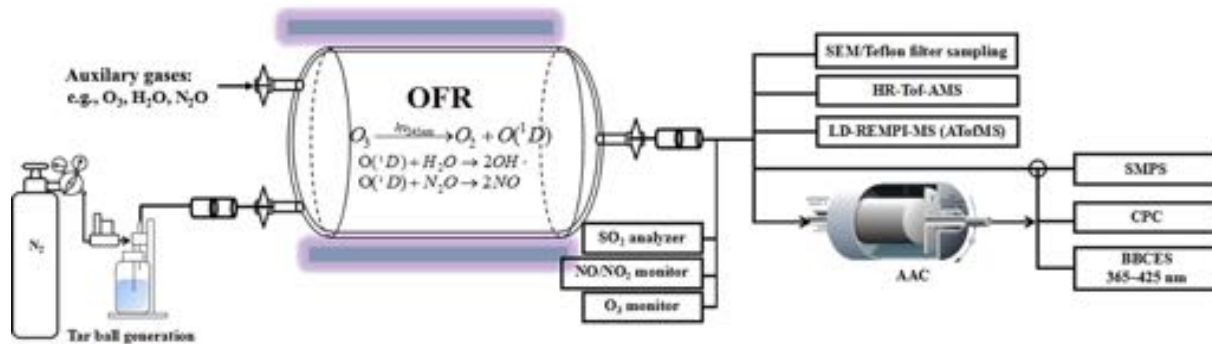
Figure 1. Experimental setup for laboratory generation and aging of tar ball aerosol, including generation setup, OFR photochemical aging, gaseous–particulate chemical monitoring, particle size distribution and optical property measurements.

to supply water vapor to the OFR. Tar ball aerosols carried by $1.0 \, L \, min^{-1}$ N_2 flow from the atomizer were introduced into OFR. The initial aerosol concentrations in the OFR were mediated by controlling the concentration of the wood tar solution to be atomized until the number of 350 nm particles was above $100 \, cm^{-3}$, as shown in Fig. S1 in the Supplement of tar ball aerosol size distribution. Finally, a total flow of $5.5 \, L \, min^{-1}$ with 36 %–38 % RH, initial 27–28 ppm O_3, and 200–$250 \, \mu g \, m^{-3}$ tar ball particles (assuming material density of $1.0 \, g \, cm^{-3}$) was maintained, with a corresponding plug flow residence time (RT) of 144 s for aerosols in the OFR.

The extent of simulated daytime oxidation by OH exposure was varied by changing the UV light intensity. Here, OH exposures in the OFR were inferred by measuring the decay of added SO_2 (monitored by Thermo SO_2 analyzer, model 43i) due to reaction with OH radicals at specific UV lamp intensity. A low concentration ($\sim 60 \, ppb$) of SO_2 was used to minimize its influence on the OH radical reactivity. Typical total OH exposures ranged from $(8.7 \pm 2.3) \times 10^{10}$ to $(8.6 \pm 1.7) \times 10^{11}$ molec cm^{-3} s or 0.5–7 equivalent daytime atmospheric oxidation days (EAD) were maintained, taking typical ambient average OH concentration as 1.5×10^6 molec cm^{-3} (Kang et al., 2007; Peng et al., 2015, 2016).

In addition to reactions with oxidants, organic aerosols may change their chemical and physical properties by photolysis (Epstein et al., 2014; Lee et al., 2014; Wong et al., 2014). Therefore, the influence of light irradiation during tar ball photochemical aging was assessed at the short exposure time in the OFR. Here, tar ball aging was repeated at the same conditions (e.g., RT, RH, N_2 / O_2 flow, tar ball concentration, UV lamp power) without O_3 supply in the OFR. The 254 nm photon flux at specific to maximal UV lamp power was calculated by fitting the OH exposure estimated from SO_2 decay and by the Aerodyne OFR Exposure Estimator (v3.1, https://sites.google.com/site/pamwiki/hardware/estimation-equations, last access: 20 December 2017).

Under polluted conditions, nitrogen oxides (NO_x) are often involved in the atmospheric transformations of organic

aerosol and alter their physiochemical properties (Rollins et al., 2012; Ng et al., 2007; Lin et al., 2015). Therefore, NO_x influence on tar ball aerosol aging was also investigated. Due to rapid conversion of NO_x ($NO + NO_2$) into nitric acid (HNO_3) under high O_3 and OH concentrations, simple addition of NO_x into OFR cannot sustain NO_x levels that compete with HO_2 radicals in the reaction with organic proxy (ROO). NO_x generated via N_2O reaction with O^1D has been modeled and tested to suit the characterization of NO_x-dependent SOA formation pathways using OFR (Peng et al., 2017; Lambe et al., 2017). In this study, N_2O (99.999 %) addition of 0.5 % vol and 2.0 % vol were used during tar ball aerosol photochemical oxidation in the OFR, and equivalent OH exposure of about 4.0 EAD was maintained. NO_x (NO and NO_2) concentrations downstream of the OFR was measured using a NO / NO_2 analyzer (Ecotech, Serinus 40 NO_x). Experimental parameters including initial O_3 and N_2O concentrations, NO_x, moisture ratio, maintained OH exposures and the corresponding photon flux at 254 nm are presented in Table 1.

2.3 Online optical and chemical characterization

Prior to the optical and chemical measurements, excess ozone and NO_x were removed from the sample air stream following the OFR using two diffusion denuders packed with Carulite (Carus Corporation, Peru, IL) and one activated charcoal tube. The streamflow was further dehydrated with two silica gel diffusion dryers. Afterward, the tar ball aerosols were characterized by a combination of online chemical and optical instruments.

Bulk chemical fragments and organic elemental ratios of tar ball aerosols were monitored in real time by the HR-ToF-AMS (Aerodyne Research Inc., Billerica, MA, USA) in alternating high-sensitivity V and high-resolution W modes. The working principles of the AMS have been described in detail elsewhere (DeCarlo et al., 2006). In short, aerosol particles are separated from the gas phase through an aerodynamic lens system and then transferred into the vac-

Table 1. Experimental conditions for tar ball particles photochemical oxidation.

Experiment	O_3 (ppm)	N_2O mixing ratio	Endpoint NO_x (ppb)	RH (%)	Water mixing ratio	Exposure	
						OH radical (molecules cm^{-3} s)	photon flux (photons cm^{-2})
P1	–	–	–	38.90	0.0126	–	7.47×10^{15}
P2	–	–	–	39.70	0.0128	–	4.83×10^{16}
P3	–	–	–	40.50	0.0130	–	1.00×10^{17}
O_0.7	24.46	–	–	37.29	0.0120	8.68×10^{10}	1.56×10^{15}
O_1.7	24.76	–	–	37.66	0.0122	2.23×10^{11}	7.47×10^{15}
O_3.9	24.63	–	–	35.58	0.0115	5.11×10^{11}	4.83×10^{16}
O_6.7	25.31	–	–	35.67	0.0116	8.65×10^{11}	5.17×10^{16}
N_0.5	24.18	0.005	96.1	36.60	0.0118	5.37×10^{11}	5.92×10^{16}
N_2.0	28.21	0.020	528.3	35.90	0.0116	4.85×10^{11}	1.00×10^{17}

Note: P1–P3 mean photolysis test, O_0.7–O_6.7 correspond to the photochemical oxidation experiment from equivalent 0.7 to 6.7 days' ageing, and N_0.5 and N_2.0 indicate photochemical oxidation with N_2O addition at 0.5 % vol and 2 % vol mixing ratios (standard deviation for the parameters was not given in above table).

uum system, where they are impacted onto a vaporizer at about 600 °C, thus vaporizing the particles. The analyte vapors are ionized with 70 eV electron impact ionization (EI). A time-of-flight mass spectrometer is used for high-resolution analysis of the ions. SQUIRREL v1.16 and PIKA v1.57 codes (http://cires.colorado.edu/jimenez-group/ ToFAMSResources/ToFSoftware/, last access: 24 November 2016) were used to process the collected AMS data. Four ion groups were classified as $C_xH_y^+$, $C_xH_yO^+$, $C_xH_yO_z^+$ ($z > 1$), and $C_xH_yO_iN_p^+$ (i0, p1) based on fragment features. The ions O^+, OH^+, and H_2O^+ were included in the $C_xH_yO_z^+$ group, as concentrations of these species were calculated from the organic CO_2^+ ion abundance using the method in Aiken et al. (2008). The ambient improved (AI) atomic ratios of oxygen to carbon (O : C), hydrogen to carbon (H : C), nitrogen to carbon (N : C), and organic mass to organic carbon (OM / OC) were generated from the measured ion fragments.

Particle-bound organic molecules were measured using a custom single-particle time-of-flight mass spectrometer. This instrument features laser desorption and resonantly enhanced multiphoton ionization (SP-LD-REMPI-ToF-MS), allowing for the detection of aromatic substances on individual particles. Detailed description and application of the instrument in LD-REMPI ionization mode is given by Bente et al. (2008) and Passig et al. (2017). Briefly, aerodynamically accelerated particles are individually sized using laser velocimetry, and heated by a pulsed CO_2 infrared laser (10.6 μm) to desorb organic molecules. Aromatic substances in the gas plume are selectively ionized via REMPI by a KrF-excimer laser pulse (248 nm) and detected in the positive MS flight tube. The REMPI-MS technique is very sensitive and selective for aromatic substances (Boesl et al., 1978; Grotemeyer et al., 1986; Rettner and Brophy, 1981) and suitable for studies on pyrolysis and (wood) combustion processes (Heger et al., 1999;

Czech et al., 2017). For the tar ball aerosols it provides complementary information to the HR-ToF-AMS spectra. A custom software on LabView basis records and calculates the aerodynamic size and individual mass spectra of the particles.

For optical measurements, tar ball aerosols were size-selected using an Aerosol Aerodynamic Classifier (AAC, Cambustion, UK). AAC has significant advantages over the commonly used Differential Mobility Analyzer (DMA) classifier. The AAC classifies particles based on the aerodynamic size without charging and hence it avoids the contribution of multiply charged particles, thus generating real monodisperse size-selected particles distribution, reducing the errors associated with multiply charged large particles. In addition, the AAC has higher particle transmission efficiency at the relevant size range (Tavakoli and Olfert, 2013, 2014). Aerodynamic size-classified particles after the AAC were further scanned by a scanning mobility particle sizer (SMPS, classifier Model 3080, DMA Model 3081, CPC model 3775, TSI) to derive their mobility size distribution. The effective density of tar balls can be estimated from Eq. (1) with assumptions of homogeneous composition and particle shape factor of 1.0, which was verified later in this study:

$$\rho_{eff} = \frac{D_{aero}}{D_m} \rho_0, \tag{1}$$

where ρ_{eff} is an effective density, and D_{aero} and D_m are aerodynamic and mobility diameters, respectively. ρ_o is unit density of $1.0\,g\,cm^{-3}$.

Based on the derived effective density, size-specific tar ball aerosols covering mobility diameters between 175 to 350 nm with an interval of 25 nm were size-selected via AAC, and monodisperse tar balls were introduced into a dual-channel broad-band cavity enhanced spectrometer (BBCES) for light extinction (α_{ext}) measurements in the wavelength of 360–395

and 385–435 nm (at resolution 0.5 nm). A detailed description of the instrument can be found elsewhere (Washenfelder et al., 2013; Flores et al., 2014a, b). With the combination of a condensation particle counter (CPC, Model 3575, TSI) to measure particle concentration (N) in series, size-specific particle extinction cross section (σ_{ext}) can be calculated by Eq. (2):

$$\sigma_{ext}(\lambda, D_p, RI) = \frac{\alpha_{ext}(\lambda, D_p, RI)}{N(D_p)}, \tag{2}$$

where λ is the wavelength of incidence light and D_p is the particle mobility diameter.

Using the Mie–Lorenz scattering theory, the wavelength-dependent complex refractive index of spherical homogeneous particles was derived (Pettersson et al., 2004; Abo Riziq et al., 2007). The retrieval algorithm was limited to search for $n1$ and $k0$ as their physical boundaries. Thereafter, spectral dependent extinction, scattering, and absorption cross sections (σ_{ext}, σ_{sca}, and σ_{abs}) were calculated from the complex RI at a specific particle size. Using these parameters, the single scattering albedo, indicating the scattering fraction of light extinction (SSA $= \sigma_{sca}/\sigma_{ext}$), was calculated.

The absorption and extinction Ångström exponents ($\mathring{A}_{abs}$ and $\mathring{A}_{ext}$) describe the spectral dependence of aerosol light properties, and are widely used in climate modeling (Russell et al., 2010). It is customary to extrapolate the optical spectral absorption and extinction fitting to the range of wavelengths using a power law $\propto \lambda^{-\mathring{A}_{abs}}$ and $\propto \lambda^{-\mathring{A}_{ext}}$, respectively. In this work, we determined $\mathring{A}_{ext}$ and $\mathring{A}_{abs}$ with a linear regression of $\ln(\sigma_{ext})$ and $\ln(\sigma_{abs})$ against $\ln(\lambda)$ over the range of 365 to 425 nm:

$$\mathring{A}_{ext} = -\frac{\ln(\sigma_{ext})}{\ln(\lambda)} \quad \mathring{A}_{abs} = -\frac{\ln(\sigma_{abs})}{\ln(\lambda)} \tag{3}$$

Here $\mathring{A}_{ext}$, $\mathring{A}_{abs}$, and SSA were calculated for tar ball aerosols with a median diameter of 150 nm.

2.4 Offline optical characterization

In addition to the in situ measurements, tar ball particles were also collected quantitatively onto Teflon filters (47 mm diameter, 0.45 μm porosity, Pall Corp.) at a sampling flow rate of $2\,L\,min^{-1}$ and then extracted using methanol (HPLC grade, purity $\geq$ 99.9 %, Merck) for offline UV–visible absorption measurement (Cary 60 UV-VIS spectroscopy, Agilent). Methanol extraction of organic compounds has been commonly performed in various studies (Hoffer et al., 2006; Laskin et al., 2009; Yee et al., 2013; Finewax et al., 2018; Xie et al., 2017). Here we verified the completeness of the extraction by extracting each filter twice with methanol. Moreover, vortex shaking (Vortex Genie-2, Scientific Industries) rather than sonication was applied to avoid chemical degradation of the extracts upon ultrasonic irradiation (Miljevic et al., 2014;

Mutzel et al., 2013). The methanol extractable BrC mass absorption cross section (MAC, $m^2\,g^{-1}$) and refractive imaginary k of the tar balls were estimated based on the following relations (Chen and Bond, 2010; Laskin et al., 2015):

$$MAC(\lambda) = \frac{Abs(\lambda) \times \ln(10)}{C \times b}, \tag{4}$$

$$k_{(\lambda)} = \frac{\lambda \times \rho \times MAC(\lambda)}{4\pi}. \tag{5}$$

$Abs_{(\lambda)}$ is the base-10 absorbance result from UV–visible spectroscopy (unitless), b is the optical length of the solution (1 cm), and C is the extracted organic carbon mass concentration in solvent ($g\,m^{-3}$), which can be determined directly by normalizing the extract concentration and OC mass fraction for tar balls as OC / OM obtained from AMS data, as no other refractory elemental carbon (EC) content was detected in our samples (see details in the Supplement). λ is the incident light wavelength, and ρ is the material density ($g\,cm^{-3}$). Here, the derived effective density ρ_{eff} was used. The absorption Ångström exponent based on MAC was also derived as $\mathring{A}_{abs-UV-Vis}$ over the 365–425 nm spectral range.

In addition, particles were impacted at a flow of $2.5\,L\,min^{-1}$ onto cyclopore track-etched polycarbonate membrane (47 mm, 0.1 μm porosity, Whatman Inc.) to investigate the morphology of tar balls using scanning electronic microscopy (SEM, JEOL JSM-7000F).

2.5 Radiative impacts of tar ball aerosols

To assess the climatic influence of tar ball aerosols, a wavelength-dependent direct shortwave aerosol simple radiative forcing efficiency (SRF, $W\,g^{-1}$) was estimated using the clear sky air mass global horizontal solar spectrum (AM1GH), assuming that tar ball aerosols form a uniform, optically thin aerosol layer at the lower troposphere or on ground (Bond and Bergstrom, 2006; Levinson et al., 2010):

$$\frac{dSRF}{d\lambda} = -\frac{1}{4}\frac{dS_{(\lambda)}}{d\lambda}\tau_{atm(\lambda)}^2(1 - F_c)\Big[2(1 - R_{sfc})^2\beta_{(\lambda)}MSC(\lambda)$$
$$-4R_{sfc} \cdot MAC(\lambda)\Big], \tag{6}$$

where $dS(\lambda)/d\lambda$ is the solar irradiance (photons $s^{-1}\,cm^{-2}$), τ_{atm} is the atmospheric transmission (taking 0.79 for simple calculation), F_c is the cloud fraction (approximately 0.6), R_{sfc} is the surface albedo (approximately 0.19 for urban area ground and 0.8 for snow) (Chen and Bond, 2010), β is the average up-scatter fraction (the fraction of scattered sunlight that is scattered into the upward hemisphere), and MSC(λ) is the wavelength-dependent mass scattering cross section, respectively. We simply calculated radiative forcing of particles with an atmospheric-relevant size of 50 to 500 nm, and SRF was estimated and integrated over the measured range of 365–425 nm. The actinic flux over 365–425 nm was obtained from the "Quick TUV Calculator", available at http://cprm.acom.ucar.edu/Models/TUV/Interactive_TUV/ (last access:

15 May 2018) using the following parameters: SZA (solar zenith angle) of 0°, noon time, 30 June 2000, 300 Dobson overhead ozone column, surface albedo of 0.19 for urban area and 0.8 for snow, and 0 km altitude.

3   Results and discussion

3.1   Chemical composition and optical properties of fresh tar ball aerosols

Negligible fractions of inorganics (e.g., sulfate, nitrate, chloride, and ammonium) in tar balls are obtained from AMS measurement as shown in Fig. S2, and these results confirm again that tar ball aerosols contain dominated carbonaceous compounds with minor amounts of N, S, and Cl (Pósfai et al., 2004; Hand et al., 2005; Adachi and Buseck, 2011). Thereafter, only organics in tar balls are considered, and the high-resolution bulk organic mass spectra for polar and nonpolar tar ball particles are given in Fig. 2. The mass spectra features and particle effective densities are summarized and compared in Table S1 in the Supplement. Distinct differences in the chemical composition were observed between polar and nonpolar tar ball aerosols. The alkyl fragments ($C_xH_y^+$, e.g., $C_nH_{2n-1}^+$, $C_nH_{2n+1}^+$) dominate the signals for nonpolar particles (accounting for $\sim 56\%$ of the total fragments), implying that the nonpolar tar balls have compositional similarity to common hydrocarbon organic aerosol (HOA). The $C_xH_yO^+$ fragments are the primary ions for the polar tar balls, contributing $\sim 42\%$ of their mass spectrum, suggesting that most of the organic constituents in the polar tar balls are substantially oxygenated. Both spectra exhibit significant intensity at m/z 28 (CO^+), m/z 29 (CHO^+), and m/z 43 ($C_2H_3O^+$), indicating the presence of carbonyl ions. The strong signal at m/z 31 (CH_3O^+) results from methoxy species that preferably partition into the polar tar fraction. In addition, the significant signals at m/z 50–52 ($C_4H_2^+$, $C_4H_3^+$, $C_4H_4^+$), m/z 65 ($C_5H_5^+$), m/z 77–78 ($C_6H_5^+$, $C_6H_6^+$), m/z 81 ($C_6H_9^+$), and m/z 91 ($C_7H_7^+$), which are characteristic of aromatic compounds, indicate that tar balls, especially from the nonpolar phase, contain a considerable amount of aromatic organics or present high aromaticity. Ion peaks at m/z 77–78, 81, and 91 are typical of monocyclic aromatics such as alkyl-substituted benzene (for m/z 77–78, 91) and heterocyclic aromatics (for m/z 81) (Li et al., 2012), while the relatively higher signal at m/z 128 ($C_{10}H_8^+$) in the nonpolar tar ball mass spectra can be assigned to the molecular ion of naphthalene (Herring et al., 2015). Moreover, signals at m/z 55 and 57 ($C_3H_3O^+$, $C_3H_5O^+$) are signature fragments of aliphatic and non-acid oxygenated organics that are used to trace cooking emissions (He et al., 2010), and these two fragments were also observed in the tar ball aerosols. Similar to ambient biomass burning emissions, $C_2H_4O_2^+$ (m/z 60) and $C_3H_5O_2^+$ (m/z 73), two characteristic fragments from levoglucosan and similar cellulose pyrolyzed

species (e.g., mannosan, galactosan) were detected in all the tar ball aerosols, and these fragments were more prominent in the polar aerosols due to the solubility of levoglucosan and analogs in water. Weimer et al. (2008) reported the percentage of m/z 60 and 73 for the burning of various woods to be 0.6 %–4.1 % and 0.1 %–2.0 %, respectively. The percentages of these two fragments in our tar ball aerosols (0.7 %–1.6 % for m/z 60 and 0.5 %–0.9 % for m/z 73) are comparable to the literature data, although the fuel and the pyrolysis procedure are different. The m/z 137 peak is dominated by fragments of $C_8H_9O_2^+$ and $C_7H_5O_3^+$, and these fragments have been determined in biomass burning emissions and were assigned to lignin-related ions with methoxy-phenolic structures (Li et al., 2012, 2014). Phenols and methoxy phenols are prominent compounds, accounting for 41 % of the identified organic species in primary BBOA (Schauer et al., 2001). The signal at m/z 137 is much higher in the nonpolar-phase tar ball aerosols (1.0 % and 0.5 % for nonpolar and polar tar balls, respectively), and the fraction of fragment m/z 137 is consistent with reference values of 0.3 %–2.0 % (Li et al., 2012). m/z 44 (CO_2^+), a marker fragment of carboxylic acids, has been parameterized as $f44$ (fraction of a mass spectrum signal at m/z 44) to present the oxidation degree of organic aerosols (Aiken et al., 2008; Ng et al., 2010). Higher $f44$ values indicate more oxidized OA (OOA), while less oxidized OA is characterized by lower $f44$ (Schauer et al., 2001). Peroxides can also produce a CO_2^+ signal via extensive fragmentation in the AMS (Aiken et al., 2008). $f44$ has also been shown to be linearly correlated with the elemental O : C ratio of OA (Aiken et al., 2008). In this study, $f44$ for the nonpolar and polar tar ball aerosols are 1.9 % and 2.4 %, and the corresponding O : C ratios are 0.25 and 0.44. The higher O : C and H : C ratios explain the polarity of the polar tar ball aerosols. The simplified average carbon oxidation state ($\overline{OSc} \approx 2O : C – H : C$) describes the oxidation level of particulate complex organic mixtures (Kroll et al., 2011). The calculated $\overline{OSc}$ for the tar ball aerosols are -1.05–0.76, which agrees well with reference values of -1.0–0.7 for primary BBOA (Kroll et al., 2011). These values are in the broad range of -1.7–1.6 for HOA and -0.5–0 for semivolatile OOA (Aiken et al., 2008). In addition, a small fraction of nitrogen-containing organic compounds (NOCs) was detected, with the $C_xH_yO_iN_p^+$ group contributing 1.6 %–3.6 % of the tar ball mass spectra with an estimated N : C ratio below 0.01, which agrees with previously reported N : C values of 0.008–0.018 for biomass burning emissions (He et al., 2010). Biomass burning is an important source of NOCs in the atmosphere, and alkaloid and nitro-aromatic constituents were detected to be abundant constituents of the NOCs (Laskin et al., 2009; Lin et al., 2017). Nitroaromatic compounds were also identified in urban fire emissions (Bluvshtein et al., 2017; Lin et al., 2017). Although these compounds constitute a small fraction of the BBOA mass, these chromophoric NOC species accounted for 50 %–80 % of the
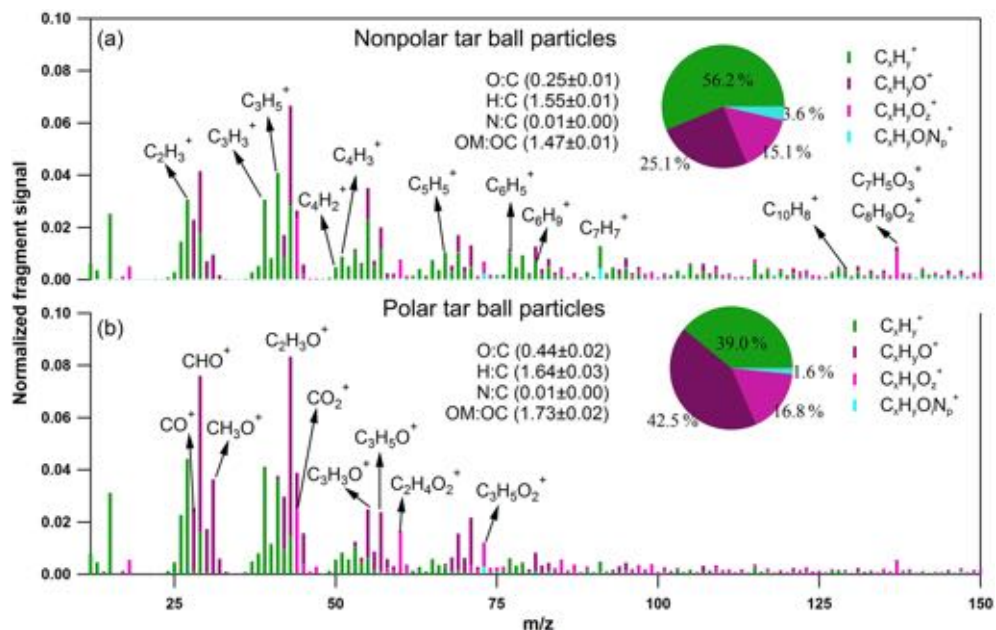
Figure 2. High-resolution AMS mass spectra of fresh polar and nonpolar tar ball particles. Four ion groups are grouped for clarity as $C_xH_y^+$ (green), $C_xH_yO^+$ (purple), $C_xH_yO_z^+$ ($z > 1$) (violet), and $C_xH_yO_iN_p^+$ (i0, p1) (light blue). The mass fractions of the four fragment groups are presented by pie charts.

total visible light absorption by the extractable BrC (Lin et al., 2017).

Fragments larger than 100 amu ($f_{m/z > 100}$) contribute a large fraction of the total organic signals for tar ball aerosols, consistent with biomass burning emissions that contain a large fraction of high-molecular weight compounds (Ge et al., 2012; Zhou et al., 2017). $f_{m/z > 100}$ is 32 % for the nonpolar tar ball aerosols, which is higher than that of the polar particles (15 %), demonstrating that the nonpolar tar balls consist of more high-molecular weight organics. The measured effective densities for polar and nonpolar tar balls are 1.33 and 1.24 g cm^{-3}. Chemical characteristics from AMS and densities for internal mixture tar balls follow the volume-linear mixing of polar and nonpolar tar solutions.

A considerable aromatic fraction in the tar ball aerosols was confirmed by the LD-REMPI-MS measurement. Fig. 3 presents the mass spectra of aromatic substances obtained for one exemplary polar and one nonpolar particle, respectively. Aerodynamic size distributions for the detected tar ball aerosols are given in Fig. S3, and substances identified in the mass spectra are listed in Table S2. The features in the mass spectra are consistent with the polarity of examined tar ball aerosols and ambient BBOA (Lin et al., 2018). The complex REMPI spectrum shows rows of intense unsubstituted and partially alkylated PAH peaks in the nonpolar tar balls, including naphthalene, acenaphthylene, phenanthrene, pyrene, and, in particular, the softwood combustion marker retene at m/z 234 and some possible derivatives (oxidized retene at m/z 250 with one oxygen addition, methyl

retene at m/z 248 with one methyl addition) (McDonald et al., 2000; Shen et al., 2012). Retene and some of the aforementioned PAHs are also observed in the polar tar ball aerosols' mass spectra with lower intensities. In contrast, the polar tar ball REMPI mass spectra show strong peaks from oxidized aromatics, more specifically, benzenediol and methoxy-phenols (e.g., catechol, guaiacol, acetovanillone, syringaldehyde, conifery aldehyde). These results are also verified in ambient BBOA, of which the nonpolar BrC consists of primary unsubstituted PAHs, while the polar fraction includes major aromatic acids and phenols (Lin et al., 2018). The REMPI mass spectra correspond to the large fractions of CHO$^+$ and CH$_3$O$^+$ fragments and high O : C ratios observed for the polar tar aerosols via HR-ToF-AMS, and remain consistent with the strong signals of typical aromatic fragments observed in the nonpolar tar aerosols in Fig. 2. The dominance of aromatic compounds in tar ball chemical composition agrees well with previous work on BBOA (Schauer et al., 2001; Wei et al., 2015; Bente et al., 2008, 2009; Czech et al., 2017). Biomass burning is a major source of environmental PAHs (alkylated PAHs, oxygenated PAHs, phenols, nitrogen-substituted PAHs, etc.) in both particulate and gaseous phases, and extensive emissions of PAHs from incomplete combustion pose a great threat to ecosystem and human health due to their carcinogenic toxicity (Li et al., 2017; Shen et al., 2013; Sigsgaard et al., 2015; Shrivastava et al., 2017). Moreover, the primary PAHs can act as precursors that substantially contribute to ambient SOA or BrC aerosol when involved in atmospheric photochemical aging,
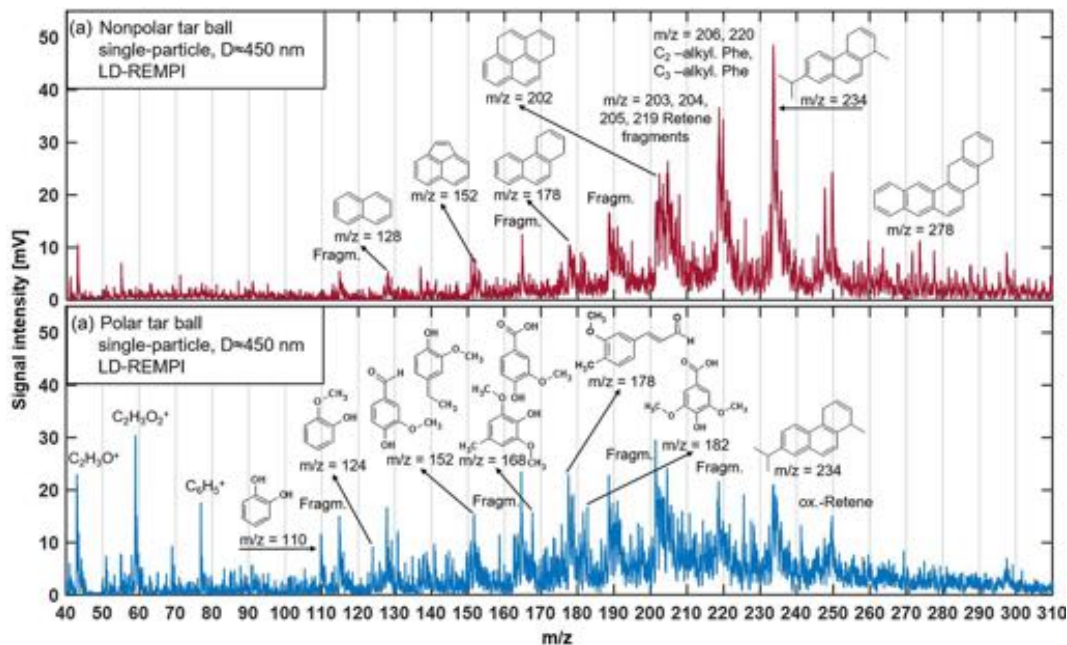
Figure 3. LD-REMPI mass spectra of exemplary single tar ball particles; some feature peaks were identified and labeled. **(a)** Nonpolar tar ball spectra show predominantly alkyl-substituted and unsubstituted PAHs. **(b)** Polar tar ball spectra reveal many oxidized aromatics, e.g., methoxy-phenol and benzenediol. Note the softwood combustion marker retene at $m/z = 234$, its characteristic fragments ($m/z = 203, 204, 205, 219$), and possible retene derivatives ($m/z = 248, 250$).

leading to profound climatic influence (Yee et al., 2013; Yu et al., 2014; Lu et al., 2011; Zhang et al., 2012).

The complex refractive index (RI) of tar ball aerosols was retrieved under the assumption that the particles have similar chemical composition and a spherical shape. The SEM images shown in Fig. S4 confirm the spherical morphology and homogeneous composition of the tar ball particles generated in this study. Electron energy-loss spectroscopy (EELS) spectra indicates that the tar ball particles contain major C and minor O, which fits the AMS result and previous work (Pósfai et al., 2004; Chakrabarty et al., 2010). Continuous spectral-dependent RI and SSA for tar balls were derived and are presented in Fig. 4, RI results for tar ball aerosol at mixing ratio of 2 : 1 and 1 : 2 are presented in Fig. S5. Although scattering dominates the light extinction, absorption in the UV and in the visible ranges was unambiguously identified for the tar ball aerosols, with characteristic absorption similar to atmospheric BrC and HULIS (Hoffer et al., 2006; Bluvshtein et al., 2017; Lin et al., 2017). The imaginary part, k, increases towards the UV range, presenting 0.02–0.03 difference over the measured spectra range. The real part, n, for the nonpolar tar balls decreased from 1.673 at 365 nm to 1.647 at 425 nm, which is almost parallel to the descending n for the polar tar balls ranging from 1.651 at 365 nm to 1.625 at 425 nm. k is 0.029–0.013 for the nonpolar tar ball over light wavelength of 365–425 nm, while the imaginary part for nonpolar aerosols is 0.007 at 365 nm and zero at wavelength longer than 410 nm, indicating that there

is no detectable absorption or k is lower than our detection limit. The overwhelming imaginary part for the nonpolar tar aerosol agrees with many reports that nonpolar or less polar organics have higher absorption compared with the polar BrC in BBOA (Lin et al., 2018; Sengupta et al., 2018). The stronger absorption and relatively higher scattering abilities resulted in a lower SSA compared with the polar tar ball aerosols. The SSA increases towards the visible wavelength from 0.86 at 365 nm to 0.90 at 425 nm for nonpolar tar ball, and the corresponding values are 0.95 to 1.0 for the polar tar balls.

The optical properties of aerosols relate to their chemical composition. Evidently, most of the PAHs identified in the tar ball aerosols with high intensity have strong absorption between 350 and 450 nm (Samburova et al., 2016; Lin et al., 2018), as shown in Fig. S6, which coincide with the range of tar ball absorption measured here, implying that PAHs could be a dominant contributor to the absorption of fresh tar balls. Higher imaginary k can be explained partly by the larger proportion of PAHs as well as more high-molecular-weight organics present in the nonpolar tar ball particles, as conjugated aromatic rings and phenols contribute to the major chromophores in the wood smoke (Laskin et al., 2015; Lin et al., 2017, 2018). High-molecular weight organics may resemble HULIS that can form charge transfer complexes (Phillips and Smith, 2004), and that can absorb light at a longer wavelength range. The result is consistent with the finding that higher molecular weight and aromaticity result in
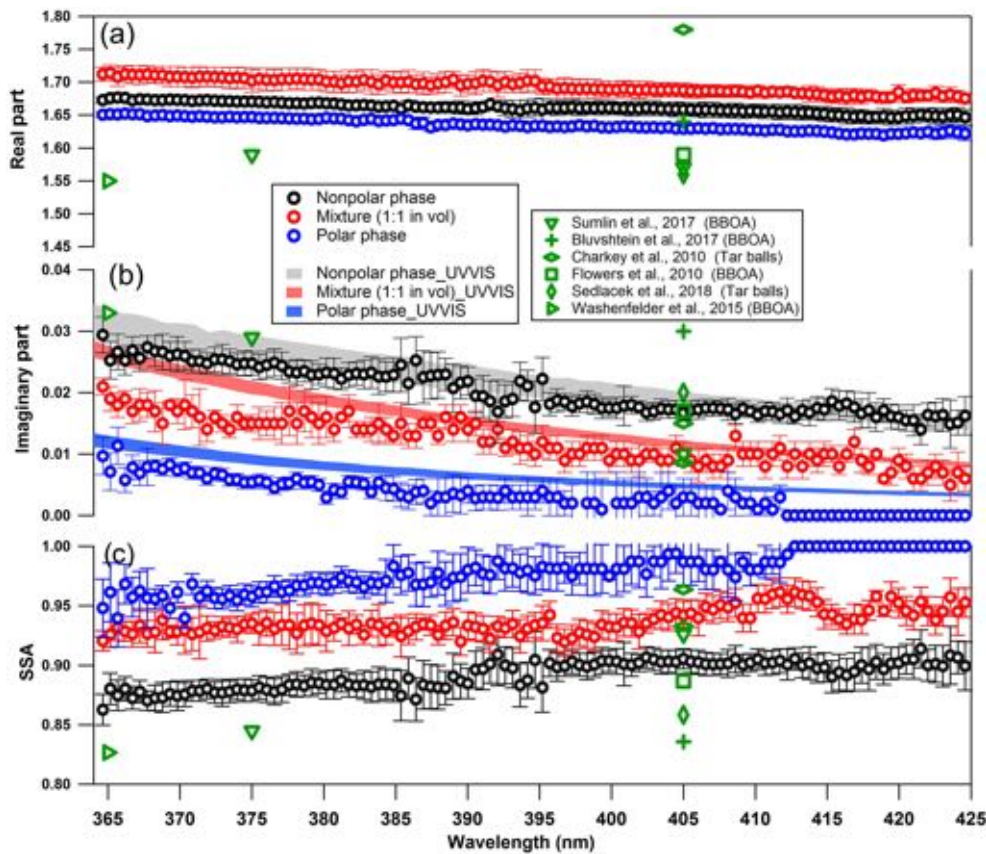
Figure 4. Wavelength-dependent RI and SSA for tar ball particles generated from polar, nonpolar and a mixture of the two-phase tarry solutions (only retrieval for a mixture of 1 : 1 in vol is shown for clarity; optical results for the other two mixtures can be found in the supporting materials). The shaded areas indicate the upper and lower limits of the imaginary part calculated from UV–visible spectra of methanol extracts from the corresponding tar ball particle samples: **(a)** real part, **(b)** imaginary part, and **(c)** SSA calculated for 150 nm particles. Overlaid in green symbols are previous measurements of biomass burning from the literature.

stronger absorption for atmospheric BrC (Dinar et al., 2008). Moreover, the higher NOC content may also contribute to the chromophores in the nonpolar tar aerosols (Lin et al., 2017, 2018).

The average RIs at 375 and 405 nm are $1.671 + 0.025i$ and $1.659 + 0.017i$ for nonpolar tar ball aerosols. The corresponding RIs are $1.647 + 0.005i$ and $1.635 + 0.04i$ for the polar tar ball aerosols. The imaginary part k retrieved from the BBCES data, though low, agrees well with k values calculated from UV–visible absorption of the bulk solution. The MAC for the methanol-extracted BrC in tar ball aerosol is shown in Fig. S7. The absorption may be different for complex materials in the particulate and aqueous phases since parameters such as shape factor and mixing state together with artifacts from the optical instruments' detection and data retrieval methods can all affect the final optical results, while solvent-dependent extraction/dissolving efficiency of chromophores or the solvent effect (e.g., pH in water solution) may impact the solution absorption coefficient (Huang et al., 2018; Lin et al., 2017). The light absorption coefficient of

particulate BrC has been reported to be 0.7–2.0 times that of bulk BrC extracts by Liu et al. (2013).

The absorption Ångström exponent ($\mathring{A}_{abs}$) is often used to describe the wavelength dependence of aerosol light absorption, with a value of nearly 1 for BC particles and values substantially larger than 1 indicating the contribution from BrC (Reid et al., 2005; Chen and Bond, 2010). In this work, $\mathring{A}_{abs}$ for the nonpolar and polar tar ball particles ranges from 5.9 to 6.8 between 365 and 425 nm, which is consistent with values of 5.7–7.8 calculated from the bulk absorption in solution. The nonpolar tar balls have a lower $\mathring{A}_{abs}$. The difference in $\mathring{A}_{abs}$ reflects the different chemical composition of chromophores in the particles, as inferred also from the AMS data. Bluvshtein et al. (2017) reported relatively low values of $\mathring{A}_{ext}$ (2–3) and $\mathring{A}_{abs}$ (4–6) over 300–650 nm for ambient fire plume, which are likely affected by BC in the smoke aerosol and are also due to lower wavelength dependence of aerosol absorption and scattering over the longwave visible range. Overall, the broadband optical results for fresh tar ball aerosols are consistent with limited discrete measurements of atmospheric BBOA as sum-

Table 2. Comparison of tar ball particle optical properties with reference values of BBOA (mean ± standard deviation).

BrC	Complex refractive index			$\mathring{A}_{abs}$	$\mathring{A}_{abs\_UVVIS}$	$\mathring{A}_{ext}$	Reference
	Average	375 nm	405 nm				
Nonpolar	$(1.661 \pm 0.008) + (0.020 \pm 0.004)i$	$(1.671 \pm 0.003) + (0.025 \pm 0.003)i$	$(1.659 \pm 0.011) + (0.017 \pm 0.002)i$	5.87 ± 0.37	5.74	3.81 ± 0.18	This work
Mixture (2 : 1 in vol)	$(1.670 \pm 0.010) + (0.017 \pm 0.004)i$	$(1.682 \pm 0.008) + (0.021 \pm 0.002)i$	$(1.668 \pm 0.007) + (0.013 \pm 0.001)i$	6.79 ± 0.91	7.08	4.01 ± 0.09	
Mixture (1 : 1 in vol)	$(1.694 \pm 0.011) + (0.013 \pm 0.003)i$	$(1.703 \pm 0.015) + (0.017 \pm 0.001)i$	$(1.689 \pm 0.011) + (0.009 \pm 0.002)i$	6.16 ± 0.54	7.38	3.73 ± 0.23	
Mixture (1 : 2 in vol)	$(1.672 \pm 0.010) + (0.011 \pm 0.004)i$	$(1.683 \pm 0.005) + (0.018 \pm 0.002)i$	$(1.667 \pm 0.003) + (0.006 \pm 0.003)i$	6.66 ± 0.63	7.24	4.06 ± 0.11	
Polar	$(1.635 \pm 0.009) + (0.003 \pm 0.003)i$	$(1.647 \pm 0.003) + (0.005 \pm 0.001)i$	$(1.635 \pm 0.004) + (0.004 \pm 0.003)i$	6.72 ± 2.28[a]	7.83	3.93 ± 0.06	
BBOA	$1.590 + 0.029i$–375 nm, $1.570 + 0.010i$–405 nm (IPN)			6.4–7.4			Sumlin et al. (2017, 2018)
BBOA	$1.590 + 0.017i$–405 nm (IPN)						Flowers et al. (2010)
BBOA	k: 0.009–404 nm (CRDS-PAS)						Lack et al. (2012)
Tar ball	$1.78 + 0.015i$; $1.83 + 0.0086i$–405 nm (IPN)			4.2–6.4			Chakrabarty et al. (2010)
Tar ball	$1.56 + 0.02i$–405 nm (CRDS-UVVIS)						Hand et al. (2005)
BBOA	$1.53 + 0.07i$ (WELAS, open fire), $1.54 + 0.04i$ (WELAS, smoldering)						Adler et al. (2011)
BBOA	$1.64 + 0.03i$–405 nm (BBCES-Neph)					2–3[b]	Bluvshtein et al. (2017)
BBOA_HULIS	$1.653 + 0.002i$; $1.685 + 0.002i$–532 nm(Nep-PAS)			4–6[b]	6–7		Hoffer et al. (2006)
BBOA_HULIS	$1.616 + 0.023i$–390 nm(CRDS)						Dinar et al. (2008)
BBOA	$1.550 + 0.033i$–365 nm (BBCES)						Washenfelder et al. (2015)
BBOA					6.9–11.4[c]		Chen and Bond (2010)
BBOA					5.3–8.1[c]		Xie et al. (2017)
BBOA					6.0–6.3[c]		Huang et al. (2018)
Ambient SOA							Shamjad et al. (2018)
Ambient SOA	k: 0.046–365 nm, 0.039–405 nm, 0.036–420 nm (LWCC)						

Note: $\mathring{A}_{abs}$ and $\mathring{A}_{ext}$ were calculated from tar ball particles with a median diameter of 150 nm in this study. [a] Regressed over a wavelength range of 365–400 nm; no absorption detected over 410 nm using the BBCES system. [b] Regressed over a wavelength range of 300–650 nm for bulk fire plume emissions. [c] $\mathring{A}_{abs\_UVVIS}$ of methanol extracts over the whole range from 300/360 to 600 nm. Instrument: IPN (integrated photoacoustic nephelometer), CRDS (cavity ring-down spectrometer), PAS (photoacoustic absorption spectrometer), WELAS (white light optical particle counter), LWCC (liquid waveguide capillary cell).

marized in Table 2. It has also been found that the biomass fuel type, combustion conditions, and atmospheric processing eventually affect the optical properties of BBOA. Lack et al. (2012) modeled core-shell absorption for primary organic matter (POM) and BC from biomass burning. They found that the imaginary part of the RI and BrC MAC of POM at 404 nm were 0.007 ± 0.005 and 0.82 ± 0.43 m^2 g^{-1}, respectively. Chakrabarty et al. (2010) compared the optical properties of tar balls from smoldering combustion of different biomass. Fuel-dependent imaginary RI for tar ball at 405 nm was 0.008–0.015 and $\mathring{A}_{abs}$ over 405–532 nm was 4.2–6.4, which is in line with the $\mathring{A}_{abs}$ value of 6–7 reported for BBOA derived HULIS (Hoffer et al., 2006). Sedlacek et al. (2018) observed a weak absorption for wildfire produced tar balls with RI of $1.56 + 0.02i$. Sumlin et al. (2018) simulated BrC formation under different pyrolysis temperatures. The BrC produced from over 300 °C combustion has imaginary part k of 0.05–0.09 and real part n of 1.59–1.68 at 375 nm, and RI at 405 nm is $1.57 + 0.03i$, corresponded $\mathring{A}_{abs}$ over 375–405 nm is 6.4–7.4.

Optical mixing rules can be used to estimate or explain the refractive indices of internally mixed substances, and three mixing rules are commonly applied in climate models: molar refraction of absorption (Jacobson, 2002), volume-weighted linear average of the refractive indices (d'Almeida et al., 1991), and the Maxwell–Garnett rule (Chýlek et al., 2000). The "linear mixing rule" and molar refraction mixing rules were tested in this work for mixtures of tar ball particles against the retrieved optical data. Relevant data analysis details are provided in the supporting materials (Tables S3–S4, Figs. S8–S12). It was found that both mixing rules can predict the index of refraction for the polar/nonpolar tar balls, and values calculated based on the "linear mixing rule" fit better with the experimental data. As mentioned above, the real fractions for polar and nonpolar BrC contributing to the mass/absorption of BBOA are undefined, some investigations reporting the dynamic polar BrC dominating in mass loading (50 %–85 %) but contributing less to the absorption in BBOA (less than 40 %) (Asa-Awuku et al., 2008; Bluvshtein et al., 2017; Lin et al., 2017, 2018; Rajput et al., 2014; Sengupta et al., 2018). The "linear mixing rule" confirmed in this study should be helpful in the mathematical modeling to assess climatic impacts of biomass burning related BrC aerosol, when their chemical composition is classified.

3.2 Photooxidation of tar ball particles

Aerosols have a wide range of atmospheric lifetimes from hours to days, during which they are involved in various atmospheric processes, resulting in changes in properties (Reid et al., 2005; Rudich et al., 2007; Jimenez et al., 2009). Therefore, we studied the effects of photochemical oxidation of the nonpolar wood-pyrolyzed tar ball aerosols to investigate the physiochemical changes that can occur during tar balls' atmospheric lifetime. Figure 5 presents the evolution
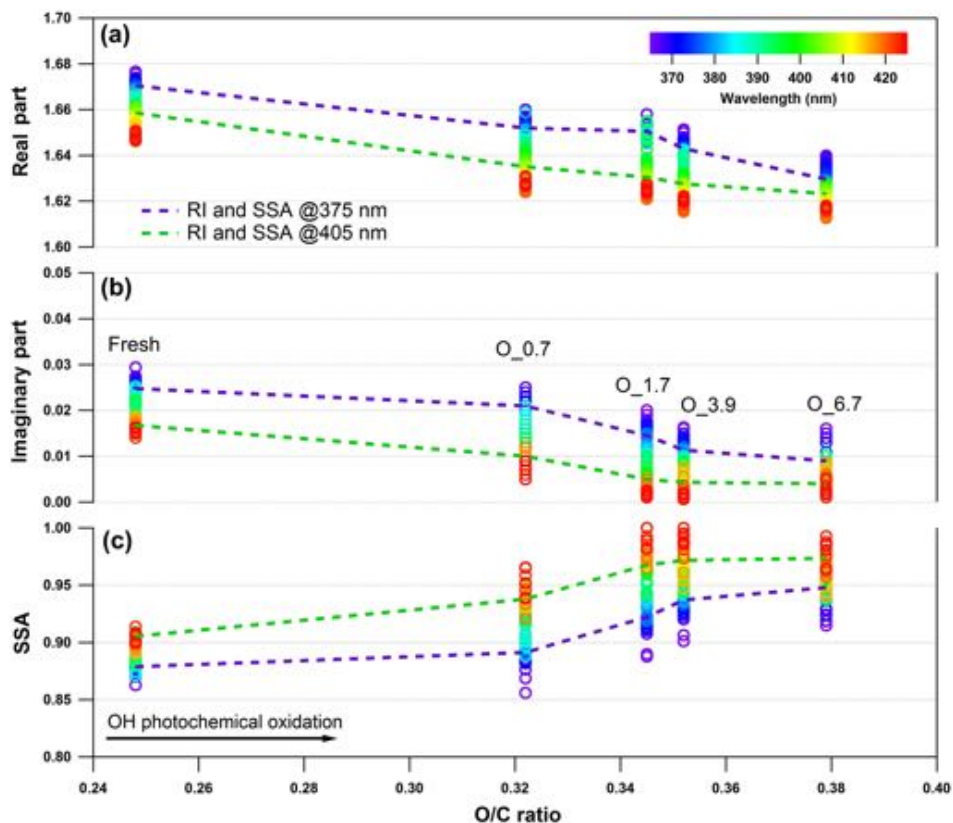
Figure 5. Evolution of the retrieved wavelength-dependent complex RI and SSA as a function of O : C ratio for tar ball particles upon OH photochemical oxidation: **(a)** real part, **(b)** imaginary part, and **(c)** SSA calculated for 150 nm particles. The color scale shows the span in the RI for the wavelengths measured from 365 to 425 nm. For clarity, error bars for O : C ratio (± 0.01), RI (± 0.007 for real part, and ± 0.003 for imaginary part on average), and SSA (± 0.006) are not shown. Two dashed lines trace the RI and SSA at 375 nm (purple) and 405 nm (green). O_0.7–O_6.7 represent equivalent atmospheric photochemical oxidation for 0.7 and up to 6.7 days.

of the wavelength-dependent RI and SSA as a function of the aerosols' O : C ratio following NO_x-free photochemical aging in the OFR. The oxidation covers 0.7–6.7 EAD. Substantial decrease in the RI and an increase in the SSA are correlated with an increase in the O : C ratio; these specific parameters are summarized in Table S5. Light scattering as well as the absorption by the tar ball aerosol decrease with increasing OH oxidation. The tar aerosols lose their scattering and absorption significantly up to 3.9 EAD aging. The average RI decreased from initial $1.661 + 0.020i$ to $1.632 + 0.007i$, and the corresponding average SSA increased from 0.89 ± 0.01 to 0.96 ± 0.02. Then, the RI by tar balls persisted with enhanced oxidation, so that the MAC values remained stable after 3.9 days' oxidation (Fig. S13), suggesting that all the photochemical–labile chromophores were largely eliminated, while the remaining fraction still presented some light absorption. Forrister et al. (2015) also observed a stable fraction of biomass burning BrC that had persistent absorption even after a long photochemical evolution time in the ambient environment. They suggested that the remaining persistent fraction determines the background BrC levels. In our study, the O : C ratio for tar ball aerosols increased con-

tinuously with photochemical oxidation, implying production of oxygenated constituents (carboxylic, carbonyl compounds, etc.) and the interaction between these increasingly oxidized species coupled with the relatively stable intrinsic chromophoric structures (e.g., fused aromatic rings in Fig. 3) in some supermolecular structure that may explain the persistent absorption for aged tar ball aerosols (Dewar and Lepley, 1961; Desyaterik et al., 2013; Samburova et al., 2016). In addition, a balance between photobleaching of intrinsic chromophores and photochemical formation of BrC via gas-particle transfer, as well as dynamic gas-particle partitioning of chromophores and products of their photo-degradation, should also be considered in the overall absorption behavior for BBOA during photochemical processes.

The observed photooxidation bleaching is consistent with previous studies on atmospheric processes of BrC. Sumlin et al. (2017) conducted multiple-day photochemical oxidation on primary biomass burning BrC aerosols and observed that BrC loses its light absorption and scattering in the near-UV wavelengths by aging. Their derived RI at 375 nm decreased from $1.59 + 0.03i$ for fresh emission to $1.50 + 0.02i$ after 4.5 EAD oxidation with a corresponding O : C ratio increase

from 0.34 to 0.40. Decrease in the overall BBOA absorption and scattering was also detected in situ following a 1-day evolution by Adler et al. (2011). They monitored an average RI of $1.53 + 0.07i$ and $1.54 + 0.04i$ for aerosols dominated by open fire and smoldering emissions, respectively, while the RI decreased to $1.49 + 0.02i$ of the aged aerosols during the following day. Zhong and Jang (2014) reported that light absorption of wood smoke BrC was modified by the photochemical process, owing to the production of BrC from SOA formation and loss of BrC from photochemical bleaching of the chromophores. The total MAC for the BrC eventually decreased by 19 %–68 % within 1 day of aging. They proposed that bleaching occurred by excitation of electrons through the absorption of sunlight via $\pi - \pi*$ (UV and near UV illumination) or $n - \pi*$ (visible wavelengths irradiation) transitions. Then, the excited electrons disrupted the conjugated structure of chromophores, leading to the fading of wood smoke color.

When tar ball aerosols were illuminated merely by 254 nm UV light at a residence time of 144 s, photolysis occurred and weakly diminished their light absorption, in line with the extent of photon flux exposure. UV irradiation similar to the O_3.9 condition slightly decreased the average RI to $1.649 + 0.018i$, indicating that photolysis played a minor role in tar ball aerosol bleaching and contributed less than 15 % of imaginary k changes in the NO_x-free photochemical aging process. Even at full power of UV lamps in the OFR, the average RI decreased by 0.012 and $0.005i$ for maximum photolyzed tar balls (Tables S6–S7, Figs. S14–S17). As we also did not observe detectable optical changes in blank tests upon exposure to O_3 in the dark (Figs. S18–S19), the bleaching of the tar balls in the OFR is mainly attributed to OH-initiated chromophore decomposition via heterogeneous reactions, rather than to O_3 oxidation or photolysis.

These results indicate a fundamental relationship between photochemical processes and impairment of light absorbing and scattering abilities in tar ball aerosols. The optical behaviors of tar balls are a consequence of their chemical composition changes, which are very sensitive to photochemical processes, and one daytime atmospheric aging even resulted in significant oxidation and bleaching of tar balls. In Fig. 6a, the H : C, OM / OC, $\overline{OSc}$, and particle effective density versus O : C ratios are shown. Figure 6b presents the contributions of $C_xH_y^+$, $C_xH_yO^+$, $C_xH_yO_z^+$, and $C_xH_yO_iN_p^+$ groups to the tar balls' composition under a range of OH exposure conditions. Mass spectra features and densities of the tar ball aerosols under various oxidation processes are summarized in Table S8. Increasing the OH exposure leads to continuous increase in O : C and H : C ratios, leading to higher $\overline{OSc}$ for the tar ball aerosols. This result is consistent with Sumlin et al. (2017), who reported that the O : C and H : C for BBOA increased by ~ 0.08 and ~ 0.03 after 4.5 EAD photochemical oxidation, respectively. In this work, the measured O : C ratio increased from 0.25 to 0.38 after maximum aging, while the H : C ratio increased by 0.07 from an initial value of 1.55.

Other previous studies also depicted a dynamic change in elemental ratios for SOA upon aging (Aiken et al., 2008). The H : C ratio may either increase or decrease, depending on the precursor type and oxidation conditions. Overall, O : C and H : C ratio changes relate to specific chemical processes or/and to gas-particle mass transfer during aging of aerosols (Heald et al., 2010; Kim et al., 2014). The tar ball aerosols consist of mostly reduced species ($\overline{OSc} < 0$), which can be oxidized primarily via oxidative formation of polar functional groups to the carbon skeletons. In OH-initiated oxidation, functionalization includes OH / OOH function group addition and COOH : carbonyl group formation that increase the net oxygen content in SOA (Kroll et al., 2011). Hydration or polar functional group addition to unsaturated C–C bonds may also increase the H : C ratio. Moreover, fragmentation or evaporation also mediates the O : C and H : C ratios of SOA in further aging (Zhang and Seinfeld, 2013; Kim et al., 2014). We attribute the increase in the H : C ratio to such oxidation mechanisms that involve bulk species in the particles. As shown in Table S8, $f_{m/z > 100}$ decreased monotonically with aging. After 6.7 EAD photooxidation, $f_{m/z > 100}$ contributed only 21 % of the total organic signals. The decrease in $f_{m/z > 100}$ indicates that fragmentation reactions are involved in the photochemical evolution, and decomposition of high-molecular weight compounds, thereby, reduced the size of the conjugated molecular system. The persistent high value of $f_{m/z > 100}$ after 6.7 EAD photooxidation implies that some high-molecular weight compounds remained in the tar ball aerosols and continue to contribute to light absorption either as individual chromophores or as charge transfer complexes. From Fig. 6b, $C_xH_y^+$ fragments deplete with OH exposure, while $C_xH_yO^+$ and $C_xH_yO_z^+$ fragments increase, implying the formation of oxygenated moieties in the tar ball aerosols. In addition, a decrease in the $C_xH_yO_iN_p^+$ fraction was measured from initial 3.6 % to 1.9 % after the maximum oxidation. Ng et al. (2010) suggested using $f44(CO_2^+)$ vs. $f43(C_2H_3O^+)$ triangle space as an indication of OA sources and for estimation of their degree of oxidation and volatility. The $C_2H_3O^+$ (less oxidized fragments) is an indicative fragment from aldehydes or ketones. A high $f44/f43$ ratio indicates low volatility and a high oxidation level of SOA. Moreover, high $f44/f43$ and O : C ratios are associated with increased hygroscopicity and possible CCN activity of OA (Hennigan et al., 2011; Lambe et al., 2011). The $f44$ vs. $f43$ in this study varied with photochemical aging and fell within the expected range for ambient OOA, as shown in Fig. 7. Increase in the $f44/f43$ ratio with OH oxidation in Fig. 6b depicted the increase in carboxylic and/or peroxide compounds compared to carbonyl species in the tar balls, which is consistent with the atmospheric evolution of ambient biomass burning plumes (Hennigan et al., 2011; Canonaco et al., 2015).

To infer the possible chemical processes, detailed mass spectra were compared between fresh and 6.7 EAD photochemical oxidized tar balls (Fig. S20). We found that decrease in alkyl/alkenyl chains (e.g., $C_nH_{2n-1}^+$, $C_nH_{2n+1}^+$), and
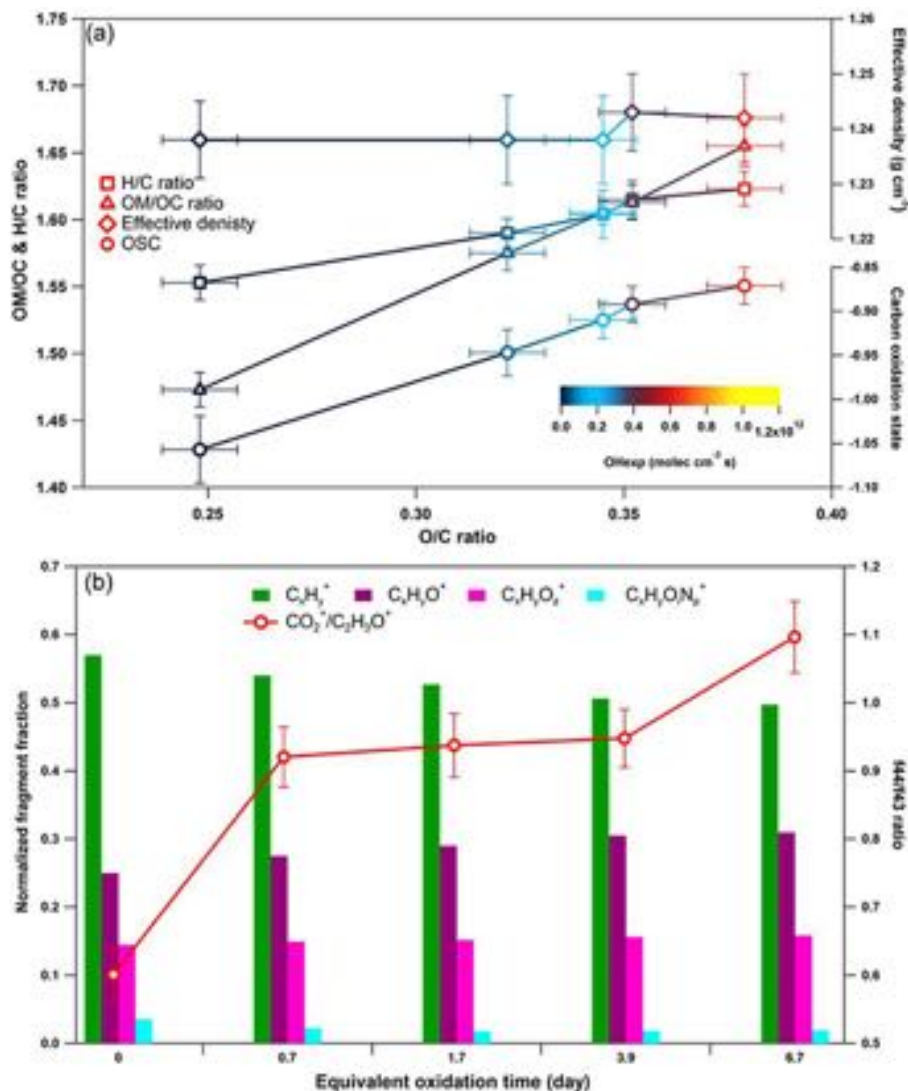
Figure 6. Dynamic changes for the chemical characteristics of tar ball particle under NO_x-free OH photochemical oxidation: **(a)** OM / OC, H : C ratio, particle density, and average carbon oxidation state ($\overline{OSc}$) changes as a function of O : C ratio; **(b)** mass spectra evolution with oxidation times in term of $C_xH_y^+$, $C_xH_yO^+$, $C_xH_yO_z^+$, and $C_xH_yO_iN_p^+$ fragment groups.

aromatic ring structure fragments (e.g., $C_6H_5^+$, $C_6H_9^+$) contributed the prominent changes in the $C_xH_y^+$ group, and a relatively higher CO_2^+ increment relative to $C_2H_3O^+$ explained the increase in the $f44/f43$ ratio. The decrease in the abundance of $C_2H_4O_2^+$ (m/z 60) and $C_3H_5O_2^+$ (m/z 73) is consistent with recent studies that levoglucosan or similar species can decay in the atmosphere due to photochemical oxidation (Hennigan et al., 2010). The pronounced decrease in intensity at m/z 137 ($C_8H_9O_2^+$ and $C_7H_5O_3^+$) suggests that the methoxy-phenol components were dissipated substantially in the aged tar balls.

In summary, photochemical oxidation by OH radicals destructed the aromatic rings and methoxy phenolic structures, which are expected to be the primary chromophores in the tar balls. The NOC content and high-molecular weight

species were also depleted via OH oxidation. These chemical changes upon OH oxidation may explain the observed diminishing in light scattering and absorption upon photochemical aging.

3.3 NO_x-dependent tar ball particles oxidation

N_2O was recently introduced for simulating NO_x-dependent SOA formation pathways in OFR under high-O_3 concentration, as $O(^1D)+N_2O$ reactions can be applied to systematically vary the branching ratio of the RO_2+NO reactions relative to the RO_2+HO_2 and/or RO_2+RO_2 reactions over a range of conditions relevant to atmospheric SOA formation (Lambe et al., 2017). Here we introduced 0.5 % vol and 2.0 % vol N_2O to investigate NO_x-involved daytime aging of
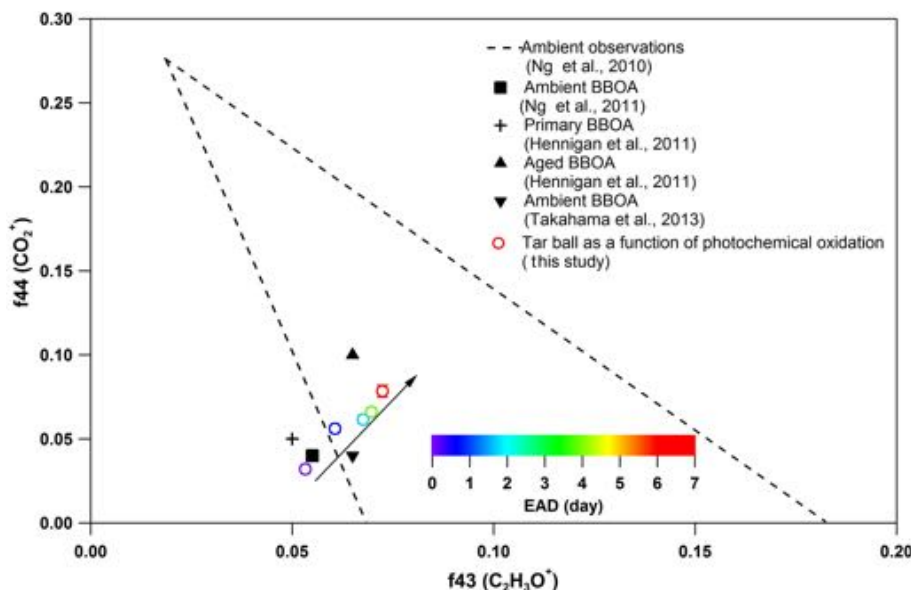
Figure 7. Comparison of $f44$ and $f43$ values from ambient data sets (Ng et al., 2010) and values from ambient biomass burning organic aerosol.

tar ball aerosols in the OFR. The OH exposures were maintained for all these tests at about 4 EAD. The corresponding NO$_2$ concentrations downstream of the OFR were measured to be 96.1 $\pm$ 1.3 and 528.3 $\pm$ 6.2 ppbv. The concentration of static NO can be neglected under these severe oxidation conditions. Figure 8 shows the mass spectrum features for fresh and aged tar balls reacted in the absence/presence of NO$_x$. Parameters including organic elemental ratios and densities are summarized in Table S8. In general, tar balls oxidized under N$_2$O addition exhibit higher O:C and relatively lower H:C ratios. NO$_y^+$ (NO$^+$ and NO$_2^+$) signals appear in the mass spectra and the intensities of NO$_y^+$ display a positive trend with N$_2$O concentration, together with an increase in oxygenated fragments (C$_x$H$_y$O$^+$ and C$_x$H$_y$O$_z^+$) and a decrease in hydrocarbon fragments (C$_x$H$_y^+$). The signal ratio of NO$^+$ (m/z 30) to NO$_2^+$ (m/z 46) is used to distinguish organic nitrate from inorganic nitrate. The signal from standard inorganic nitrate (e.g., NH$_4$NO$_3$) has a typical NO$_2^+$ / NO$^+$ ratio of 0.485 obtained from our AMS data (detailed mass spectra are shown in Fig. S21). The ratio and standard mass spectra are similar to previous studies (Zhou et al., 2017). The fraction of NO$_y^+$ (NO$^+$ and NO$_2^+$) signals in the aged tar balls increased from 0 % to 0.7 % and 1.5 % at 0.5 % vol and 2.0 % vol N$_2$O additions, respectively. The corresponding values of the NO$_2^+$ / NO$^+$ ratio are 0.162 and 0.174, which are much lower than that for inorganic nitrates. Furthermore, the contribution of C$_x$H$_y$O$_i$N$_p^+$ fragments increased from 1.9 % to 4.4 % and 4.5 % over the course of aging. Therefore, we can conclude that NOC rather than inorganic nitrate formed in the NO$_x$-dependent photooxidation process, resulting in an overall increase in the N:C ratio from 0.010 to 0.012 and 0.015. Additionally, the density of tar

balls slightly increased from 1.24 for the fresh tar balls to 1.26 for the one aged in the presence of 2 % vol N$_2$O.

Detailed changes in the mass spectra over the course of the experiment are shown in Fig. S22. Indicative ions of cyclolakyl fragments (e.g., C$_2$H$_3^+$, C$_3$H$_5^+$, C$_4$H$_7^+$) decreased, while NO$_x$ addition increased the CO$^+$ and CO$_2^+$ intensities relative to C$_2$H$_3$O$^+$, leading to a higher $f44/f43$ ratio. Ng et al. (2007) observed a similar change for photooxidation of terpenes in the presence of NO$_x$. Changes in AMS spectra with NO$_x$ addition may mark differences between the dominating reaction pathways in tar ball photooxidation as RO$_2$+NO versus RO$_2$+HO$_2$ and/or RO$_2$+RO$_2$ reactions.

Photochemical oxidation with NO$_x$ addition enhances the oxidation level and increases both the absorption and scattering of tar ball aerosols. Dynamic changes in the complex RI are shown in Fig. 9 and summarized in Table S5. The RI of tar ball aerosols increased from an average of $1.632 + 0.007i$ for pure OH-initiated photooxidation to $1.635 + 0.015i$ with the addition of 0.5 % vol N$_2$O, and a greater increase up to $1.648 + 0.019i$ with 2.0 % vol N$_2$O. The increase in RI is therefore primarily attributed to NOC formation. Zhong and Jang (2014) observed that a higher NO$_x$ level slowed photo-bleaching of wood smoke BrC, and they suggested that NO$_x$-modified reaction pathways produce secondary NOC chromophores (i.e., nitro-phenols). Liu et al. (2016) simulated daytime chemistry of various VOCs in the presence of NO$_x$ and found that light absorption of produced SOA, especially aromatic ones, increased with NO$_x$ concentration. These findings were also corroborated by the experimental study of Lin et al. (2015), where the chemical composition and the light absorption properties of laboratory-generated toluene SOA were reported to have a strong positive depen-
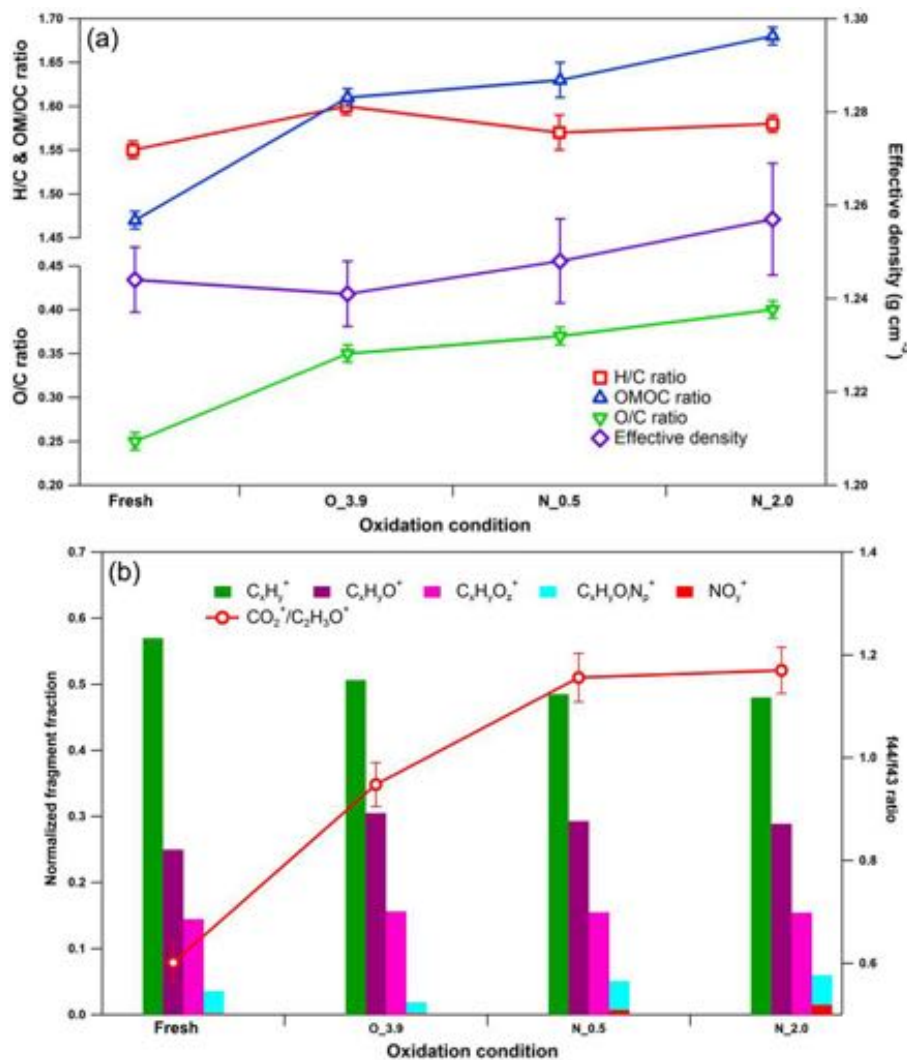
Figure 8. Dynamic changes for chemical characteristics of tar ball aerosols under NO_x-dependent OH photochemical oxidation: **(a)** OM / OC, O : C, H : C, and particle density changes; **(b)** mass spectra changes with different oxidation conditions in terms of $C_xH_y^+$, $C_xH_yO^+$, $C_xH_yO_z^+$, and $C_xH_yO_zN_p^+$ fragment groups. $C_xH_yO_zN_p^+$ include all nitrogen-containing fragments (e.g., $C_xH_yON^+$, $C_xH_yO_zN_i^+$, and $C_xH_yN^+$); NO_y^+ include NO^+ and NO_2^+. O_3.9 represents 3.9 days' equivalent atmospheric photochemical aging in the absence of NO_x; N_0.5 and N_2.0 indicate photochemical oxidation with 0.5 % vol and 2.0 % vol N_2O addition at ~ 4.0 days' atmospheric oxidation.

dence on the presence of nitro-phenols formed at high-NO_x oxidation conditions. The color of the BrC diminished with photolysis, correlated with a decline of the NOC fraction. Nitration of aromatic species via NO_x / N_2O_5 / NO_3 has been proposed as one of the main mechanisms to produce secondary BrC in the atmosphere (Lu et al., 2011; Lin et al., 2015, 2017; Bluvshtein et al., 2017).

The imaginary part at 2.0 % vol N_2O addition was almost comparable with that of the fresh tar ball aerosols (average value: RI = 1.661 + 0.020i), although the real part was lower, suggesting that photooxidation in the presence of NO_x promotes the formation of N-containing chromophores via secondary processes. In our experiments, formation of the N-

containing chromophores overweighed the bleaching from OH photooxidation to eventually regain the absorption of the aged tar balls. The average SSA calculated for 150 nm particles decreased from 0.96 to 0.91 and 0.89 with N_2O addition. Absorption enhancement with N_2O addition for tar balls upon photooxidation can also be seen in the MAC changes shown in Fig. S23, where MAC at 375 nm for fresh tar balls was 0.854 $m^2\,g^{-1}$; it decreased to 0.416 $m^2\,g^{-1}$ via OH photo-bleaching, and then MAC increased to 0.459 $m^2\,g^{-1}$ at 0.5 % vol N_2O addition, and up to 0.598 $m^2\,g^{-1}$ at 2.0 % vol N_2O addition due to chromophore formation.
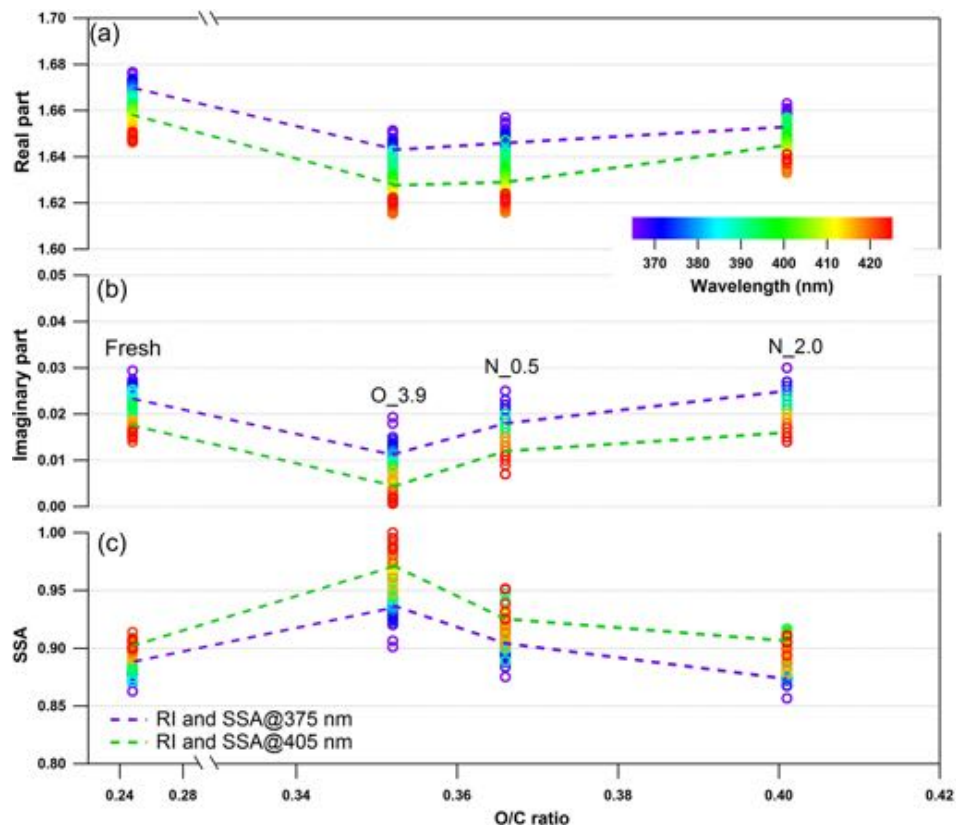
Figure 9. Changes in retrieved spectrum-dependent RI as a function of O : C ratio for tar ball particles upon NO_x-dependent photochemical oxidation: **(a)** real part, **(b)** imaginary part, and **(c)** SSA calculated from 150 nm particles. For clarity, error bars for O : C ratio (± 0.01), RI (± 0.006 for real part, and ± 0.003 for imaginary part on average), and SSA (± 0.007) are not shown. O_3.9 represents 3.9-day equivalent atmospheric photochemical aging in the absence of NO_x, N_0.5 and N_2.0 indicate photochemical oxidation with 0.5 and 2.0 % vol N_2O addition at ~ 4.0 days' atmospheric oxidation.

3.4 Atmospheric and climate implication

Atmospheric aging alters the RI of SOA, and the dynamic changes in RI depend on complicated reaction pathways (Liu et al., 2016). OH-initiated photochemical oxidation and photolysis decrease the RI of laboratory proxies of tar balls under NO_x-free conditions, while photooxidation under high NO_x has an opposite effect on the RI of tar balls. We investigated the relationship between the dynamic RI values of tar ball particles and their possible climatic implications, including the change in light extinction/absorption efficiency and the clear-sky direct radiative forcing. For clarity, light extinction/absorption efficiencies were calculated and compared at wavelengths of 375 and 405 nm, while radiative forcing was estimated over all the measured wavelengths from 365 to 425 nm. Atmospheric and climatic implications were assessed for fresh and oxidized tar balls upon NO_x-dependent ~ 3.9 EAD photooxidation (O_3.9, N_0.5, and N_2.0), in which fresh tar balls were taken as a reference.

As shown in Fig. 10, photochemical oxidation under NO_x-free condition (O_3.9) diminished light extinction and absorption efficiency of tar ball aerosols in the atmospheric rel-

evant size of 50–300 nm, causing about 5 %–40 % decrease in extinction at 375 and 405 nm wavelength. For aerosols larger than 400 nm, the extinction efficiency of tar ball aerosols increased instead after photochemical aging. The light extinction efficiency presented higher size-dependence than absorption, and extinction changes were more sensitive to particle size, especially in the smaller sizes. The decreased absorption was more pronounced, with an ~ 60 % decrease at 375 nm and over 75 % at 405 nm. Previous studies have confirmed the relationship between biomass burning emissions and acute regional visibility deterioration (Huang et al., 2012; Chen et al., 2017). Our results demonstrate that OH radical initiated daytime aging may play an important role in improving visibility degradation caused by primary biomass BrC. However, photochemical evolution under high-NO_x conditions may compensate effects of the photooxidation bleaching of tar ball aerosols via the formation of NOC chromophores. At N_0.5 conditions, the light extinction decreased by 4 % to 20 % at 375 nm and 5 % to 24 % at 405 nm, respectively. The corresponding absorption decrease was 20 %–27 % at both wavelengths. With more N_2O addi-
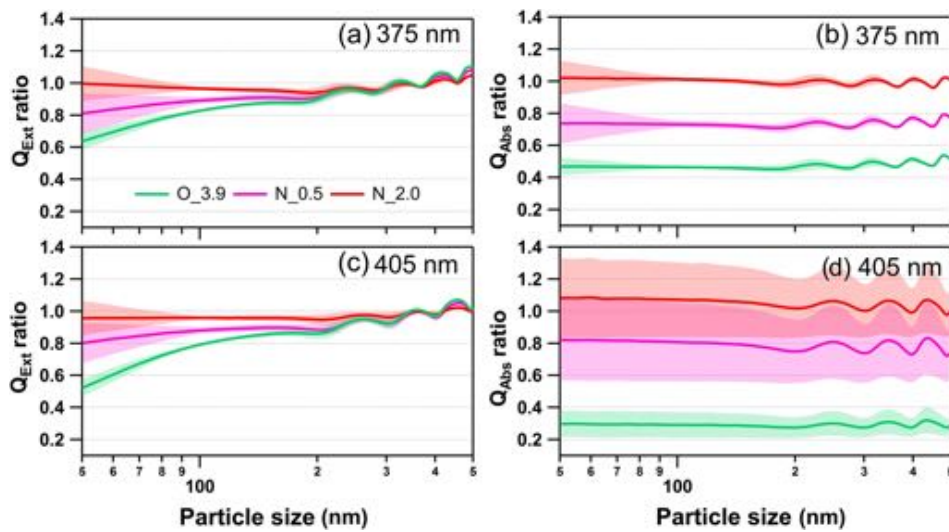
Figure 10. Size-resolved light extinction and absorption efficiency ratio of NO_x-dependent photooxidized tar balls compared to the fresh tar ball particles: **(a)** and **(c)** extinction ratios at 375 and 405 nm; **(b)** and **(d)** absorption ratios at 375 and 405 nm. O_3.9 represents 3.9 days' equivalent atmospheric photochemical aging in the absence of NO_x; N_0.5 and N_2.0 indicate photochemical oxidation with 0.5 % vol and 2.0 % vol N_2O addition at ~ 4.0 days' atmospheric oxidation.

tion, formation of secondary N-containing chromophores almost completely offsets light extinction/absorption decrease caused by photooxidation. Under the N_2.0 conditions, enhancement of light absorption efficiency for tar ball was about 0 %–9 % at 405 nm in the entire size range of 50–500 nm.

Radiative forcing from aerosols over both ground and snow is vital to climate models (Barnett et al., 2005; Kanakidou et al., 2005). Integrated radiative forcing for tar ball aerosols as a function of particle size under various oxidation conditions is shown in Fig. 11. Size-/wavelength-resolved SRF are also shown in Figs. S24 and S25. Integrated SRF over ground has negative values for tar balls over almost all the atmospheric relevant sizes, indicating a radiative cooling effect by tar ball aerosols except at 195–210 nm, where fresh tar ball particles present warming effect with SRF up to $\sim 0.48\,W\,g^{-1}$. In practical fire emissions, the size of tar balls depends on the burning and environment conditions and biomass fuel types with typical values between tens to hundreds of nanometers (Reid et al., 2005; Pósfai et al., 2004). The complicated size-dependence character of SRF makes it difficult to assess the real climatic effect of tar ball particles without extensive calculations. Figure 11a suggests fresh tar balls have SRF values of $-7.46\,W\,g^{-1}$ at 150 nm and $0.45\,W\,g^{-1}$ at 200 nm, respectively. The SRF decreased for all size ranges due to photochemical oxidation to $-7.93\,W\,g^{-1}$ at 150 nm and $-1.37\,W\,g^{-1}$ at 200 nm for tar ball aerosols under O_3.9 condition. At N_0.5 conditions, SRF was $-7.37\,W\,g^{-1}$ at 150 nm and $0.16\,W\,g^{-1}$ at 200 nm, and the corresponding values at N_2.0 conditions increased to $-7.20\,W\,g^{-1}$ at 150 nm and $0.31\,W\,g^{-1}$ at 200 nm.
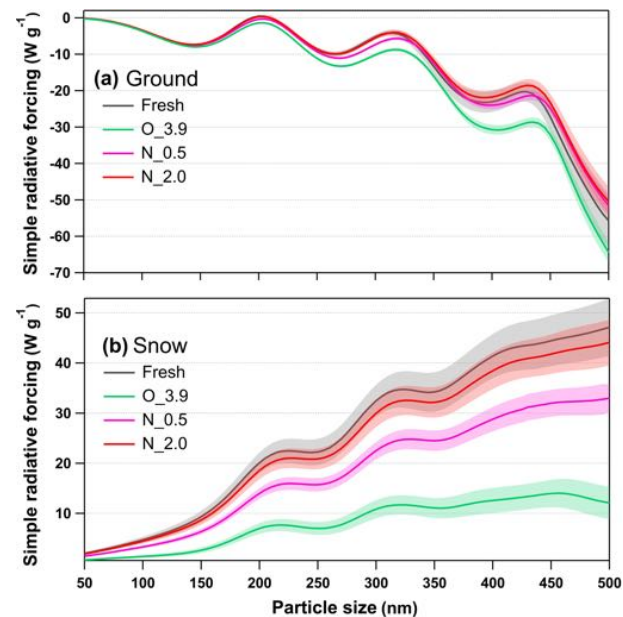
Figure 11. Calculated size-resolved simple radiative forcing (SRF, $W\,g^{-1}$) by tar ball aerosols, integrated over 365–425 nm incident solar irradiation for fresh and NO_x-dependent photooxidized tar balls: **(a)** ground-based radiative forcing, **(b)** snow-based radiative forcing.

In contrast, tar ball particles contributed to positive forcing (warming effect) over the bright terrain throughout the atmospheric aging, as shown in Fig. 11b. Radiative forcing over the snow showed a simple increasing trend with particle size, indicating that larger BrC aerosol with identical mass

loading in the air have a higher warming effect. The changes in snow-based radiative forcing upon photochemical aging followed the same trends as in the ground-based cases. Fresh tar ball at size of 200 nm has SRF of 20.12 W g^{-1} over the incident solar wavelength of 365–425 nm on the snow terrain. With photochemical oxidation under NO$_x$-free condition, radiative forcing decreased significantly. After 3.9 EAD atmospheric aging, snow-based radiative forcing for tar ball decreased by 65 %–73 % over the size range of 50–500 nm, the value of 200 nm tar ball became 6.99 W g^{-1}. When NO$_x$ was involved in the photochemical oxidation of tar balls, the decrement of radiative forcing was weakened. At N_0.5, SRF for 200 nm tar ball was 14.01 W g^{-1}, while at N_2.0 condition, size-dependent SRF from the aged tar ball was almost comparable with that from fresh tar ball, and SRF for 200 nm tar ball was 18.56 W g^{-1}.

Although less than 10 % of the solar spectrum's energy is distributed between 365 and 425 nm, the radiative forcing over this range represents a significant warming or cooling potential over the arctic terrain. In conclusion, photochemical oxidation under NO$_x$-free conditions can decrease radiative forcing of tar ball aerosols, resulting in enhancement in the cooling effect over ground and decreased in warming effect over the snow. However, NO$_x$ involvement in photooxidation inhibits the decrease in radiative forcing of tar ball aerosols. Overall, the complex changes in optical properties of tar balls at long aging times impose great uncertainties in traditional model-based estimation of BBOA. Our study emphasizes the importance of taking this atmospheric process into consideration to refine the understanding of the climatic and atmospheric influences from these aerosols.

4   Conclusions

In this study, proxies for tar ball aerosols were generated in the laboratory following a flameless wood pyrolysis process. The optical and chemical properties of the generated tar balls were constrained using BBCES and HR-Tof-AMS/SP-LD-REMPI-MS and were shown to have many similarities to ambient biomass burning aerosols. Laboratory-generated fresh tar ball aerosols have light absorption characteristics similar to atmospheric BrC with higher absorption efficiency towards the UV. The average complex refractive indices between 365 and 425 nm are 1.661 + 0.020i and 1.635 + 0.003i for nonpolar and polar tar ball aerosols, respectively.

Atmospheric evolution for tar ball aerosols was experimentally simulated using an oxidation flow reactor. The study focused on dynamic changes in the optical and chemical properties due to NO$_x$-dependent photochemical oxidation. Furthermore, the relationship between oxidation level and the resulting RI of the tar ball aerosols was explored. We found a substantial decrease in the scattering and absorption properties of tar balls, with a corresponding increase in SSA with OH oxidation in the absence of NO$_x$.

A correlation between the RI decrease and increase in the O : C and H : C ratios was observed. The decrease in light scattering and absorption is attributed to the destruction of aromatic/phenolic/NOC and high-molecular weight species chromophores via OH-initiated photooxidation of tar balls. Over longer aging times, the average RI of the tar ball aerosols decreased from 1.661 + 0.020i to 1.632 + 0.007i upon atmospheric equivalent to 3.9 days' aging, and the corresponding O : C and H : C ratio increased from an initial 0.25 and 1.55 to 0.35 and 1.59, respectively.

Our results suggest that OH oxidation rather than photolysis or ozone reactions plays the dominant role that determines the optical and chemical properties in tar ball aging. The observed decrease in absorption results from depletion of chromophores such as aromatic rings, phenolic compounds and high-molecular weight species.

Simulations under high-NO$_x$ environments enhanced the aerosol oxidation state and increased the scattering and absorption of tar ball aerosols relative to OH photooxidation in the absence of NO$_x$. At $\sim$ 3.9 EAD, addition of 0.5 % vol and 2.0 % vol N$_2$O increased the organic elemental ratios (O : C, H : C, and N : C ratios) and doubled the organic nitrate fraction in the particles from 1.9 % to $\sim$ 4.4 %. The formation of NOC chromophores overweighs the intrinsic depletion of chromophores, leading to a higher RI of 1.635 + 0.015i and 1.648 + 0.019i.

The atmospheric and climatic implications from tar ball aerosols under various oxidation conditions were assessed using a simple radiative forcing model in terms of extinction/absorption efficiency changes and ground-/snow-based radiative forcing. These results demonstrate that the optical and chemical properties of tar ball particles are dynamically related to atmospheric aging, and optical changes are governed by both photobleaching and secondary chromophore formation. Therefore, the atmospheric process should be emphasized in model predictions for evaluating biomass burning BrC aerosol radiative forcing as well as climate change.

Author contributions. YR was the project leader. YR, CL, and QF designed the experiment, and CL and QF conducted the experiment. JS, JP, and RZ contributed the REMPI-MS measurement and revised related paragraphs in the manuscript. DM improved the code in the SRF calculation. CL wrote the manuscript with the contribution and help of LA.

References

Abo Riziq, A., Erlick, C., Dinar, E., and Rudich, Y.: Optical properties of absorbing and non-absorbing aerosols retrieved by cavity ring down (CRD) spectroscopy, Atmos. Chem. Phys., 7, 1523–1536, https://doi.org/10.5194/acp-7-1523-2007, 2007.

Adachi, K. and Buseck, P. R.: Atmospheric tar balls from biomass burning in Mexico, J. Geophys. Res.-Atmos., 116, D05204, https://doi.org/10.1029/2010JD015102, 2011.

Adler, G., Riziq, A. A., Erlick, C., and Rudich, Y.: Effect of intrinsic organic carbon on the optical properties of fresh diesel soot, Proc. Natl. Acad. Sci. USA, 107, 6699–6704, https://doi.org/10.1073/pnas.0903311106, 2010.

Adler, G., Flores, J. M., Abo Riziq, A., Borrmann, S., and Rudich, Y.: Chemical, physical, and optical evolution of biomass burning aerosols: a case study, Atmos. Chem. Phys., 11, 1491–1503, https://doi.org/10.5194/acp-11-1491-2011, 2011.

Aiken, A. C., Decarlo, P. F., Kroll, J. H., Worsnop, D. R., Huffman, J. A., Docherty, K. S., Ulbrich, I. M., Mohr, C., Kimmel, J. R., and Sueper, D.: O / C and OM / OC ratios of primary, secondary, and ambient organic aerosols with high-resolution time-of-flight aerosol mass spectrometry, Environ. Sci. Technol., 42, 4478–4485, https://doi.org/10.1021/es703009q, 2008.

Alexander, D. T., Crozier, P. A., and Anderson, J. R.: Brown carbon spheres in East Asian outflow and their optical properties, Science, 321, 833–836, https://doi.org/10.1126/science.1155296, 2008.

Andreae, M. O. and Gelencsér, A.: Black carbon or brown carbon? The nature of light-absorbing carbonaceous aerosols, Atmos. Chem. Phys., 6, 3131–3148, https://doi.org/10.5194/acp-6-3131-2006, 2006.

Asa-Awuku, A., Sullivan, A. P., Hennigan, C. J., Weber, R. J., and Nenes, A.: Investigation of molar volume and surfactant characteristics of water-soluble organic compounds in biomass burning aerosol, Atmos. Chem. Phys., 8, 799–812, https://doi.org/10.5194/acp-8-799-2008, 2008.

Bahadur, R., Praveen, P. S., Xu, Y., and Ramanathan, V.: Solar absorption by elemental and brown carbon determined from spectral observations, Proc. Natl. Acad. Sci. USA, 109, 17366–17371, https://doi.org/10.1073/pnas.1205910109, 2012.

Barnett, T. P., Adam, J. C., and Lettenmaier, D. P.: Potential impacts of a warming climate on water avail-

ability in snow-dominated regions, Nature, 438, 303–309, https://doi.org/10.1038/nature04141, 2005.

Bente, M., Sklorz, M., Streibel, T., and Zimmermann, R.: Online laser desorption-multiphoton postionization mass spectrometry of individual aerosol particles: molecular source indicators for particles emitted from different traffic-related and wood combustion sources, Anal. Chem., 80, 8991–9004, https://doi.org/10.1021/ac801295f, 2008.

Bente, M., Sklorz, M., Streibel, T., and Zimmermann, R.: Thermal desorption-multiphoton ionization time-of-flight mass spectrometry of individual aerosol particles: A simplified approach for online single-particle analysis of Polycyclic Aromatic Hydrocarbons and their derivatives, Anal. Chem., 81, 2525–2536, https://doi.org/10.1021/ac802296f, 2009.

Bluvshtein, N., Lin, P., Flores, J. M., Segev, L., Mazar, Y., Tas, E., Snider, G., Weagle, C., Brown, S. S., and Laskin, A.: Broadband optical properties of biomass-burning aerosol and identification of brown carbon chromophores, J. Geophys. Res.-Atmos. 122, 5441–5456, https://doi.org/10.1002/2016JD026230, 2017.

Boesl, U., Neusser, H., and Schlag, E.: Two-photon ionization of polyatomic molecules in a mass spectrometer, Z. Naturforsch. A, 33, 1546–1548, https://doi.org/10.1515/zna-1978-1218, 1978.

Bond, T. C. and Bergstrom, R. W.: Light absorption by carbonaceous particles: An investigative review, Aerosol Sci. Tech., 40, 27–67, https://doi.org/10.1080/02786820500421521, 2006.

Canonaco, F., Slowik, J. G., Baltensperger, U., and Prévôt, A. S. H.: Seasonal differences in oxygenated organic aerosol composition: implications for emissions sources and factor analysis, Atmos. Chem. Phys., 15, 6993–7002, https://doi.org/10.5194/acp-15-6993-2015, 2015.

Chakrabarty, R. K., Moosmüller, H., Chen, L.-W. A., Lewis, K., Arnott, W. P., Mazzoleni, C., Dubey, M. K., Wold, C. E., Hao, W. M., and Kreidenweis, S. M.: Brown carbon in tar balls from smoldering biomass combustion, Atmos. Chem. Phys., 10, 6363–6370, https://doi.org/10.5194/acp-10-6363-2010, 2010.

Chen, Y. and Bond, T. C.: Light absorption by organic carbon from wood combustion, Atmos. Chem. Phys., 10, 1773–1787, https://doi.org/10.5194/acp-10-1773-2010, 2010.

Chen, J., Li, C., Ristovski, Z., Milic, A., Gu, Y., Islam, M. S., Wang, S., Hao, J., Zhang, H., and He, C.: A review of biomass burning: Emissions and impacts on air quality, health and climate in China, Sci. Total Environ., 579, 1000–1034, https://doi.org/10.1016/j.scitotenv.2016.11.025, 2017.

Chung, C. E., Ramanathan, V., and Decremer, D.: Observationally constrained estimates of carbonaceous aerosol radiative forcing, P. Natl. Acad. Sci. USA,, 109, 11624–11629, https://doi.org/10.1073/pnas.1203707109, 2012.

Chýlek, P., Videen, G., Geldart, D., Dobbie, J. S., and Tso, H.: Effective medium approximations for heterogeneous particles, Light scattering by nonspherical particles: theory, measurements, and applications, 273–308, edited by: Mishchenko, M. I., Hovenier, J. W., and Travis, L. D., Academic Press, San Diego, 2000.

Czech, H., Pieber, S. M., Tiitta, P., Sippula, O., Kortelainen, M., Lamberg, H., Grigonyte, J., Streibel, T., Prévôt, A. S., and Jokiniemi, J.: Time-resolved analysis of primary volatile emissions and secondary aerosol formation potential from a small-scale pellet boiler, Atmos. Environ., 158, 236–245, https://doi.org/10.1016/j.atmosenv.2017.03.040, 2017.

d'Almeida, G. A., Koepke, P., and Shettle, E. P.: Atmospheric aerosols: global climatology and radiative characteristics, A. Deepak Publishing, Hampton, Va, 1991.

DeCarlo, P. F., Kimmel, J. R., Trimborn, A., Northway, M. J., Jayne, J. T., Aiken, A. C., Gonin, M., Fuhrer, K., Horvath, T., and Docherty, K. S.: Field-deployable, high-resolution, time-of-flight aerosol mass spectrometer, Anal. Chem., 78, 8281–8289, https://doi.org/10.1021/ac061249n, 2006.

Desyaterik, Y., Sun, Y., Shen, X., Lee, T., Wang, X., Wang, T., and Collett, J. L.: Speciation of "brown" carbon in cloud water impacted by agricultural biomass burning in eastern China, J. Geophys. Res.-Atmos., 118, 7389–7399, https://doi.org/10.1002/jgrd.50561, 2013.

Dewar, M. J. and Lepley, A. R.: π-Complexes. I. Charge Transfer Spectra of π-Complexes Formed by Trinitrobenzene with Polycyclic Aromatic Compounds, J. Am. Chem. Soc., 83, 4560–4563, 1961.

Dinar, E., Riziq, A. A., Spindler, C., Erlick, C., Kiss, G., and Rudich, Y.: The complex refractive index of atmospheric and model humic-like substances (HULIS) retrieved by a cavity ring down aerosol spectrometer (CRD-AS), Faraday Discuss., 137, 279–295, https://doi.org/10.1039/B703111D, 2008.

Epstein, S. A., Blair, S. L., and Nizkorodov, S. A.: Direct photolysis of α-pinene ozonolysis secondary organic aerosol: effect on particle mass and peroxide content, Environ. Sci. Technol., 48, 11251–11258, https://doi.org/10.1021/es502350u, 2014.

Feng, Y., Ramanathan, V., and Kotamarthi, V. R.: Brown carbon: a significant atmospheric absorber of solar radiation?, Atmos. Chem. Phys., 13, 8607–8621, https://doi.org/10.5194/acp-13-8607-2013, 2013.

Finewax, Z., de Gouw, J. A., and Ziemann, P. J.: Identification and quantification of 4-Nitrocatechol formed from OH and NO_3 radical-initiated reactions of catechol in air in the presence of NO_x: Implications for secondary organic aerosol formation from biomass burning, Environ. Sci. Technol., 52, 1981–1989, https://doi.org/10.1021/acs.est.7b05864, 2018.

Flores, J. M., Zhao, D. F., Segev, L., Schlag, P., Kiendler-Scharr, A., Fuchs, H., Watne, Å. K., Bluvshtein, N., Mentel, Th. F., Hallquist, M., and Rudich, Y.: Evolution of the complex refractive index in the UV spectral region in ageing secondary organic aerosol, Atmos. Chem. Phys., 14, 5793–5806, https://doi.org/10.5194/acp-14-5793-2014, 2014a.

Flores, J. M., Washenfelder, R., Adler, G., Lee, H., Segev, L., Laskin, J., Laskin, A., Nizkorodov, S., Brown, S., and Rudich, Y.: Complex refractive indices in the near-ultraviolet spectral region of biogenic secondary organic aerosol aged with ammonia, Phys. Chem. Chem. Phys., 16, 10629–10642, https://doi.org/10.1039/C4CP01009D, 2014b.

Flowers, B. A., Dubey, M. K., Mazzoleni, C., Stone, E. A., Schauer, J. J., Kim, S.-W., and Yoon, S. C.: Optical-chemical-microphysical relationships and closure studies for mixed carbonaceous aerosols observed at Jeju Island; 3-laser photoacoustic spectrometer, particle sizing, and filter analysis, Atmos. Chem. Phys., 10, 10387–10398, https://doi.org/10.5194/acp-10-10387-2010, 2010.

Forrister, H., Liu, J., Scheuer, E., Dibb, J., Ziemba, L., Thornhill, K. L., Anderson, B., Diskin, G., Perring, A. E., and Schwarz, J. P.: Evolution of brown carbon in wildfire plumes, Geophys. Res. Lett., 42, 4623–4630, https://doi.org/10.1002/2015GL063897, 2015.

Forster, P. M. F. and Taylor, K. E.: Climate forcings and climate sensitivities diagnosed from coupled climate model integrations, J. Climate, 19, 6181–6194, https://doi.org/10.1175/JCLI3974.1, 2006.

Fu, H., Zhang, M., Li, W., Chen, J., Wang, L., Quan, X., and Wang, W.: Morphology, composition and mixing state of individual carbonaceous aerosol in urban Shanghai, Atmos. Chem. Phys., 12, 693–707, https://doi.org/10.5194/acp-12-693-2012, 2012.

Ge, X., Setyan, A., Sun, Y., and Zhang, Q.: Primary and secondary organic aerosols in Fresno, California during wintertime: Results from high resolution aerosol mass spectrometry, J. Geophys. Res.-Atmos., 117, D19301, https://doi.org/10.1029/2012JD018026, 2012.

Grotemeyer, J., Boesl, U., Walter, K., and Schlag, E. W.: A general soft ionization method for mass spectrometry: Resonance-enhanced multi-photon ionization of biomolecules, Org. Mass. Spectrom., 21, 645–653, https://doi.org/10.1002/oms.1210211008, 1986.

Hand, J. L., Malm, W., Laskin, A., Day, D., Lee, T. B., Wang, C., Carrico, C., Carrillo, J., Cowin, J. P., and Collett, J.: Optical, physical, and chemical properties of tar balls observed during the Yosemite Aerosol Characterization Study, J. Geophys. Res.-Atmos., 110, D21210, https://doi.org/10.1029/2004JD005728, 2005.

He, L.-Y., Lin, Y., Huang, X.-F., Guo, S., Xue, L., Su, Q., Hu, M., Luan, S.-J., and Zhang, Y.-H.: Characterization of high-resolution aerosol mass spectra of primary organic aerosol emissions from Chinese cooking and biomass burning, Atmos. Chem. Phys., 10, 11535–11543, https://doi.org/10.5194/acp-10-11535-2010, 2010.

He, Q., Bluvshtein, N., Segev, L., Meidan, D., Flores, J. M., Brown, S. S., Brune, W., and Rudich, Y.: Evolution of the complex refractive index of secondary organic aerosols during atmospheric aging, Environ. Sci. Technol., 52, 3456–3465, https://doi.org/10.1021/acs.est.7b05742, 2018.

Heald, C., Kroll, J., Jimenez, J., Docherty, K., DeCarlo, P., Aiken, A., Chen, Q., Martin, S., Farmer, D., and Artaxo, P.: A simplified description of the evolution of organic aerosol composition in the atmosphere, Geophys. Res. Lett., 37, L08803, https://doi.org/10.1029/2010GL042737, 2010.

Hennigan, C. J., Sullivan, A. P., Collett Jr., J. L., and Robinson, A. L.: Levoglucosan stability in biomass burning particles exposed to hydroxyl radicals, Geophys. Res. Lett., 37, L09806, https://doi.org/10.1029/2010GL043088, 2010.

Hennigan, C. J., Miracolo, M. A., Engelhart, G. J., May, A. A., Presto, A. A., Lee, T., Sullivan, A. P., McMeeking, G. R., Coe, H., Wold, C. E., Hao, W.-M., Gilman, J. B., Kuster, W. C., de Gouw, J., Schichtel, B. A., Collett Jr., J. L., Kreidenweis, S. M., and Robinson, A. L.: Chemical and physical transformations of organic aerosol from the photo-oxidation of open biomass burning emissions in an environmental chamber, Atmos. Chem. Phys., 11, 7669–7686, https://doi.org/10.5194/acp-11-7669-2011, 2011.

Heger, H. J., Zimmermann, R., Dorfner, R., Beckmann, M., Griebel, H., Kettrup, A., and Boesl, U.: On-line emission analysis of polycyclic aromatic hydrocarbons down to pptv concentration levels in the flue gas of an incineration pilot

plant with a mobile resonance-enhanced multiphoton ioniza-
tion time-of-flight mass spectrometer, Anal. Chem., 71, 46–57,
https://doi.org/10.1021/ac980611y, 1999.

Herring, C. L., Faiola, C. L., Massoli, P., Sueper, D., Erickson,
M. H., McDonald, J. D., Simpson, C. D., Yost, M. G., Jobson,
B. T., and VanReken, T. M.: New methodology for quantifying
polycyclic aromatic hydrocarbons (PAHs) using high-resolution
aerosol mass spectrometry, Aerosol Sci. Tech., 49, 1131–1148,
https://doi.org/10.1080/02786826.2015.1101050, 2015.

Hoffer, A., Gelencsér, A., Guyon, P., Kiss, G., Schmid, O., Frank, G.
P., Artaxo, P., and Andreae, M. O.: Optical properties of humic-
like substances (HULIS) in biomass-burning aerosols, Atmos.
Chem. Phys., 6, 3563–3570, https://doi.org/10.5194/acp-6-3563-
2006, 2006.

Hoffer, A., Tóth, A., Nyiro-Kósa, I., Pósfai, M., and Gelenc-
sér, A.: Light absorption properties of laboratory-generated
tar ball particles, Atmos. Chem. Phys., 16, 239–246,
https://doi.org/10.5194/acp-16-239-2016, 2016.

Huang, K., Zhuang, G., Lin, Y., Fu, J. S., Wang, Q., Liu, T.,
Zhang, R., Jiang, Y., Deng, C., Fu, Q., Hsu, N. C., and Cao,
B.: Typical types and formation mechanisms of haze in an East-
ern Asia megacity, Shanghai, Atmos. Chem. Phys., 12, 105–124,
https://doi.org/10.5194/acp-12-105-2012, 2012.

Huang, R. J., Yang, L., Cao, J. J., Chen, Y., Chen, Q., Li, Y.,
Duan, J., Zhu, C., Dai, W., and Wang, K.: Brown carbon aerosol
in Urban Xi'an, Northwest China: the composition and light
absorption properties, Environ. Sci. Technol., 52, 6825–6833,
https://doi.org/10.1021/acs.est.8b02386, 2018.

IPCC: Climate Change 2013: the physical science basis. Contribu-
tion of working group I to the fifth assessment report of the in-
tergovernmental panel on climate change, Cambridge, and New
York, NY, Cambridge University Press, 2013.

Jacobson, M. Z.: Analysis of aerosol interactions with numer-
ical techniques for solving coagulation, nucleation, conden-
sation, dissolution, and reversible chemistry among multi-
ple size distributions, J. Geophys. Res.-Atmos., 107, 4366,
https://doi.org/10.1029/2001JD002044, 2002.

Jacobson, M. Z.: Investigating cloud absorption effects: Global
absorption properties of black carbon, tar balls, and soil
dust in clouds and aerosols, J. Geophys. Res.-Atmos., 117,
https://doi.org/10.1029/2011JD017218, 2012.

Jacobson, M. Z.: Effects of biomass burning on climate, account-
ing for heat and moisture fluxes, black and brown carbon, and
cloud absorption effects, J. Geophys. Res.-Atmos., 119, 8980–
9002, doi.org/10.1002/2014JD021861, 2014.

Jimenez, J., Canagaratna, M., Donahue, N., Prevot, A., Zhang, Q.,
Kroll, J. H., DeCarlo, P. F., Allan, J. D., Coe, H., and Ng, N.:
Evolution of organic aerosols in the atmosphere, Science, 326,
1525–1529, https://doi.org/10.1126/science.1180353, 2009.

Jo, D. S., Park, R. J., Lee, S., Kim, S.-W., and Zhang, X.: A global
simulation of brown carbon: implications for photochemistry
and direct radiative effect, Atmos. Chem. Phys., 16, 3413–3432,
https://doi.org/10.5194/acp-16-3413-2016, 2016.

Kanakidou, M., Seinfeld, J. H., Pandis, S. N., Barnes, I., Dentener,
F. J., Facchini, M. C., Van Dingenen, R., Ervens, B., Nenes, A.,
Nielsen, C. J., Swietlicki, E., Putaud, J. P., Balkanski, Y., Fuzzi,
S., Horth, J., Moortgat, G. K., Winterhalter, R., Myhre, C. E.
L., Tsigaridis, K., Vignati, E., Stephanou, E. G., and Wilson, J.:
Organic aerosol and global climate modelling: a review, Atmos.

Chem. Phys., 5, 1053–1123, https://doi.org/10.5194/acp-5-1053-
2005, 2005.

Kang, E., Root, M. J., Toohey, D. W., and Brune, W. H.: Introduc-
ing the concept of Potential Aerosol Mass (PAM), Atmos. Chem.
Phys., 7, 5727–5744, https://doi.org/10.5194/acp-7-5727-2007,
2007.

Kim, H., Liu, S., Russell, L. M., and Paulson, S. E.: Dependence
of real refractive indices on O : C, H : C and mass fragments of
secondary organic aerosol generated from ozonolysis and pho-
tooxidation of limonene and α-pinene, Aerosol Sci. Tech., 48,
498–507, https://doi.org/10.1080/02786826.2014.893278, 2014.

Kroll, J. H., Donahue, N. M., Jimenez, J. L., Kessler, S. H., Cana-
garatna, M. R., Wilson, K. R., Altieri, K. E., Mazzoleni, L. R.,
Wozniak, A. S., and Bluhm, H.: Carbon oxidation state as a met-
ric for describing the chemistry of atmospheric organic aerosol,
Nat. Chem., 3, 133, https://doi.org/10.1038/NCHEM.948, 2011.

Lack, D. A., Langridge, J. M., Bahreini, R., Cappa, C. D., Mid-
dlebrook, A. M., and Schwarz, J. P.: Brown carbon and internal
mixing in biomass burning particles, Proc. Natl. Acad. Sci. USA,
109, 14802–14807, https://doi.org/10.1073/pnas.1206575109,
2012.

Lambe, A. T., Onasch, T. B., Massoli, P., Croasdale, D. R., Wright,
J. P., Ahern, A. T., Williams, L. R., Worsnop, D. R., Brune,
W. H., and Davidovits, P.: Laboratory studies of the chemi-
cal composition and cloud condensation nuclei (CCN) activity
of secondary organic aerosol (SOA) and oxidized primary or-
ganic aerosol (OPOA), Atmos. Chem. Phys., 11, 8913–8928,
https://doi.org/10.5194/acp-11-8913-2011, 2011.

Lambe, A., Massoli, P., Zhang, X., Canagaratna, M., Nowak, J.,
Daube, C., Yan, C., Nie, W., Onasch, T., Jayne, J., Kolb, C.,
Davidovits, P., Worsnop, D., and Brune, W.: Controlled nitric
oxide production via O(^{1}D) + N$_2$O reactions for use in oxida-
tion flow reactor studies, Atmos. Meas. Tech., 10, 2283–2298,
https://doi.org/10.5194/amt-10-2283-2017, 2017.

Laskin, A., Smith, J. S., and Laskin, J.: Molecular characterization
of nitrogen-containing organic compounds in biomass burning
aerosols using high-resolution mass spectrometry, Environ. Sci.
Technol., 43, 3764–3771, https://doi.org/10.1021/es803456n,
2009.

Laskin, A., Laskin, J., and Nizkorodov, S. A.: Chemistry of
atmospheric brown carbon, Chem. Rev., 115, 4335–4382,
https://doi.org/10.1021/cr5006167, 2015.

Lee, H. J., Aiona, P. K., Laskin, A., Laskin, J., and Nizko-
rodov, S. A.: Effect of solar radiation on the optical proper-
ties and molecular composition of laboratory proxies of atmo-
spheric brown carbon, Environ. Sci. Technol., 48, 10217–10226,
https://doi.org/10.1021/es502515r, 2014.

Levinson, R., Akbari, H., and Berdahl, P.: Measuring so-
lar reflectance-Part I: Defining a metric that accurately
predicts solar heat gain, Sol. Energy, 84, 1717–1744,
https://doi.org/10.1016/j.solener.2010.04.018, 2010.

Li, C., Ma, Z., Chen, J., Wang, X., Ye, X., Wang, L., Yang, X.,
Kan, H., Donaldson, D., and Mellouki, A.: Evolution of biomass
burning smoke particles in the dark, Atmos. Environ., 120, 244–
252, https://doi.org/10.1016/j.atmosenv.2015.09.003, 2015.

Li, C., Hu, Y., Zhang, F., Chen, J., Ma, Z., Ye, X., Yang, X.,
Wang, L., Tang, X., Zhang, R., Mu, M., Wang, G., Kan, H.,
Wang, X., and Mellouki, A.: Multi-pollutant emissions from the
burning of major agricultural residues in China and the related

health-economic effects, Atmos. Chem. Phys., 17, 4957–4988, https://doi.org/10.5194/acp-17-4957-2017, 2017.

Li, Y. J., Yeung, J. W., Leung, T. P., Lau, A. P., and Chan, C. K.: Characterization of organic particles from incense burning using an aerodyne high-resolution time-of-flight aerosol mass spectrometer, Aerosol Sci. Tech., 46, 654–665, https://doi.org/10.1080/02786826.2011.653017, 2012.

Li, Y. J., Huang, D. D., Cheung, H. Y., Lee, A. K. Y., and Chan, C. K.: Aqueous-phase photochemical oxidation and direct photolysis of vanillin – a model compound of methoxy phenols from biomass burning, Atmos. Chem. Phys., 14, 2871–2885, https://doi.org/10.5194/acp-14-2871-2014, 2014.

Lin, P., Liu, J., Shilling, J. E., Kathmann, S. M., Laskin, J., and Laskin, A.: Molecular characterization of brown carbon (BrC) chromophores in secondary organic aerosol generated from photo-oxidation of toluene, Phys. Chem. Chem. Phys., 17, 23312–23325, https://doi.org/10.1039/C5CP02563J, 2015.

Lin, P., Aiona, P. K., Li, Y., Shiraiwa, M., Laskin, J., Nizkorodov, S. A., and Laskin, A.: Molecular characterization of brown carbon in biomass burning aerosol particles, Environ. Sci. Technol., 50, 11815–11824, https://doi.org/10.1021/acs.est.6b03024, 2016.

Lin, P., Bluvshtein, N., Rudich, Y., Nizkorodov, S. A., Laskin, J., and Laskin, A.: Molecular Chemistry of Atmospheric Brown Carbon Inferred from a Nationwide Biomass Burning Event, Environ. Sci. Technol., 51, 11561–11570, https://doi.org/10.1021/acs.est.7b02276, 2017.

Lin, P., Fleming, L. T., Nizkorodov, S. A., Laskin, J., and Laskin, A.: Comprehensive Molecular Characterization of Atmospheric Brown Carbon by High Resolution Mass Spectrometry with Electrospray and Atmospheric Pressure Photoionization, Anal. Chem., 90, 12493–12502, https://doi.org/10.1021/acs.analchem.8b02177, 2018.

Liu, J., Bergin, M., Guo, H., King, L., Kotra, N., Edgerton, E., and Weber, R. J.: Size-resolved measurements of brown carbon in water and methanol extracts and estimates of their contribution to ambient fine-particle light absorption, Atmos. Chem. Phys., 13, 12389–12404, https://doi.org/10.5194/acp-13-12389-2013, 2013.

Liu, J., Lin, P., Laskin, A., Laskin, J., Kathmann, S. M., Wise, M., Caylor, R., Imholt, F., Selimovic, V., and Shilling, J. E.: Optical properties and aging of light-absorbing secondary organic aerosol, Atmos. Chem. Phys., 16, 12815–12827, https://doi.org/10.5194/acp-16-12815-2016, 2016.

Lu, J. W., Flores, J. M., Lavi, A., Abo-Riziq, A., and Rudich, Y.: Changes in the optical properties of benzo[a]pyrene-coated aerosols upon heterogeneous reactions with NO$_2$ and NO$_3$, Phys. Chem. Chem. Phys., 13, 6484–6492, https://doi.org/10.1039/C0CP02114H, 2011.

McDonald, J. D., Zielinska, B., Fujita, E. M., Sagebiel, J. C., Chow, J. C., and Watson, J. G.: Fine particle and gaseous emission rates from residential wood combustion, Environ. Sci. Technol., 34, 2080–2091, https://doi.org/10.1021/es9909632, 2000.

Miljevic, B., Hedayat, F., Stevanovic, S., Fairfull-Smith, K. E., Bottle, S., and Ristovski, Z.: To sonicate or not to sonicate PM filters: reactive oxygen species generation upon ultrasonic irradiation, Aerosol Sci. Tech., 48, 1276–1284, https://doi.org/10.1080/02786826.2014.981330, 2014.

Moise, T., Flores, J. M., and Rudich, Y.: Optical properties of secondary organic aerosols and their changes by chemical processes, Chem. Rev., 115, 4400–4439, https://doi.org/10.1021/cr5005259, 2015.

Mutzel, A., Rodigast, M., Iinuma, Y., Böge, O., and Herrmann, H.: An improved method for the quantification of SOA bound peroxides, Atmos. Environ., 67, 365–369, https://doi.org/10.1016/j.atmosenv.2012.11.012, 2013.

Ng, N. L., Chhabra, P. S., Chan, A. W. H., Surratt, J. D., Kroll, J. H., Kwan, A. J., McCabe, D. C., Wennberg, P. O., Sorooshian, A., Murphy, S. M., Dalleska, N. F., Flagan, R. C., and Seinfeld, J. H.: Effect of NOx level on secondary organic aerosol (SOA) formation from the photooxidation of terpenes, Atmos. Chem. Phys., 7, 5159–5174, https://doi.org/10.5194/acp-7-5159-2007, 2007.

Ng, N. L., Canagaratna, M. R., Zhang, Q., Jimenez, J. L., Tian, J., Ulbrich, I. M., Kroll, J. H., Docherty, K. S., Chhabra, P. S., Bahreini, R., Murphy, S. M., Seinfeld, J. H., Hildebrandt, L., Donahue, N. M., DeCarlo, P. F., Lanz, V. A., Prévôt, A. S. H., Dinar, E., Rudich, Y., and Worsnop, D. R.: Organic aerosol components observed in Northern Hemispheric datasets from Aerosol Mass Spectrometry, Atmos. Chem. Phys., 10, 4625–4641, https://doi.org/10.5194/acp-10-4625-2010, 2010.

Ng, N. L., Canagaratna, M. R., Jimenez, J. L., Chhabra, P. S., Seinfeld, J. H., and Worsnop, D. R.: Changes in organic aerosol composition with aging inferred from aerosol mass spectra, Atmos. Chem. Phys., 11, 6465–6474, https://doi.org/10.5194/acp-11-6465-2011, 2011.

Park, R. J., Kim, M. J., Jeong, J. I., Youn, D., and Kim, S.: A contribution of brown carbon aerosol to the aerosol light absorption and its radiative forcing in East Asia, Atmos. Environ., 44, 1414–1421, https://doi.org/10.1016/j.atmosenv.2010.01.042, 2010.

Passig, J., Schade, J., Oster, M., Fuchs, M., Ehlert, S., Jäger, C., Sklorz, M., and Zimmermann, R.: Aerosol mass spectrometer for simultaneous detection of polyaromatic hydrocarbons and inorganic components from individual particles, Anal. Chem., 89, 6341–6345, https://doi.org/10.1021/acs.analchem.7b01207, 2017.

Peng, Z. and Jimenez, J. L.: Modeling of the chemistry in oxidation flow reactors with high initial NO, Atmos. Chem. Phys., 17, 11991–12010, https://doi.org/10.5194/acp-17-11991-2017, 2017.

Peng, Z., Day, D. A., Stark, H., Li, R., Lee-Taylor, J., Palm, B. B., Brune, W. H., and Jimenez, J. L.: HO$_x$ radical chemistry in oxidation flow reactors with low-pressure mercury lamps systematically examined by modeling, Atmos. Meas. Tech., 8, 4863–4890, https://doi.org/10.5194/amt-8-4863-2015, 2015.

Peng, Z., Day, D. A., Ortega, A. M., Palm, B. B., Hu, W., Stark, H., Li, R., Tsigaridis, K., Brune, W. H., and Jimenez, J. L.: Non-OH chemistry in oxidation flow reactors for the study of atmospheric chemistry systematically examined by modeling, Atmos. Chem. Phys., 16, 4283–4305, https://doi.org/10.5194/acp-16-4283-2016, 2016.

Pettersson, A., Lovejoy, E. R., Brock, C. A., Brown, S. S., and Ravishankara, A.: Measurement of aerosol optical extinction at 532 nm with pulsed cavity ring down spectroscopy, J. Aerosol Sci., 35, 995–1011, https://doi.org/10.1016/j.jaerosci.2004.02.008, 2004.

Phillips, S. M. and Smith, G. D.: Light absorption by charge transfer complexes in brown carbon aerosols, Environ. Sci. Technol. Lett., 1, 382–386, https://doi.org/10.1021/ez500263j, 2014.

Pósfai, M., Gelencsér, A., Simonics, R., Arató, K., Li, J., Hobbs, P. V., and Buseck, P. R.: Atmospheric tar balls: Particles from biomass and biofuel burning, J. Geophys. Res.-Atmos., 109, D06213, https://doi.org/10.1029/2003JD004169, 2004.

Rajput, P. and Sarin, M.: Polar and non-polar organic aerosols from large-scale agricultural-waste burning emissions in Northern India: implications to organic mass-to-organic carbon ratio, Chemosphere, 103, 74–79, https://doi.org/10.1016/j.chemosphere.2013.11.028, 2014.

Reid, J. S., Eck, T. F., Christopher, S. A., Koppmann, R., Dubovik, O., Eleuterio, D. P., Holben, B. N., Reid, E. A., and Zhang, J.: A review of biomass burning emissions part III: intensive optical properties of biomass burning particles, Atmos. Chem. Phys., 5, 827–849, https://doi.org/10.5194/acp-5-827-2005, 2005.

Rettner, C. T. and Brophy, J. H.: Resonance enhanced laser ionisation mass spectrometry of four aromatic molecules, Chem. Phys., 56, 53–61, https://doi.org/10.1016/0301-0104(81)85099-9, 1981.

Rollins, A. W., Browne, E. C., Min, K. E., Pusede, S. E., Wooldridge, P. J., Gentner, D. R., Goldstein, A. H., Liu, S., Day, D. A., and Russell, L. M.: Evidence for NO_x control over nighttime SOA formation, Science, 337, 1210–1212, https://doi.org/10.1126/science.1221520, 2012.

Rudich, Y.: Data from: Dynamic changes of optical and chemical properties of tar ball aerosols by atmospheric photochemical aging [electronic resource], Weizmann Institute of Science, available at: https://weizmann.alma.exlibrisgroup.com/view/delivery/972WIS_INST/1245276980003596, last access: 25 December 2018.

Rudich, Y., Donahue, N. M., and Mentel, T. F.: Aging of organic aerosol: Bridging the gap between laboratory and field studies, Annu. Rev. Phys. Chem., 58, 321–352, https://doi.org/10.1146/annurev.physchem.58.032806.104432, 2007.

Russell, P. B., Bergstrom, R. W., Shinozuka, Y., Clarke, A. D., DeCarlo, P. F., Jimenez, J. L., Livingston, J. M., Redemann, J., Dubovik, O., and Strawa, A.: Absorption Angstrom Exponent in AERONET and related data as an indicator of aerosol composition, Atmos. Chem. Phys., 10, 1155–1169, https://doi.org/10.5194/acp-10-1155-2010, 2010.

Samburova, V., Connolly, J., Gyawali, M., Yatavelli, R. L., Watts, A. C., Chakrabarty, R. K., Zielinska, B., Moosmüller, H., and Khlystov, A.: Polycyclic aromatic hydrocarbons in biomass-burning emissions and their contribution to light absorption and aerosol toxicity, Sci. Total Environ., 568, 391–401, https://doi.org/10.1016/j.scitotenv.2016.06.026, 2016.

Schauer, J. J., Kleeman, M. J., Cass, G. R., and Simoneit, B. R.: Measurement of emissions from air pollution sources. 3. C1-C29 organic compounds from fireplace combustion of wood, Environ. Sci. Technol., 35, 1716–1728, https://doi.org/10.1021/es001331e, 2001.

Sedlacek III, A. J., Buseck, P. R., Adachi, K., Onasch, T. B., Springston, S. R., and Kleinman, L.: Formation and evolution of tar balls from northwestern US wildfires, Atmos. Chem. Phys., 18, 11289–11301, https://doi.org/10.5194/acp-18-11289-2018, 2018.

Seinfeld, J. H. and Pandis, S. N.: Atmospheric chemistry and physics: from air pollution to climate change, 3rd edition, John Wiley & Sons, Inc., Hoboken, New Jersey, USA, 2016.

Sengupta, D., Samburova, V., Bhattarai, C., Kirillova, E., Mazzoleni, L., Iaukea-Lum, M., Watts, A., Moosmüller, H., and Khlystov, A.: Light absorption by polar and non-polar aerosol compounds from laboratory biomass combustion, Atmos. Chem. Phys., 18, 10849–10867, https://doi.org/10.5194/acp-18-10849-2018, 2018.

Shamjad, P. M., Satish, R. V., Thamban, N. M., Rastogi, N., and Tripathi, S.: Absorbing refractive index and direct radiative forcing of atmospheric Brown Carbon over Gangetic Plain, ACS Earth Space Chem., 2, 31–37, https://doi.org/10.1021/acsearthspacechem.7b00074, 2018.

Shen, G., Tao, S., Wei, S., Zhang, Y., Wang, R., Wang, B., Li, W., Shen, H., Huang, Y., and Yang, Y.: Retene emission from residential solid fuels in China and evaluation of retene as a unique marker for soft wood combustion, Environ. Sci. Technol., 46, 4666–4672, https://doi.org/10.1021/es300144m, 2012.

Shen, H., Huang, Y., Wang, R., Zhu, D., Li, W., Shen, G., Wang, B., Zhang, Y., Chen, Y., and Lu, Y.: Global atmospheric emissions of polycyclic aromatic hydrocarbons from 1960 to 2008 and future predictions, Environ. Sci. Technol., 47, 6415–6424, https://doi.org/10.1021/es400857z, 2013.

Shrivastava, M., Cappa, C. D., Fan, J., Goldstein, A. H., Guenther, A. B., Jimenez, J. L., Kuang, C., Laskin, A., Martin, S. T., and Ng, N. L.: Recent advances in understanding secondary organic aerosol: Implications for global climate forcing, Rev. Geophys., 55, 509–559, https://doi.org/10.1002/2016RG000540, 2017.

Sigsgaard, T., Forsberg, B., Annesi-Maesano, I., Blomberg, A., Bølling, A., Boman, C., Bønløkke, J., Brauer, M., Bruce, N., and Héroux, M. E.: Health impacts of anthropogenic biomass burning in the developed world, Eur. Respir. J., 46, 1577–1588, https://doi.org/10.1183/13993003.01865-2014, 2015.

Sumlin, B. J., Pandey, A., Walker, M. J., Pattison, R. S., Williams, B. J., and Chakrabarty, R. K.: Atmospheric Photooxidation Diminishes Light Absorption by Primary Brown Carbon Aerosol from Biomass Burning, Environ. Sci. Technol. Lett., 4, 540–545, https://doi.org/10.1021/acs.estlett.7b00393, 2017.

Sumlin, B. J., Oxford, C. R., Seo, B., Pattison, R. R., Williams, B. J., and Chakrabarty, R. K.: Density and homogeneous internal composition of primary brown carbon aerosol, Environ. Sci. Technol., 52, 3982–3989, https://doi.org/10.1021/acs.est.8b00093, 2018.

Takahama, S., Johnson, A., Morales, J. G., Russell, L. M., Duran, R., Rodriguez, G., Zheng, J., Zhang, R., Toom-Sauntry, D., and Leaitch, W. R.: Submicron organic aerosol in Tijuana, Mexico, from local and Southern California sources during the CalMex campaign, Atmos. Environ., 70, 500–512, https://doi.org/10.1016/j.atmosenv.2012.07.057, 2013.

Tavakoli, F. and Olfert, J.: An instrument for the classification of aerosols by particle relaxation time: theoretical models of the aerodynamic aerosol classifier, Aerosol Sci. Tech., 47, 916–926, https://doi.org/10.1080/02786826.2013.802761, 2013.

Tavakoli, F. and Olfert, J. S.: Determination of particle mass, effective density, mass-mobility exponent, and dynamic shape factor using an aerodynamic aerosol classifier and a differential mobility analyzer in tandem, J. Aerosol Sci., 75, 35–42, https://doi.org/10.1016/j.jaerosci.2014.04.010, 2014.

Tóth, A., Hoffer, A., Nyiro-Kósa, I., Pósfai, M., and Gelencsér, A.: Atmospheric tar balls: aged primary droplets

from biomass burning?, Atmos. Chem. Phys., 14, 6669–6675, https://doi.org/10.5194/acp-14-6669-2014, 2014.

Washenfelder, R. A., Flores, J. M., Brock, C. A., Brown, S. S., and Rudich, Y.: Broadband measurements of aerosol extinction in the ultraviolet spectral region, Atmos. Meas. Tech., 6, 861–877, https://doi.org/10.5194/amt-6-861-2013, 2013.

Washenfelder, R., Attwood, A., Brock, C., Guo, H., Xu, L., Weber, R., Ng, N., Allen, H., Ayres, B., and Baumann, K.: Biomass burning dominates brown carbon absorption in the rural southeastern United States, Geophys. Res. Lett., 42, 653–664, https://doi.org/10.1002/2014GL062444, 2015.

Wei, C., Bandowe, B. A. M., Han, Y., Cao, J., Zhan, C., and Wilcke, W.: Polycyclic aromatic hydrocarbons (PAHs) and their derivatives (alkyl-PAHs, oxygenated-PAHs, nitrated-PAHs and azaarenes) in urban road dusts from Xi'an, Central China, Chemosphere, 134, 512–520, https://doi.org/10.1016/j.chemosphere.2014.11.052, 2015.

Weimer, S., Alfarra, M., Schreiber, D., Mohr, M., Prévôt, A., and Baltensperger, U.: Organic aerosol mass spectral signatures from wood-burning emissions: Influence of burning conditions and wood type, J. Geophys. Res.-Atmos., 113, D10304, https://doi.org/10.1029/2007JD009309, 2008.

Wong, J. P., Zhou, S., and Abbatt, J. P.: Changes in secondary organic aerosol composition and mass due to photolysis: relative humidity dependence, J. Phys. Chem. A, 119, 4309–4316, https://doi.org/10.1021/jp506898c, 2014.

Xie, M., Hays, M. D., and Holder, A. L.: Light-absorbing organic carbon from prescribed and laboratory biomass burning and gasoline vehicle emissions, Sci. Rep. UK, 7, 7318, https://doi.org/10.1038/s41598-017-06981-8, 2017.

Yee, L. D., Kautzman, K. E., Loza, C. L., Schilling, K. A., Coggon, M. M., Chhabra, P. S., Chan, M. N., Chan, A. W. H., Hersey, S. P., Crounse, J. D., Wennberg, P. O., Flagan, R. C., and Seinfeld, J. H.: Secondary organic aerosol formation from biomass burning intermediates: phenol and methoxyphenols, Atmos. Chem. Phys., 13, 8019–8043, https://doi.org/10.5194/acp-13-8019-2013, 2013.

Yu, L., Smith, J., Laskin, A., Anastasio, C., Laskin, J., and Zhang, Q.: Chemical characterization of SOA formed from aqueous-phase reactions of phenols with the triplet excited state of carbonyl and hydroxyl radical, Atmos. Chem. Phys., 14, 13801–13816, https://doi.org/10.5194/acp-14-13801-2014, 2014.

Zhang, H. and Ying, Q.: Secondary organic aerosol from polycyclic aromatic hydrocarbons in Southeast Texas, Atmos. Environ., 55, 279–287, https://doi.org/10.1016/j.atmosenv.2012.03.043, 2012.

Zhang, X. and Seinfeld, J. H.: A functional group oxidation model (FGOM) for SOA formation and aging, Atmos. Chem. Phys., 13, 5907–5926, https://doi.org/10.5194/acp-13-5907-2013, 2013.

Zhong, M. and Jang, M.: Dynamic light absorption of biomass-burning organic carbon photochemically aged under natural sunlight, Atmos. Chem. Phys., 14, 1517–1525, https://doi.org/10.5194/acp-14-1517-2014, 2014.

Zhou, S., Collier, S., Jaffe, D. A., Briggs, N. L., Hee, J., Sedlacek III, A. J., Kleinman, L., Onasch, T. B., and Zhang, Q.: Regional influence of wildfires on aerosol chemistry in the western US and insights into atmospheric aging of biomass burning organic aerosol, Atmos. Chem. Phys., 17, 2477–2493, https://doi.org/10.5194/acp-17-2477-2017, 2017.

Atmospheric
Chemistry
and Physics

Supplement of

Dynamic changes in optical and chemical properties of tar ball aerosols by atmospheric photochemical aging

Chunlin Li et al.

Correspondence to: Yinon Rudich (yinon.rudich@weizmann.ac.il)

Contents

1. Tar ball aerosol size distribution at downstream of the OFR

Tar ball particles were generated via TSI atomizer, and concentration of tar ball particles was mediated in the OFR before these aerosols being photochemically oxidized. Polar, nonpolar, and mixture tar ball particles present similar size distributions.
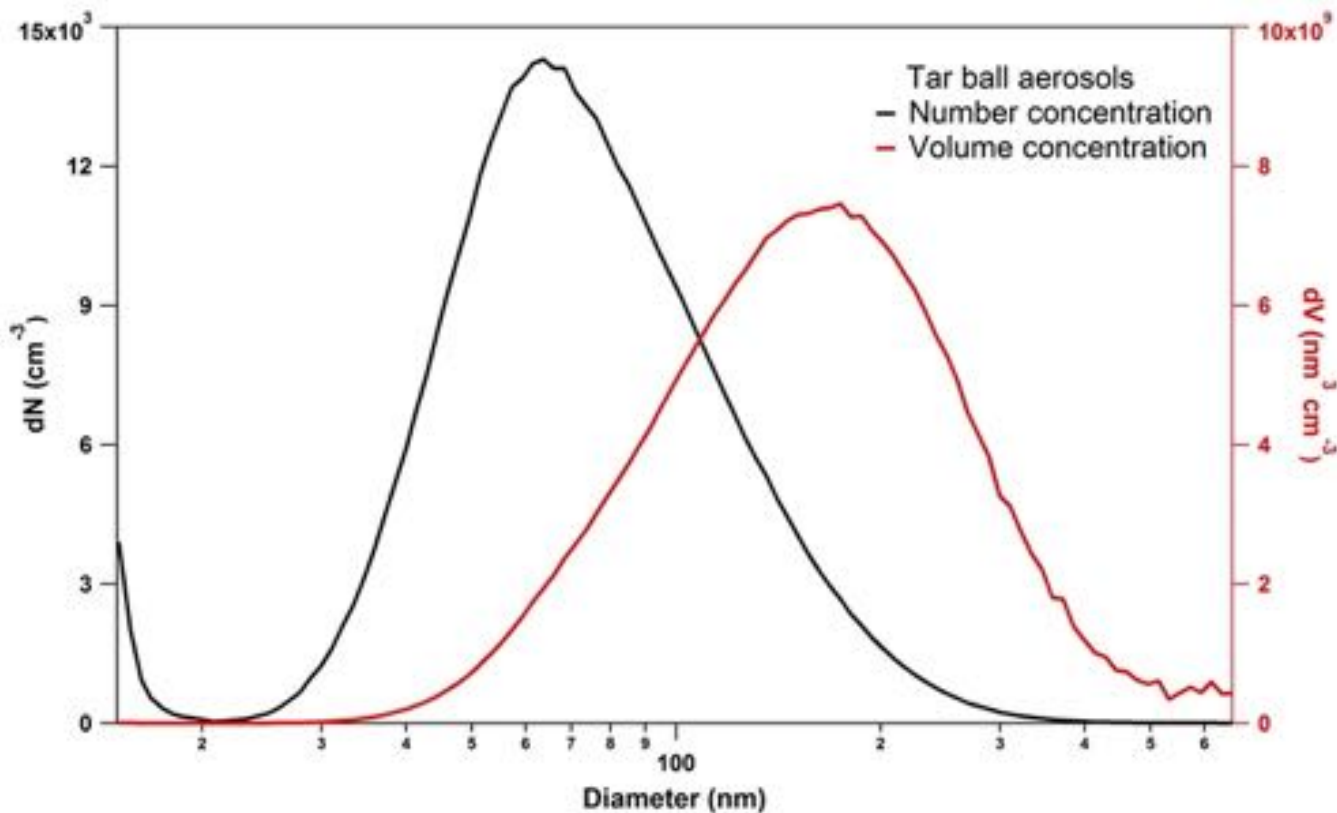
Figure S1. Size distribution of laboratory generated tar ball aerosols at downstream of the OFR. The distribution presents a norrow range with a single peak at ~70 nm diameter, similar to the size distribution of practical tar balls obtained from the wildfires and domestic biofuel burning (Pósfai et al., 2004; Chakrabarty et al., 2010).

2. OC-EC content of fresh polar and nonpolar tar ball aerosols

Non-refractory organic carbon (OC) and refractory elemental carbon (EC) in fresh tar ball aerosols were analyzed using a DRI Model 2015 multi-wavelength thermal/optical carbon analyzer (Desert Research Institute, Nevada, USA) with the IMPROVE_A protocol (Chow et al., 2011; Li et al., 2018). In details, fresh nonpolar and polar tar balls were collected onto pretreated quartz filters (Whatman, Mainstone, UK, baked over 450 °C for 6 hr to eliminate any contamination), a circular punch (0.8 cm in diameter) of each loaded filter including operational blank filter was taken and analyzed. Four OC fractions (OC1, OC2, OC3, and OC4 correspond to gradient cutting temperature at 140, 280, 480, and 580 °C, respectively, in a helium atmosphere), three EC fractions (EC1, EC2, EC3 with cutting temperature of 590, 780, and 840 °C, respectively, in a 2% oxygen/98% helium atmosphere), and one PC fraction (pyrolyzed carbon content determined when transmitted laser returned to its original intensity after the sample was exposed to oxygen) were determined for each sample, and OC=OC1+OC2+OC3+OC4+PC, EC=EC1+EC2+EC3-PC, total carbon (TC) equals the sum of OC and EC. The blank-corrected and normalized carbon fractions for fresh tar ball aerosols were given below:

Tar ball	OC1	OC2	OC3	OC4	PC	EC1	EC2	EC3	OC	EC
Polar	38.8%	32.2%	18.4%	0.0%	10.6%	10.6%	0.0%	0.0%	100.0%	0.0%
Nonpolar	28.7%	25.8%	16.0%	7.7%	21.1%	21.7%	0.0%	0.0%	99.3%	0.7%

It is clear EC content was almost below detection limit for both polar- and nonpolar-tar balls, the slight EC fraction in nonpolar tar ball is less than 0.7% of TC content and resides in EC1, which can be termed as non-refractory char-EC, empirically defined as EC1−PC. Char-EC is stripped from some OC under oxygen-free heating during OC/EC measurement, which has much weak absorption, and thus can be distinguished as brown carbon rather than black carbon (Andreae and Gelencsér, 2006; Arora et al., 2015; Kim et al., 2011; Han et al., 2008, 2009). Many other studies on biomass burning emissions from wildfires and domestic burning have also reported negligible EC content in tar ball aerosols (Chakrabarty et al., 2010; Tivanski et al., 2007; Hand et al., 2005; China et al., 2013).

## 3. Fresh tar ball composition from HR-Tof-AMS measurement
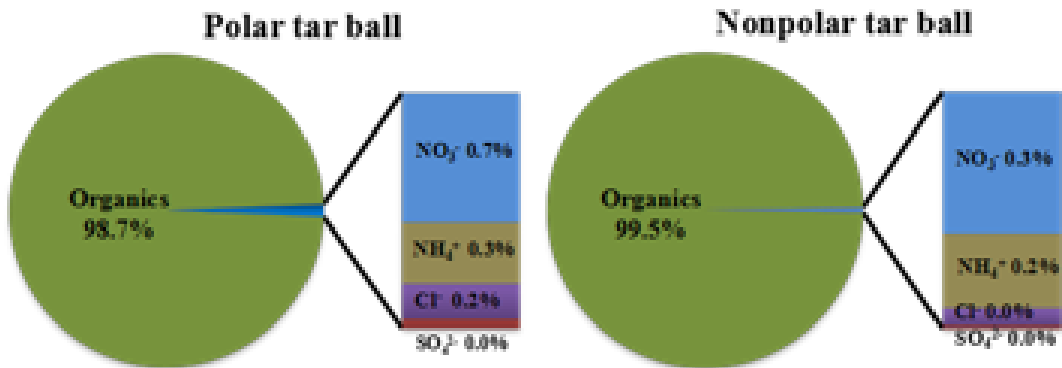
Figure S2. Fresh polar and nonpolar tar balls composition from HR-Tof-AMS measurement. Color mapping: organics-green, nitrates-blue, ammonium-yellow, chloride-purple, sulfates-red.

4. Organic elemental ratios for fresh tar ball aerosols were derived from AMS measurement at W mode, and effective densities of tar ball aerosols were calculated from aerodynamic diameter divided by mobility diameter assuming tar ball with sphericity of 1.0

Table S1. Summary of fresh tar ball particles chemical elemental ratios and effective densities

BBOA	Mass spectra			Density (g cm^{-3})	Reference
	O:C	H:C	M/z>100 fraction		
Nonpolar	0.25±0.01	1.55±0.01	0.32	1.24±0.01	
Mixture (2:1 in vol.)	0.30±0.01	1.59±0.02	0.29	1.27±0.02	
Mixture (1:1 in vol.)	0.36±0.01	1.62±0.04	0.27	1.29±0.02	this work
Mixture (1:2 in vol.)	0.39±0.01	1.61±0.03	0.24	1.30±0.01	
Polar	0.44±0.02	1.64±0.03	0.15	1.33±0.02	
BBOA	0.3~0.4				Aiken et al., 2008
BBOA	0.29~0.33	1.51~1.58			Li et al., 2012
BBOA	0.18~0.26	1.4~1.5			He et al., 2010
BBOA	0.15~0.7	1.5~1.6	0.11~0.20	1.4	Zhou et al., 2017
BBOA				1.5	Sedlacek III et al., 2018
BBOA	0.33	1.90		1.18~1.19	Sumlin et al., 2017; 2018

5. Aerodynamic size distribution for tar ball particles measured by SP-LD-REMPI-ToF-MS
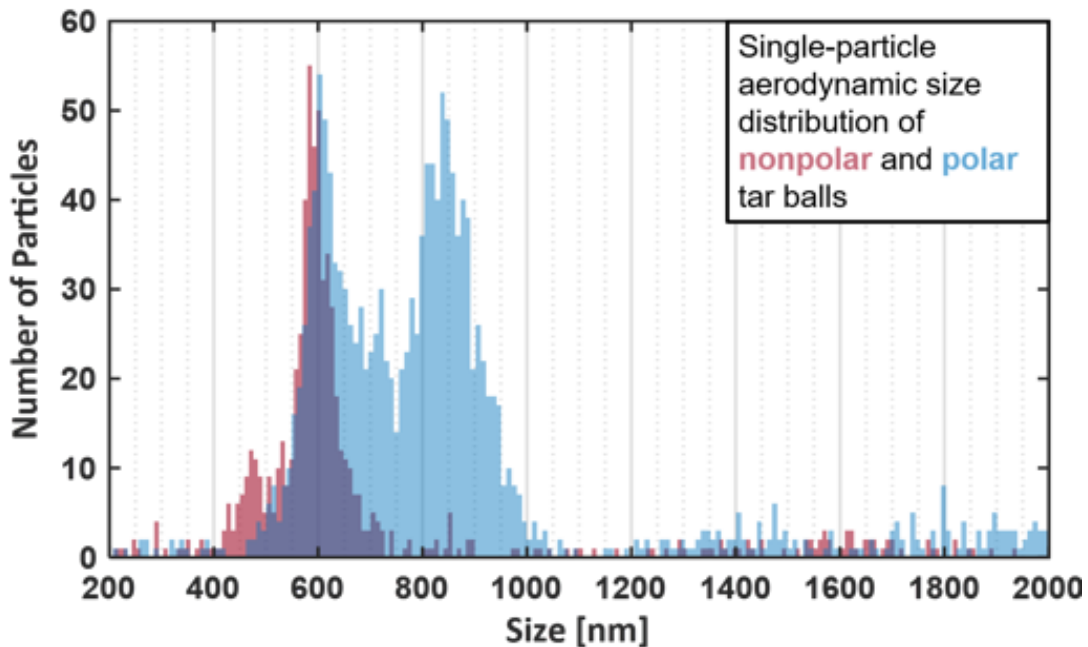
Figure S3. Particle aerodynamic size distributions for fresh nonpolar (red) and polar (blue) tar ball aerosols measured via laser velocimetry by the SP-LD-REMPI-ToF-MS instrument. The major mode peaks at about 550 nm for both particle classes while a second mode of larger particles occurs for polar tar balls and a second mode of smaller particles appears for nonpolar tar balls. Note that the detection efficiency drops rapidly below 250 nm due to the descending Mie scattering efficiency for particles much smaller than the wavelength (532 nm).

6. Exemplary Proper Polyaromatic Compounds indicated by the REMPI PAH Spectra in this study (Table S2)

Table S2.Exemplary proper (poly)aromatic compounds indicated by the REMPI PAH Spectra in Figure 3

m/z	Name	Formula	Polar tar ball	Nonpolar tar ball	BBOA Reference
110	Catechol	$C_6H_6O_2$	√		Veres et al., 2010; Yee et al., 2013
115	PAHs fragments		√	√	Adler et al., 2011; Bruns et al., 2015
124	Guaiacol	$C_7H_8O_2$	√		Li et al., 2017; Yee et al., 2013; Hoffmann et al., 2007
128	Naphthalene	$C_{10}H_8$	√	√	Samburova et al., 2016; Passig et al., 2017; Bruns et al., 2015
138	4-Methylguajacol	$C_8H_{10}O_2$	√	√	Adler et al., 2011; Yee et al., 2013
152	Vanillin 4-Ethylguajacol	$C_8H_8O_3$ $C_9H_{12}O_2$	√	√	Li et al., 2014; Passig et al., 2017;Yee et al., 2013; Hoffmann et al., 2007
158	Methoxynaphthalene 1,4-Naphthalenedione Methylnaphthol	$C_{11}H_{10}O$ $C_{10}H_6O_2$ $C_{11}H_{10}O$	√		Santos et al., 2016; Yee et al., 2013; Hoffmann et al., 2007
165	PAHs fragments		√	√	Adler et al., 2011; Bruns et al., 2015
168	4-Methylsyringol Vanillic acid	$C_9H_{12}O_3$ $C_8H_8O_4$	√		Santos et al., 2016; Hoffmann et al., 2007; Bruns et al., 2015
178	Phenanthrene Conifery aldehyde	$C_{14}H_{10}$ $C_{10}H_{10}O_3$	√	√	Samburova et al., 2016; Bente et al., 2008, 2009; Passig et al., 2017
182	Syringaldehyde 4-Ethylsyringol	$C_9H_{10}O_4$ $C_{10}H_{14}O_3$	√		Santos et al., 2016; Yee et al., 2013; Hoffmann et al., 2007
189, 190, 191	Retene fragments		√	√	Bente et al., 2008, 2009; Mandalakis et al., 2005
192	Methylphenanthrene	$C_{15}H_{12}$	√	√	Samburova et al., 2016; Bente et al., 2008, 2009; Passig et al., 2017
202	Pyrene Fluoranthene	$C_{16}H_{10}$	√	√	Adler et al., 2011; Bente et al., 2008, 2009; Passig et al., 2017
203, 204, 205	Retene fragments		√	√	Passig et al., 2017; Mandalakis et al., 2005
206	Ethylphenanthrene	$C_{16}H_{14}$		√	Samburova et al., 2016
219, 220	Retene fragments		√	√	Bente et al., 2008, 2009; Passig et al., 2017
234	Retene	$C_{18}H_{18}$	√	√	Samburova et al., 2016; Bente et al., 2008, 2009; Passig et al., 2017

248	Methyl. Retene	$C_{19}H_{20}$		√	Passig et al., 2017; Mandalakis et al., 2005
250	Ox. Retene	$C_{18}H_{18}O$	√	√	Samburova et al., 2016

Note: only some major and most proper aromatic compounds were listed in the table

7. Morphology of tar ball aerosols
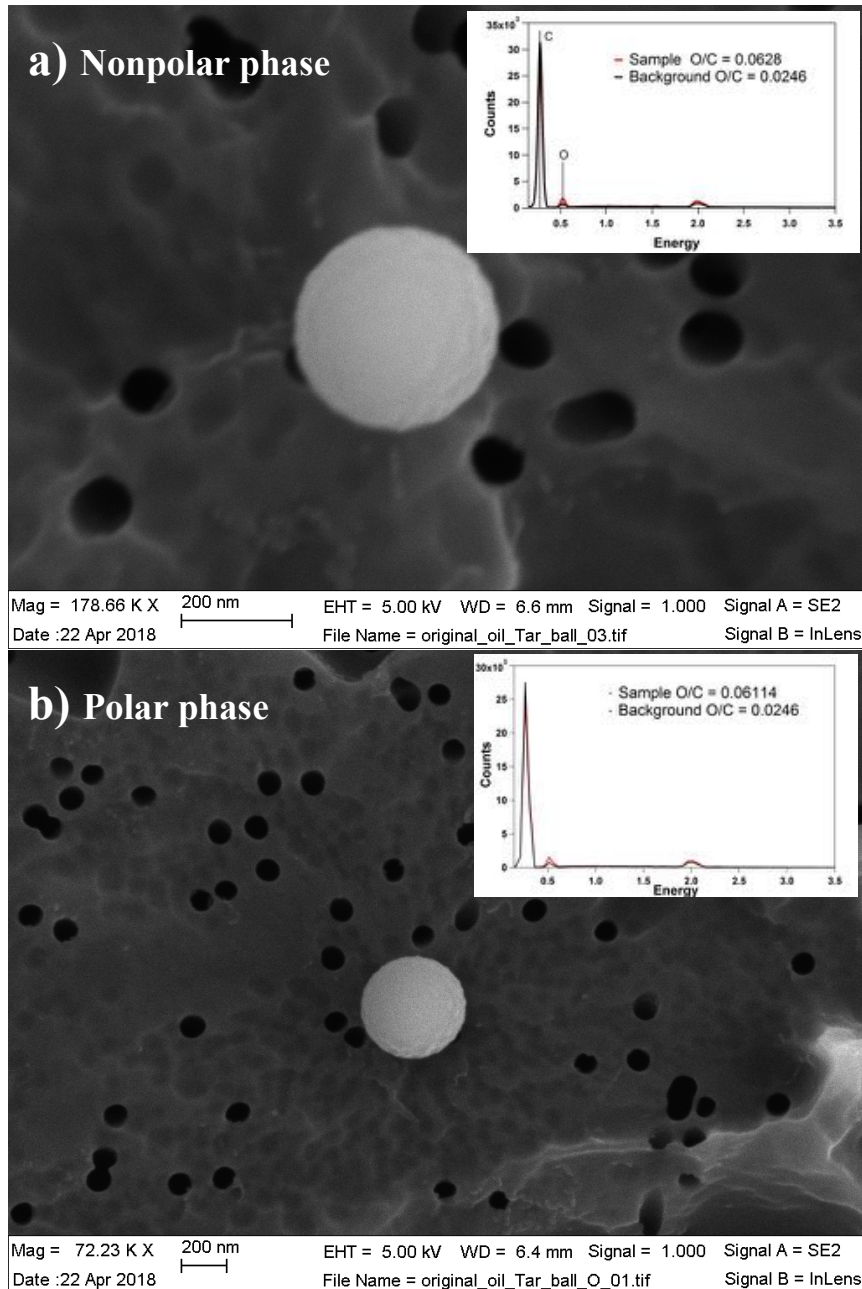
Figure S4. Morphology of fresh tar ball particles generated from polar and nonpolar phase tarry solutions. The particles are perfect spherical and amorphous in internal composition.

8. Refractive index for tar ball at mixture of 2:1 and 1:2 in volume of polar and nonpolar materials
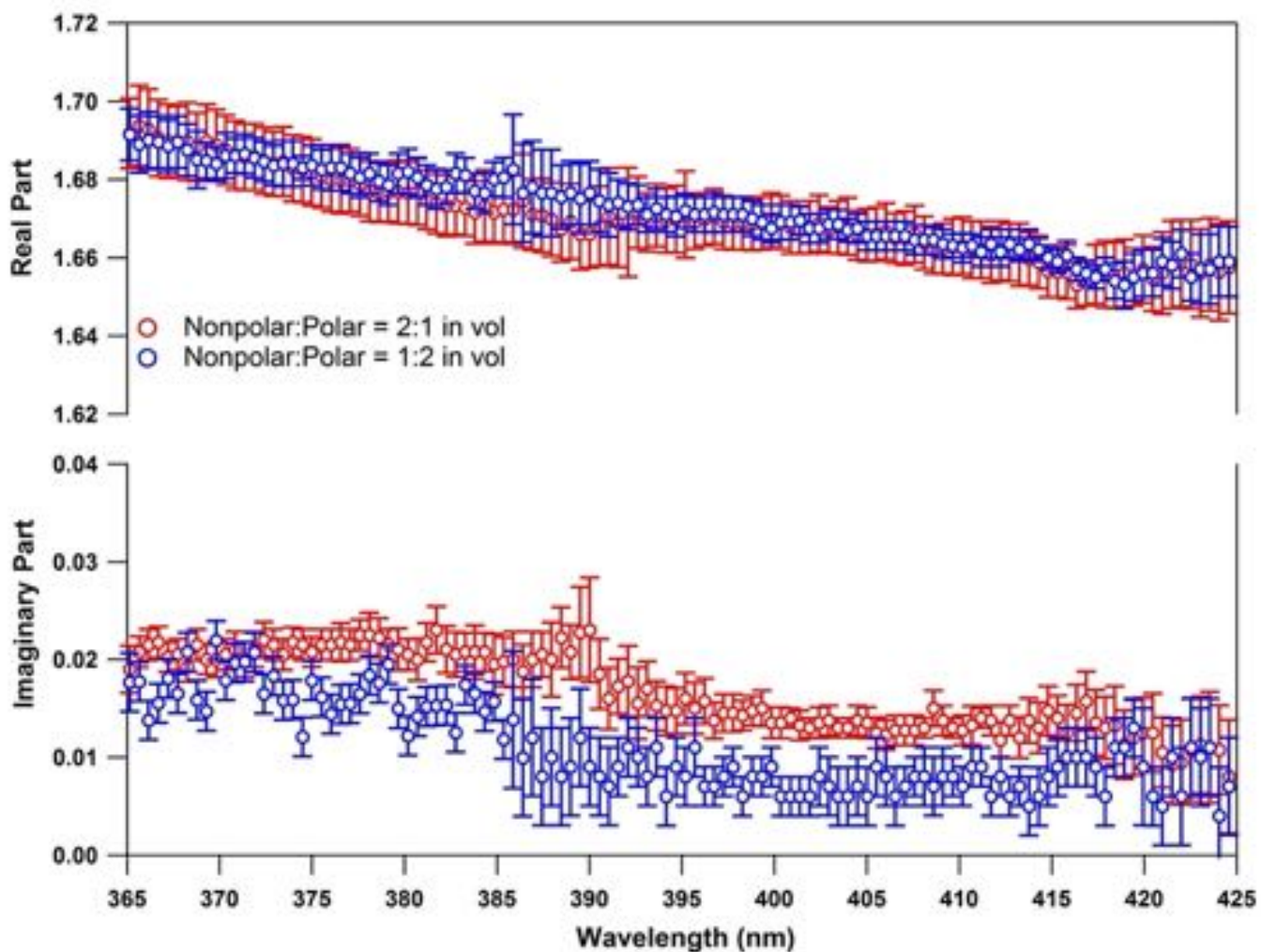
Figure S5. Wavelength-dependent refractive index (RI) for tar ball particles generated from polar and nonpolar phase solution mixtures

0

9. Example of absorption coefficients for some of the most absorbing PAHs identified in BBOA
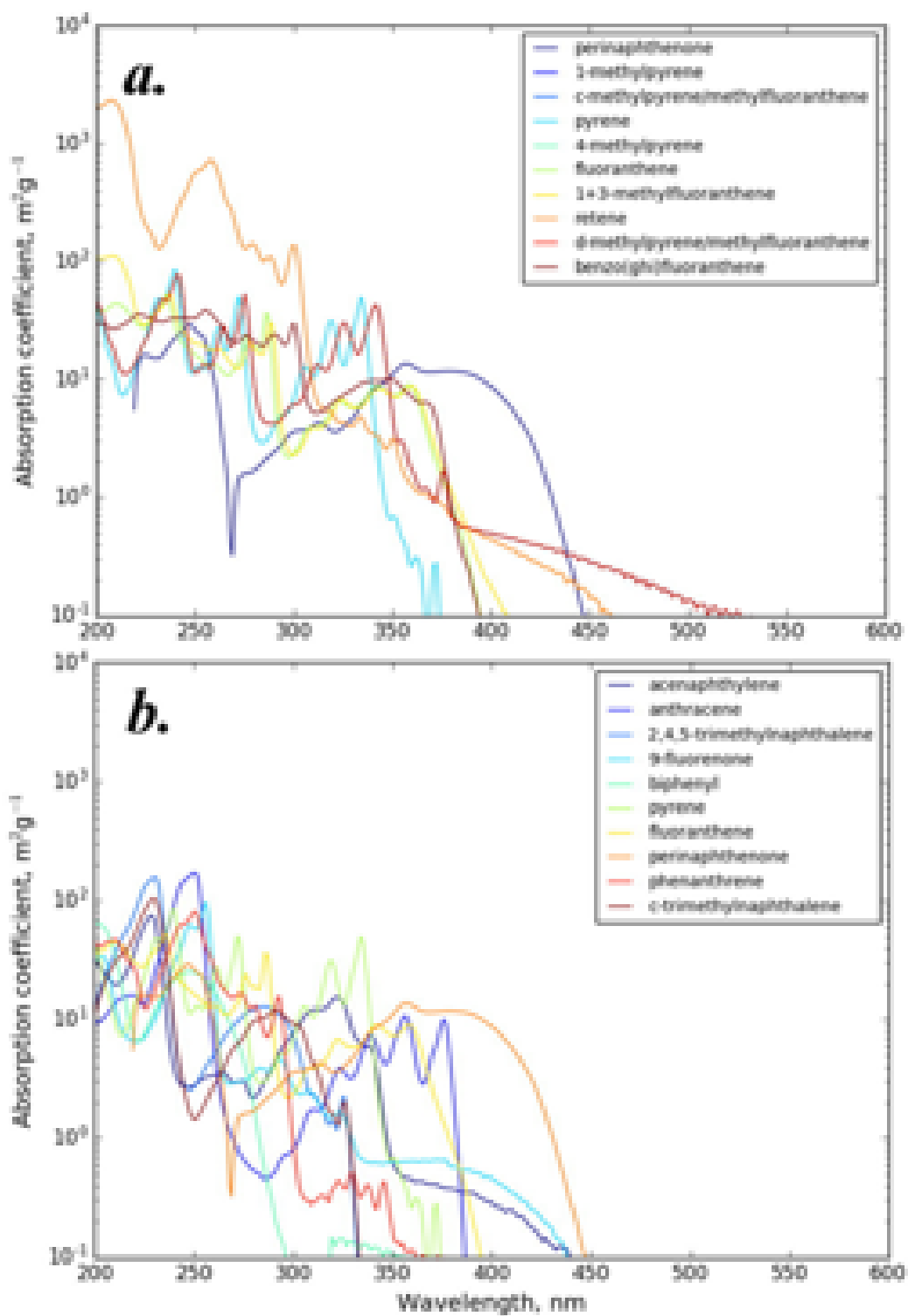
Figure S6. Absorption coefficients for some of the most absorbing PAHs identified in biomass burning emissions (Samburova et al., 2016).

5

10. Methanol extractable BrC mass absorption cross sections (MAC) for fresh tar ball aerosols from 360 to 450 nm
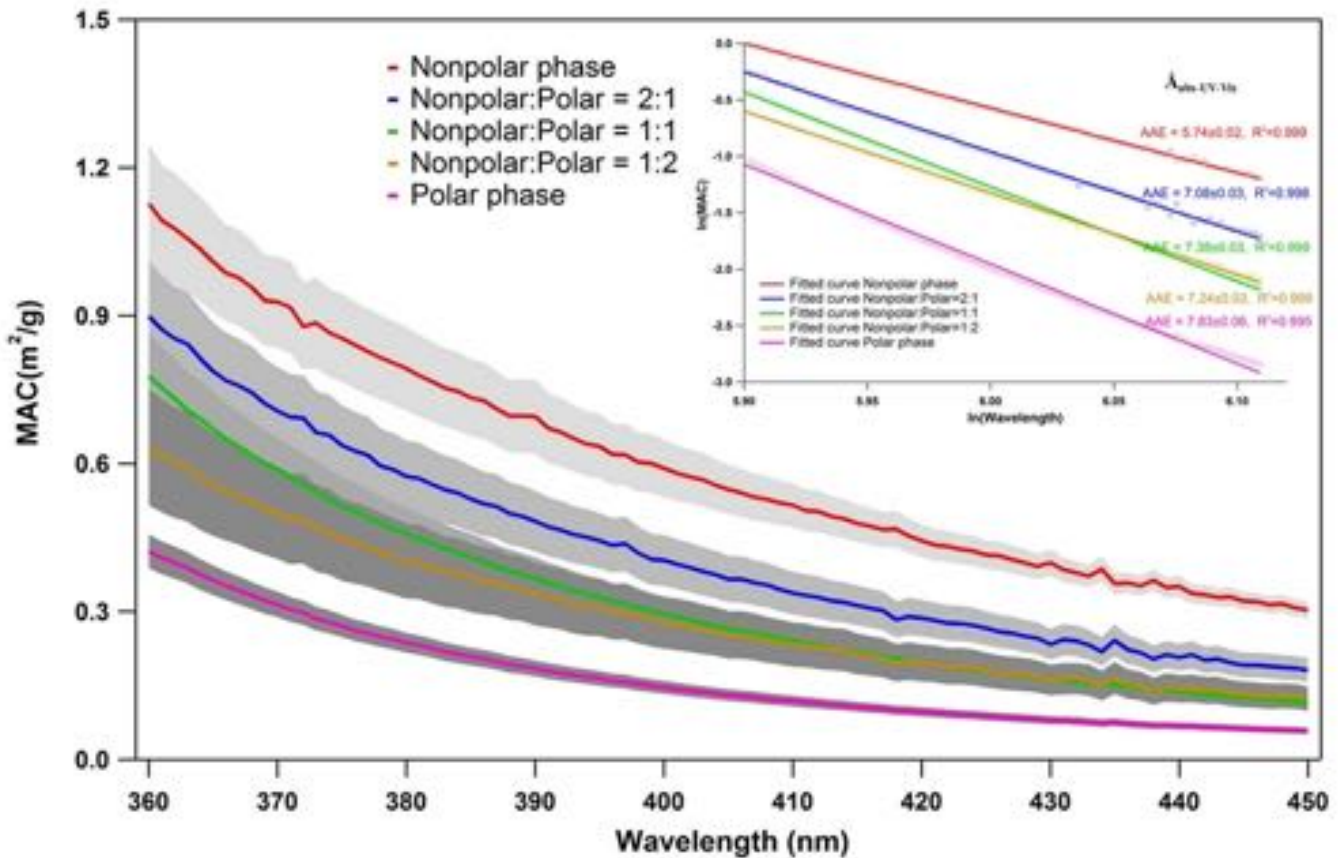
Figure S7. BrC mass absorption cross section (MAC) for methanol extracted fresh tar ball particles. Inset chart presents example of $Å_{abs\_UV\text{-}Vis}$ calculated from natural logarithm regression of MAC and wavelength.

11. Prediction of mixture tar ball optical properties based on different mixing rules

There are many mixing rules currently in use to predict optical properties of aerosol from matrix of various substances: 1) molar refraction and absorption (Jacobson, 2002; Tang, 1997); 2) a volume-weighted linear average of the refractive indices (d'Almeida et al., 1991); 3) the Maxwell-Garnet rule (Chýlek et al., 1984); and 4) the dynamic effective medium approximation (Jacobson, 2006). Due to the complexity of undefined chemical composition of tar ball particles, the Maxwell-Garnet and dynamic effective medium approximation are not feasible in this study, therefore, the simple molar fraction and volume-weighted mixing rules were discussed to fit the optical results.

The "linear mixing rule" simplifies mixing state and interaction between matrix, assumes that total real and imaginary refractive indices of the mixture are result of the indices of the components weighted by their their volume fractions:

$$n_{tot} = \sum_n f_i n_i$$
$$k_{tot} = \sum_n f_i k_i$$
[1]

Where f_i, n_i, and k_i are the volume fraction, real part, and imaginary part of each component

The molar fraction mixing rule assumes that the total molar refraction of a mixture is given by the linear average of the molar refraction of each component weighted by their molar volumes, i.e.,

$$\frac{\overline{M}}{\rho}\frac{n^2-1}{n^2+2} = \sum_n \chi_i \frac{M_i}{\rho_i}\frac{n_i^2-1}{n_i^2+2}$$
$$\frac{\overline{M}}{\rho}k = \sum_n \chi_i \frac{M_i}{\rho_i}k_i$$
$$\sum_n \chi_i = 1$$
[2]

Where x_i, M_i, and ρ_i are the molar fraction, molecular weight, and material density.

Refractive indices for tar ball generated from polar and nonpolar fraction mixture at solution mixing ratios of 1:2, 1:1, and 2:1 will be calculated from RI of polar and nonpolar optical results based on above two rules. The exact volume and molar fraction for bulk polar and nonpolar part in particles can be estimated from particle density and chemical elemental ratios:

$$\rho_{tot} = f_1\rho_1 + f_2\rho_2$$
$$f_1 + f_2 = 1$$
[3]

$$R_{\overline{O/C}} = \chi_1 R_{\overline{O/C_1}} + \chi_2 R_{\overline{O/C_2}}$$
$$\chi_1 + \chi_2 = 1$$
[4]

Where $R_{O/C}$ is oxygen to carbon ratio from AMS measurement of tar ball particles, and calculated particulate volume and molar fraction are given below:

Table S3. Particulate molar and volume fractions of bulk polar and nonpolar tar

Polar:Nonpolar prepared solution ratio	O/C molar ratio	O/C retrieved molar mixing ratio	Density (g cm^{-3})	density retrieved volume mixing ratio
1:0	0.44	1:0	1.329±0.021	1:0
2:1	0.39	2.8:1	1.298±0.022	1.8:1
1:1	0.36	1.4:1	1.285±0.019	0.98:1
1:2	0.3	1:2.8	1.274±0.013	1:1.72
0:1	0.25	0:1	1.242±0.005	0:1

Molecular weight for polar and nonpolar fractions were simplified as $M_{bulk-polar}$ and $M_{bulk-nonpolar}$, and mixture tar ball particles follow the function below:

$$\frac{\overline{M}}{\overline{\rho}} = \frac{x_1 M_{bulk-polar}}{\rho_1} + \frac{x_2 M_{bulk-nonpolar}}{\rho_2}$$

$$\overline{M} = x_1 M_{bulk-polar} + x_2 M_{bulk-nonpolar}$$

[5]

And it was calculated as $M_{bulk-nonpolar} \approx 1.3 M_{bulk-polar}$

For convenience and clarity, wavelength-dependent RI for tar ball were exponential or power-law fitted, the results were showed in Figure S8 and corresponded parameters were summarized in Table S4:
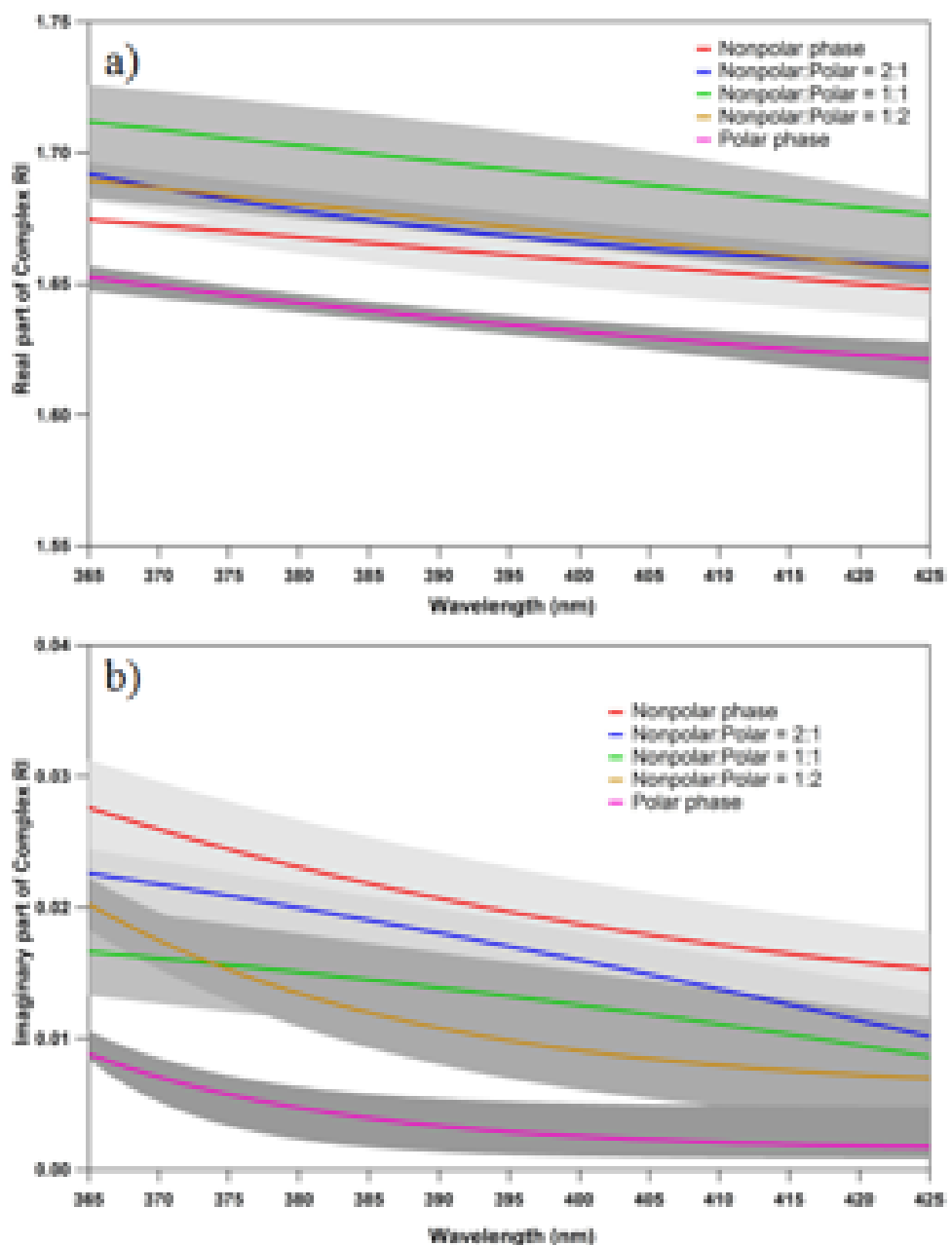
Figure S8. Regressed RI for tar ball particles of various mixing ratios: a) real part, and b) imaginary part

Table S4. Parameterization of the Wavelength-Dependent (365 to 425 nm) Effective Complex RI of tar ball particles

Tar ball		Real			Imaginary		
		Co	C1	C2	Co	C1	C2
Nonpolar phase	min	1.604	7.148	-1.27E-02	0.164	-8.89E-02	1.27E-03
	average	1.033	0.831	-7.08E-04	0.010	2.37E+01	-1.97E-02
	max	1.677	-1.95E-09	3.80E-02	0.010	8.75E+00	-1.65E-02
Nonpolar:polar 2:1	min	1.627	22.067	-1.65E-02	0.028	-1.05E-05	1.80E-02
	average	1.646	321.800	-2.43E-02	0.046	-1.81E-03	7.06E-03
	max	1.658	2819.637	-3.04E-02	0.330	-2.47E-01	5.86E-04
Nonpolar:polar 1:1	min	1.657	55.140	-1.98E-02	-0.291	3.52E-01	-4.01E-04
	average	1.324	0.697	-1.61E-03	0.023	-5.69E-16	5.10E+00
	max	1.754	-5.09E-18	6.145	-0.220	3.00E-01	-6.09E-04
Nonpolar:polar 1:2	min	1.832	-0.044	3.35E-03	0.002	6.88E+04	-4.19E-02
	average	1.306	0.683	-1.58E-03	0.006	8.43E+04	-4.27E-02
	max	1.550	0.826	-4.75E-03	0.009	1.56E+40	-1.64E+01
Polar phase	min	1.921	-0.133	1.97E-03	0.016	-5.83E-19	6.33E+00
	average	1.585	3.174	-1.06E-02	0.001	3.02E+06	-5.43E-02
	max	1.615	53.051	-1.95E-02	0.005	5.43E+11	-8.81E-02

Note: Non-shaded cells were fitted with an exponent; $n\&k(\lambda)=C_0+C_1\times e^{(C_2\times\lambda)}$. Shaded cells were fitted with a power law; $n\&k(\lambda)=C_0+ C_1^{\lambda\times C_2}$

The calculated RI following "volume linear mixing rules" for tar ball were presented in Figure S9 and compared with experimental data in Figure S10.
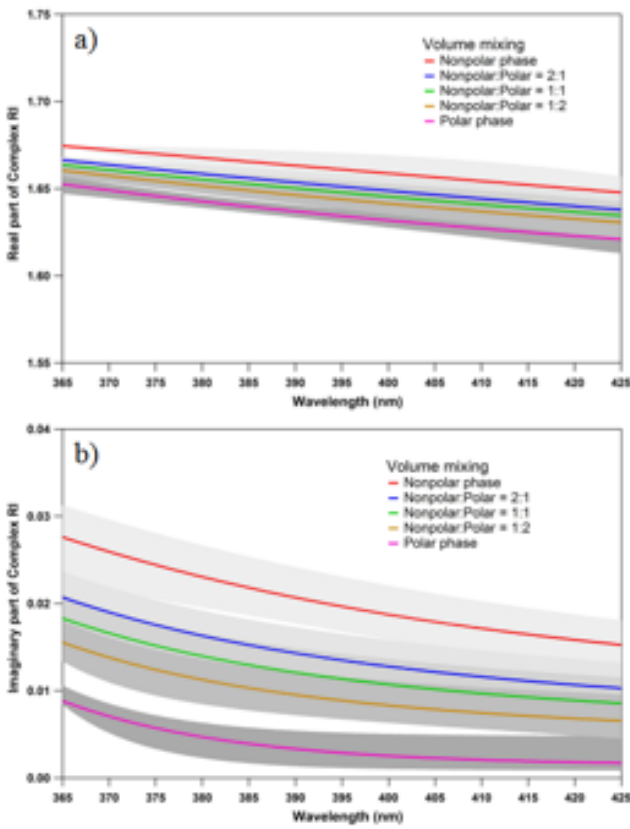
Figure S9. Estimated RI for tar ball particles of various mixing ratios based on volume linear mixing rule: a) real part, and b) imaginary part
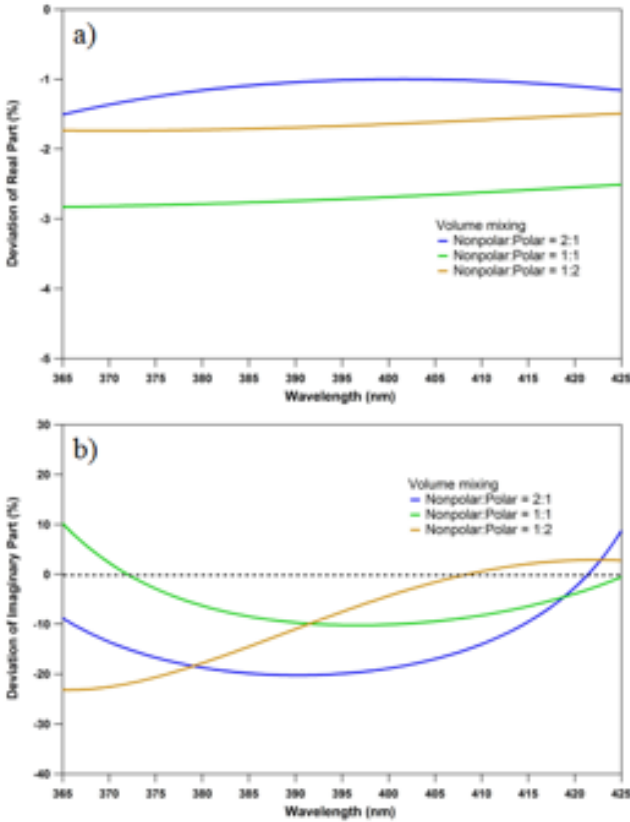

Figure S10. Deviation between experimental RI and predicted RI from volume linear mixing rule: a) real part, and b) imaginary part

1

The calculated RI following "molar fraction mixing rules" for tar ball were presented in Figure S11 and compared with experimental data in Figure S12.
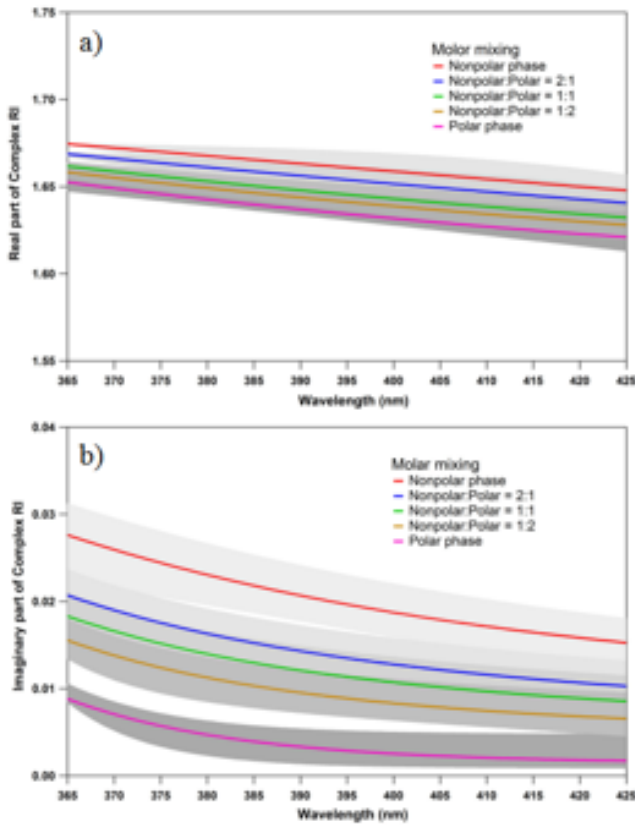

Figure S11. Estimated RI for tar ball particles of various mixing ratios based on molar fraction mixing rule: a) real part, and b) imaginary part
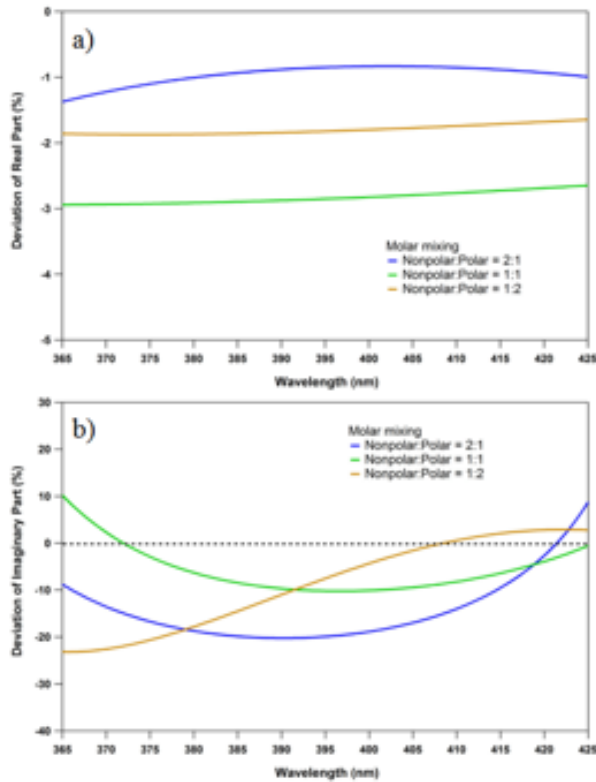
Figure S12. Deviation between experimental RI and predicted RI from molar fraction mixing rule: a) real part, and b) imaginary part

12. Summary of optical parameters for tar ball aerosol upon NOx-dependent photochemical aging

Table S5. Summary of RI and Ångström exponent changes for tar ball particles upon photochemical oxidation (mean ± standard deviation)

Tar ball	Complex Refractive index			SSA (average)	Å$_{abs}$	Å$_{abs\_UVVIS}$	Å$_{ext}$
	Average	375nm	405nm				
Fresh	(1.661±0.008)+(0.020±0.004)i	(1.671±0.003)+(0.025±0.003)i	(1.659±0.011)+(0.017±0.002)i	0.89 ± 0.01	5.87 ± 0.37	6.74	3.81 ± 0.18
O_0.7	(1.641±0.010)+(0.014±0.006)i	(1.652±0.001)+(0.021±0.001)i	(1.635±0.001)+(0.010±0.002)i	0.92 ± 0.02	9.33 ± 3.38	6.11	4.21 ± 0.07
O_1.7	(1.639±0.011)+(0.008±0.005)i	(1.651±0.002)+(0.015±0.004)i	(1.631±0.002)+(0.005±0.003)i	0.96 ± 0.03	10.96 ± 3.23	6.46	4.33 ± 0.04
O_3.9	(1.632±0.010)+(0.007±0.004)i	(1.643±0.001)+(0.011±0.002)i	(1.628±0.002)+(0.004±0.001)i	0.96 ± 0.02	10.63 ± 3.17	6.31	4.11 ± 0.09
O_6.7	(1.624±0.007)+(0.007±0.003)i	(1.630±0.003)+(0.009±0.003)i	(1.623±0.002)+(0.004±0.003)i	0.96 ± 0.02	9.89 ± 2.59	6.02	3.74 ± 0.06
N_0.5	(1.635±0.011)+(0.015±0.004)i	(1.646±0.001)+(0.018±0.001)i	(1.629±0.001)+(0.012±0.002)i	0.91 ± 0.01	6.92 ± 1.35	6.41	4.01 ± 0.07
N_2.0	(1.648±0.008)+(0.019±0.004)i	(1.653±0.002)+(0.025±0.003)i	(1.645±0.002)+(0.016±0.001)i	0.89 ± 0.01	5.60 ± 0.69	6.35	3.76 ± 0.10

13. Methanol extractable BrC mass absorption cross sections (MAC) for NOx-free photochemical aged tar ball aerosols from 360 to 450 nm
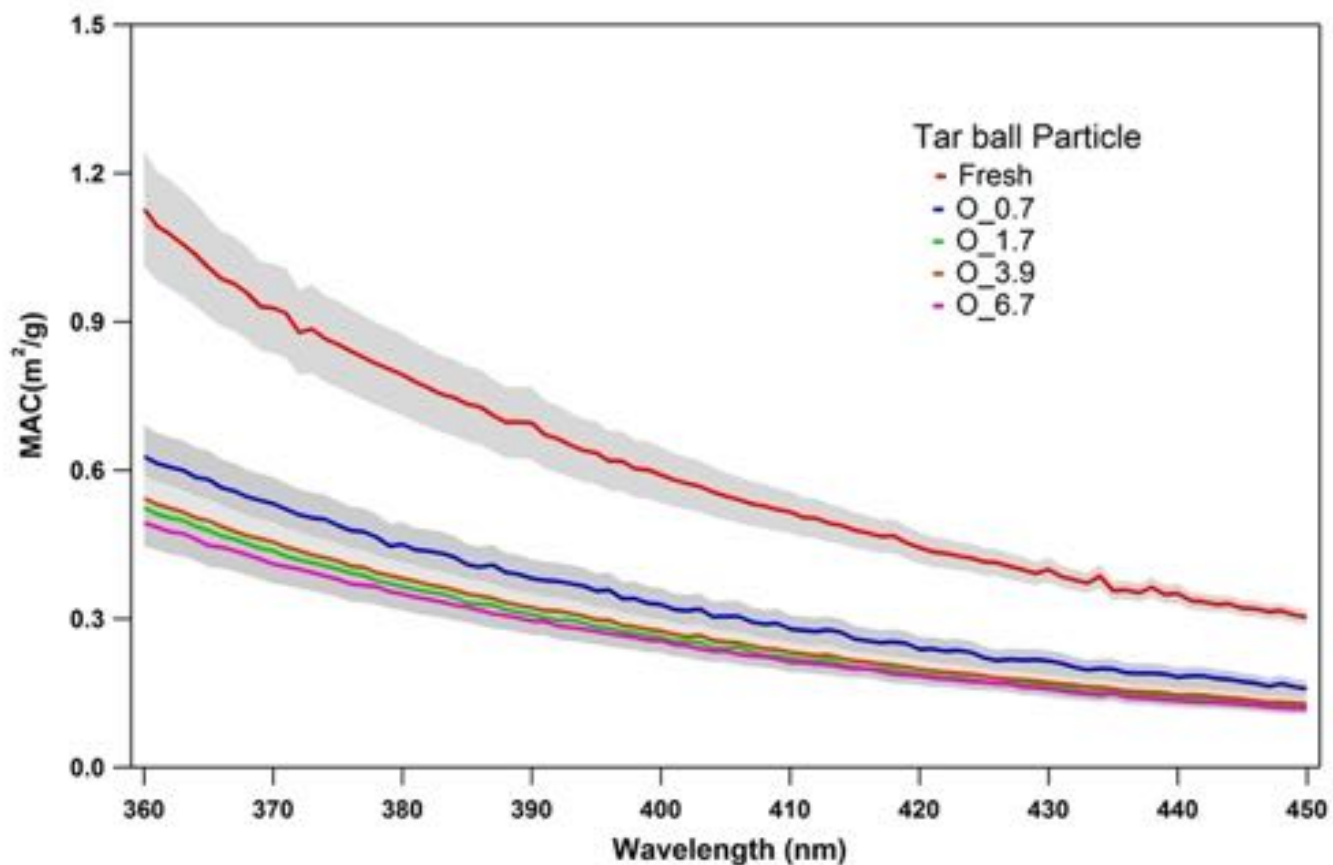

Figure S13. Diminishing in tar ball BrC mass absorption cross section (MAC) upon daytime NOx-free photochemical oxidation

14. Optical and chemical changes for tar ball aerosols due to photolysis from UV light irradiation in the OFR

Studies have reported that BrC formation and SOA decomposition due to directly UV/near UV-short visible light irradiation of various precursors in both liquid and air (Bateman et al., 2011; Malecha and Nizkorodov, 2016; Wong et al., 2017). During photochemical aging through the OFR at residence time of 144s, tar ball particles were also exposed to high photon flux at 254 nm. We performed several experiments to estimate the influence of UV illumination on tar ball evolution. Irradiation tests of P1 and P2 repeated the same aging process of O_1.7 and O_3.9 without external O_3, and P3 was conducted at a full power of the UV lamps in the OFR. We observed slight chemical composition changes in the tar ball aerosols due to photolysis, as the O/C ratio continuously increased while H/C decreased with extension of irradiation (Table S6 and Figure S14). The O/C ratio increased by 0.04 for maximal irradiation exposure, which was much smaller than that from photochemical oxidation. This indicates that OH-initiated oxidation rather than photolysis reactions play a more dominate role in tar ball aging.

The decrease of the H/C ratio due to photolysis exhibited a distinct different chemical pathway than by OH photooxidation. According to the mass spectra analysis, particularly for the P3 experiment shown in Figure S14, the fractions of signals attributed to $C_xH_y^+$ and $C_xH_yO_z^+$ fragments decreased, and as a consequence, the contribution of the $C_xH_yO^+$ fractions increased in photolyzed tar ball aerosols. Comparing to the fresh tar ball mass spectra, alkyl/alkenyl chains, carboxylic acids/peroxides (CO_2^+, CHO_2^+), and carbonyl/aldehyde groups (CO^+, CHO^+, $C_2H_3O^+$) fragments depleted due to irradiation by UV light. Furthermore, increase of the $f44/f43$ ratio with photolysis shown in Figure S14, indicates decay of CO_2^+ to a less extent compared to the loss of $C_2H_3O^+$. Photolysis occurs in the condensed phase as particles containing photolabile compounds that efficiently absorb light at actinc wavelengths. Oxygenated species such as carbonyls, carboxylic acids, and peroxides are more vulnerable to photolysis, especially in the UV. With cleavage of the oxygenated functional groups, molecules become more volatile and may desorb to the gas phase (Henry and Donahue, 2012). Considerable amount of VOCs productions, including small molecular acids, ketones, aldehydes (e.g., acetic acid, formic acid, acetaldehyde, acetone, etc.), and hydrocarbon species (e.g., methane, ethene, propane, etc.), were detected from photo-degradation of various SOA (Malecha and Nizkorodov, 2016; Mang et al., 2008), and photocleavage of carbonyls has been emphasized in photolysis of SOA. Bateman et al. (2011) reported that exposure to UV irradiation increased the O/C ratio of dissolved ambient SOA, and they attributed the chemical changes to photodissociation of molecules containing carbonyl groups and net production of carboxylic acids that overweigh their decomposition in pH modified solution. Detailed mechanisms were proposed such as n-π^* Norrish type-I and -II splitting of carbonyls and n-σ^* photolysis of peroxides to form production of carboxylic acids in the presence of dissolved oxygen (Norrish, 1934; Pitts et al., 1964).

In the current experiments, photolysis occurred in particle phase which can be different from photolysis in liquid phase. First, the photolysis of particles should be less efficient as quenching is more likely and fragment caging can prevent rapid recombination. Second, photolysis products (volatile molecules and radicals) can more easily transfer to the gas phase rather than accumulate in the solution and be involved in further reactions. Epstein et al. (2014) isolated photolysis influence on α-pinene SOA. They reported suppression of SOA mass loading and marked decomposition of particle-bound organic peroxides from UV light illumination. The fraction of $C_xH_y^+$ fragments slightly decreased while the oxygenated fragments increased upon irradiation. Wong et al. (2014) highlighted RH-dependent photolysis as a sink for SOA in the atmosphere, in particular, photolysis results in more oxidized SOA due to kinetic preference for degradation of less oxidized components, and they attributed the slower decay of $f44$ (CO_2^+) to photodissociation of peroxides and the formation of carboxylic acids in SOA upon UV irradiation.

The optical properties of SOA can change upon photolysis of photolabile carbonyl/carboxylic organics, peroxides, and other chromophores. Liu et al. (2016) investigated the influences of various environmental factors on light absorption of aromatic SOA from ozonolysis in the presence of NO_x. They suggested that photolysis, rather than hydrolysis, bleached SOA absorption due to degradation of nitrogen-containing chromophores. This conclusion was also confirmed by similar studies by Lee et al. (2014) and Aiona et al. (2018). In our study, the changes in the optical properties as a function of O/C ratio for tar balls upon photolysis are

shown in Figure S16. The relevant parameters are summarized in Table S7, MAC changes for tar ball upon photolysis are presented in Figure S17. RI of both real and imaginary parts weakly diminished during irradiation, and the average RI at 375 nm decreased by 0.012+0.006i for maximum photolyzed tar ball, corresponded MAC at 375 nm decreased by ~31.3%.

Table S6. Summary of mass spectra characters and effective density changes for tar ball particles upon photolysis from UV light irradiation (mean ± standard deviation)

Tar ball	O:C	H:C	N:C	m/z>100 fraction	density
Fresh	0.25±0.01	1.55±0.01	0.012±0.002	0.32	1.24±0.01
P1	0.26±0.01	1.53±0.01	0.013±0.003	0.33	1.24±0.01
P2	0.27±0.01	1.51±0.01	0.011±0.001	0.32	1.24±0.01
P3	0.29±0.01	1.49±0.01	0.012±0.002	0.33	1.24±0.01
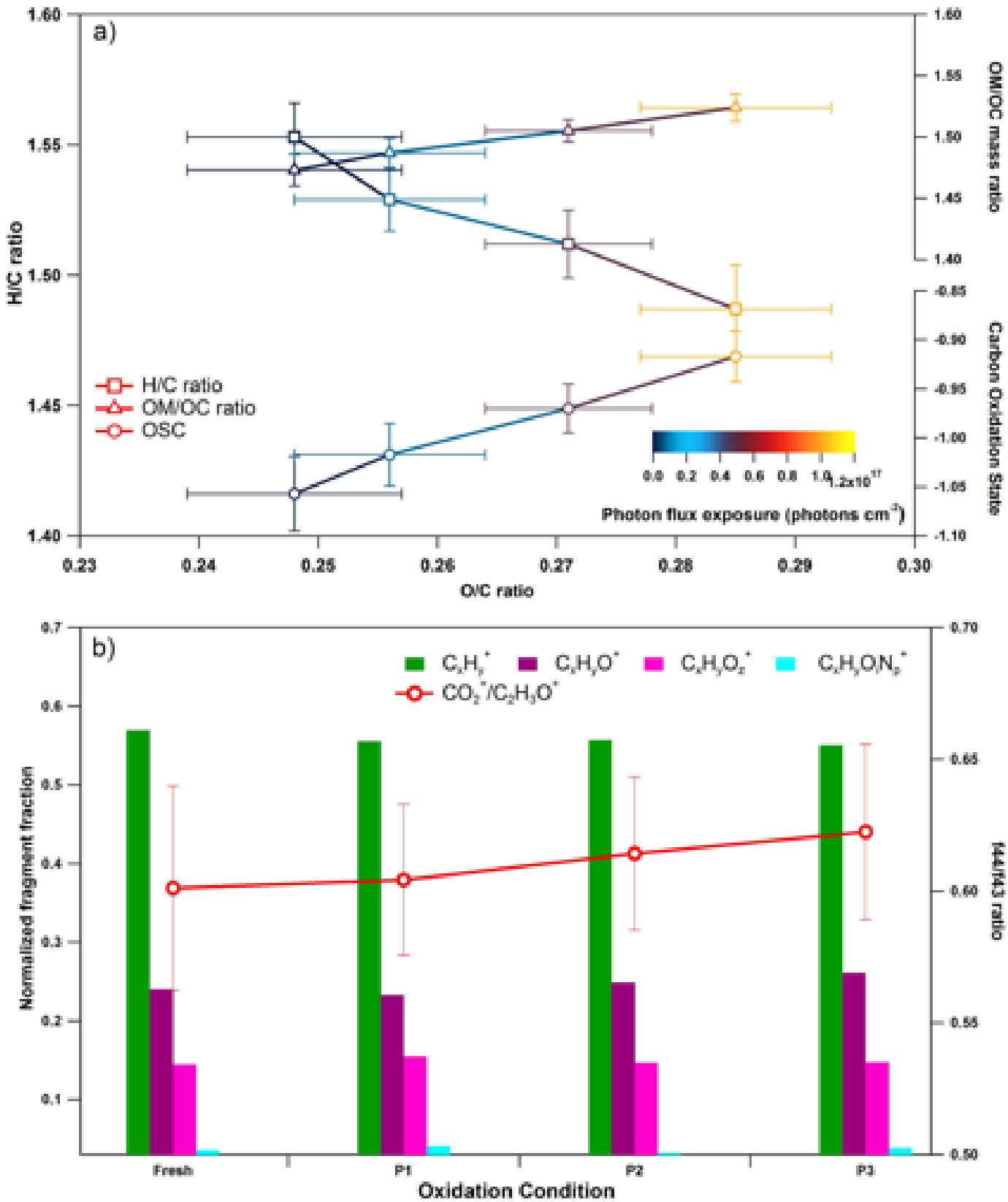
Figure S14. Dynamic changes for chemical characteristics of tar ball particle upon UV light irradiation: a) OM/OC, H/C ratio, and average carbon oxidation state ($\overline{OSc}$) changes as a function of O/C ratio; b) mass spectra evolution with photolysis extension in term of $C_xH_y^+$, $C_xH_yO^+$, $C_xH_yO_z^+$, and $C_xH_yO_iN_p^+$ fragment groups
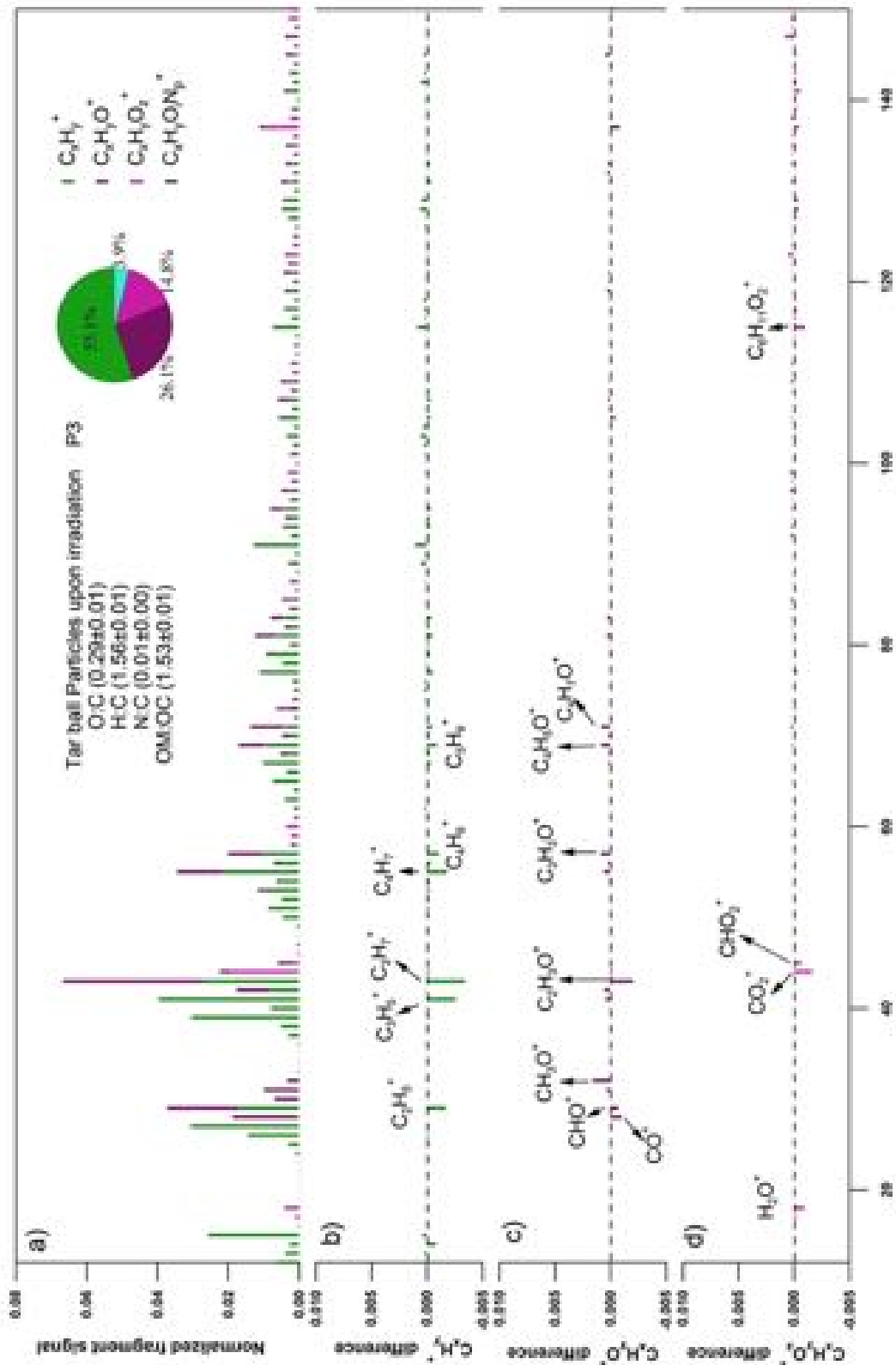
Figure S15. High-resolution mass spectra changes for nonpolar tar ball particles after maximum photolysis in P3 test, four ion groups were grouped for clarity as: $C_xH_y^+$, $C_xH_yO^+$, $C_xH_yO_z^+$ ($z>1$), $C_xH_yO_iN_p^+$($i≧0,p≧1$). Ions O^+, OH^+, and H_2O^+ were included in the $C_xH_yO_z^+$ group. Mass fraction of the four fragment groups was pie-chart presented. a) normalized mass spectra of aged tar ball particles, b)–d) changes of $C_xH_y^+$, $C_xH_yO^+$, $C_xH_yO_z^+$, and $C_xH_yO_iN_p^+$ comparing with fresh tar ball normalized mass spectra

2

Table S7. Summary of RI and Ångström exponent changes for tar ball particles upon photolysis (mean ± standard deviation)

Tar ball	Complex Refractive index			SSA (average)	$\mathring{A}_{abs}$	$\mathring{A}_{abs\_UVVIS}$	$\mathring{A}_{ext}$
	Average	375nm	405nm				
Fresh	(1.661±0.008)+(0.020±0.004)i	(1.671±0.003)+(0.025±0.003)i	(1.659±0.011)+(0.017±0.002)i	0.89 ± 0.01	5.87 ± 0.37	6.74	3.81 ± 0.18
P1	(1.658±0.010)+(0.022±0.006)i	(1.668±0.001)+(0.027±0.001)i	(1.653±0.002)+(0.018±0.001)i	0.88 ± 0.02	6.92 ± 0.60	6.59	3.94 ± 0.03
P2	(1.649±0.008)+(0.018±0.004)i	(1.656±0.002)+(0.023±0.002)i	(1.647±0.002)+(0.014±0.003)i	0.90 ± 0.02	6.99 ± 1.22	6.50	3.79 ± 0.05
P3	(1.649±0.010)+(0.015±0.004)i	(1.659±0.005)+(0.019±0.004)i	(1.644±0.004)+(0.013±0.003)i	0.92 ± 0.01	7.42 ± 0.53	6.56	4.01 ± 0.01
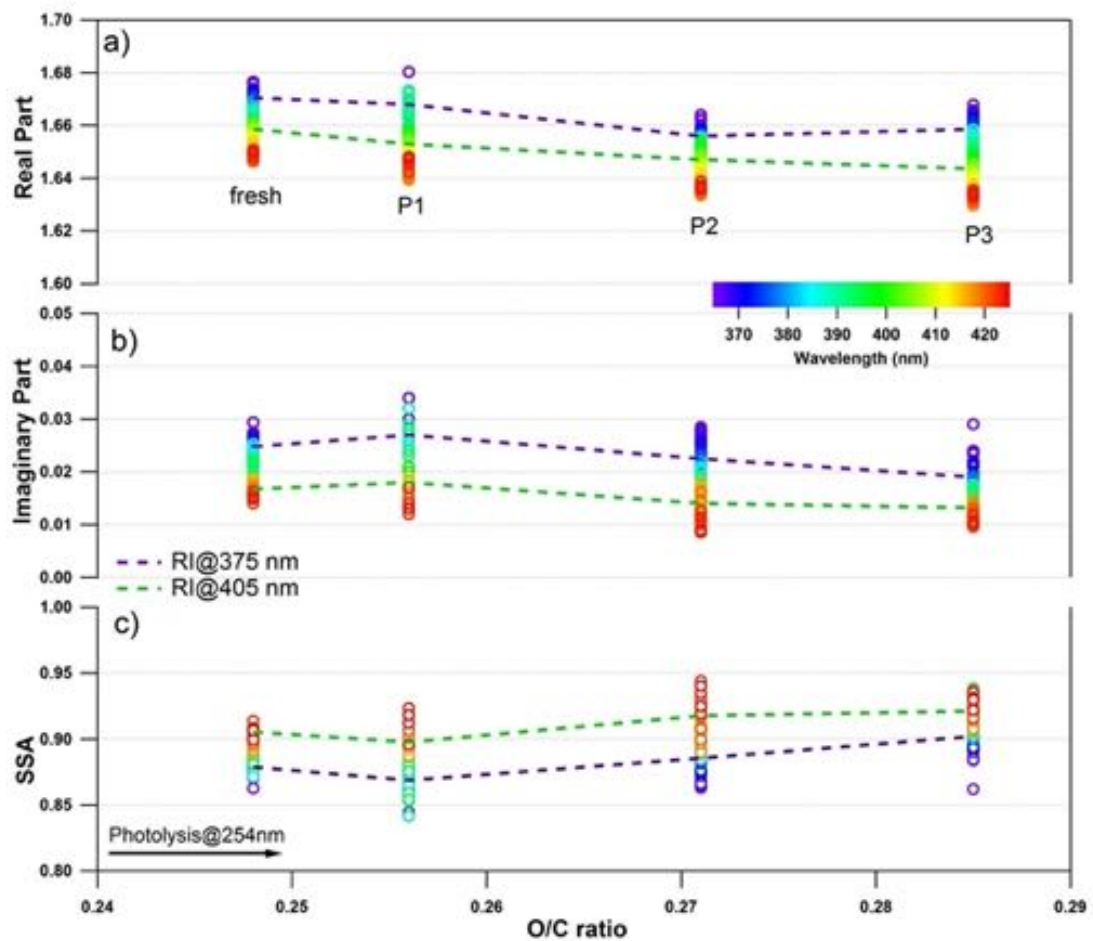
Figure S16. Changes in the retrieved spectral-dependent complex RI and SSA as a function of O/C ratio for tar ball particles upon 254 nm illumination: a) real part, b) imaginary part, and c) SSA calculated for 150 nm particles. The color scale shows the span in the RI for the wavelengths measured from 365 to 425 nm. For clarity, error bars for O/C ratio (±0.01), RI (±0.008 for real part, and ±0.003 for imaginary part on average) and SSA (±0.006) are not shown. The two dashed lines trace RI and SSA at 375nm (purple) and 405nm (green). P1~P3 represent photolysis studies with low to maximal photon flux exposures.
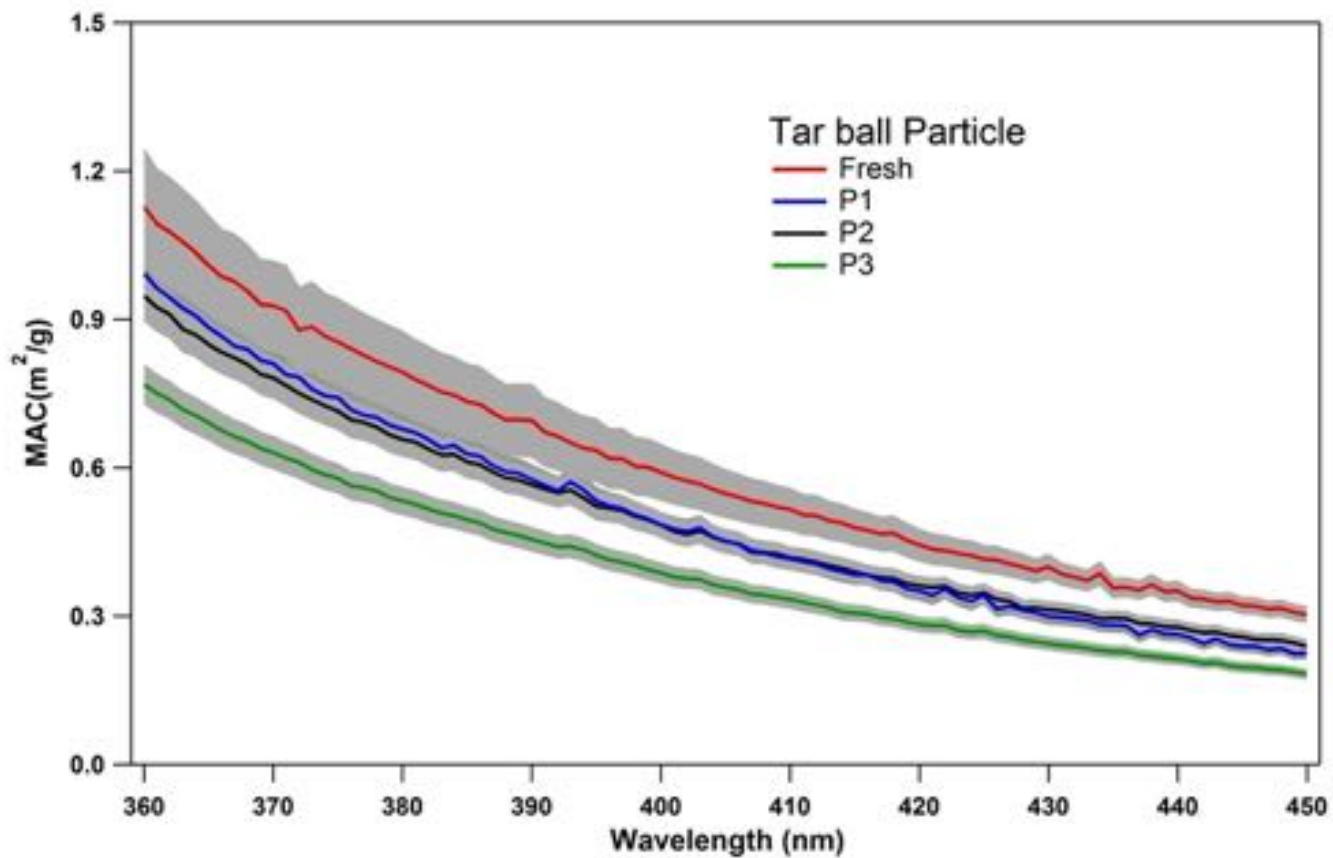
Figure S17. Changes of tar ball BrC mass absorption cross section (MAC) as a function of wavelength upon UV photolysis

15. Optical and chemical changes of tar ball aerosols due to O₃ oxidation

Prior to photochemical aging experiments, blank test of tar ball oxidation via O_3 under dark was conducted in the OFR. Initial environmental conditions (e.g., O_3 and tar balls concentrations, relative humidity, residence time, etc) were maintained the same with following daytime evolution simulations, while UV lamps were not turned on. Dynamic optical and chemical changes for tar balls were characterized and presented in Figure S18 and S19. We did not observe significant refractive index changes for tar balls after 28.6 ppm O_3 oxidation, taking ambient O_3 concentration of 50 ppb, equivalent atmospheric O_3 exposure for tar balls through the OFR was about one day. RIs of fresh tar ball are $(1.671\pm0.003)+(0.025\pm0.003)i$ and $(1.659\pm0.011)+(0.017\pm0.002)i$ at 375 and 405 nm, respectively. After O_3 oxidation, RIs became $(1.677\pm0.012)+(0.023\pm0.003)i$ and $(1.668\pm0.011)+(0.013\pm0.004)i$ at at 375 and 405 nm, respectively. In Figure S19, O_3 oxidation weakly increased O/C and OM/OC ratios of tar balls, O/C ratio increased by 0.02 from initial 0.25, and OM/OC increased from 1.47 to 1.50, while H/C ratio remained during O_3 oxidation of tar ball particles. It was found $C_xH_y^+$ fractions slight decreased in compensation of more $C_xH_yO^+$ and $C_xH_yO_z^+$ fragments formation, indicating oxygenated moieties produced.
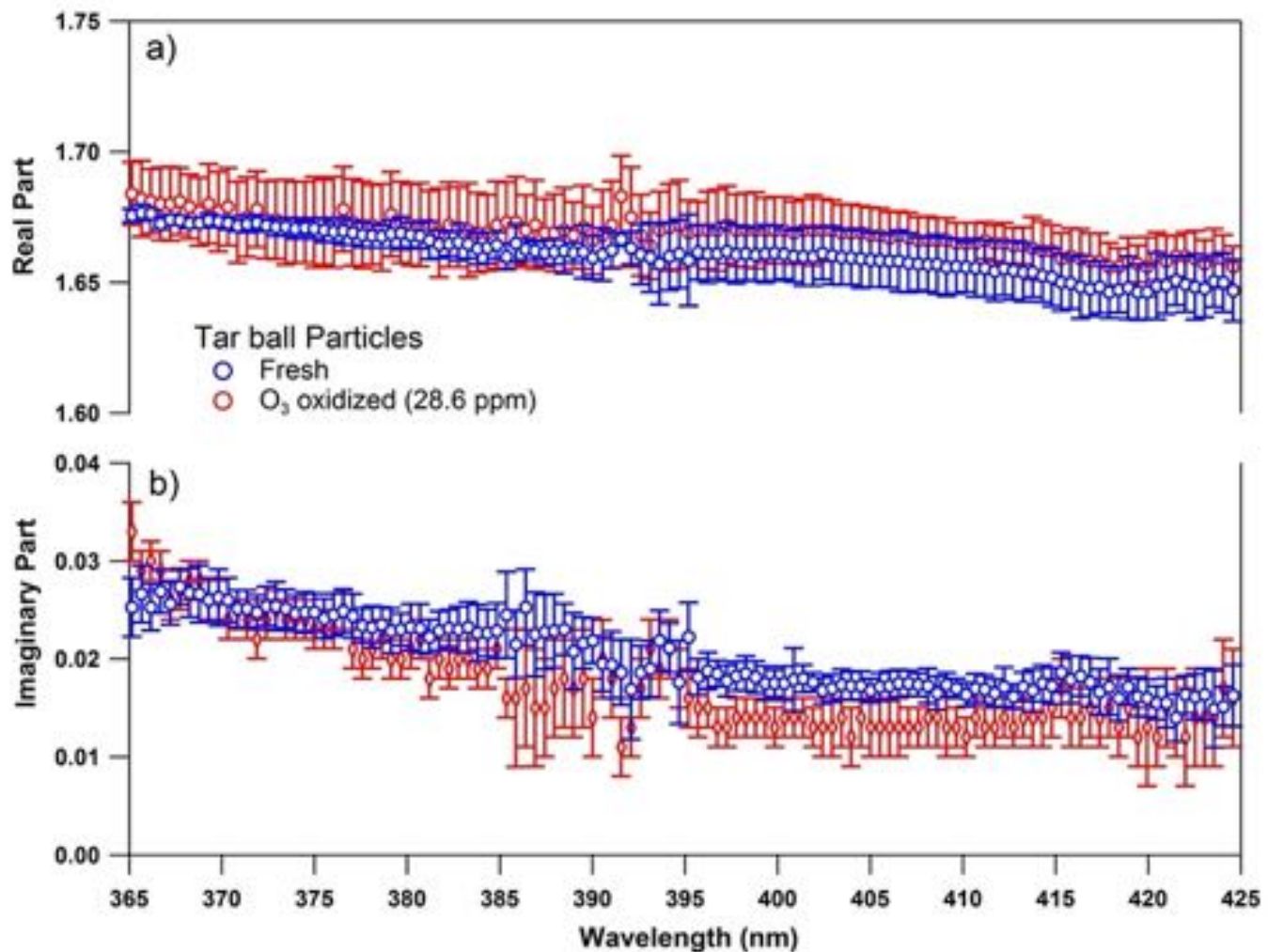
Figure S18. Refractive index as a function of wavelength for fresh and O3 oxidized tar balls, a) real part, b) imaginary part

3
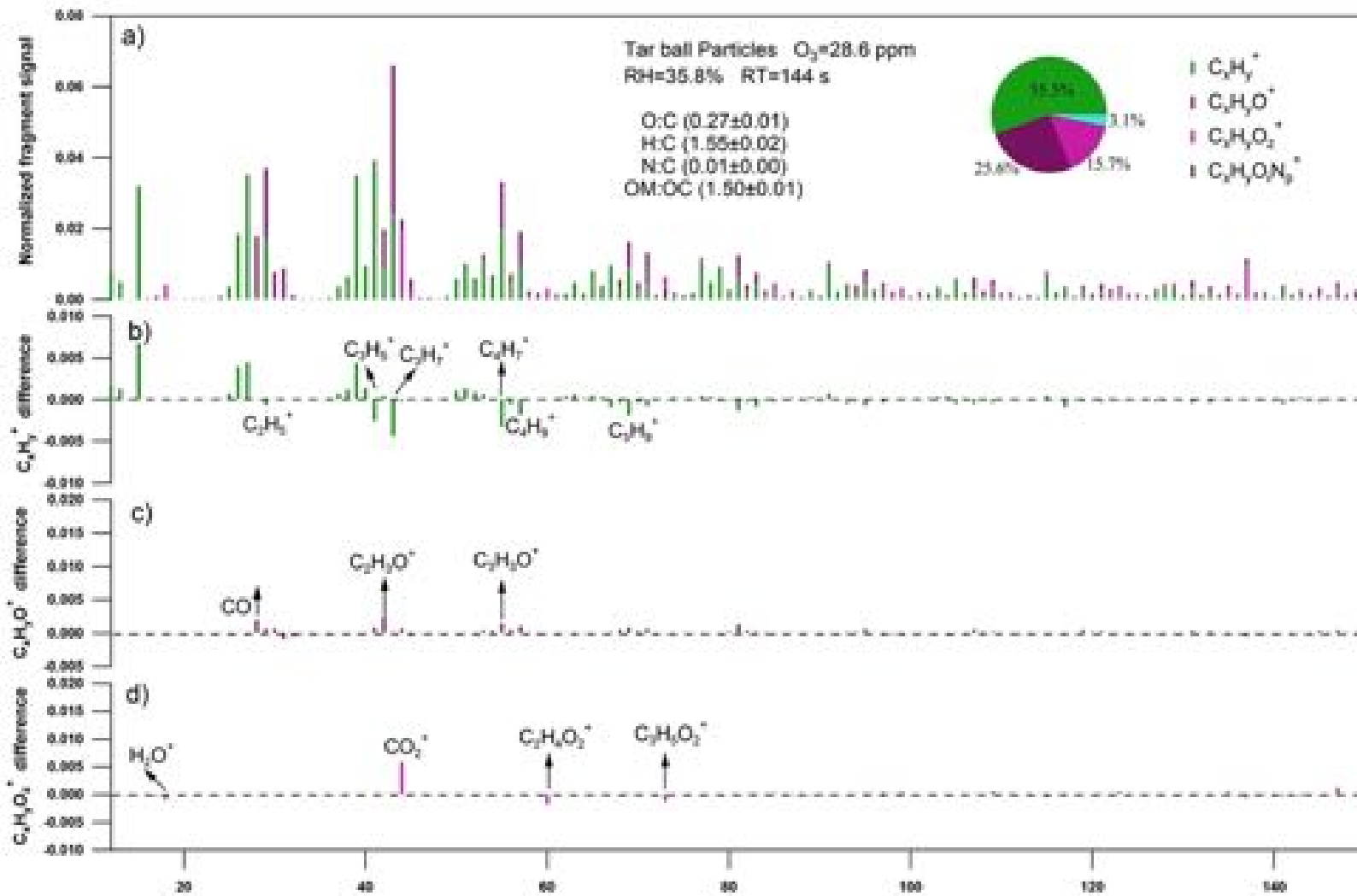
Figure S19. High-resolution mass spectral changes for nonpolar tar ball particles oxidized via O_3. Four ion groups were grouped for clarity: $C_xH_y^+$, $C_xH_yO^+$, $C_xH_yO_z^+$ (z>1), $C_xH_yO_iN_p^+$(i$\geq$0,p$\geq$1). Ions O^+, OH^+, and H_2O^+ were included in the $C_xH_yO_z^+$ group. Mass fraction of the four fragment groups was pie-chart presented. a) normalized mass spectra of O_3 oxidized tar ball particles, b)~d) changes of $C_xH_y^+$, $C_xH_yO^+$, $C_xH_yO_z^+$, and $C_xH_yO_iN_p^+$ comparing with fresh tar ball normalized mass spectra

16. Mass spectra characters and effective density changes for tar ball particles upon photochemical oxidation

Table S8. Summary of mass spectra characters and effective density changes for tar ball particles upon photochemical oxidation (mean ± standard deviation)

Tar ball	O:C	H:C	N:C	m/z>100 fraction	density
Fresh	0.25±0.01	1.55±0.01	0.012±0.002	0.32	1.24±0.01
O_0.7	0.32±0.01	1.59±0.01	0.012±0.000	0.28	1.24±0.01
O_1.7	0.35±0.01	1.60±0.01	0.009±0.002	0.24	1.24±0.01
O_3.9	0.35±0.01	1.59±0.01	0.010±0.003	0.24	1.24±0.01
O_6.7	0.38±0.01	1.62±0.03	0.011±0.001	0.21	1.24±0.01
N_0.5	0.37±0.01	1.57±0.02	0.012±0.001	0.25	1.25±0.01
N_2.0	0.41±0.01	1.58±0.01	0.015±0.004	0.25	1.26±0.01

17. Detailed mass spectra changes for tar ball upon 6.7 EAD photochemical aging
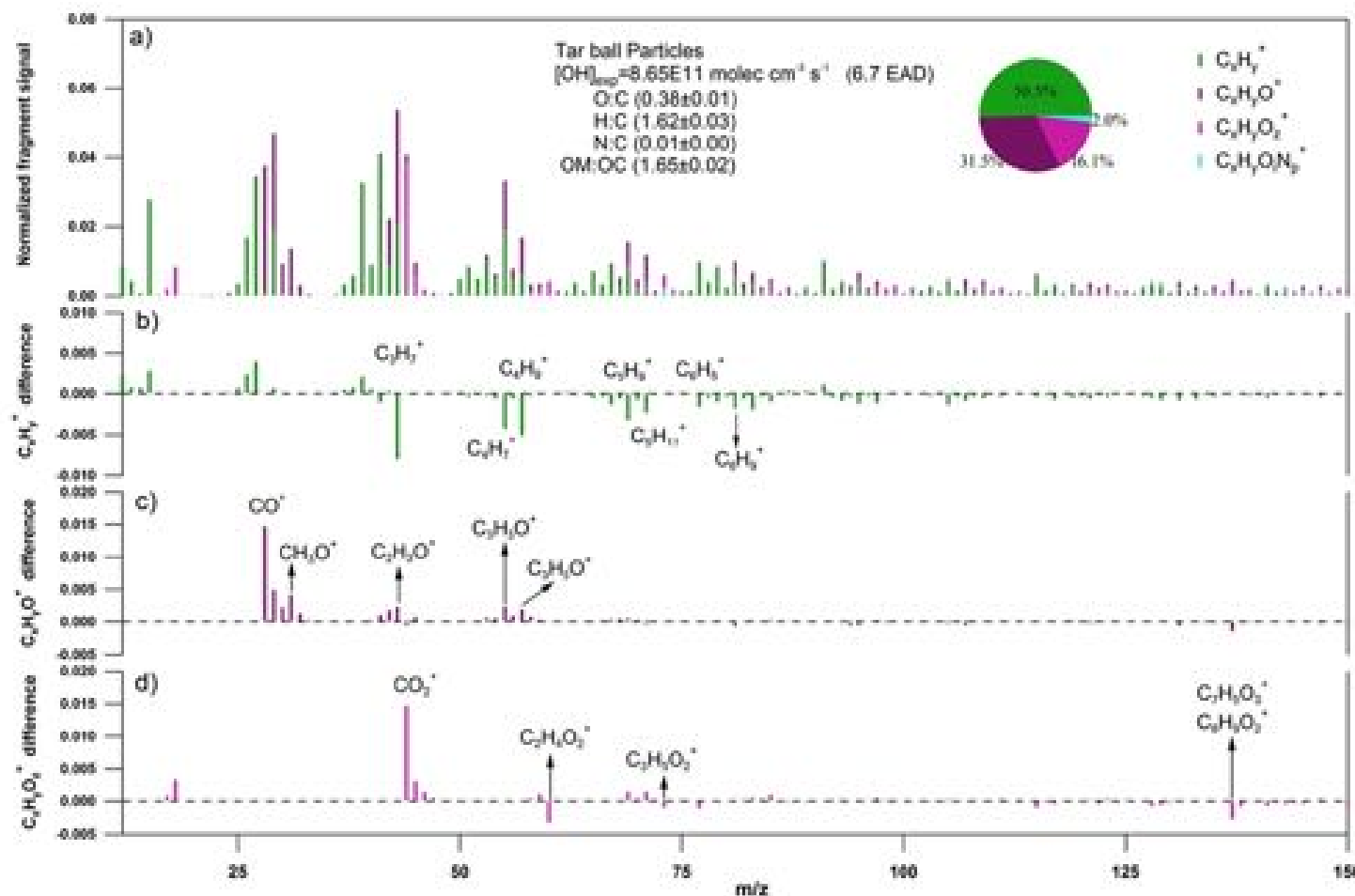
Figure S20. High-resolution mass spectral changes for nonpolar tar ball particles upon 6.7 EAD photochemical oxidation in absence of NOx. Four ion groups were grouped for clarity: $C_xH_y^+$, $C_xH_yO^+$, $C_xH_yO_z^+$ ($z>1$), $C_xH_yO_iN_p^+$($i\geqq0,p\geqq1$). Ions O^+, OH^+, and H_2O^+ were included in the $C_xH_yO_z^+$ group. Mass fraction of the four fragment groups was pie-chart presented. a) normalized mass spectra of 6.7 EAD aged tar ball particles, b)~d) changes of $C_xH_y^+$, $C_xH_yO^+$, $C_xH_yO_z^+$, and $C_xH_yO_iN_p^+$ comparing with fresh tar ball normalized mass spectra

3

18. Standard AMS spectra for inorganic salt of NH₄NO₃
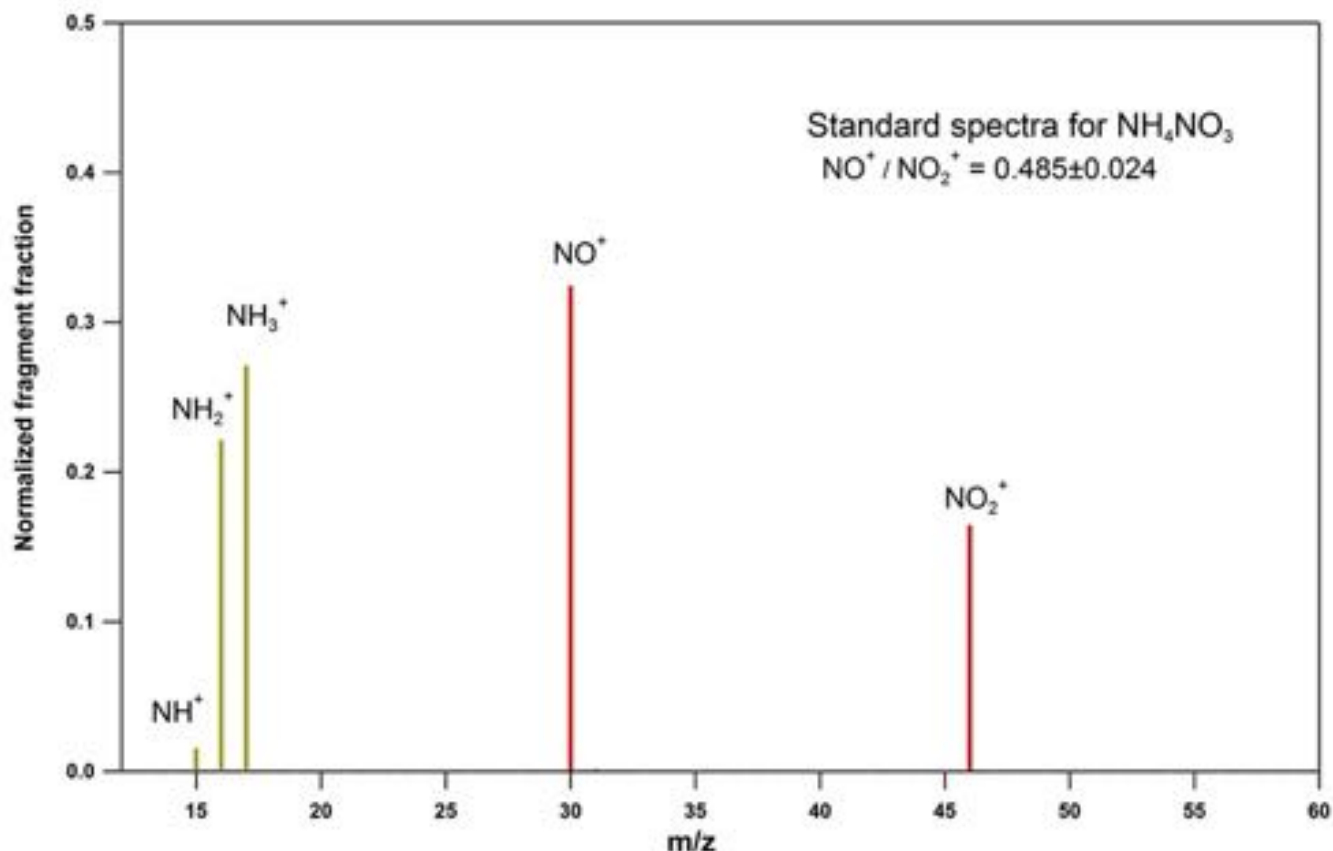
Figure S21. Standard mass spectra for NH₄NO₃ measured using HR-Tof-AMS system: NO^+ and NO_2^+ for nitrate, NH^+, NH_2^+, and NH_3^+ for ammonium

19. Detailed mass spectra changes for tar ball aerosols upon 4 EAD photochemical aging with 2.0 vol.% N₂O addition
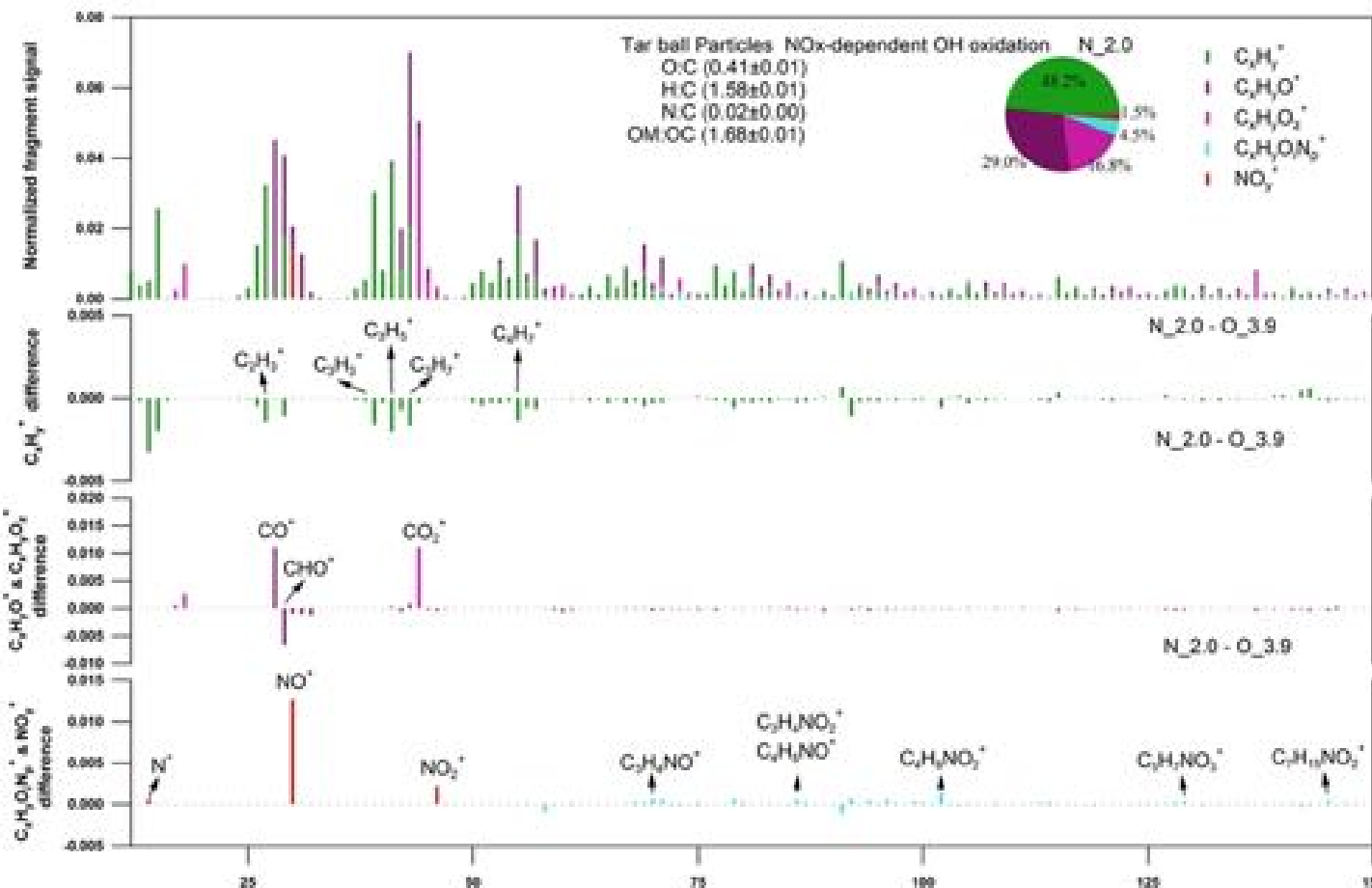

Figure S22. High-resolution mass spectra changes for nonpolar tar ball particles upon photochemical oxidation in presence of NOx, five ion groups were grouped for clarity as: $C_xH_y^+$, $C_xH_yO^+$, $C_xH_yO_z^+$ (z>1), $C_xH_yO_iN_p^+$(i≧0,p≧1), and NO_y^+ (NO^+ and NO_2^+). Ions O^+, OH^+, and H_2O^+ were included in the $C_xH_yO_z^+$ group. Mass fraction of the four fragment groups was pie-chart presented. a) normalized mass spectra of aged tar ball particles, b)~d) changes of $C_xH_y^+$, $C_xH_yO^+$, $C_xH_yO_z^+$, $C_xH_yO_iN_p^+$, and NO_y^+ comparing with photochemical oxidized tar ball in absence of NOx

1 **20. Methanol extractable BrC mass absorption cross section (MAC) for tar ball aerosols upon various NOx-dependent**
2 **photochemical aging processes**
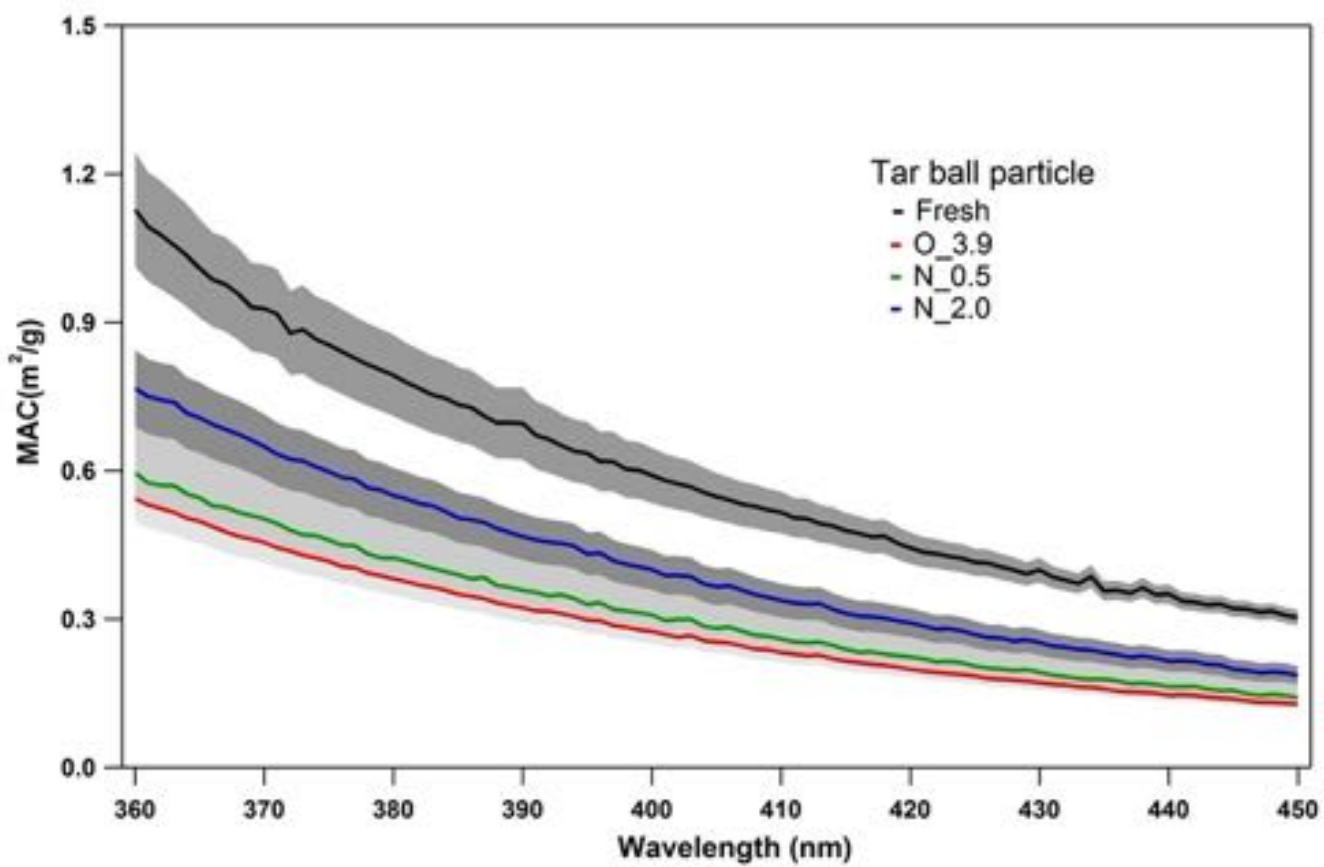
3

4 **Figure S23.** Methanol extractable BrC mass absorption cross section (MAC) for tar ball upon NOx-dependent photochemical
5 oxidation as a function of wavelength
6

21. Particle size- and light wavelength-resolved radiative forcing for tar ball aerosols oxidized via various NOx-dependent oxidation processes
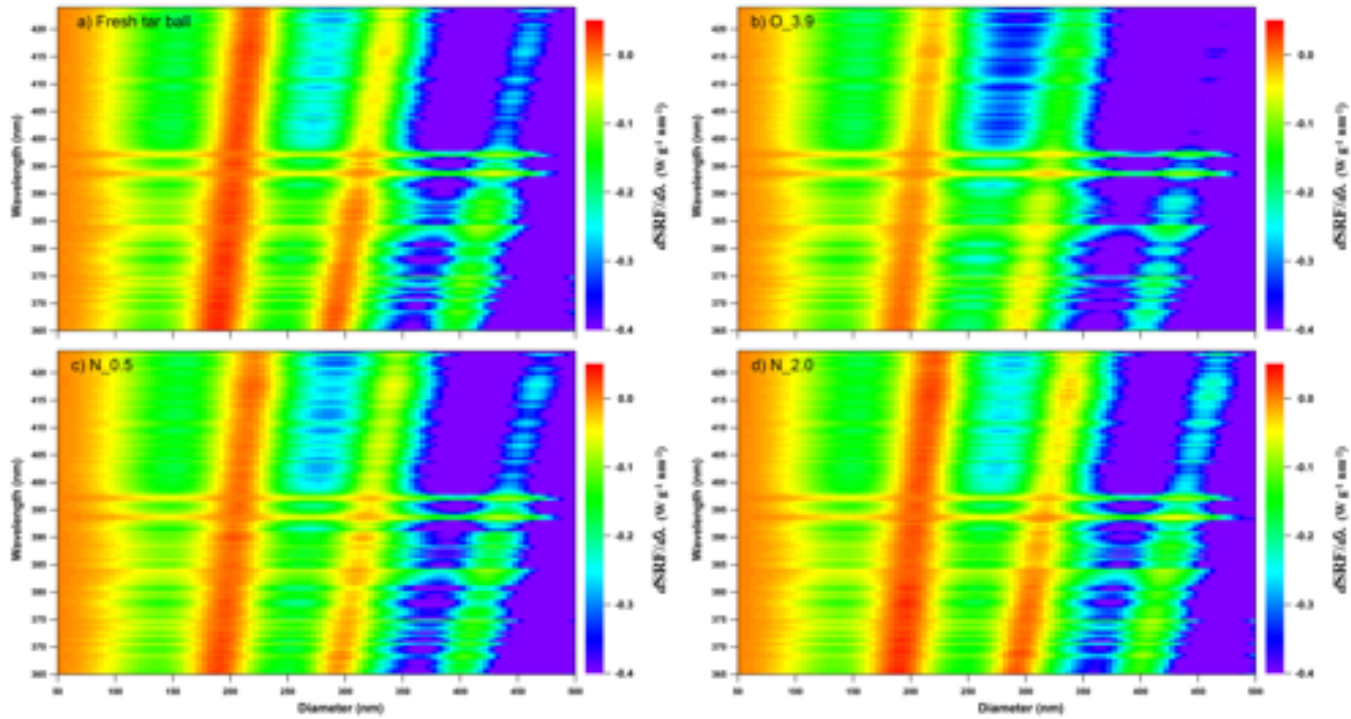

Figure S24. Ground based size-resolved radiative forcing spectra over solar irradiation of 365~425 nm for tar ball under various oxidation: a) fresh tar ball, b) 3.9 EAD daytime photochemical oxidized tar ball, c) photooxidized tar ball with 0.5 vol.% N_2O addition, d) photooxidized tar ball with 2.0 vol.% N_2O addition.
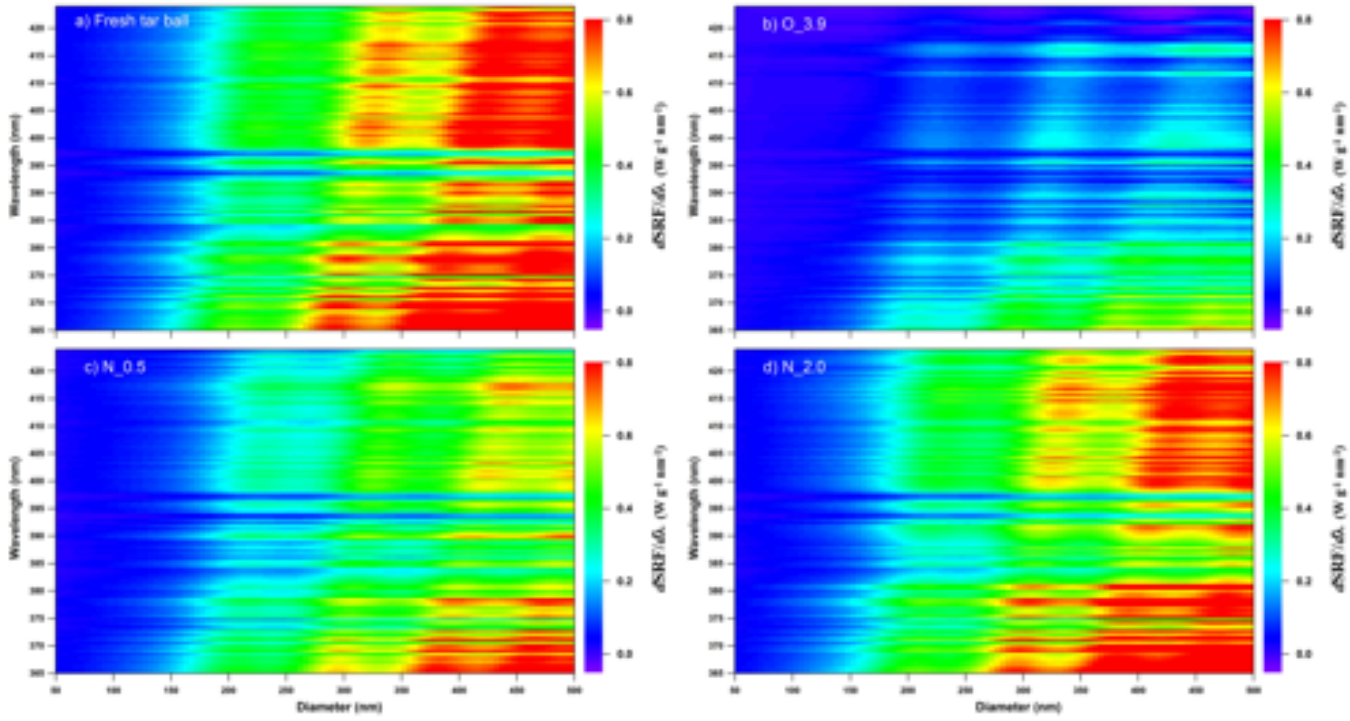
Figure S25. Snow based size-resolved radiative forcing spectra over solar irradiation of 365~425 nm for tar ball under various oxidation: a) fresh tar ball, b) 3.9 EAD OH initiated photochemical oxidized tar ball, c) photooxidized tar ball with 0.5 vol.% N₂O addition, d) photooxidized tar ball with 2.0 vol.% N₂O addition.

Reference

Adler, G., Flores, J. M., Abo Riziq, A., Borrmann, S., and Rudich, Y.: Chemical, physical, and optical evolution of biomass burning aerosols: a case study, Atmos. Chem. Phys., 11, 1491-1503, doi:10.5194/acp-11-1491-2011, 2011.

Aiken, A. C., Decarlo, P. F., Kroll, J. H., Worsnop, D. R., Huffman, J. A., Docherty, K. S., Ulbrich, I. M., Mohr, C., Kimmel, J. R., and Sueper, D.: O:C and OM/OC ratios of primary, secondary, and ambient organic aerosols with high-resolution time-of-flight aerosol mass spectrometry, Environ. Sci. Technol., 42, 4478-4485, doi:10.1021/es703009q, 2008.

Aiona, P. K., Luek, J. L., Timko, S. A., Powers, L., Gonsior, M., and Nizkorodov, S. A.: Effect of Photolysis on Absorption and Fluorescence Spectra of Light-Absorbing Secondary Organic Aerosols, ACS Earth Space Chem., 2, 235-245, doi:10.1021/acsearthspacechem.7b00153, 2018.

Andreae, M., and Gelencsér, A.: Black carbon or brown carbon? The nature of light-absorbing carbonaceous aerosols, Atmos. Chem. Phys., 6, 3131-3148, doi:10.5194/acp-6-3131-2006, 2006.

Arora, P., and Jain, S.: Estimation of organic and elemental carbon emitted from wood burning in traditional and improved cookstoves using controlled cooking test, Environ. Sci. Technol., 49, 3958-3965, doi:10.1021/es504012v, 2015.

Bateman, A. P., Nizkorodov, S. A., Laskin, J., and Laskin, A.: Photolytic processing of secondary organic aerosols dissolved in cloud droplets, Phys. Chem. Chem. Phys., 13, 12199-12212, doi:10.1039/C1CP20526A, 2011.

Bente, M., Sklorz, M., Streibel, T., and Zimmermann, R.: Online laser desorption-multiphoton postionization mass spectrometry of individual aerosol particles: molecular source indicators for particles emitted from different traffic-related and wood combustion sources, Anal. Chem., 80, 8991-9004, doi:10.1021/ac801295f, 2008.

Bruns, E., Krapf, M., Orasche, J., Huang, Y., Zimmermann, R., Drinovec, L., Močnik, G., El-Haddad, I., Slowik, J., and Dommen, J.: Characterization of primary and secondary wood combustion products generated under different burner loads, Atmos. Chem. Phys., 15, 2825-2841, doi:10.5194/acp-15-2825-2015, 2015.

Chakrabarty, R., Moosmüller, H., Chen, L. W., Lewis, K., Arnott, W., Mazzoleni, C., Dubey, M., Wold, C., Hao, W., and Kreidenweis, S.: Brown carbon in tar balls from smoldering biomass combustion, Atmos. Chem. Phys., 10, 6363-6370, doi:10.5194/acp-10-6363-2010, 2010.

China, S., Mazzoleni, C., Gorkowski, K., Aiken, A. C., and Dubey, M. K.: Morphology and mixing state of individual freshly emitted wildfire carbonaceous particles, Nature communications, 4, 2122, doi:10.1038/ncomms3122, 2013.

Chow, J. C., Watson, J. G., Robles, J., Wang, X., Chen, L.-W. A., Trimble, D. L., Kohl, S. D., Tropp, R. J., and Fung, K. K.: Quality assurance and quality control for thermal/optical analysis of aerosol samples for organic and elemental carbon, Anal. Bioanal. Chem., 401, 3141-3152, doi:10.1007/s00216-011-5103-3, 2011.

Chýlek, P., Ramaswamy, V., and Cheng, R. J.: Effect of graphitic carbon on the albedo of clouds, J. Atmos. Sci., 41, 3076-3084, doi:10.1175/1520-0469, 1984.

d'Almeida, G. A., Koepke, P., and Shettle, E. P.: Atmospheric aerosols: global climatology and radiative characteristics, A. Deepak Publishing, Hampton, Va, 1991.

Epstein, S. A., Blair, S. L., and Nizkorodov, S. A.: Direct photolysis of α-pinene ozonolysis secondary organic aerosol: effect on particle mass and peroxide content, Environ. Sci. Technol., 48, 11251-11258, doi:10.1021/es502350u, 2014.

Hand, J. L., Malm, W., Laskin, A., Day, D., Lee, T.-b., Wang, C., Carrico, C., Carrillo, J., Cowin, J. P., and Collett, J.: Optical, physical, and chemical properties of tar balls observed during the Yosemite Aerosol Characterization Study, J. Geophys. Res.: Atmos., 110, D21210, doi:10.1029/2004JD005728, 2005.

Han, Y., Han, Z., Cao, J., Chow, J., Watson, J., An, Z., Liu, S., and Zhang, R.: Distribution and origin of carbonaceous aerosol over a rural high-mountain lake area, Northern China and its transport significance, Atmos. Environ., 42, 2405-2414, doi:10.1016/j.atmosenv.2007.12.020, 2008.

Han, Y., Lee, S., Cao, J., Ho, K., and An, Z.: Spatial distribution and seasonal variation of char-EC and soot-EC in the atmosphere over China, Atmos. Environ., 43, 6066-6073, doi:10.1016/j.atmosenv.2009.08.018, 2009.

He, L. Y., Lin, Y., Huang, X. F., Guo, S., Xue, L., Su, Q., Hu, M., Luan, S. J., and Zhang, Y. H.: Characterization of high-resolution aerosol mass spectra of primary organic aerosol emissions from Chinese cooking and biomass burning, Atmos. Chem. Phys., 10, 11535-11543, doi:10.5194/acp-10-11535-2010, 2010.

Henry, K. M., and Donahue, N. M.: Photochemical aging of α-pinene secondary organic aerosol: effects of OH radical sources and photolysis, J. Phys. Chem. A, 116, 5932-5940, doi:10.1021/jp210288s, 2012.

Hoffmann, D., Iinuma, Y., and Herrmann, H.: Development of a method for fast analysis of phenolic molecular markers in biomass burning particles using high performance liquid chromatography/atmospheric pressure chemical ionisation mass spectrometry, J. Chromatography A, 1143, 168-175, doi:10.1016/j.chroma.2007.01.035, 2007.

Jacobson, M. Z.: Analysis of aerosol interactions with numerical techniques for solving coagulation, nucleation, condensation, dissolution, and reversible chemistry among multiple size distributions, J. Geophys. Res.-Atmos., 107, D19, 4366, doi:10.1029/2001JD002044, 2002.

Jacobson, M. Z.: Effects of externally-through-internally-mixed soot inclusions within clouds and precipitation on global climate, J. Phys. Chem. A, 110, 6860-6873, doi:10.1021/jp056391r, 2006.

Kim, K. H., Sekiguchi, K., Kudo, S., and Sakamoto, K.: Characteristics of Atmospheric Elemental Carbon (Char and Soot) in Ultrafine and Fine Particles in a Roadside Environment, Japan, Aerosol Air Qual. Res., 11, 1-12, doi:10.4209/aaqr.2010.07.0061, 2011.

Lee, H. J., Aiona, P. K., Laskin, A., Laskin, J., and Nizkorodov, S. A.: Effect of solar radiation on the optical properties and molecular composition of laboratory proxies of atmospheric brown carbon, Environ. Sci. Technol., 48, 10217-10226, doi:10.1021/es502515r, 2014.

Li, C., Hu, Y., Zhang, F., Chen, J., Ma, Z., Ye, X., Yang, X., Wang, L., Tang, X., and Zhang, R.: Multi-pollutant emissions from the burning of major agricultural residues in China and the related health-economic effects, Atmos. Chem. Phys., 17, 4957-4988, doi:10.5194/acp-17-4957-2017, 2017.

Li, Y., Huang, D., Cheung, H. Y., Lee, A., and Chan, C. K.: Aqueous-phase photochemical oxidation and direct photolysis of vanillin-a model compound of methoxy phenols from biomass burning, Atmos. Chem. Phys., 14, 2871-2885, doi:10.5194/acp-14-2871-2014, 2014.

Li, Y. J., Yeung, J. W., Leung, T. P., Lau, A. P., and Chan, C. K.: Characterization of organic particles from incense burning using an aerodyne high-resolution time-of-flight aerosol mass spectrometer, Aerosol Sci. Tech., 46, 654-665, doi:10.1080/02786826.2011.653017, 2012.

Li, S., Zhu, M., Yang, W., Tang, M., Huang, X., Yu, Y., Fang, H., Yu, X., Yu, Q., and Fu, X.: Filter-based measurement of light absorption by brown carbon in $PM_{2.5}$ in a megacity in South China, Sci. Total Environ., 633, 1360-1369, doi:10.1016/j.scitotenv.2018.03.235, 2018.

Liu, J., Lin, P., Laskin, A., Laskin, J., Kathmann, S. M., Wise, M., Caylor, R., Imholt, F., Selimovic, V., and Shilling, J. E.: Optical properties and aging of light-absorbing secondary organic aerosol, Atmos. Chem. Phys., 16, 12815-12827, doi:10.5194/acp-16-12815-2016, 2016.

Malecha, K. T., and Nizkorodov, S. A.: Photodegradation of secondary organic aerosol particles as a source of small, oxygenated volatile organic compounds, Environ. Sci. Technol., 50, 9990-9997, doi:10.1021/acs.est.6b02313, 2016.

Mandalakis, M., Gustafsson, Ö., Alsberg, T., Egebäck, A. L., Reddy, C. M., Xu, L., Klanova, J., Holoubek, I., and Stephanou, E. G.: Contribution of biomass burning to atmospheric polycyclic aromatic hydrocarbons at three European background sites, Environ. Sci. Technol., 39, 2976-2982,doi:10.1021/es048184v, 2005.

Mang, S. A., Henricksen, D. K., Bateman, A. P., Andersen, M. P. S., Blake, D. R., and Nizkorodov, S. A.: Contribution of carbonyl photochemistry to aging of atmospheric secondary organic aerosol, J. Phys. Chem. A, 112, 8337-8344, doi:10.1021/jp804376c, 2008.

Ng, N., Canagaratna, M., Zhang, Q., Jimenez, J., Tian, J., Ulbrich, I., Kroll, J., Docherty, K., Chhabra, P., and Bahreini, R.: Organic aerosol components observed in Northern Hemispheric datasets from Aerosol Mass Spectrometry, Atmos. Chem. Phys., 10, 4625-4641, doi:10.5194/acp-10-4625-2010, 2010.

Ng, N., Canagaratna, M., Jimenez, J., Chhabra, P., Seinfeld, J., and Worsnop, D.: Changes in organic aerosol composition with aging inferred from aerosol mass spectra, Atmos. Chem. Phys., 11, 6465-6474, doi:10.5194/acp-11-6465-2011, 2011.

Norrish, R. G.: Part II. Free radicals of short life: chemical aspects. A. General and inorganic. The primary photochemical production of some free radicals, Transactions of the Faraday Society, 30, 103-113, 1934.

7.3.   Publication 3: Schade et al., *Anal. Chem.,* 91 (2019), 10282-10288

Title: Spatially Shaped Laser Pulses for the Simultaneous Detection of Polycyclic Aromatic Hydrocarbons as well as Positive and Negative Inorganic Ions in Single Particle Mass Spectrometry

Authors: Julian Schade, Johannes Passig, Robert Irsig, Sven Ehlert, Martin Sklorz, Thomas Adam, Chunlin Li, Yinon Rudich, and Ralf Zimmermann

Journal: Analytical Chemistry, 91, 10282-10288

Year: 2019

DOI: 10.1021/acs.analchem.9b02477

7.4.   Publication 4: Passig and Schade et al., *Atmos. Chem. Phys.,* 20 (2020), 7139-7152

Title: Resonance-enhanced detection of metals in aerosols using single-particle mass spectrometry

Authors: Johannes Passig, <u>Julian Schade</u>, Ellen Iva Rosewig, Robert Irsig, Thomas Kröger-Badge, Hendryk Czech, Martin Sklorz, Thorsten Streibel, Lei Li, Xue Li, Zhen Zhou, Henrik Fallgren, Jana Moldanova, and Ralf Zimmermann

Journal: Atmospheric Chemistry and Physics, 20, 7139-7152

Year: 2020

DOI: 10.5194/acp-20-7139-2020

Atmospheric
Chemistry
and Physics

Resonance-enhanced detection of metals in aerosols using single-particle mass spectrometry

Johannes Passig[1,2,3], Julian Schade[2,3], Ellen Iva Rosewig[2,3], Robert Irsig[3,4], Thomas Kröger-Badge[2,3], Hendryk Czech[1,2,3], Martin Sklorz[1], Thorsten Streibel[1,2], Lei Li[5,6], Xue Li[5,6], Zhen Zhou[5,6], Henrik Fallgren[7], Jana Moldanova[7], and Ralf Zimmermann[1,2,3]

[1]Joint Mass Spectrometry Centre, Cooperation Group "Comprehensive Molecular Analytics" (CMA),
Helmholtz Zentrum München, 85764 Neuherberg, Germany
[2]Joint Mass Spectrometry Centre, Chair of Analytical Chemistry, University Rostock, 18059 Rostock, Germany
[3]Department Life, Light & Matter, University of Rostock, 18051 Rostock, Germany
[4]Photonion GmbH, 19061 Schwerin, Germany
[5]Institute of Mass Spectrometry and Atmospheric Environment, Jinan University, Guangzhou 510632, China
[6]Guangzhou Hexin Instrument Co., Ltd, Guangzhou 510530, China
[7]IVL Swedish Environmental Research Institute, 411 33 Gothenburg, Sweden

Correspondence: Johannes Passig (johannes.passig@uni-rostock.de)

Abstract. We describe resonance effects in laser desorption–ionization (LDI) of particles that substantially increase the sensitivity and selectivity to metals in single-particle mass spectrometry (SPMS). Within the proposed scenario, resonant light absorption by ablated metal atoms increases their ionization rate within a single laser pulse. By choosing the appropriate laser wavelength, the key micronutrients Fe, Zn and Mn can be detected on individual aerosol particles with considerably improved efficiency. These ionization enhancements for metals apply to natural dust and anthropogenic aerosols, both important sources of bioavailable metals to marine environments. Transferring the results into applications, we show that the spectrum of our KrF-excimer laser is in resonance with a major absorption line of iron atoms. To estimate the impact of resonant LDI on the metal detection efficiency in SPMS applications, we performed a field experiment on ambient air with two alternately firing excimer lasers of different wavelengths. Herein, resonant LDI with the KrF-excimer laser (248.3 nm) revealed iron signatures for many more particles of the same aerosol ensemble compared to the more common ArF-excimer laser line of 193.3 nm (nonresonant LDI of iron). Many of the particles that showed iron contents upon resonant LDI were mixtures of sea salt and organic carbon. For nonresonant ionization, iron was exclusively detected in particles with a soot contribution. This suggests that resonant LDI allows a more universal and secure metal detection in SPMS. Moreover, our field study indicates relevant atmospheric iron transport by mixed organic particles, a pathway that might be underestimated in SPMS measurements based on nonresonant LDI. Our findings show a way to improve the detection and source attribution capabilities of SPMS for particle-bound metals, a health-relevant aerosol component and an important source of micronutrients to the surface oceans affecting marine primary productivity.

1 Introduction

Natural and anthropogenic aerosols play a pivotal role in global climate and biogeochemical cycles, yet limited available ambient observations result in large uncertainties. While sulfate and carbonaceous aerosols are intensively investigated for their climate effects (Wang et al., 2016; Seinfeld and Pandis, 2016; Kanakidou et al., 2005; Bond et al., 2013; Sofiev et al., 2018), the particle-bound metals have far-reaching impacts on ecosystems and human health. The redox cycling activity of inhaled transition metals such as

iron (Fe) induces oxidative stress and is involved in severe health effects from air pollution (Ye et al., 2018; Oakes et al., 2012; Fang et al., 2017). Furthermore, atmospheric particles are important sources of marine micronutrients (Mahowald et al., 2018; Jickells et al., 2005). The highly soluble and thus more bioavailable Fe from anthropogenic aerosols that adds to the larger flux of rather insoluble mineral dust is assumed to affect primary production and carbon export in a significant part of the world's oceans (Ito and Shi, 2016; Li et al., 2017; Ito, 2015). Beyond Fe, further biologically important trace metals exert health effects (Gaur and Agnihotri, 2019) or can modulate primary production (Mahowald et al., 2018). For example, as enzyme cofactors they can determine which enzymes cells can express, affecting the composition of microbial communities (Boyd et al., 2017). Productivity-limiting deficiencies of, e.g., manganese (Mn) and zinc (Zn) have been reported for marine regions (Mahowald et al., 2018). Zinc is also associated with toxicological responses to wood combustion aerosols (Uski et al., 2015; Kanashova et al., 2018). However, the magnitude and variability of anthropogenic sources of bioavailable metals in the sea are poorly characterized. Recently, anthropogenic fluxes and sources of Fe were estimated using isotope fingerprinting (Conway et al., 2019). Such studies require measurable differences between natural and anthropogenic isotope distributions of the respective metals. Alternative methods, preferably providing detailed source information, indicating the metal's bioavailability and acquiring episodic deposition events are required to refine the global distribution models with observational data.

Several mass-spectrometry-based analytical techniques for aerosol characterization have been developed, with single-particle mass spectrometry (SPMS) being a real-time method obtaining the size and a chemical profile from individual particles (Pratt and Prather, 2012; Laskin et al., 2018). In SPMS, the particles are introduced into a vacuum, individually sized and exposed to intense UV laser pulses that form a partly ionized plume (laser desorption–ionization, LDI) (Hinz and Spengler, 2007; Murphy, 2007). Ions are extracted and analyzed with respect to their mass-to-charge ratio (m/z). Typically observed ions are, e.g., organic fragments, salts, ammonia, nitrate, sulfate, alkali metals, mineral components such as silicate, and carbon clusters from elemental or organic carbon (EC or OC). Along with the single-particle aspect, SPMS stands out for its metal detection capabilities that yield unique source information data (Dall'Osto et al., 2016a, b; Pratt and Prather, 2012; Arndt et al., 2017). For example, vanadium can indicate ship emissions (Healy et al., 2009; Ault et al., 2010) and signal patterns of, e.g., aluminum, silicon and calcium point on soil dust particles (Sullivan et al., 2007). However, compound-specific ionization efficiencies differ significantly. For example, the particle's humidity and its main composition can have a strong effect on the detection of particle compounds (Neubauer et al., 1998), known as matrix effects. These effects are associated with

several poorly determined interactions at the particle surface and in the desorbed plume affect ion formation (Reilly et al., 2000; Reinard and Johnston, 2008; Hinz and Spengler, 2007; Murphy, 2007; Wade et al., 2008; Hatch et al., 2014; Schoolcraft et al., 2000), reduce detection efficiencies, and complicate quantification approaches (Healy et al., 2013; Gemayel et al., 2017; Gross et al., 2000; Fergenson et al., 2001; Qin et al., 2006; Zhou et al., 2016; Shen et al., 2019). These difficulties can be mitigated if the desorption and ionization are separated in a two-step process and ions are formed in the gaseous plume as demonstrated for aromatic hydrocarbons (Morrical et al., 1998; Bente et al., 2008; Woods et al., 2001). In such a two-step approach, thermal or laser desorption (LD) is often followed by resonance-enhanced multiphoton ionization (REMPI), a gas-phase ionization technique that is highly sensitive and selective for aromatic molecules (Gunzer et al., 2019). The LD-REMPI approach yields detailed mass spectra of the health-relevant polycyclic aromatic hydrocarbons (PAHs) – ubiquitous trace compounds of combustion particles (Bente et al., 2009; Li et al., 2019; Passig et al., 2017; Schade et al., 2019). Resonant laser ablation of metals, where the leading edge of the laser pulse ablates atoms from a solid sample that are then ionized by the same pulse, have been studied some time ago for laser microprobe mass analysis (LAMMA) from surfaces (Verdun et al., 1987; McLean et al., 1990). However, to the best of our knowledge, such effects have so far not been recognized and applied in aerosol and single-particle mass spectrometry. In the current study, we report on such wavelength-dependent enhancements in LDI ion yields of transition metals from aerosol particles. Using an optical parametric oscillator (OPO), we demonstrate that besides Fe, the sparsely detected and biologically relevant trace metals Zn and Mn can also be observed in anthropogenic particles with much higher sensitivity. We show that the resonant absorption of iron coincides with the spectrum of the field-deployable KrF-excimer laser and with the REMPI absorption spectra of most aromatic molecules. Thus, the enhanced detection sensitivity for metals can be combined with detailed spectra of aromatic substances via REMPI. Finally, we demonstrate the application potential of the resonance effects in a field study comparing the KrF-excimer laser with a commonly used ArF-excimer laser for their Fe detection capabilities in ambient aerosols. We found that resonant LDI also reveals Fe signatures in particle types that produced no Fe signals upon nonresonant LDI, suggesting that the relevance of organic aerosols and salts as a source for Fe might have been underestimated in earlier SPMS studies.

2   Methods

2.1   Single-particle mass spectrometer and optical setup

The basic SPMS instrument (Hexin Instruments Ltd., Guangzhou, China, and Photonion GmbH, Schwerin, Ger-

many) is described in other publications (Li et al., 2011). Briefly, its instrumental layout is conceptually close to the aerosol time-of-flight mass spectrometer (ATOF-MS) (Su et al., 2004), with an aerodynamic lens inlet and an optical sizing unit that is comprised of a pair of 75 mW continuous-wave lasers at a wavelength of 532 nm, ellipsoidal mirrors and photomultipliers. The dual-polarity mass spectrometer is designed in Z-TOF geometry, as introduced by Pratt et al. (2009). For further details, e.g., the inlet particle transmission and detection efficiency, we refer to the literature (Li et al., 2011; Zhou et al., 2016). After the laboratory experiments, we implemented delayed ion extraction ($\Delta t = 0.4\,\mu s$) using high-voltage switches (HTS31-03-GSM, Behlke GmbH, Germany) to improve the peak quality in the ambient air experiments (Vera et al., 2005; Li et al., 2018). Major modifications to the commercial device are made to the ionization laser and the optical setup. We equipped the instrument with both a tuneable laser system (optical parametric oscillator, OPO) and excimer lasers ($\lambda = 248$ nm and $\lambda = 193$ nm) and replaced the Nd:YAG solid-state laser ($\lambda = 266$ nm, fourth harmonic frequency) that belongs to the instruments standard configuration. Apart from the wavelength, most beam parameters were comparable throughout the experiments; see Table 1 for details. The pulse energy was measured at the optical entrance and exit of the mass spectrometer and the position of the focal lens ($f = 200$ mm) was adjusted to maintain a comparable spot area, with a respective intensity for all wavelength comparison experiments. The OPO wavelengths and the KrF-excimer laser spectrum were measured with a LRL-005 spectrometer (MK Photonics Inc. USA).

2.2 Data analysis

In the laboratory experiments, only particles with both a positive and negative ion spectrum, each showing at least two peaks above the noise level, were considered. Raw time-of-flight data were converted to mass spectra considering peak area within nominal mass resolution by custom software on MATLAB platform (MathWorks Inc.). For particle classification in the ambient air study, we utilized the adaptive resonance theory neural network, ART-2a (Song et al., 1999) from the open-source toolkit FATES (Flexible Analysis Toolkit for the Exploration of SPMS data) (Sultana et al., 2017) with a learning rate 0.05, a vigilance factor of 0.8 and 20 iterations.

2.3 Model particles, sampling and setup for ambient air experiments

Diesel exhaust particles from an old van (Volkswagen Transporter 1.7 D, 1988 model) were collected from the inner surface of the exhaust tube. These particles exhibit a rather uniform chemical composition, as demonstrated in previous experiments (Passig et al., 2017; Schade et al., 2019). Model

particles for mineral dust were Arizona test dust 0–3 μm diameter (Powder Technology Inc., USA), and complex anthropogenic aerosols with trace metals were mimicked using NIST urban dust 1649b (Gonzalez and Choquette, 2016). Using a turntable-based powder disperser (Model 3433, TSI Inc., USA), particles were introduced into a 1 L min^{-1} carrier gas stream (N$_2$, purity: 5.0) from which 0.1 L min^{-1} were guided in an isokinetic flow into the instrument. For the experiments on ambient air, the SPMS instrument was set up at a meteorological station in a rural environment on the western coast of Sweden, about 30 km south of Gothenburg (coordinates 57°23′37.8″ N, 11°54′51.4″ E). Ambient air was sampled at a height of 7 m above ground (15 m above sea level). Aerosols from a 300 L min^{-1} intake airflow were concentrated into the 1 L min^{-1} carrier gas stream first using a virtual impactor device (Model 4240, MSP corp., USA). After passing a dryer (Model MD-700-12S-1, Perma Pure LLC, USA), they were further concentrated to 0.1 L min^{-1} in a second step directly at the SPMS aerodynamic lens inlet. The concentration is most effective for particles of around 1 μm in size, while it drops below 0.5 μm; see Fig. S1 in the Supplement for a comparison of particle numbers in ambient air with and without using the concentrator. The two KrF and ArF excimer lasers used in this experiment were alternately triggered to particles using a custom electronic circuit based on a complex programmable logic device (Intel Max V) with 8.5 ns pin-to-pin delay and programmed using the Very High Speed Integrated Circuit Hardware Description Language (VHDL). The excimer laser beams were focused from opposite sides onto the particle beam; see Table 1 and Sect. 3.3 for details.

3 Results and discussion

3.1 Resonance enhancements of Fe signals

We measured the Fe signals from diesel soot and Arizona desert dust particles as representative models of relevant anthropogenic and natural aerosols transporting Fe into the oceans. Figure 1a and b show the respective mass spectra of positive and negative ions from LDI with two different wavelengths using the OPO. The mass spectra were accumulated over every 400 particles, without normalization or further processing. The observed peak-broadening results mainly from accumulation over single-particle spectra with varying ion energy and starting positions. Typical signatures for (diesel) engine emissions (Toner et al., 2006) are recognizable, e.g., clusters of elemental carbon (EC, from soot) and organic hydrocarbon fragments (OC) (Silva and Prather, 2000). Also, alkali metals are frequently detected due to their low ionization energy. The desert dust particles (Fig. 1b) reveal typical mineral dust signals from metals and metal oxides (Sullivan et al., 2007; Dall'Osto et al., 2010). The slightly different laser wavelengths yield rather similar mass

Table 1. Light sources and details of the optical setup.

Laser source	Opolette HE 355 LD UV, Opotek LLC, USA	PhotonEx, Photonion GmbH, Germany	ATLEX-I 300, ATL GmbH, Germany
Laser medium	Optical Parametric Oscillator, Nd:YAG pumped	KrF gas (excimer)	ArF gas (excimer)
Wavelength (nm), photon energy (eV)	Tuneable 210–2400	248, 4.99	193, 6.41
Pulse duration (ns)		≈ 5	
Beam size (mm)	Ø3 nearly Gaussian	3×6 Gaussian $\times$ flat top	3×6 Gaussian $\times$ flat top
Interaction spot distance to focus (mm)	≈ 8–11	7	7
Rayleigh length (mm)	≈ 1.2–1.5	1.4	1.1
Interaction spot size (µm)	Ø160	105×210	105×210
Pulse energy (mJ)	0.4	3	
Pulse intensity at interaction spot (GW cm^{-2})	0.8	5	

spectra. However, much stronger Fe signals can be observed for 248.3 nm for both particle types (see insets in Fig. 1a and b). This wavelength matches the $3d^6 4s^2 \rightarrow 3d^6 4s 4p$ transition of Fe atoms, a line that is also typically used for Fe determination in atomic absorption spectroscopy. As apparent from the histogram plots in Fig. 1c and d, the enhancement effect does not result from some especially Fe-rich particles. Instead, most particles show higher Fe signals at the resonance wavelength, and the fraction of particles without Fe signals drops considerably. However, the high Fe content of Arizona dust particles ($\approx 4\%$–7\%) often leads to saturated signals on the single-particle level. Even stronger saturation effects producing highly corrupted Fe peaks were observed for hematite, which is consequently not shown here. Because interferences with CaO$^+$ and organic fragments such as $C_3H_4O^+$ can affect the signal differences at $m/z = 56$, the histograms show the signal of the ^{54}Fe isotope. Contributions from organic fragments to $m/z = 54$ are assumed to be rather small, as apparent from the signal strengths of principal fragments in the respective mass range at $m/z = 51$, 53 and 55; see inset of Fig. 1a. However, such interferences might lead to a moderate underestimation of the resonance enhancement. A further resonance effect can be noticed for lithium at the reference wavelength of 242.2 nm because of the $1s^2 2s \rightarrow 1s^2 7p$ transition close to this wavelength. Experimental results on hemoglobin powder, representing a particle model with uniform organic composition, are shown in Fig. S4 and confirm the resonance enhancements for Fe.

To further investigate the enhancement effects, we measured the wavelength-dependent total ion yield of ^{54}Fe from every 1200 particles, exposed to OPO laser pulses of the same intensity. As shown in Fig. 2, the maximum Fe signal is achieved near the resonance, with a 3–4-fold enhancement for diesel soot and mineral dust particles and hemoglobin

particles; see Fig. S4. The ion yield curves have a remarkable width and are much broader than the atomic lines or the OPO linewidth (4–6 cm^{-1}). The absorption spectrum of Fe atoms (blue) represents data from the NIST atomic spectra library (Kramida et al., 2019). Such signal enhancements at specific wavelengths were not reported in previous SPMS studies, apart from the aforementioned REMPI techniques. Thomson et al. (1997) observed that the threshold intensity for ion formation decreased with increasing absorbance of the bulk material for different salts. Generally, more substances are ionized at higher photon energies and lower laser intensities are required, but these effects tend to saturate at higher laser intensities (Thomson et al., 1997; Murphy, 2007). Even in a study using two matrix-assisted LDI (MALDI) matrix materials absorbing at different wavelengths, Wade et al. (2008) found only minimal wavelength effects on ion yields but a stronger dependence on the intensity and particle size. However, these results are not conflicting with the Fe resonance we observed. Several studies indicate that above a minimum intensity, effects in the plume dominate the ionization yield rather than the absorbance of the particle itself (Carson et al., 1997; Wade et al., 2008; Reinard and Johnston, 2008). The resonance begins to take effect as soon as Fe atoms are formed and vaporized from the particle during the initial phase of the laser pulse.

While not recognized for SPMS so far, such resonance enhancements were previously reported and explained for laser ablation from solid surfaces. Using dye lasers, about 5-fold signal increases were observed at the atomic lines of several metals and semiconductors (Verdun et al., 1987). The widths of the resonances were also rather broad, i.e., 0.4–0.7 nm. For low laser intensity, grazing incidence and two-step excitation, the width dropped below 0.05 nm (McLean et al., 1990) approaching the values of the respective atoms in
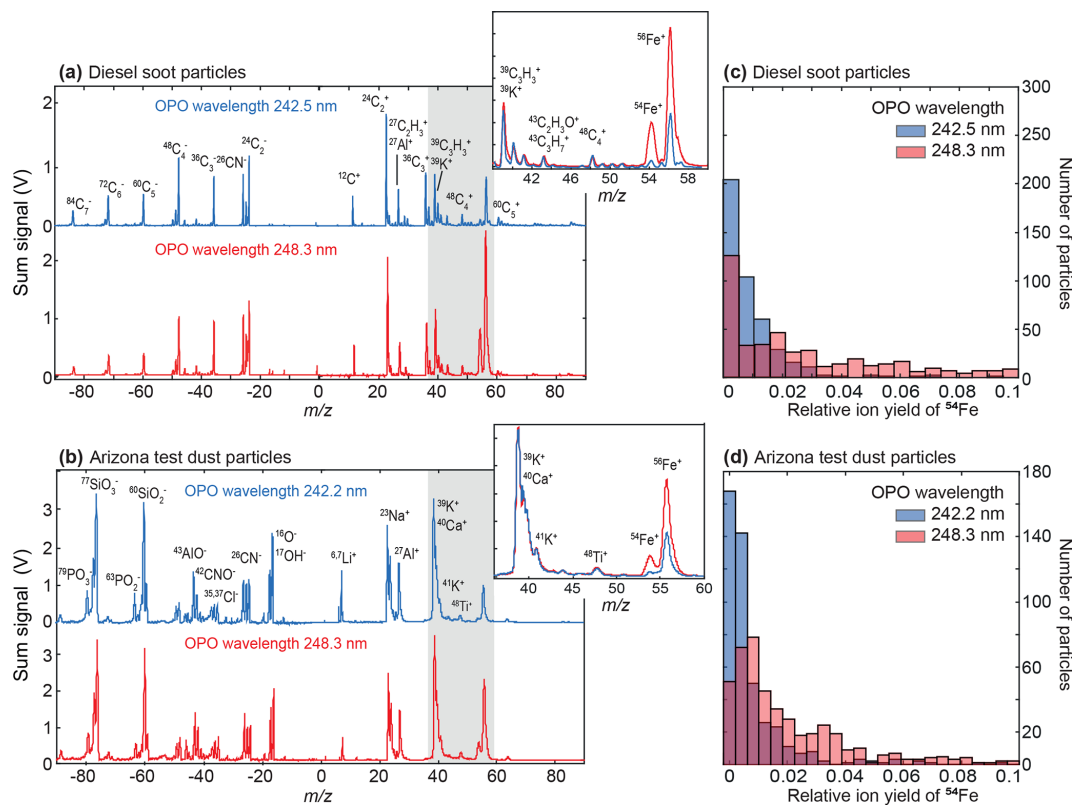
Figure 1. (a) Accumulated mass spectra (every $n = 400$) of re-dispersed diesel soot particles ionized using the tuneable OPO laser. In the case of resonant ionization of Fe at 248.3 nm (red), the Fe signal is substantially enhanced compared to the nonresonant ionization at 242.5 nm (blue); see the inset for an enlarged view of the grey area. Most other signals are similar. **(b)** A comparable Fe enhancement can be observed for mineral dust particles. The histogram panels **(c)** and **(d)** of the single-particle relative ion signal ($^{54}Fe^+$ signal normalized to the particle's total ion yield) illustrate that the ionization enhancement accounts for the majority of analyzed particles. Corresponding normalized mass spectra are shown in Fig. S2, and the particle size distributions are depicted in Fig. S3.

gas-phase ionization (resonant ionization MS, RIMS; Young et al., 1989). The explanation for the broad signals in resonant ablation from surfaces and particles is rather simple: broadening and transition wavelength shifts can be expected if the excitation happens when atoms are still bound in the matrix close to the surface (Verdun et al., 1987; McLean et al., 1990). Additionally, the plasma pressure could contribute to these effects. With increasing time and distance from the dense target, the surface bonds vanish and the conditions become similar to RIMS. Minor contributions to the measured width could result from Stark broadening (typically at higher laser power; Hübert and Ankerhold, 2011) and interferences with the adjacent absorption lines.

3.2 Resonance enhancements of trace metals

The resonant ionization of particle-bound Fe raises the question whether the SPMS-based detection of other biologically relevant metals may also benefit from the enhancement. We used NIST reference material urban dust 1649b (National Standard Institute of Technology, USA) as a well-characterized anthropogenic particle model containing several transition metals at low concentrations. Figure 3 shows accumulated cation mass spectra from resonant and nonresonant ionization with respect to strong atomic lines of Fe, Mn and Zn. The mass fraction of Fe is rather high ($\approx 3\%$) and the signal enhancement at 248.3 nm (see Fig. 3a) corresponds to the results from diesel soot and Arizona dust. Manganese contributes a mass fraction of only 0.024 % to the dust. In general, for particles with organic content, the Mn signature at $m/z = 55$ can hardly be distinguished from molecular fragments of the same mass. However, when the OPO wavelength is in resonance with the $3d^54s^2 \rightarrow 3d^54s4p$ transition of Mn at 279.5 nm, a clear signal appears at $m/z = 55$, nearly as high as the peak of the much more abundant ^{56}Fe in the sum spectrum; see Fig. 3b. Additionally, for Zn (mass fraction 0.17 %) there is a substantial difference and a clear signature appears in resonance case (Fig. 3c). Because the resonance wavelength of 213.8 nm is near the UV limit of the OPO, the pulse energy of 0.25 mJ is lower than for the other metals and, in contrast to all other wavelength comparisons, the reference wavelength is higher than the resonance wavelength. After resonant excitation at the respec-
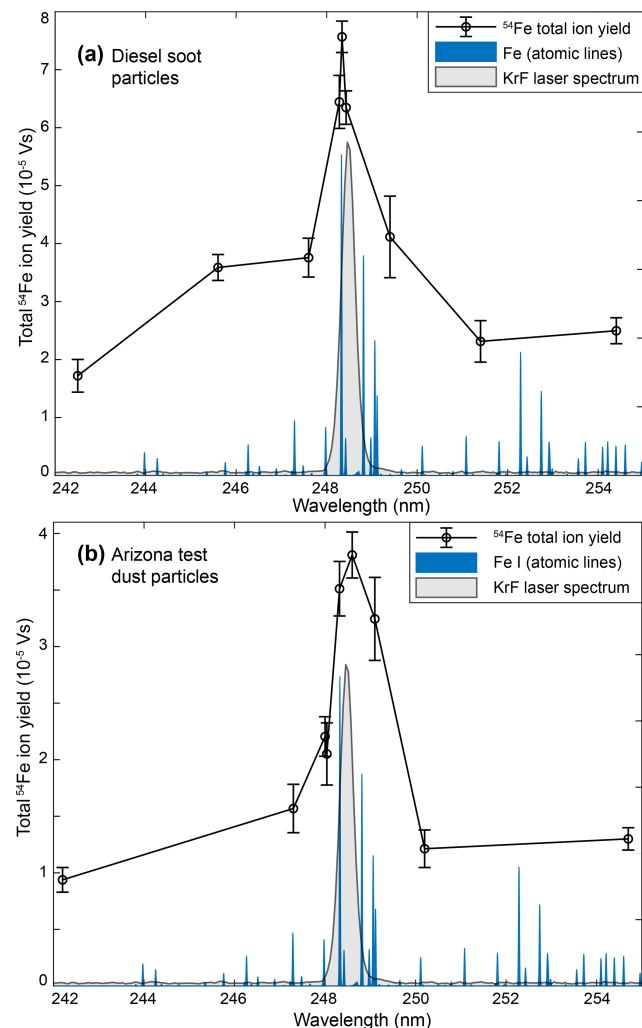
Figure 2. Wavelength-dependent total ion yield of ^{54}Fe in SPMS of re-dispersed particles (black circles, $n = 1200$; three replicates of 400 each). For both **(a)** diesel soot particles and **(b)** Arizona desert dust particles, the signal peaks for wavelengths match a major atomic transition of Fe (blue lines). The large width of the curve is attributed to line broadening through interaction with the dense particle surface. Coincidentally, the Fe lines are also addressed by our KrF-excimer laser (measured spectrum in grey; arbitrary units). Atomic spectra from the NIST library (Kramida et al., 2019). Mass spectra are shown in Fig. 1, the respective curves of the normalized ion signals and size distributions are given in Fig. S3.

tive wavelength, the absorption of a further single photon is sufficient for ionization of all three metals. The histogram plots (Fig. 3d–f) prove that the enhancement does not only result from a minority of particles that contribute especially strong ion signals. In contrast, a higher number of individual particles reveal signatures of the respective metals, which indicates a more secure and sensitive detection. The results suggest that tuneable laser systems can be advantageous to enhance the detectability of various elements of interest in SPMS.

3.3   Application to long-range transported aerosols

While our laboratory experiments revealed remarkable resonance effects for several metals and particle types, these results have to be transferred into applications for ambient aerosols. Tuneable laser systems are of limited suitability for field studies because of their complexity, low pulse power and repetition rate. In our experiments, thermal lensing problems of the irregularly triggered OPO system reduced its pulse power and stability, resulting in a shot-to-shot variability of the pulse power up to about 30 %. However, a freely triggerable OPO-SPMS with sufficient pulse energy is under development. In contrast to tuneable light sources, excimer lasers are cheaper, more robust and powerful. Of note, the KrF-excimer laser line at 248.3 nm coincidentally matches the strongest UV absorption line of Fe, a fact that has gained little attention in the last few decades (Trainor and Mani, 1978; Seder et al., 1986). The spectrum of our laser is shown in Fig. 2. We directly compare the Fe detection efficiencies of two field-deployable excimer lasers for the same ambient aerosol ensemble. The KrF line is in resonance with the Fe absorption, while the often-used ArF line is not. To exclude all effects from different instrumentation, both lasers are integrated into the same SPMS, firing with the same pulse parameters from opposite sites onto the particles; see Fig. 4a and Table 1. A custom electronic circuit triggers the lasers alternately. With regard to the important application of detecting Fe-containing aerosols in remote regions, we designed our experiment to observe long-range transported anthropogenic particles with high secondary contributions in a marine environment. Therefore, we set up our instrument on the western coast of Sweden and measured aerosols from central Europe after transport over the Baltic Sea; see the back trajectories in Fig. 4b.

With each of the lasers, we analyzed 15 000 individual particles on the 14 November 2019 between 15:00 and 24:00 local time. The mean particle mass concentration was 7.8 µg m^{-3} (PM$_{2.5}$) and 5.0 µg m^{-3} (PM$_{1.0}$) as measured by the station's dust monitor (Grimm EDM-180 MC). Figure 4c shows the resulting sum mass spectra of cations for each ionization wavelength. The enhanced Fe signature for the Krf laser is clearly visible in the sum spectrum. All further wavelength-dependent differences will be discussed in a future publication. From every 15 000 particles exposed to the ArF laser (KrF laser), 13 776 (6364) produced a negative spectrum, 12 217 (5577) a positive signature and 12 189 (5258) yielded bipolar mass spectra. The higher hit rate of the ArF laser results from the lower intensity thresholds for ion formation due to its higher photon energy (Thomson et al., 1997), thus also yielding mass spectra from particles that were not fully hit. Nearly all particles (> 98 %) with negative spectra showed nitrate (^{46}NO$_2^-$ and ^{62}NO$_3^-$). Because the steady onshore wind during the experiment excludes local sources of nitrate, these ions indicate condensation of NO$_3$ and replacement of Cl$^-$ by NO$_3^-$ (Gard et
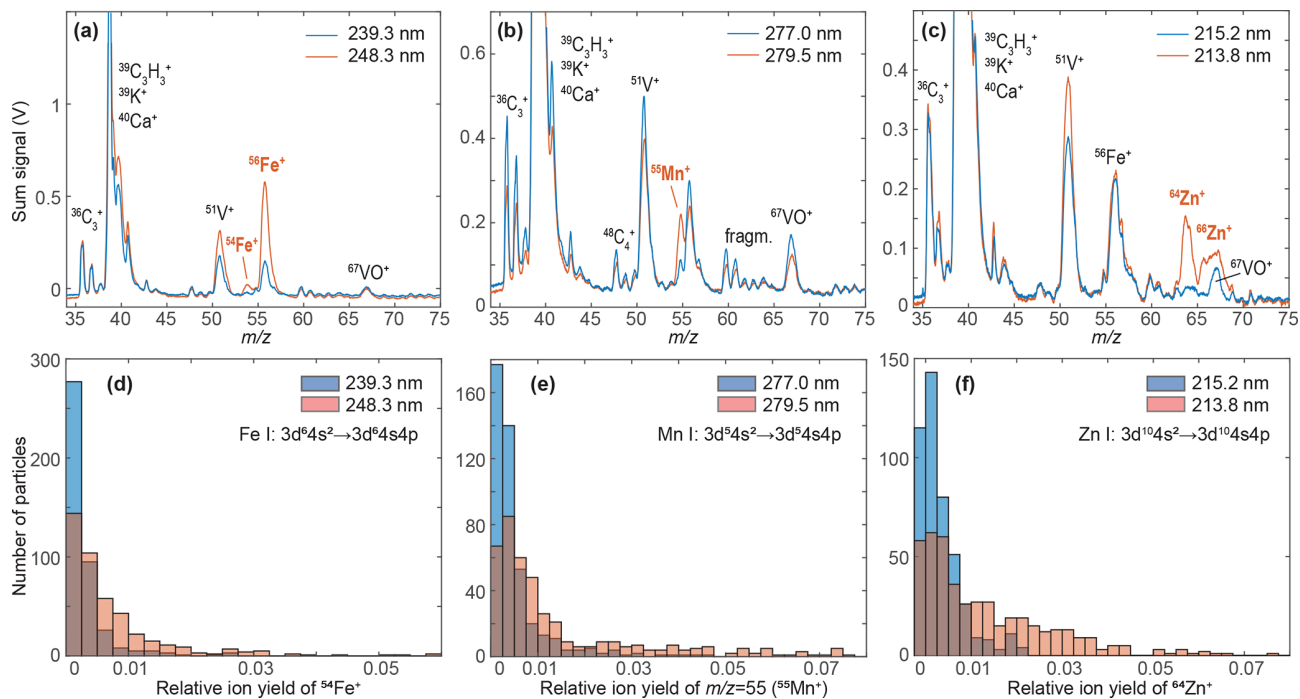
Figure 3. Accumulated cation mass spectra ($n = 400$) of re-dispersed urban dust particles (reference material NIST 1649b). Using the tuneable OPO, the spectra were recorded at resonance wavelengths of each metal (red) and for the nonresonant case at a slightly different wavelength (blue). While carbon and molecular fragment signals are similar in the pairwise comparison, the resonant enhancements for **(a)** Fe, **(b)** Mn and **(c)** Zn are clearly visible. Complete bipolar mass spectra and the size distribution are shown in Fig. S5. **(d–f)** The single-particle distribution of the relative ion signals illustrates that the resonant ionization enhancement allows metal detection for many more particles. The respective resonance wavelengths (red) address the indicated transitions.
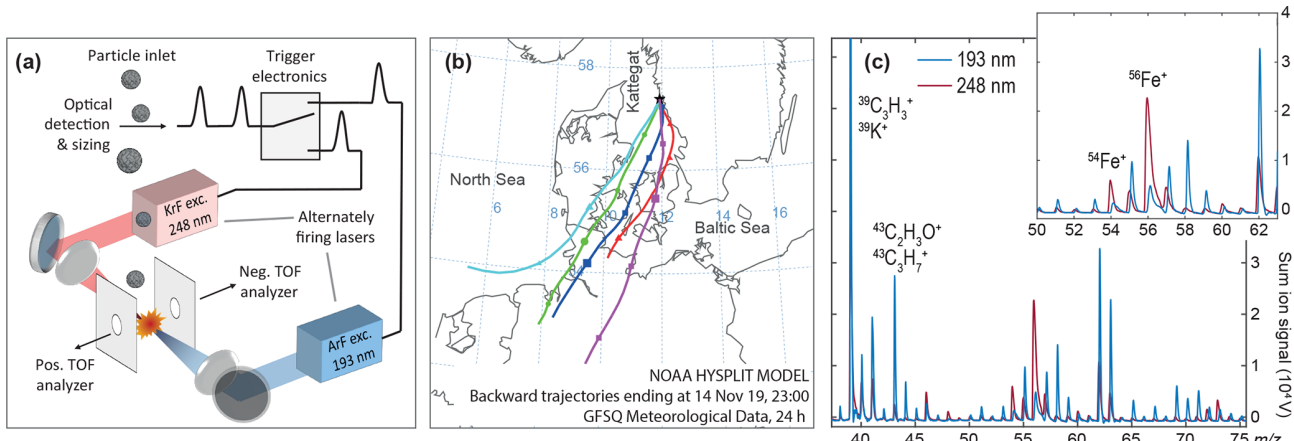
Figure 4. (a) Schematic view of the setup for direct comparison of nonresonant and resonant ionization of Fe in ambient air particles using the same mass spectrometer. The two lasers fired alternately on 15 000 particles each. **(b)** Back trajectories from the HYSPLIT webtool (http://www.ready.noaa.gov/HYSPLIT.php, last access: 13 December 2019) (Stein et al., 2015; Rolph et al., 2017), ending at the sampling site (sea level) during the experiment on long-range transported particles. **(c)** Accumulated cation mass spectra (every $n = 15\,000$) show a Fe^+-signal enhancement for ionization with the KrF excimer laser (248 nm, red) versus the ArF excimer laser (193 nm, blue). Further differences will be discussed in a different publication.

al., 1998; Arndt et al., 2017; Dall'Osto et al., 2016b) during long-range transport from central Europe (Dall'Osto et al., 2016a). Most single-particle spectra are dominated by either sea salt signatures ($^{23}Na^+$, $^{46}Na_2^+$, $^{62}Na_2O^+$, $^{63}Na_2OH^+$ and $^{81,83}Na_2Cl^+$) (Murphy et al., 2019) or organic fragments (e.g., $^{27}C_2H_3^+$, $^{39}C_3H_3^+$, $^{43}C_2H_3O^+$ and $^{43}C_3H_7^+$) (Silva and Prather, 2000) or they reveal internal mixtures of these main components. To investigate the Fe enhancements on the single-particle level and to analyze the role of the particle's main components, we performed a cluster analysis for each set of bipolar single-particle spectra, excluding the mass channels $m/z = 54$–56 that bear potential Fe signatures. The ART-2a algorithm yielded 149 clusters for the particles ionized with the ArF laser and 106 clusters for the KrF laser ionization. Clusters with less than 20 particles were excluded from the analysis. Furthermore, clusters with comparable average mass spectra and the same major ions but slightly varying relative signal intensities were manually merged.

The particle ensemble revealed six dominating particle groups, as summarized in Table 2. The corresponding ART-2a area matrices representing the average intensity for each m/z and thus reflecting the typical mass spectra within a group are shown in Figs. S6 and S7. Further separation into subgroups, e.g., with respect to signals from $^{18}NH_4^+$, $^{30}NO^+$ or trimethylamine (TMA, $m/z = 58$–59) (Healy et al., 2015; Köllner et al., 2017), had only limited effects on Fe detection and is consequently not shown here. Mineral dust particles were not observed in appreciable numbers. The measured size distribution is rather narrow, reflecting the instruments optimum detection efficiency that roughly coincides with the typical size mode undergoing long-range transport; see Fig. S8.

The particle numbers within the main classes are shown in Fig. 5. There are several differences between the two ionization wavelengths, e.g., the aforementioned overall hit rate. However, here we focus on the detection of Fe. In order to ensure a conservative effect registration (i.e., signals at $m/z = 56$ that may also stem from CaO^+ or molecular fragments such as $C_3H_4O^+$), Fe content is only accounted for particles with a peak area at $m/z = 56$ that is larger than both the signals at $m/z = 40$ (Ca^+) and $m/z = 55$ (principal fragment signal). To further strengthen the screening, as recommended by previous studies (Zhang et al., 2014; Dall'Osto et al., 2016a), particles with an additional signal at $m/z = 54$ from the ^{54}Fe isotope, which is lower than a tenth of the peak area of ^{56}Fe, are represented by black bars. Half of the particle spectra that were identified by the algorithm to show the ^{54}Fe isotope, were manually cross-checked on a random basis to prevent false positive results. From the 15 000 particles exposed to the 193 nm laser pulses, fewer than 100 particles show Fe signatures according to this stringent criterion. As is apparent from the enlarged view on the right of Fig. 5a, nearly all of these particles also revealed strong carbon cluster signals from EC. This suggests that they either belong to a particular Fe-rich aerosol class, e.g., from ship emis-

Table 2. Main particle classes from ART-2a clustering and subsequent merging with respect to the major components. The respective mass spectra are shown in Figs. S6 and S7.

|	Aged sea salt	Aged sea salt and minor OC	Salt/OC mixed	OC	OC+EC	Fe	Anions only
Dominating ion signals	$^{23}Na^+$, $^{46}Na_2^+$ $^{62}Na_2O^+$ $^{63}Na_2OH^+$, $^{46}NO_2^-$, $^{62}NO_3^-$		$^{23}Na^+$, $^{46}Na_2^+$, $^{39}K^+$ and molec. fragments	$^{39}K^+$, $^{43}C_2H_3O^+$ and molec. fragments, $^{18}NH_4^+$, $^{30}NO^+$, $^{59}C_3H_9N^+$ (TMA)	$^{24}C_2^+$, $^{36}C_3^+$, $^{24}C_2^-$, $^{36}C_3^-$,	$^{56}Fe^+$, $^{73}FeOH^+$	$^{46}NO_2^-$, $^{62}NO_3^-$
Further required signals for assignment	$^{81,83}Na_2Cl^+$, $^{35,37}Cl^-$	$^{39}K^+$ and molec. fragments	balanced ratio between salt and OC signatures	no or minimal salt signatures		no cations	
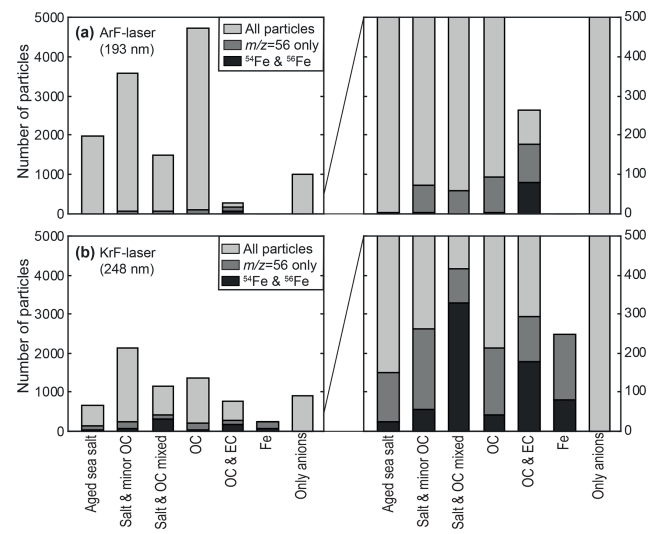
Figure 5. Number of particles within the main classes according to Table 2. Dark grey fractions represent particles with a peak area at $m/z = 56$ being larger than at $m/z = 55$ (molecular fragments) and $m/z = 40$ (Ca^+ because of interference with $^{56}CaO^+$), indicating Fe content. Black fractions illustrate particles showing an additional signal of the less abundant isotope $^{54}Fe^+$. **(a)** If ionized with 193 nm pulses, substantial fragmentation leads to dominating fragment signals in many of the 15 000 exposed particles. Fe signals are almost exclusively observed for particles with EC signatures (see the enlarged view on the right), indicating a particularly high Fe content or possible interactions with strongly absorbing soot during ionization. **(b)** Although fewer particles produce ion signals if exposed to 248 nm pulses, the particle fraction showing Fe signatures is much larger, and a cluster with dominating Fe signals even appears. It is important to note that the Fe signals are not limited to EC-containing particles but can be observed for all classes. This suggests that the resonant ionization allows a more universal and secure detection of Fe.

sions, or that the EC matrix augments the ionization process of Fe (Zimmermann et al., 2003) in contrast to a salt/OC matrix, where energetically preferred ions survive collisional charge transfer in the plume (Reinard and Johnston, 2008). Additionally, a suppression of specific ions by the presence of water is conceivable (Neubauer et al., 1998), although a dryer was applied in our experiment. A very different Fe detection was achieved with the resonant ionization at 248 nm; see Fig. 5b. Even though the total particle hit rate was lower, many more particles with Fe signatures were detected. A key finding is that the Fe detection is not limited to particles with EC signatures anymore, but the Fe appears to be internally mixed within particles of several classes. The relatively low abundance of Fe in the OC class can be explained by the high contribution of wood and biomass combustion particles. Remarkably, many particles with low cation signals reveal nearly exclusively Fe signatures, providing its own group after further classification into subgroups (Fe signatures were excluded from the first ART-2a clustering).

Since the same aerosol ensemble was probed with both laser wavelengths, the appearance of Fe signals for several particle matrices disagrees with the assumption of a particular Fe-rich class. In contrast, different ionization mechanisms are likely to determine the Fe detection, and resonant LDI appears to feature a more universal and secure detection approach for iron.

Although our field study provides only a limited dataset, some general implications can already be derived. The internal mixing of Fe with sulfate or organic acids is assumed to be crucial for Fe dissolution and thus for the anthropogenic increase in bioavailable iron input to the oceans (Li et al., 2017). Previous studies indicated that the Fe transport into the sea is dominated by coal combustion particles containing sulfate in Asia (Furutani et al., 2011; Moffet et al., 2012), while the majority of Fe-containing particles in Europe are mixed with nitrate and were attributed to traffic activities (Dall'Osto et al., 2016a). Similar to our experiment, these studies found strong internal mixing of many Fe-containing particles, such as biomass burning signals with coal combustion contributions in Asia and secondary nitrate with Fe in Europe. However, Fe particles with sea salt signatures were negligible in the SPMS studies and mixtures of Fe and OC were a minor fraction (Furutani et al., 2011; Dall'Osto et al., 2016a). In our study, these particles were the most abundant types of Fe-containing particles if resonant ionization was applied (see Fig. 5b), while for nonresonant ionization, particles with EC signatures were dominant (Fig. 5a). Taking into account that the aforementioned SPMS studies utilized nonresonant LDI of Fe at 266 nm, Fe transport in organic and salt or mixed aerosols might have been underestimated. Electron microscopy studies of individual particles in Asia frequently revealed thick coatings of secondary compounds and organic matter around Fe-rich particle components (Li et al., 2017; Moffet et al., 2012). Ultrafine Fe-containing particles, such as soot from traffic emissions, can enter the long-range transported accumulation mode via agglomeration with larger particles and condensation of organic vapors, secondary nitrate or sulfate. In our study, we observed a high prevalence of Fe in sea salt and OC particle types, indicating the importance of these pathways for transport of biologically relevant Fe.

4 Conclusions

In summary, we described enhancements in particle laser desorption–ionization that rely on resonant light absorption by metal atoms. Combining laboratory and field experiments, we showed that the mechanism can be exploited to improve the detection of relevant metals in both natural and anthropogenic aerosols on the single-particle level. Not all physical details are fully understood, and the signal enhancement effects providing the basis for the improved metal detection efficiency are difficult to quantify for the different particle types. However, our results show that the increase in sensi-

tivity is moderate for particular Fe-rich aerosols, such as the about 3-fold signal enhancement for Arizona test dust. The resonance enhancement appears to become more effective for mixed particles with smaller Fe contributions, such as in the ambient air experiment, where about 10 times more particles revealed Fe signatures in direct comparison with nonresonant ionization. Taking into account the lower hit rate of the KrF laser that is related to its lower photon energy, the overall efficiency for identifying Fe signatures in a single-particle mass spectrum was increased by a factor of about 20 in our ambient air study.

The coincidental matching of the KrF laser line with a strong absorption of Fe atoms allows an easy and straightforward application of the resonance effect in the field. For direct comparison of KrF with ArF lasers, it has to be considered that the lower photon energy of KrF laser is associated with a reduced hit rate and different mass spectral signatures of other particle components, e.g., organics. Further studies are required to evaluate these differences. Note that, because of its rather high pulse energy and the flat-top beam profile, the hit rate of the KrF laser was about 40 %–50 % in our experiment, which is still more than the values that are typically achieved with the most common laser line in SPMS, the Nd:YAG at 266 nm. Exploiting the resonance effect for metals other than Fe requires a tuneable Nd:YAG–OPO system, which is, however, more difficult to operate.

With the improved detection of Fe and its inherent sensitivity to further key nutrients such as nitrate and phosphate, SPMS becomes an interesting complement to established methods for investigating atmospheric Fe transport. Moreover, several key parameters for the metal's bioavailability, including the particle size or the presence of carboxylic acids and sulfate (Fang et al., 2017), can be determined on a single-particle level. Because of the high time resolution, SPMS-based Fe detection may be particularly helpful for studies on the oceans' rapid response to the naturally episodic depositions of Fe and other micronutrients. Beyond these direct applications, more studies are required to elucidate the promising implications for SPMS quantification approaches (Healy et al., 2013; Gemayel et al., 2017). Of note, the Fe-containing particles can further be characterized with regard to their organic content using multistep ionization techniques (Schade et al., 2019; Czech et al., 2017). This is of importance for health-related studies, as two of the most relevant adverse aerosol compounds, transition metals and PAHs, can be addressed with the same easily accessible KrF-excimer laser wavelength.

Such hyphenated single-particle schemes have great potential to elucidate intriguing interactions in atmospheric heterogeneous and multiphase chemistry (Pöschl and Shiraiwa, 2015), for example with regard to possible catalytic activities of the in particle's metal content (Sullivan et al., 2007). In conclusion, the described resonance effects pave a new route towards improved detection of air pollutants and a more pro-

found understanding of the aerosol impact on biogeochemical cycles and human health.

Author contributions. JP and JS contributed equally to this work. JP conceived the experiments. JS, EIR, JP, TKB and RI performed the experiments. LL, XL and ZZ provided the SPMS instrument and technical support. TKB developed the electronics. HC, MS, TS and RZ provided assistance with data interpretation. JM and HF hosted and supported the field study. JS, JP and EIR analyzed data and prepared the figures. JP wrote the manuscript with contributions from all authors.

References

Arndt, J., Sciare, J., Mallet, M., Roberts, G. C., Marchand, N., Sartelet, K., Sellegri, K., Dulac, F., Healy, R. M., and Wenger, J. C.: Sources and mixing state of summertime background aerosol in the north-western Mediterranean basin, Atmos. Chem. Phys., 17, 6975–7001, https://doi.org/10.5194/acp-17-6975-2017, 2017.

Ault, A. P., Gaston, C. I., Wang, Y., Dominguez, G., Thiemens, M. H., and Prather, K. A.: Characterization of the single par-

ticle mixing state of individual ship plume events measured at the Port of Los Angeles, Environ. Sci. Technol., 44, 1954–1961, https://doi.org/10.1021/es902985h, 2010.

Bente, M., Sklorz, M., Streibel, T., and Zimmermann, R.: On-line laser desorption-multiphoton postionization mass spectrometry of individual aerosol particles: molecular source indicators for particles emitted from different traffic-related and wood combustion sources, Anal. Chem., 80, 8991–9004, https://doi.org/10.1021/ac801295f, 2008.

Bente, M., Sklorz, M., Streibel, T., and Zimmermann, R.: Thermal desorption-multiphoton ionization time-of-flight mass spectrometry of individual aerosol particles: a simplified approach for online single-particle analysis of polycyclic aromatic hydrocarbons and their derivatives, Anal. Chem., 81, 2525–2536, https://doi.org/10.1021/ac802296f, 2009.

Bond, T. C., Doherty, S. J., Fahey, D. W., Forster, P. M., Berntsen, T., DeAngelo, B. J., Flanner, M. G., Ghan, S., Kärcher, B., Koch, D., Kinne, S., Kondo, Y., Quinn, P. K., Sarofim, M. C., Schultz, M. G., Schulz, M., Venkataraman, C., Zhang, H., Zhang, S., Bellouin, N., Guttikunda, S. K., Hopke, P. K., Jacobson, M. Z., Kaiser, J. W., Klimont, Z., Lohmann, U., Schwarz, J. P., Shindell, D., Storelvmo, T., Warren, S. G., and Zender, C. S.: Bounding the role of black carbon in the climate system: A scientific assessment, J. Geophys. Res., 118, 5380–5552, https://doi.org/10.1002/jgrd.50171, 2013.

Boyd, P. W., Ellwood, M. J., Tagliabue, A., and Twining, B. S.: Biotic and abiotic retention, recycling and remineralization of metals in the ocean, Nat. Geosci., 10, 167–173, https://doi.org/10.1038/ngeo2876, 2017.

Carson, P. G., Johnston, M. V., and Wexler, A. S.: Real-Time Monitoring of the Surface and Total Composition of Aerosol Particles, Aerosol Sci. Technol., 26, 291–300, https://doi.org/10.1080/02786829708965431, 1997.

Conway, T. M., Hamilton, D. S., Shelley, R. U., Aguilar-Islas, A. M., Landing, W. M., Mahowald, N. M., and John, S. G.: Tracing and constraining anthropogenic aerosol iron fluxes to the North Atlantic Ocean using iron isotopes, Nat. Commun., 10, 1–10, https://doi.org/10.1038/s41467-019-10457-w, 2019.

Czech, H., Stengel, B., Adam, T., Sklorz, M., Streibel, T., and Zimmermann, R.: A chemometric investigation of aromatic emission profiles from a marine engine in comparison with residential wood combustion and road traffic: Implications for source apportionment inside and outside sulphur emission control areas, Atmos. Environ., 167, 212–222, https://doi.org/10.1016/j.atmosenv.2017.08.022, 2017.

Dall'Osto, M., Harrison, R. M., Highwood, E. J., O'Dowd, C., Ceburnis, D., Querol, X., and Achterberg, E. P.: Variation of the mixing state of Saharan dust particles with atmospheric transport, Atmos. Environ., 44, 3135–3146, https://doi.org/10.1016/j.atmosenv.2010.05.030, 2010.

Dall'Osto, M., Beddows, D. C. S., Harrison, R. M., and Onat, B.: Fine Iron Aerosols Are Internally Mixed with Nitrate in the Urban European Atmosphere, Environ. Sci. Technol., 50, 4212–4220, https://doi.org/10.1021/acs.est.6b01127, 2016a.

Dall'Osto, M., Beddows, D. C. S., McGillicuddy, E. J., Esser-Gietl, J. K., Harrison, R. M., and Wenger, J. C.: On the simultaneous deployment of two single-particle mass spectrometers at an urban background and a roadside site during SAPUSS, At-

mos. Chem. Phys., 16, 9693–9710, https://doi.org/10.5194/acp-16-9693-2016, 2016b.

Fang, T., Guo, H., Zeng, L., Verma, V., Nenes, A., and Weber, R. J.: Highly Acidic Ambient Particles, Soluble Metals, and Oxidative Potential: A Link between Sulfate and Aerosol Toxicity, Environ. Sci. Technol., 51, 2611–2620, https://doi.org/10.1021/acs.est.6b06151, 2017.

Fergenson, D. P., Song, X. H., Ramadan, Z., Allen, J. O., Hughes, L. S., Cass, G. R., Hopke, P. K., and Prather, K. A.: Quantification of ATOFMS data by multivariate methods, Anal. Chem., 73, 3535–3541, https://doi.org/10.1021/ac010022j, 2001.

Furutani, H., Jung, J., Miura, K., Takami, A., Kato, S., Kajii, Y., and Uematsu, M.: Single-particle chemical characterization and source apportionment of iron-containing atmospheric aerosols in Asian outflow, J. Geophys. Res., 116, 5504, https://doi.org/10.1029/2011JD015867, 2011.

Gard, E. E., Kleeman, M. J., Gross, D. S., Hughes, L. S., Allen, J. O., Morrical, B. D., Fergenson, D. P., Dienes, T., Gälli, M. E., Johnson, R. J., Cass, G. R., and Prather, K. A.: Direct observation of heterogeneous chemistry in the atmosphere, Science, 279, 1184–1187, https://doi.org/10.1126/science.279.5354.1184, 1998.

Gaur, S. and Agnihotri, R.: Health Effects of Trace Metals in Electronic Cigarette Aerosols-a Systematic Review, Biol. Trace Elem. Res., 188, 295–315, https://doi.org/10.1007/s12011-018-1423-x, 2019.

Gemayel, R., Temime-Roussel, B., Hayeck, N., Gandolfo, A., Hellebust, S., Gligorovski, S., and Wortham, H.: Development of an analytical methodology for obtaining quantitative mass concentrations from LAAP-ToF-MS measurements, Talanta, 174, 715–724, https://doi.org/10.1016/j.talanta.2017.06.050, 2017.

Gonzalez, C. A. and Choquette, S. J.: Certificate of Analysis: Standard Reference Material 1649b, available at: https://www-s.nist.gov/srmors/certificates/1649b.pdf, last access: 23 April 2020.

Gross, D. S., Gälli, M. E., Silva, P. J., and Prather, K. A.: Relative Sensitivity Factors for Alkali Metal and Ammonium Cations in Single-Particle Aerosol Time-of-Flight Mass Spectra, Anal. Chem., 72, 416–422, https://doi.org/10.1021/ac990434g, 2000.

Gunzer, F., Krüger, S., and Grotemeyer, J.: Photoionization and photofragmentation in mass spectrometry with visible and UV lasers, Mass Spectrom. Rev., 38, 202–217, https://doi.org/10.1002/mas.21579, 2019.

Hatch, L. E., Pratt, K. A., Huffman, J. A., Jimenez, J. L., and Prather, K. A.: Impacts of Aerosol Aging on Laser Desorption/Ionization in Single-Particle Mass Spectrometers, Aerosol Sci. Technol., 48, 1050–1058, https://doi.org/10.1080/02786826.2014.955907, 2014.

Healy, R. M., O'Connor, I. P., Hellebust, S., Allanic, A., Sodeau, J. R., and Wenger, J. C.: Characterisation of single particles from in-port ship emissions, Atmos. Environ., 43, 6408–6414, https://doi.org/10.1016/j.atmosenv.2009.07.039, 2009.

Healy, R. M., Sciare, J., Poulain, L., Crippa, M., Wiedensohler, A., Prévôt, A. S. H., Baltensperger, U., Sarda-Estève, R., McGuire, M. L., Jeong, C.-H., McGillicuddy, E., O'Connor, I. P., Sodeau, J. R., Evans, G. J., and Wenger, J. C.: Quantitative determination of carbonaceous particle mixing state in Paris using single-particle mass spectrometer and aerosol mass spectrometer measurements, Atmos. Chem. Phys., 13, 9479–9496, https://doi.org/10.5194/acp-13-9479-2013, 2013.

Healy, R. M., Evans, G. J., Murphy, M., Sierau, B., Arndt, J., McGillicuddy, E., O'Connor, I. P., Sodeau, J. R., and Wenger, J. C.: Single-particle speciation of alkylamines in ambient aerosol at five European sites, Anal. Bioanal. Chem., 407, 5899–5909, https://doi.org/10.1007/s00216-014-8092-1, 2015.

Hinz, K.-P. and Spengler, B.: Instrumentation, data evaluation and quantification in on-line aerosol mass spectrometry, J. Mass Spectrom., 42, 843–860, https://doi.org/10.1002/jms.1262, 2007.

Hübert, W. and Ankerhold, G.: Elemental misinterpretation in automated analysis of LIBS spectra, Analytical and bioanalytical chemistry, 400, 3273–3278, https://doi.org/10.1007/s00216-011-4793-x, 2011.

Ito, A.: Atmospheric Processing of Combustion Aerosols as a Source of Bioavailable Iron, Environ. Sci. Technol. Lett., 2, 70–75, https://doi.org/10.1021/acs.estlett.5b00007, 2015.

Ito, A. and Shi, Z.: Delivery of anthropogenic bioavailable iron from mineral dust and combustion aerosols to the ocean, Atmos. Chem. Phys., 16, 85–99, https://doi.org/10.5194/acp-16-85-2016, 2016.

Jickells, T. D., An, Z. S., Andersen, K. K., Baker, A. R., Bergametti, G., Brooks, N., Cao, J. J., Boyd, P. W., Duce, R. A., Hunter, K. A., Kawahata, H., Kubilay, N., laRoche, J., Liss, P. S., Mahowald, N., Prospero, J. M., Ridgwell, A. J., Tegen, I., and Torres, R.: Global iron connections between desert dust, ocean biogeochemistry, and climate, Science, 308, 67–71, https://doi.org/10.1126/science.1105959, 2005.

Kanakidou, M., Seinfeld, J. H., Pandis, S. N., Barnes, I., Dentener, F. J., Facchini, M. C., Van Dingenen, R., Ervens, B., Nenes, A., Nielsen, C. J., Swietlicki, E., Putaud, J. P., Balkanski, Y., Fuzzi, S., Horth, J., Moortgat, G. K., Winterhalter, R., Myhre, C. E. L., Tsigaridis, K., Vignati, E., Stephanou, E. G., and Wilson, J.: Organic aerosol and global climate modelling: a review, Atmos. Chem. Phys., 5, 1053–1123, https://doi.org/10.5194/acp-5-1053-2005, 2005.

Kanashova, T., Sippula, O., Oeder, S., Streibel, T., Passig, J., Czech, H., Kaoma, T., Sapcariu, S. C., Dilger, M., Paur, H.-R., Schlager, C., Mülhopt, S., Weiss, C., Schmidt-Weber, C., Traidl-Hoffmann, C., Michalke, B., Krebs, T., Karg, E., Jakobi, G., Scholtes, S., Schnelle-Kreis, J., Sklorz, M., Orasche, J., Müller, L., Reda, A., Rüger, C., Neumann, A., Abbaszade, G., Radischat, C., Hiller, K., Grigonyte, J., Kortelainen, M., Kuuspalo, K., Lamberg, H., Leskinen, J., Nuutinen, I., Torvela, T., Tissari, J., Jalava, P., Kasurinen, S., Uski, O., Hirvonen, M.-R., Buters, J., Dittmar, G., Jokiniemi, J. K., and Zimmermann, R.: Emissions from a modern log wood masonry heater and wood pellet boiler Composition and biological impact on air-liquid interface exposed human lung cancer cells, Journal of Molecular and Clinical Medicine, 1, 23, https://doi.org/10.31083/j.jmcm.2018.01.004, 2018.

Köllner, F., Schneider, J., Willis, M. D., Klimach, T., Helleis, F., Bozem, H., Kunkel, D., Hoor, P., Burkart, J., Leaitch, W. R., Aliabadi, A. A., Abbatt, J. P. D., Herber, A. B., and Borrmann, S.: Particulate trimethylamine in the summertime Canadian high Arctic lower troposphere, Atmos. Chem. Phys., 17, 13747–13766, https://doi.org/10.5194/acp-17-13747-2017, 2017.

Kramida, A., Ralchenko, Yu., Reader, J., and NIST ASD Team: NIST Atomic Spectra Database (version 5.7.1), National Institute of Standards and Technology, Gaithersburg, MD, https://doi.org/10.18434/T4W30F, 2019.

Laskin, J., Laskin, A., and Nizkorodov, S. A.: Mass Spectrometry Analysis in Atmospheric Chemistry, Anal. Chem., 90, 166–189, https://doi.org/10.1021/acs.analchem.7b04249, 2018.

Li, C., He, Q., Schade, J., Passig, J., Zimmermann, R., Meidan, D., Laskin, A., and Rudich, Y.: Dynamic changes in optical and chemical properties of tar ball aerosols by atmospheric photochemical aging, Atmos. Chem. Phys., 19, 139–163, https://doi.org/10.5194/acp-19-139-2019, 2019.

Li, L., Huang, Z., Dong, J., Li, M., Gao, W., Nian, H., Fu, Z., Zhang, G., Bi, X., Cheng, P., and Zhou, Z.: Real time bipolar time-of-flight mass spectrometer for analyzing single aerosol particles, Int. J. Mass Spectrom., 303, 118–124, https://doi.org/10.1016/j.ijms.2011.01.017, 2011.

Li, L., Liu, L., Xu, L., Li, M., Li, X., Gao, W., Huang, Z., and Cheng, P.: Improvement in the Mass Resolution of Single Particle Mass Spectrometry Using Delayed Ion Extraction, J. Am. Soc. Mass Spectrom., 29, 2105–2109, https://doi.org/10.1007/s13361-018-2037-4, 2018.

Li, W., Xu, L., Liu, X., Zhang, J., Lin, Y., Yao, X., Gao, H., Zhang, D., Chen, J., Wang, W., Harrison, R. M., Zhang, X., Shao, L., Fu, P., Nenes, A., and Shi, Z.: Air pollution-aerosol interactions produce more bioavailable iron for ocean ecosystems, Sci. Adv., 3, e1601749, https://doi.org/10.1126/sciadv.1601749, 2017.

Mahowald, N. M., Hamilton, D. S., Mackey, K. R. M., Moore, J. K., Baker, A. R., Scanza, R. A., and Zhang, Y.: Aerosol trace metal leaching and impacts on marine microorganisms, Nat. Commun., 9, 2614, https://doi.org/10.1038/s41467-018-04970-7, 2018.

McLean, C. J., Marsh, J. H., Land, A. P., Clark, A., Jennings, R., Ledingham, K. W. D., McCombes, P. T., Marshall, A., Singhal, R. P., and Towrie, M.: Resonant laser ablation (RLA), Int. J. Mass Spectrom., 96, R1–R7, https://doi.org/10.1016/0168-1176(90)80047-7, 1990.

Moffet, R. C., Furutani, H., Rödel, T. C., Henn, T. R., Sprau, P. O., Laskin, A., Uematsu, M., and Gilles, M. K.: Iron speciation and mixing in single aerosol particles from the Asian continental outflow, J. Geophys. Res., 117, D07204, https://doi.org/10.1029/2011JD016746, 2012.

Morrical, B. D., Fergenson, D. P., and Prather, K. A.: Coupling two-step laser desorption/ionization with aerosol time-of-flight mass spectrometry for the analysis of individual organic particles, J. Am. Soc. Mass Spectrom., 9, 1068–1073, https://doi.org/10.1016/S1044-0305(98)00074-9, 1998.

Murphy, D. M.: The design of single particle laser mass spectrometers, Mass Spectrom. Rev., 26, 150–165, https://doi.org/10.1002/mas.20113, 2007.

Murphy, D. M., Froyd, K. D., Bian, H., Brock, C. A., Dibb, J. E., DiGangi, J. P., Diskin, G., Dollner, M., Kupc, A., Scheuer, E. M., Schill, G. P., Weinzierl, B., Williamson, C. J., and Yu, P.: The distribution of sea-salt aerosol in the global troposphere, Atmos. Chem. Phys., 19, 4093–4104, https://doi.org/10.5194/acp-19-4093-2019, 2019.

Neubauer, K. R., Johnston, M. V., and Wexler, A. S.: Humidity effects on the mass spectra of single aerosol particles, Atmos. Environ., 32, 2521–2529, https://doi.org/10.1016/S1352-2310(98)00005-3, 1998.

Oakes, M., Ingall, E. D., Lai, B., Shafer, M. M., Hays, M. D., Liu, Z. G., Russell, A. G., and Weber, R. J.: Iron solubility related to particle sulfur content in source emission and

ambient fine particles, Environ. Sci. Technol., 46, 6637–6644, https://doi.org/10.1021/es300701c, 2012.

Passig, J., Schade, J., Oster, M., Fuchs, M., Ehlert, S., Jäger, C., Sklorz, M., and Zimmermann, R.: Aerosol Mass Spectrometer for Simultaneous Detection of Polyaromatic Hydrocarbons and Inorganic Components from Individual Particles, Anal. Chem., 89, 6341–6345, https://doi.org/10.1021/acs.analchem.7b01207, 2017.

Pöschl, U. and Shiraiwa, M.: Multiphase chemistry at the atmosphere-biosphere interface influencing climate and public health in the anthropocene, Chem. Rev., 115, 4440–4475, https://doi.org/10.1021/cr500487s, 2015.

Pratt, K. A. and Prather, K. A.: Mass spectrometry of atmospheric aerosols – recent developments and applications. Part II: On-line mass spectrometry techniques, Mass Spectrom. Rev., 31, 17–48, https://doi.org/10.1002/mas.20330, 2012.

Pratt, K. A., Mayer, J. E., Holecek, J. C., Moffet, R. C., Sanchez, R. O., Rebotier, T. P., Furutani, H., Gonin, M., Fuhrer, K., Su, Y., Guazzotti, S., and Prather, K. A.: Development and characterization of an aircraft aerosol time-of-flight mass spectrometer, Anal. Chem., 81, 1792–1800, https://doi.org/10.1021/ac801942r, 2009.

Qin, X., Bhave, P. V., and Prather, K. A.: Comparison of two methods for obtaining quantitative mass concentrations from aerosol time-of-flight mass spectrometry measurements, Anal. Chem., 78, 6169–6178, https://doi.org/10.1021/ac060395q, 2006.

Reilly, P. T. A., Lazar, A. C., Gieray, R. A., Whitten, W. B., and Ramsey, J. M.: The Elucidation of Charge-Transfer-Induced Matrix Effects in Environmental Aerosols Via Real-Time Aerosol Mass Spectral Analysis of Individual Airborne Particles, Aerosol Sci. Technol., 33, 135–152, https://doi.org/10.1080/027868200410895, 2000.

Reinard, M. S. and Johnston, M. V.: Ion formation mechanism in laser desorption ionization of individual nanoparticles, J. Am. Soc. Mass Spectrom., 19, 389–399, https://doi.org/10.1016/j.jasms.2007.11.017, 2008.

Rolph, G., Stein, A., and Stunder, B.: Real-time Environmental Applications and Display sYstem: READY, Environ. Model. Softw., 95, 210–228, https://doi.org/10.1016/j.envsoft.2017.06.025, 2017.

Schade, J., Passig, J., Irsig, R., Ehlert, S., Sklorz, M., Adam, T., Li, C., Rudich, Y., and Zimmermann, R.: Spatially Shaped Laser Pulses for the Simultaneous Detection of Polycyclic Aromatic Hydrocarbons as well as Positive and Negative Inorganic Ions in Single Particle Mass Spectrometry, Anal. Chem., 91, 10282–10288, https://doi.org/10.1021/acs.analchem.9b02477, 2019.

Schoolcraft, T. A., Constable, G. S., Zhigilei, L. V., and Garrison, B. J.: Molecular dynamics simulation of the laser disintegration of aerosol particles, Anal. Chem., 72, 5143–5150, https://doi.org/10.1021/ac0007635, 2000.

Seder, T. A., Ouderkirk, A. J., and Weitz, E.: The wavelength dependence of excimer laser photolysis of Fe(CO) 5 in the gas phase. Transient infrared spectroscopy and kinetics of the Fe(CO) x ($x = 4, 3, 2$) photofragments, J. Chem. Phys., 85, 1977–1986, https://doi.org/10.1063/1.451141, 1986.

Seinfeld, J. H. and Pandis, S. N.: Atmospheric chemistry and physics: From air pollution to climate change, 3rd edn., Wiley, Hoboken, New Jersey, 1120 pp., 2016.

Shen, X., Saathoff, H., Huang, W., Mohr, C., Ramisetty, R., and Leisner, T.: Understanding atmospheric aerosol particles with improved particle identification and quantification by single-particle mass spectrometry, Atmos. Meas. Tech., 12, 2219–2240, https://doi.org/10.5194/amt-12-2219-2019, 2019.

Silva, P. J. and Prather, K. A.: Interpretation of Mass Spectra from Organic Compounds in Aerosol Time-of-Flight Mass Spectrometry, Anal. Chem., 72, 3553–3562, https://doi.org/10.1021/ac9910132, 2000.

Sofiev, M., Winebrake, J. J., Johansson, L., Carr, E. W., Prank, M., Soares, J., Vira, J., Kouznetsov, R., Jalkanen, J.-P., and Corbett, J. J.: Cleaner fuels for ships provide public health benefits with climate tradeoffs, Nat. Commun., 9, 406, https://doi.org/10.1038/s41467-017-02774-9, 2018.

Song, X.-H., Hopke, P. K., Fergenson, D. P., and Prather, K. A.: Classification of Single Particles Analyzed by ATOFMS Using an Artificial Neural Network, ART-2A, Anal. Chem., 71, 860–865, https://doi.org/10.1021/ac9809682, 1999.

Stein, A. F., Draxler, R. R., Rolph, G. D., Stunder, B. J. B., Cohen, M. D., and Ngan, F.: NOAA's HYSPLIT atmospheric transport and dispersion modeling system, B. Am. Meteorol. Soc., 96, 2059-2077, https://doi.org/10.1175/BAMS-D-14-00110.1, 2015.

Su, Y., Sipin, M. F., Furutani, H., and Prather, K. A.: Development and characterization of an aerosol time-of-flight mass spectrometer with increased detection efficiency, Anal. Chem., 76, 712–719, https://doi.org/10.1021/ac034797z, 2004.

Sullivan, R. C., Guazzotti, S. A., Sodeman, D. A., and Prather, K. A.: Direct observations of the atmospheric processing of Asian mineral dust, Atmos. Chem. Phys., 7, 1213–1236, https://doi.org/10.5194/acp-7-1213-2007, 2007.

Sultana, C. M., Cornwell, G. C., Rodriguez, P., and Prather, K. A.: FATES: a flexible analysis toolkit for the exploration of single-particle mass spectrometer data, Atmos. Meas. Tech., 10, 1323–1334, https://doi.org/10.5194/amt-10-1323-2017, 2017.

Thomson, D. S., Middlebrook, A. M., and Murphy, D. M.: Thresholds for Laser-Induced Ion Formation from Aerosols in a Vacuum Using Ultraviolet and Vacuum-Ultraviolet Laser Wavelengths, Aerosol Sci. Technol., 26, 544–559, https://doi.org/10.1080/02786829708965452, 1997.

Toner, S. M., Sodeman, D. A., and Prather, K. A.: Single Particle Characterization of Ultrafine and Accumulation Mode Particles from Heavy Duty Diesel Vehicles Using Aerosol Time-of-Flight Mass Spectrometry, Environ. Sci. Technol., 40, 3912–3921, https://doi.org/10.1021/es051455x, 2006.

Trainor, D. W. and Mani, S. A.: Pumping iron: A KrF laser pumped atomic iron laser, J. Chem. Phys., 68, 5481–5485, https://doi.org/10.1063/1.435727, 1978.

Uski, O., Jalava, P. I., Happo, M. S., Torvela, T., Leskinen, J., Mäki-Paakkanen, J., Tissari, J., Sippula, O., Lamberg, H., Jokiniemi, J., and Hirvonen, M.-R.: Effect of fuel zinc content on toxicological responses of particulate matter from pellet combustion in vitro, Sci. Total Environ., 511, 331–340, https://doi.org/10.1016/j.scitotenv.2014.12.061, 2015.

Vera, C. C., Trimborn, A., Hinz, K.-P., and Spengler, B.: Initial velocity distributions of ions generated by in-flight laser desorption/ionization of individual polystyrene latex microparticles as studied by the delayed ion extraction method, Rapid Commun. Mass Spectrom., 19, 133–146, https://doi.org/10.1002/rcm.1753, 2005.

Verdun, F. R., Krier, G., and Muller, J. F.: Increased sensitivity in laser microprobe mass analysis by using resonant two-photon ionization processes, Anal. Chem., 59, 1383–1387, https://doi.org/10.1021/ac00137a003, 1987.

Wade, E. E., Farquar, G. R., Steele, P. T., McJimpsey, E. L., Lebrilla, C. B., and Fergenson, D. P.: Wavelength and size dependence in single particle laser aerosol mass spectra, J. Aerosol Sci., 39, 657–666, https://doi.org/10.1016/j.jaerosci.2008.03.007, 2008.

Wang, G., Zhang, R., Gomez, M. E., Yang, L., Levy Zamora, M., Hu, M., Lin, Y., Peng, J., Guo, S., Meng, J., Li, J., Cheng, C., Hu, T., Ren, Y., Wang, Y., Gao, J., Cao, J., An, Z., Zhou, W., Li, G., Wang, J., Tian, P., Marrero-Ortiz, W., Secrest, J., Du, Z., Zheng, J., Shang, D., Zeng, L., Shao, M., Wang, W., Huang, Y., Wang, Y., Zhu, Y., Li, Y., Hu, J., Pan, B., Cai, L., Cheng, Y., Ji, Y., Zhang, F., Rosenfeld, D., Liss, P. S., Duce, R. A., Kolb, C. E., and Molina, M. J.: Persistent sulfate formation from London Fog to Chinese haze, P. Natl. Acad. Sci. USA, 113, 13630–13635, https://doi.org/10.1073/pnas.1616540113, 2016.

Woods, E., Smith, G. D., Dessiaterik, Y., Baer, T., and Miller, R. E.: Quantitative Detection of Aromatic Compounds in Single Aerosol Particle Mass Spectrometry, Anal. Chem., 73, 2317–2322, https://doi.org/10.1021/ac001166l, 2001.

Ye, D., Klein, M., Mulholland, J. A., Russell, A. G., Weber, R., Edgerton, E. S., Chang, H. H., Sarnat, J. A., Tolbert, P. E., and Ebelt Sarnat, S.: Estimating Acute Cardiovascular Effects of Ambient $PM_{2.5}$ Metals, Environ. Health Persp., 126, 27007, https://doi.org/10.1289/EHP2182, 2018.

Young, J. P., Shaw, R. W., and Smith, D. H.: Resonance ionization mass spectrometry, Anal. Chem., 61, 1271A–1279A, https://doi.org/10.1021/ac00197a002, 1989.

Zhang, G., Bi, X., Lou, S., Li, L., Wang, H., Wang, X., Zhou, Z., Sheng, G., Fu, J., and Chen, C.: Source and mixing state of iron-containing particles in Shanghai by individual particle analysis, Chemosphere, 95, 9–16, https://doi.org/10.1016/j.chemosphere.2013.04.046, 2014.

Zhou, Y., Huang, X. H., Griffith, S. M., Li, M., Li, L., Zhou, Z., Wu, C., Meng, J., Chan, C. K., Louie, P. K. K., and Yu, J. Z.: A field measurement based scaling approach for quantification of major ions, organic carbon, and elemental carbon using a single particle aerosol mass spectrometer, Atmos. Environ., 143, 300–312, https://doi.org/10.1016/j.atmosenv.2016.08.054, 2016.

Zimmermann, R., Ferge, T., Gälli, M., and Karlsson, R.: Application of single-particle laser desorption/ionization time-of-flight mass spectrometry for detection of polycyclic aromatic hydrocarbons from soot particles originating from an industrial combustion process, Rapid Commun. Mass Spectrom., 17, 851–859, https://doi.org/10.1002/rcm.979, 2003.

Atmospheric
Chemistry
and Physics

Supplement of

Resonance-enhanced detection of metals in aerosols using single-particle mass spectrometry

Johannes Passig et al.

*Correspondence to:* Johannes Passig (johannes.passig@uni-rostock.de)
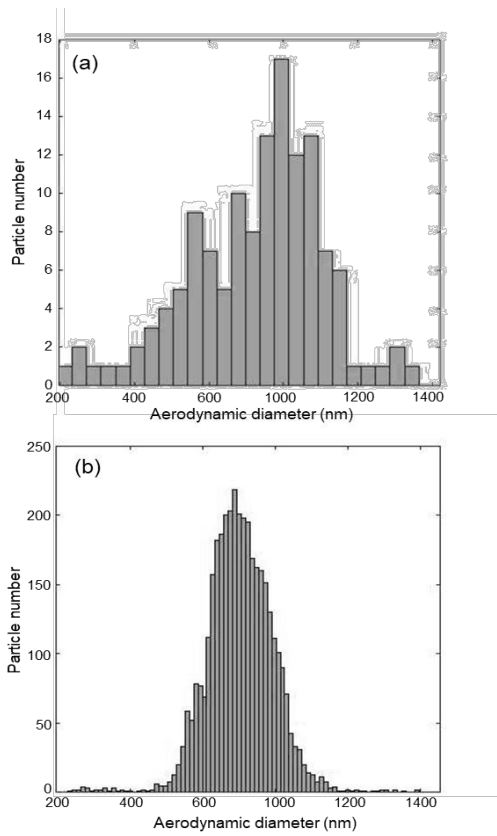
Figure S1: Particle size distributions for ambient air, measured with the optical detection unit of the SPMS at the site in Onsala, Sweden on the 09th Oct 2019 for each 1h, respectively; (a) without using the aerosol concentrator and (b) with the concentrator as described in the methods section. The real particle concentration factor in our experiment is obviously lower than the ratio of air intake and outlet volume (300:1).
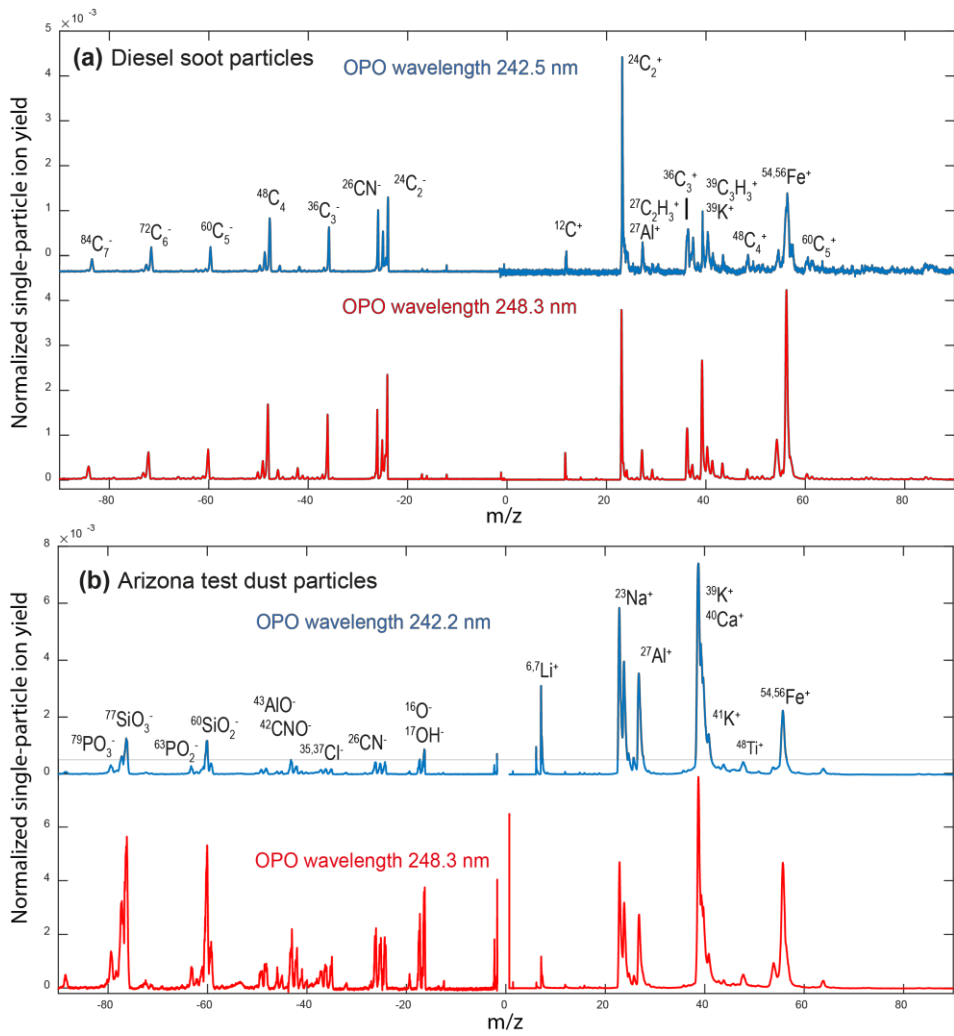
Figure S2: Averaged mass spectra (n=400) of the single-particle signal normalized to the total ion signal of each particle for (a) re-dispersed diesel soot (b) Arizona test dust particles.
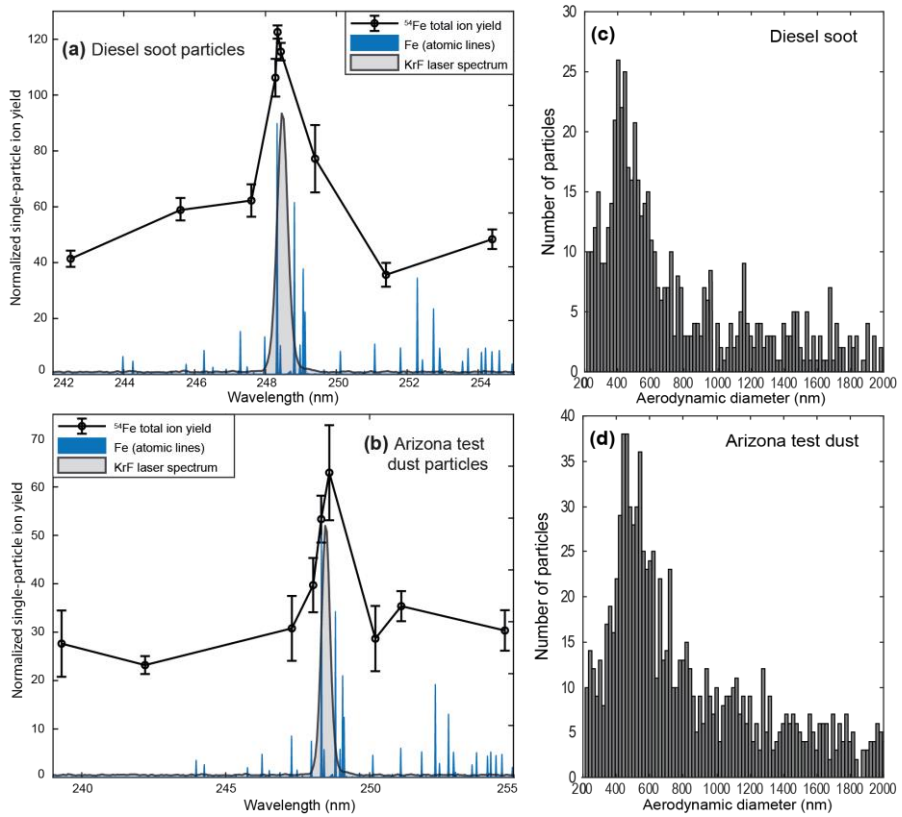
Figure S3: (a) Wavelength-dependent relative ion yield of ^{54}Fe (normalized to single-particle total ion signal) in SPMS of re-dispersed diesel soot particles (black circles, n=1200 in three replicates of 400 each). (b) The same results for Arizona desert dust particles. Major atomic transition lines of Fe in blue. Coincidentally, the Fe-lines are also addressed by our KrF-excimer laser (measured spectrum in grey, arbitrary units). Atomic spectra from the NIST library (Kramida and Ralchenko). Mass spectra are shown in Supplemental Figure S2.

(c) Size distribution of diesel soot particles, and (d) re-dispersed Arizona test dust particles, measured with the laser velocimetry sizing unit of the SPMS instrument.
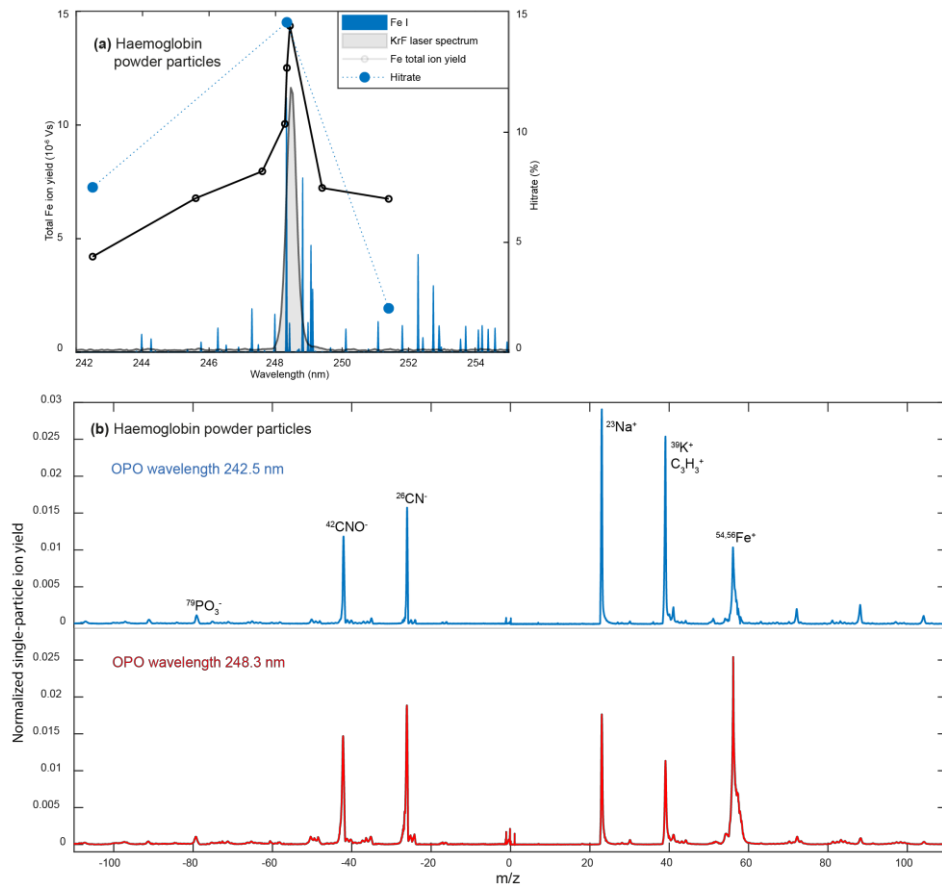
Figure S4: Results for hemoglobin from bovine blood (lyophilized powder, Merck Sigma Aldrich). (a) Wavelength-dependent total ion yield of ^{54}Fe (black circles, each n=250). The hit rate in this experiment (blue circles) dropped considerably for wavelengths above the Fe-resonance, complicating measurements beyond the resonance peak. However, the enhancement is clearly visible.

(b) Corresponding mass spectra for non-resonant (blue) and resonant (red) ionization, averaged over n=250 mass spectra, each normalized to single-particle total ion yield, respectively.
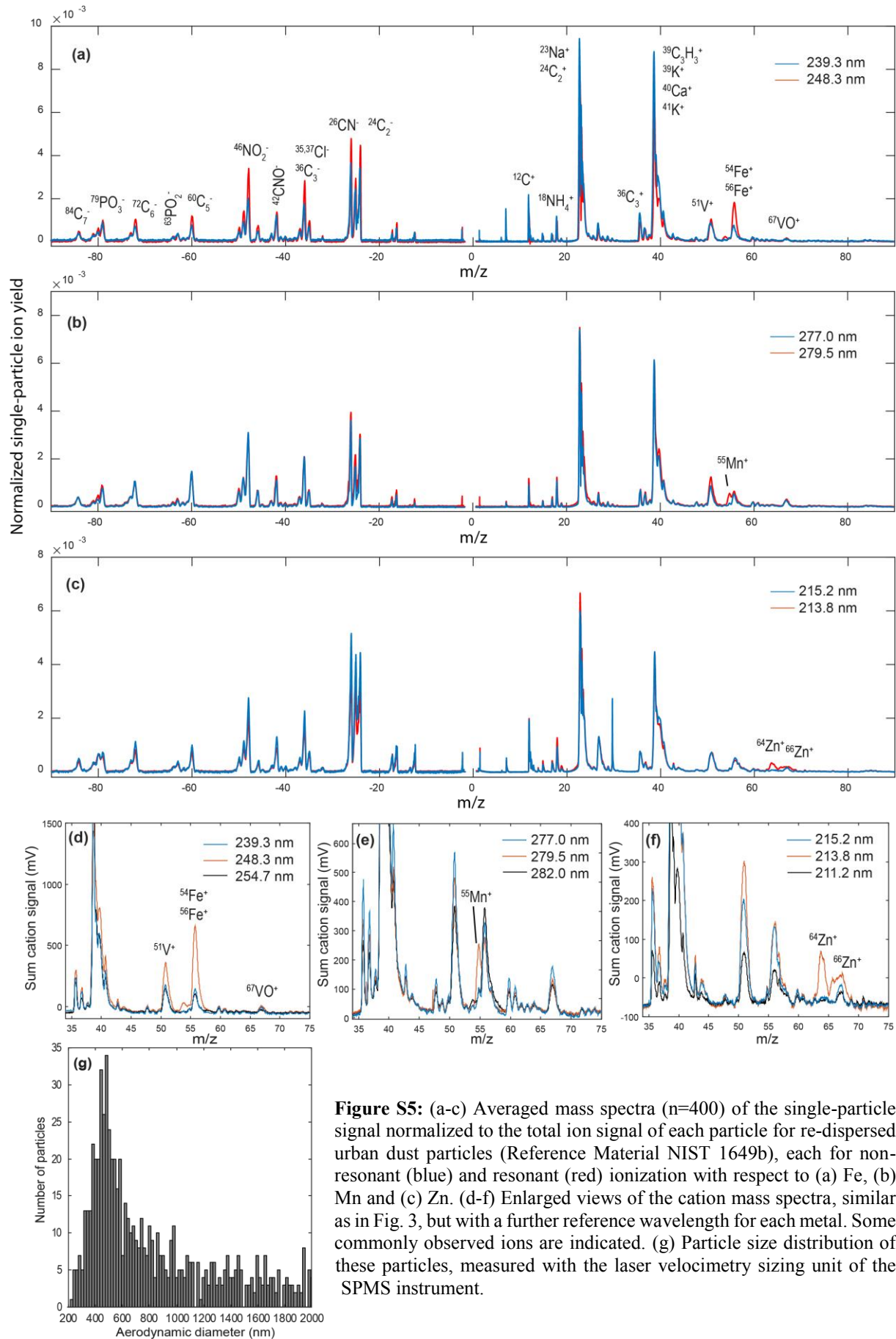
Figure S5: (a-c) Averaged mass spectra (n=400) of the single-particle signal normalized to the total ion signal of each particle for re-dispersed urban dust particles (Reference Material NIST 1649b), each for non-resonant (blue) and resonant (red) ionization with respect to (a) Fe, (b) Mn and (c) Zn. (d-f) Enlarged views of the cation mass spectra, similar as in Fig. 3, but with a further reference wavelength for each metal. Some commonly observed ions are indicated. (g) Particle size distribution of these particles, measured with the laser velocimetry sizing unit of the SPMS instrument.
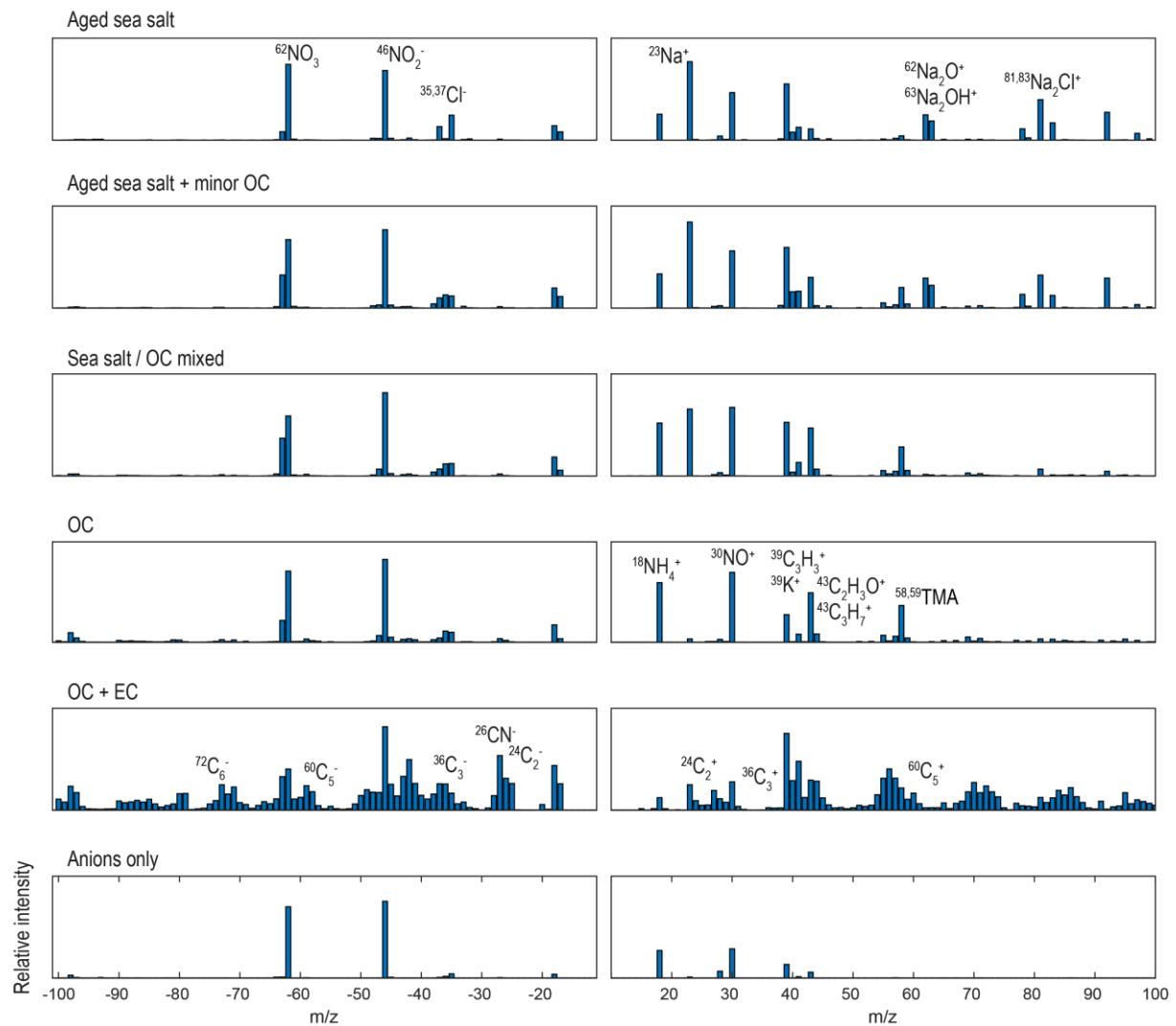
Figure S6: Main particle categories from the ambient air experiment with the 193 nm ArF laser after ART-2a clustering followed by manual merging with respect to the main compounds, see Table 2 for further details. Most particles were mixed of sea salt contributions, nitrate and organic fragments. EC signatures were detected in only 250 particles, along with strong fragment signals and partly with Fe signatures. They appeared occasionally over the full time and not within a single episode.
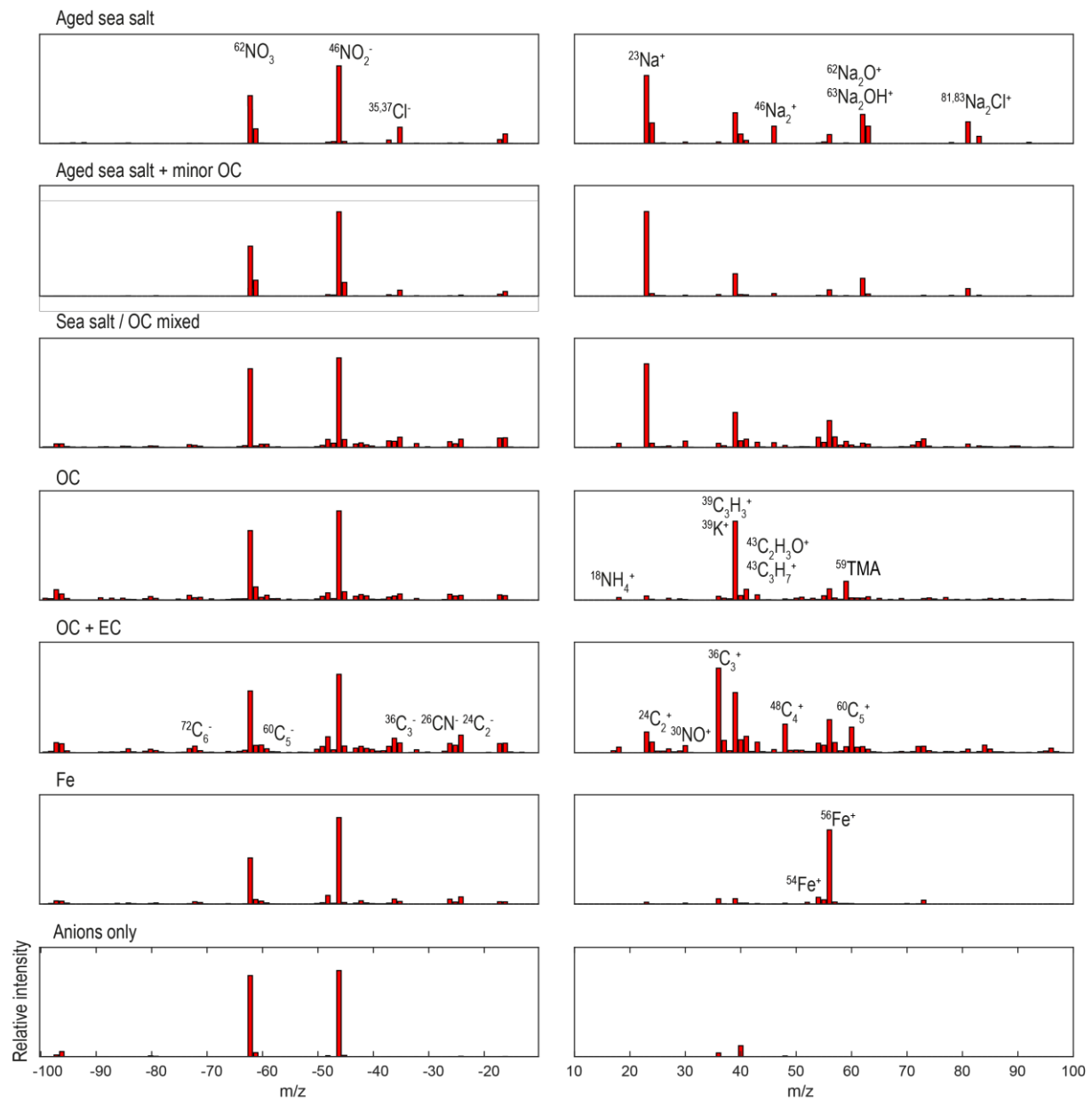
Figure S7: Main particle categories from the ambient air experiment with the 248 nm KrF laser after ART-2a clustering followed by manual merging with respect to the main compounds, see Table 2 for further details. Most particles were mixed of sea salt contributions, nitrate and organic fragments. Many particles that showed only anions (m/z=+54…56 were excluded from the ART-2a clustering) revealed exclusively Fe-signature in their cation spectra, contributing an own cluster. Fe-signatures appeared also for many particles with organic content. Differences between the two wavelengths beyond Fe-detection will be discussed in a future publication.
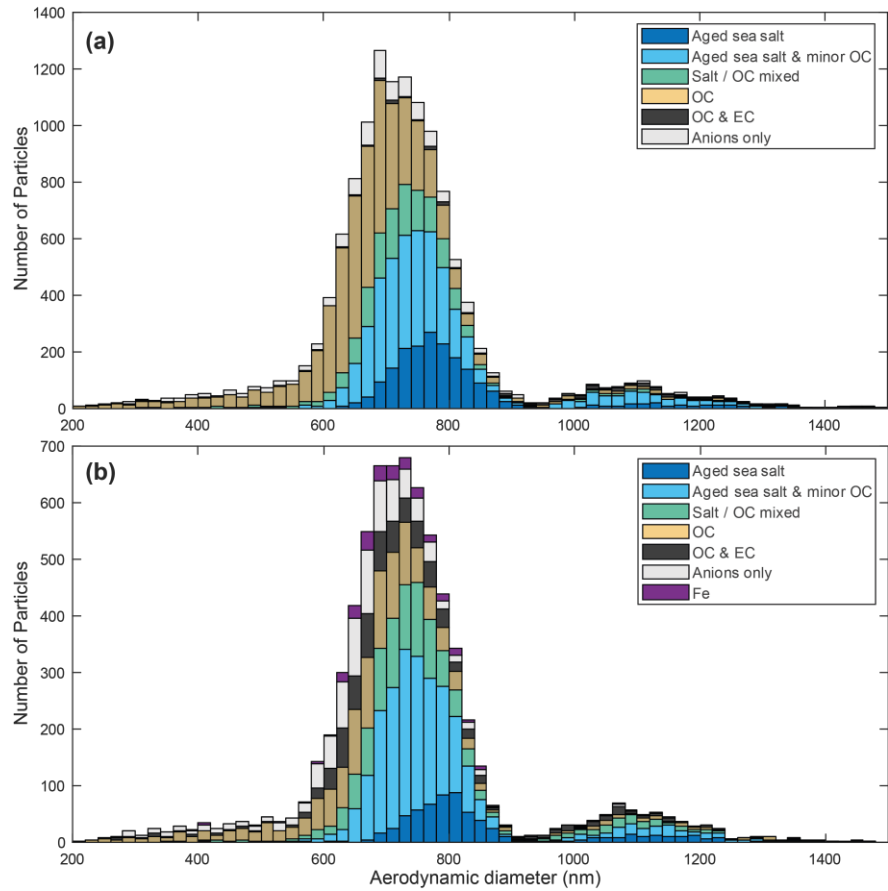
Figure S8: Particle size distribution of the main particle classes in the ambient air experiment; (a) for ionization with the 193 nm ArF-laser and (b) for the 248 nm KrF-laser. Note that the cutpoint for efficient aerosol concentration (≈0.5…1 µm), for optimum optical detection efficiency and the typical long-range transport size mode roughly coincide, thus the size distribution is rather narrow and biased by the instrument. However, it can be noticed that OC-dominated particles dominate the smaller size range while sea salt particles contribute mainly to the larger sizes and to the second mode at 1-1.2 µm.